Dynamics and stability of a non-Newtonian falling film

Symphony Chakraborty

Dynamics and stability of a non-Newtonian falling film

SYMPHONY CHAKRABORTY

2nd July 2012
Laboratoire FAST - UMR 7608 (UPMC-UPS-CNRS)
Bat. 502 - Campus Universitaire
91405 Orsay Cedex, FRANCE.

Submitted on 7th May 2012 in partial fulfillment of the requirements for the degree of Doctor of Philosophy
UPMC Paris VI, FRANCE.

Members of Jury:

Dr. Neil RIBE	Director
Dr. Christian RUYER-QUIL	Co-Supervisor
Dr. Valéry BOTTON	Reviewer
Prof. Richard CRASTER	Reviewer
Prof. Huai-Zhi LI	Examiner
Dr. Maurice ROSSI	Examiner

Dynamique et stabilité d'un film tombant non-Newtonien

SYMPHONY CHAKRABORTY

soutenance prévue le 2 Juillet 2012
Laboratoire FAST - UMR 7608 (UPMC-UPS-CNRS)
Bat. 502 - Campus Universitaire
91405 Orsay Cedex, FRANCE.

Soumis le 7 Mai 2012
UPMC Paris VI, FRANCE.

Membres du Jury:

Dr. Neil RIBE	directeur
Dr. Christian RUYER-QUIL	co-directeur
Dr. Valéry BOTTON	rapporteur
Prof. Richard CRASTER	rapporteur
Prof. Huai-Zhi LI	examinateur
Dr. Maurice ROSSI	examinateur

Disclaimer

This thesis includes part of the research I have published with my supervisor Dr. Christian Ruyer-Quil, in the following articles:
a) Ruyer-Quil, C., Chakraborty, S. and Dandapat, B.S. 2012. Wavy regime of a power-law film flow. *J. Fluid Mech.*, **692**, 220-256.
b) Chakraborty, S., Ruyer-Quil, C., Nguyen, P.-K. and Bontozoglou, V. Numerical prediction of the properties of solitary waves in the drag-inertia regime. 4th International Symposium on Bifurcations and Instabilities in Fluid Dynamics - BIFD 2011.
The research reported in this document is original and the work of any other researcher has been appropriately referenced.

"karmaṇy evādhikāras te
mā phaleṣu kadāchana
mā karma – phala – hetur bhūr
mā te saṅgo 'stv akarmaṇi"

- You have a right to perform your prescribed duty, but you are not entitled to the fruits of action. Never consider yourself the cause of the results of your activities, and never be attached to not doing your duty.

- The Bhagavad Gita, *the Science of the Supreme Spirit*
Chapter 2, entitled: The Philosophy of Discrimination.

I dedicate this thesis to my parents, Smt. Sukla Chakraborty and Mr. Pranesh Ranjan Chakraborty who have been my inspiration and great support throughout my life.

Acknowledgements

I have now come to the end of another chapter of my life. Looking back, I must admit that it was a long journey and of course very challenging too. From last three years in this project, I have received a great amount of help and support from many people and here I would like to extend my gratitude.

I would like to sincerely acknowledge the support that I have received from my supervisor, Dr.Christian Ruyer-Quil, during the course of my doctoral study. He introduced me to research profession and provided me with much needed encouragement to overcome the technical challenges. I am grateful to him for devoting much of his time towards numerous discussions on the physical aspects of my research. I am indebted to him a lot and little would have been possible without him. I am also indebted to him to introduced me to the software AUTO and Gerris. Without his great guidance and support, it would have been difficult to remain focused due to many obstacles that were presented during the course of this journey. I am also greatful to him, Béatrice Guerrier and Frédéric Doumenc for making sure that all the French administrative work finished in time without any trouble which helped me in saving my valuable research time and give a comfortable working environment.

I would also like to thank Prof.Bhabani Shankar Dandapat for his moral support and guidance. I am also convey my thanks to Didier who was a former intern student of Dr.Christian Ruyer-quil to help me to understand and deal with the problems in Gerris. My thanks also goes to Arghya Samanta, a PhD student working with Dr.Christian Ruyer-Quil, for all the helps he give me to understand the subject and his support and encouragement. I would like to convey my thanks to Prof.Vasilis Bontozoglou in Volos (Greece) to give me his FORTRAN Code to perform numerical simulations; and Khanh, Zhehui, Judith and Anna to make my life comfortable during my staying in Volos for two months and collaboration with UTh group.

I would also like to thank Dr.Sandeep Saha for correcting me on every occasion when my usage of the English language was incorrect. Also, I would like to mention his frequent jokes which kept the atmosphere of my office lively. I have always found in him the person whom I could approach for any help at any hour and he has never disappointed me. My gratitude is also reserved for Ching Hsueh, a fellow student one of my closest friends. She has been a great moral support and has kept me company every time I was lonely.

Neil Ribe, Ching, Sandeep, Anna, Floriane, Jesica, Francesco and Chia-ling also deserve a special mention in this section as they are responsible to keep my social life in Paris active by always inviting me to various events. I would like to thank all my fellow students and friends for all the good times within the laboratory FAST as well as number of outingd to different places. I am also very greatful to the EU/FP7 PEOPLE under Marie Curie Actions - Network for Initial Training - “MULTIFLOW" for organizing sightseeing trip, banquet in many conferences and workshop to give the opportunity to visit different places in different countries. During these trips I met many people who belongs to the network became very good friends. The fun times with them will definitely be missed, but one aspect of this chapter in life I can never forget.

Finally, I would like to acknowledge the love and affection of my parents. No words can express my appreciation and gratitude for all the love and blessings showered by my parents on me and the support from my brother during all these years. They have always encouraged me to pursue the noblest of dreams and advised me appropriately in all my endeavours. I would not have reached this milestone, had it not been for their support.

Abstract

A thin film of a non-Newtonian flowing down an inclined plane under the action of gravity is studied focusing on the effects of the fluid rheology on the complex wave dynamics that develops at the free surface. In chapter 3, the properties of the solitary waves, which organize the disordered dynamics of the Newtonian film, are considered. Direct numerical simulations (DNSs) of purely solitary waves have been performed and compared to the results from the four-equation model derived in [112]. The evolution of a power-law laminar film flow is considered in chapter 5 and modeled within the frame of the lubrication approximation by means of the weighted residual approach. Comparisons to Orr-Sommerfeld stability analysis and to DNS show convincing agreement in both linear and nonlinear regimes. A viscoplasctic film is modeled by the Herschel and Bulkley law and is presented in chapter 6. The elasticity of the pseudo-plug region close to the interface is taken into account by an elasto-visco-plastic constitutive relation derived by Saramito [121]. A model is derived in terms of four-equations for the film thickness, local flow rate and amplitudes of the normal and tangential stresses. A linear stability analysis gives values of the critical Reynolds number in remarkable agreement with the Orr-Sommerfeld analysis.

Key words : Non-Newtonian Fluid, Falling Film, Elasto-visco-plastic, Power laws, Weighted Residuals.

Résumé

On étudie la dynamique d'un film mince d'un fluide non-newtonien s'écoulant sur un plan incliné sous l'action de la gravité en tenant compte des effets d'une rhéologie complexe sur la dynamique des ondes de surface. Au chapitre 3, les propriétés des ondes solitaires, qui organisent la dynamique désordonnée d'un film Newtonien, sont considérées. Des simulations numériques directes (DNSs) d'ondes solitaires ont été effectués et comparés aux résultats d'un modèle à quatre équations formulé dans [112]. Au chapitre 5, l'évolution d'un film de fluide en loi de puissance film est modélisée au moyen de l'approche aux résidus pondérés. Les comparaisons avec l'analyse de stabilité d'Orr-Sommerfeld et de la DNS est en bon accord dans les régimes linéaires et non linéaires. Un film de fluide viscoplastique est modélisé par la loi Herschel et Bulkley est étudié au chapitre 6. L'élasticité du pseudo-bouchon à l'interface est pris en compte par une relation constitutive élasto-visco-plastique proposée par Saramito [121]. Un modèle est formulé en termes de quatre équations pour l'épaisseur du film, le débit local et les amplitudes des contraintes normales et tangentielles. Une analyse de stabilité linéaire donne des valeurs du nombre de Reynolds critique en bon accord avec l'analyse d'Orr-Sommerfeld.

Mots clés : fluide non-newtonien, film tombant, élasto-visco-plastique, Loi de puissance, résidus pondérés.

Contents

List of Figures

List of Tables

Nomenclature

Names	Notations, Expressions
angle of inclination	β
slope coefficient	$\cot\beta$
density	ρ
surface tension	σ
kinametic viscosity	ν
dynamic viscosity	μ_0
viscosity	μ_n
apparent viscosity	μ
effective viscosity	μ_{eff}
For Newtonian fluid:	
viscous gravity length scale	$l_\nu = (\nu^2 g \sin\beta)^{1/3}$
capillary length	$l_c = (\sigma/(\rho g \sin\beta))^{1/2}$
For power-law fluid:	
viscous gravity length scale	$l_\nu = (\mu_n/\rho)^{2/(n+2)}(g\sin\beta)^{(n-2)/(n+2)}$
viscous gravity time scale	$t_\nu = (\mu_n/\rho)^{1/(n+2)}(g\sin\beta)^{-2/(n+2)}$
power-law index	n
gravity acceleration	g
shear stress	τ
yield stress	τ_0
rate of strain tensor	D_{ij}
strain rate	$\dot{\gamma}$
uniform film thickness	$\bar{h}_{\mathrm{N}}$
Froude number	Fr
Reynolds number	Re
Bingham number	Bi
Deborah number	De
reduced Reynolds number	δ
viscous dispersion number	η
reduced angle	ζ

Names	Notations, Expressions
Weber number	We
Elastic modulus	G
consistency parameter	K
Kapitza number	$\Gamma = (l_c/l_\nu)^2$
threshold	s
film thickness	h
average film thickness	$\langle h \rangle$
substrate film thickness	h_{S}
Nusselt film thickness	h_{N}
free surface velocity	V_{N}
film parameter	ϵ
wave number	k
phase speed	c
frequency	f
angular frequency	ω
local flow rate	$q = \int_0^h u\, dy$
average flow rate	$\langle q \rangle$
space coordinates	x, X, y, Y
velocity coordinates	u, U, v, V
Nusselt solution	h_{N}, u_{N}, q_{N}
linear operator	$\mathcal{L} \equiv \partial_{\bar{y}} [n(f_0')^{n-1} \partial_{\bar{y}} \cdot\,]$
fixed points	$\mathbf{U}_{\mathrm{I}}$, $\mathbf{U}_{\mathrm{II}}$
scalar product	$\langle \cdot | \cdot \rangle$

Chapter 1

Introduction

In this thesis, the wave dynamics and stability of a falling film over a plane surface is studied. A thin film flowing down an inclined plane or a vertical wall in the presence of free surface displays a variety of fascinating dynamical behaviors. The dynamics of thin film waves has attracted the attention of various industries due to its dramatic effects on the transport rate of mass, heat and momentum in designing distillation and adsorption columns, evaporators and condensers, in the modern precision coating of photographic emulsions, protective paints and so on. Further, the stability of a falling film flow system along an inclined plane under the action of gravity is a wide research subject. I am mainly focused on the study of the stability of Newtonian and non-Newtonian falling film in this thesis.

Falling liquid films have attracted a considerable interest since the pioneering work by Kapitza & his son [60]. They are examples of open flows for which a sequence of symmetry breaking can lead to a disordered state organized by dissipative structures in interaction, i.e. a weakly turbulent state as defined by Manneville [79]. Falling films have the peculiarity to be low-Reynolds-number flows whose wavy regime is supercritically triggered by a long-wave instability. Therefore, observed surface waves are much longer than the typical thickness of the film and a separation of scales can be used with the introduction of a formal film parameter $\epsilon \sim \partial_{x,t}$ accounting for the slow evolutions in time and space of the waves when compared to the relatively quick viscous diffusion across the film layer. Falling films are therefore amenable to a thorough description in terms of low-dimensional modeling, i.e., a description of the flow in terms of a limited sets of variables depending on time t and position x on the plane may be substituted to the Navier-Stokes equation after elimination of the continuous dependency on the cross-stream coordinate y.

The problem of the stability of the laminar flow of an ordinary viscous fluid film flowing down an inclined plane under gravity was first formulated and solved numerically by Yih [147]. Initially proposed by Benney [9], the long-wave expansion of the velocity field $u = u^{(0)} + \epsilon u^{(1)} + \dots$ leads to a single evolution equation for the film thickness h.

By essence, such a *surface equation* is a generalized kinematic wave equations written as $\partial_t h + \partial_x Q(h) = 0$ [146], where the local flow rate $q \equiv \int_0^h u dy = Q(h)$ is an explicit function of h and its derivatives. It expresses the slaving of the velocity field to the kinematics of the free surface, an assumption that is sustained only at low Reynolds numbers when inertia effects are weak. At moderate Reynolds numbers, time-dependent solutions to the Benney surface equation are known to lead to unphysical blow-up in finite time [103, 123]. This drawback was cured by Ooshida [93] by introducing a Padé-like regularization, however at the cost of an underestimation of the wave speed and amplitude.

Another way to remedy to the drawbacks of the long-wave approach is to relax the strict slaving of the dynamics of the flow to the kinematics of the free surface by introducing one or several variables, or "degrees of freedom" taking into account the imperfect slaving of the velocity distribution on the evolution of the free surface. This idea was initially introduced by Shkadov [126] who proposed to expand the velocity field as

$$u = \sum_i a_i(x,t) f_i(y/h(x,t)) \tag{1.1}$$

and to truncate the Navier-Stokes equation at order $O(\epsilon)$. At that order, the pressure distribution is the hydrostatic one corrected by the Laplace law. After substitution of the pressure, one is lead to a streamwise momentum balance analogous to the Prandtl equation in boundary layer theory, which is thus generally referred to as a boundary layer (BL) equation. In practice, Shkadov truncated (1.1) to only one test function corresponding to the parabolic velocity profile of the Nusselt uniform film solution [91] and integrated the BL equation across the film thickness. Shkadov's averaged momentum equation coupled to the exact mass balance $\partial_t h + \partial_x q = 0$ form a closed system of evolution equations for the film thickness h and the flow rate q, which may be referred to as the integral boundary layer (IBL) model. The Shkadov model has been used extensively by Chang and coworkers at Notre Dame University to study the dynamics of falling films (see [25] and references therein). Comparisons to experiments show a reasonable agreement in the nonlinear regime. However, the Shkadov model does not correctly capture the onset of the primary instability and leads to an erroneous prediction of the instability threshold $Re_c^{\mathrm{IBL}} = \cot\beta$ as function of the inclination angle β, a result that must be contrasted with the the correct threshold $Re_c = \frac{5}{6}\cot\beta$ obtained by Benjamin [10].

A number of studies have followed Shkadov's integral boundary layer approach using different numbers of degrees of freedom and different choices of the test functions (see for instance [149, 86, 96, 111, 112, 113] and the review by Craster [30]). One way to avoid hypotheses on the velocity distribution such as (1.1) is the center manifold approach developed by Robert [107, 108]. The idea comes from the center manifold analysis of dynamical systems of finite dimensions. Considering a fixed point and a linear operator $\mathcal{L}$ that governs the evolution of the trajectories in the vicinity of the fixed point, the center manifold is tangent to the eigenspace spanned by the eigenvectors corresponding to the eigenvalues of zero real parts.

In most cases, a system of two evolution equations for the film thickness h and the flow rate q is obtained. Further, the analysis of the non-linear wave evolution equation is in general very complicated. So, to extract more results from it, most of the previous studies on non-linear wave process are based on the assumption of stationary waves which does not change its phase speed and shape during the course of propagation.

Dandapat & Mukhopadhay [32] analyzed the evolution equation of a power-law film flow on an inclined plane based on a quasi-stationary wave process. They found that the non-linear interaction between kinematic, inertial and gravitational waves are responsible for the formation of waves on a thin film and power-law index n plays a vital role in the wave formation mechanism. Alekseenko *et al.* [2] have initiated this analysis to study the wave formation in a liquid film flow on a vertical wall. It is therefore desirable to investigate the characteristics of the waves in a large range of parameters for a better understanding of the physical phenomena observed on a power-law fluid film flowing down an inclined plane. A power-law model represents a class of generalized Newtonian fluids which do not exhibit any elastic, yield or stress relaxation properties but these fluids show the behavior of shear-thinning (pseudo-plastic) or shear-thickening (dilatant) properties (for details see in chapter 4 and 5). Power-law models have been found to be successful in describing the behavior of colloids and suspensions and a variety of polymeric liquids and low molecular weight biological liquids, in the field of glaciology, blood-rheology and geology. Since this model is different from a Newtonian fluid only in that its viscosity depends on the symmetric part of the velocity gradient so that in a simple shear flow, the viscosity depends on the shear rate. To be more precise such effects are inconsequential, the dominant departure from the Newtonian behavior being shear-thinning or shear-thickening.

Roll waves, i.e. hydraulic jumps connected by sections of gradually varying flows, are generally encountered in torrential regimes of river flows and in man-made conducts like spillways [41, 24, 58]. The possible onset of roll waves was already accounted for in the design of aqueducts by Roman engineers [45]. The onset of roll waves results from an instability mechanism that is similar to the formation of teardrop-like solitary waves on a laminar film falling down an inclined plane. In the latter case surface tension prevents the wave from breaking and arrests the formation of hydraulic jumps. These waves are sometimes referred to as 'capillary roll waves' [8]. As such, film flows can be viewed as a toy system whose wavy dynamics is closely related to the torrential regime of rivers at larger flow rates.

Roll waves can also be observed in overland flows, especially in rill flows, with a potential increase of the soil erosion [72]. In estuaries, rivers may carry large amount of clay and the resulting mud flows are frequently pulsating and resemble roll waves in turbulent flows of clear water [73]. For these two latter examples, interactions between clay particles create extensive microscopic structures that are deformed and gradually broken down when a stress is applied. As a consequence the response of the fluid to a stress is non-linear and mud presents a shear-thinning behavior. Ng & Mei [85] studied the

roll waves on a shallow layer of mud modeled as a power-law fluid. The results indicated that longer roll waves, with dissipation at the discontinuous fronts, cannot be maintained if the uniform flow is linearly stable, when the fluid is slightly non-Newtonian. However, when the fluid is highly non-Newtonian, very long roll waves may still exist even if the corresponding uniform flow is stable to infinitesimal disturbances. Hwang *et al.* [52] studied the linear stability of a power-law liquid film flows down an inclined plane by using the integral method. The results reveal that the system will be more unstable when power-law index n decreases.

Intermittent surges have been observed in mud flows in flooded rivers and flumes (Engelund & Wan [43], Coussot [29]). Besides shear-thinning, another important property of mud is that the interactions between clay particles create an extensive microscopic structure that withstands a certain stress before deforming and allowing the fluid to flow i.e., mud has a yield stress. These viscoplastic effects play key roles in the fluid dynamics of mud and place this fluid in the realm of non-Newtonian fluid mechanics. In fact, certain stability arguments indicate that roll-wave instability is completely absent in viscoplastic films [8]. The essence of this argument is associated with how one perturbs the regions of the flow which are not yet yielded. In uniform viscoplastic films flowing down an inclined planes, one such region always occurs adjacent to the free surface, forming a rigid plug. Balmforth & Liu's [8] concern was the onset of roll waves that are observable in mud surges. As a consequence they did not consider surface tension nor streamwise viscous effects. For that reason, small amplitude perturbations of the free surface are sufficient to trigger the instability and viscosplastic film flows should be conditionally unstable. In order to describe the dynamics of a viscoplastic film, surface tension and streamwise viscous diffusion must be accounted for. Therefore the pseudo-plug theory proposed by Balmforth and Liu [8] need to be extended by introducing for instance the elastic response of the pseudo-plug region to a free surface deformation.

I will organize my work according to the different problems of increasing complexity that have been noticed above. First, reconsidering Newtonian film, I will aim at a thorough analyses of the properties (phase speed, maximum amplitude and shape) of the solitary waves, which is explored in chapter 3. This part of the thesis will be used as a validation of the weighted residual technique initiated by Ruyer-Quil & Manneville [111, 112, 113, 114]. In chapter 4 I have mentioned different types of non-Newtonian fluids and its rheological models which I will consider in chapter 5 and chapter 6 for falling film problems. In chapter 5, I will consider a power-law film flow applying the weighted residual technique and focusing on the effect of a shear-thinning an shear-thickening on the stability of the thin film. In chapter 6, I will present a preliminary study of a viscoplastic film who's rheology is governed by an elasto-viscoplastic constitutive relation introduced by Saramito [121]. A four-equation model is formulated by using the weighted residual approach and Orr-Sommerfeld problem is derived to study the linear stability analysis. Finally, chapter 7 presents a summary of this work along with possible perspectives.

Chapter 2

Instability of a Newtonian falling film

2.1 Introduction

The objective of this chapter is to give a short review of the phenomenology of a Newtonian falling films and to provide a brief description of the modeling attempts to describe such phenomena. Considering a Newtonian incompressible parallel flow, a stability analysis leads to the well-known Orr-Sommerfeld equations. The inertia terms in the Orr-Sommerfeld case is weakly destabilizing only in the sense that large Reynolds numbers are needed for instability, in practice, once breakdown of symmetric flow occurs, the periodic disturbances that grow tend themselves to be unstable and so an essentially random turbulent flow usually develops. For a homogeneous fluid of constant density the effects of gravity are effectively concentrated at interfaces with other fluids. When these surfaces are deformable, the possibility of instability arises; a typical example is that of a uniform flow of a thin liquid layer down an inclined plane (Javdani & Goren [54]). In practice, gravity forces are usually stabilizing and lead to horizontal interfaces between fluids of different density, with the heavier fluid underlying the lighter fluid. Genuinely, the instability usually arises only from a fairly complex interaction of gravity and inertia forces. Instability in Newtonian fluids also arises from interfacial forces.

Generally, the flows of thin fluid films can be found in several aspects of our daily lives, even something as trivial as the flow of tears from the eye. It is initially surprising that the same mathematical frame can be used to model flows on different length scales such as the fluid film flow from eye and, at the other extreme, large scale lava flow or continental ice sheet flows. Thin fluid films can generate a host of intriguing and fascinating behaviors including complex dynamics featuring the formation of regular or chaotic structures, periodic waves, shocks and fronts, and "fingering" phenomena, this pattern formation has attracted many physicists, mathematicians, and engineers toward the field of thin films.

Flows of thin fluid films spreading on solid surfaces have a distinguished history having

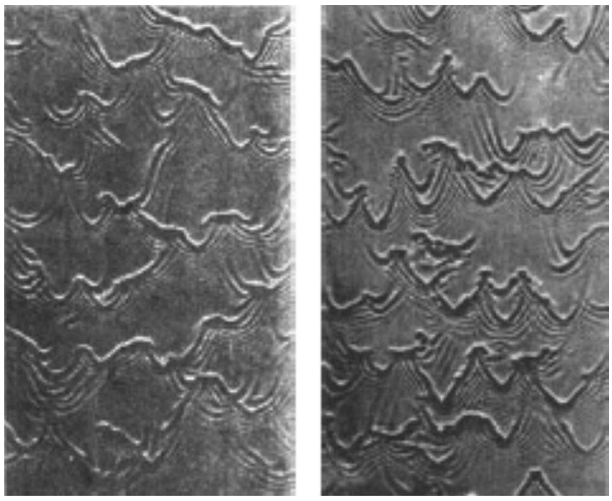

Figure 2.1: Experiments of a water-ethanol mixture flowing down an inclined plate with increasing inertial influence, the Reynolds numbers, Re are 16 and 45 in the left and right panels, respectively. These results demonstrate the development of noise-driven large-amplitude three-dimensional waves in falling films. From Alekseenko *et al.* [4] and Craster & Matar [30].

been studied since the days of Reynolds, who was among the first to examine lubrication flows [105]. Since the pioneering experiment by the father-son team of the Kapitza family during their house arrest in the late forties (Kapitza & Kapitza [60]), wave evolution on a falling film has intrigued many researchers. One of its main attractions is its simplicity-it is an open-flow hydrodynamic instability that occurs at very low flow rates. It can hence be studied with a rather simple experimental apparatus, an obviously important factor for the Kapitzas. Yet, it yields a rich spectrum of fascinating wave dynamics, including a very unique and experimentally well-characterized sequence of nonlinear secondary transitions that begins with a selected monochromatic disturbance and leads eventually to non-stationary and broad-banded (in both frequency and wave number) "turbulent" wave dynamics (turbulence here is used interchangeably with irregular spatio-temporal fluctuations).

Careful experiments by Beauchamp Towers in 1883 and 1884 prompted Reynolds to create what is now called as "lubrication theory", which, subsequently, has been widely used to study thin film flows. A commonly observed "windscreen flow", involves a thin film flowing down an incline at moderate Reynolds number, (see Fig. 2.1, [30]). In this case, inertia is important and the experiments reports the onset of strongly coherent structure which further evolution ultimately yield three-dimensional waves. Despite the highly complex flow structures, recent advances and improvements in both theoretical and numerical techniques now allow one to capture this complex behavior within the context

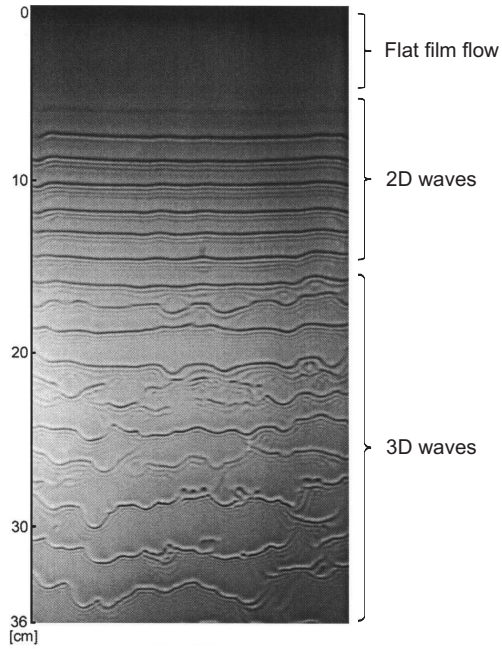

Figure 2.2: Shadow images of waves naturally occurring on a film of water flowing along a vertical plate at $Re = 33$ by Park & Nosoko [97] (from [59]).

of a thin film model [123]. The instability appears at much lower Reynolds numbers than those typically required for a transition to turbulence. The wave patterns evolve in the falling film can show a rich variety of behavior both in space and time.

2.2 Flow evolution on a falling film

The two and three dimensional waves in falling films can be observed on vertical and nearly-vertical configuration in experiments [1, 4, 71, 89, 90, 97]. Generally a falling liquid film exhibits a cascade of symmetry-breaking bifurcations leading from the flat-film flow to a two-dimensional (streamwise dimension and height) periodic wave train, which eventually evolves into solitary waves and further to three-dimensional (streamwise, spanwise dimensions and height) solitary waves and complex flows/wave patterns, observed in experiments as well as predicted by theory. For a two-dimensional flow there is no spanwise dependence and no spanwise velocity component, while the surface elevation varies in the streamwise direction only. For a three-dimensional flow there is dependence in all three directions, while the surface elevation varies in both the streamwise and spanwise directions (see Fig. 2.2).

I give a short description of the phenomenology observed in experiments based on Liu

& Gollub [70] work, the review paper by Chang [19] and the book by Kalliadasis *et al.* [59]. Liu & Gollub considered a moderately inclined plane and its wave dynamics relatively close to the onset of the instability, $Re_c = 5\cot\beta/6$, where the sequence of the primary instability of the Nusselt flat film leading to a primary saturated wavetrain followed by secondary instabilities of the primary wavetrain, is more easily identified than in the vertical case for which the flow is always unstable ($Re_c = 0$) and therefore, by definition, in the experiments one is already far from onset.

The first linear stage is followed by a second stage with non-linear saturation of this growth. Further downstream the wave loses stability, e.g., as a consequence of interaction between the wave harmonics, and the wave pattern is altered, embracing a wide spectrum. This process eventually yields highly asymmetric and nonlinear waves containing most of the liquid, and each of which consisting of a hump with a long flat tail behind. The front of the hump is steep and is preceded by small ripples (also denoted radiations) with a wavelength close to the originally linearly fastest growing wave. These highly asymmetric and nonlinear waves are what we already referred to as solitary waves and have a velocity that increases with their amplitude.

The onset of wave patterns at the surface of a falling film can be very sensitive to the frequency contain of the perturbations applied at the inlet, as shown in Fig. 2.3. For sufficiently large frequencies, the waves are initially two-dimensional but they easily become three-dimensional, and exhibit rather irregular patterning, eventually leading to a seemingly turbulent flow (at a forcing frequency of $100Hz$). Various distinct wave flow features can be identified as the flow rate is increased or the frequency of the forcing at the inlet is varied, as illustrated in Fig. 2.3. For instance, there is a first region that corresponds to growing infinitesimal perturbations introduced by a noise near the inlet that eventually yield a two-dimensional wave of well-defined wavelength downstream. Without forcing (first panel from the left) the wave selected in the first stage corresponds to the fastest growing wave according to the linear stability analysis of the uniform laminar flow. Also, at sufficiently low-frequency of the inlet-forcing, solitary waves appear right after infinitesimal ones saturate (see, e.g., in Fig. 2.3).

Based on the experimental observations, the different secondary instabilities in film flows leading to irregular patterns are schematically summarized in Fig. 2.4. The evolution of film flow along an inclined plane can be broadly distinguished into four regimes, each corresponding to a different region on the inclined plane. The inception region is the domain close to the inlet where the primary linear instability of the flat film develops in space. The observed primary waves are two-dimensional because the fastest growing perturbations are spanwise-independent, stipulated by Squire's theorem [147]. The amplitude of the waves saturates and their shape remains practically unchanged over distances corresponding to a few wavelengths (region II). Subsequent events depend on the forcing frequency.

It is observed that at large frequencies but below the cut-off frequency, the primary waves are slow and are characterized by wide bumpy crests and deep thin troughs, whereas

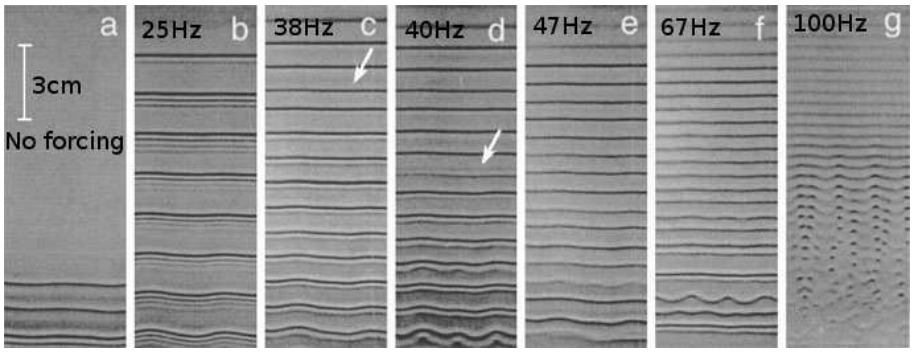

Figure 2.3: Shadow images of waves in a film of water flowing down a vertical plate at $Re = 52$. With the exception of the first panel on the left, the inlet flow rate is periodically forced at the frequencies indicated in the upper right corner of each panel (in Hz). The white arrows indicate the appearance of double-peaked waves. From Nosoko *et al.* [89] and [59].

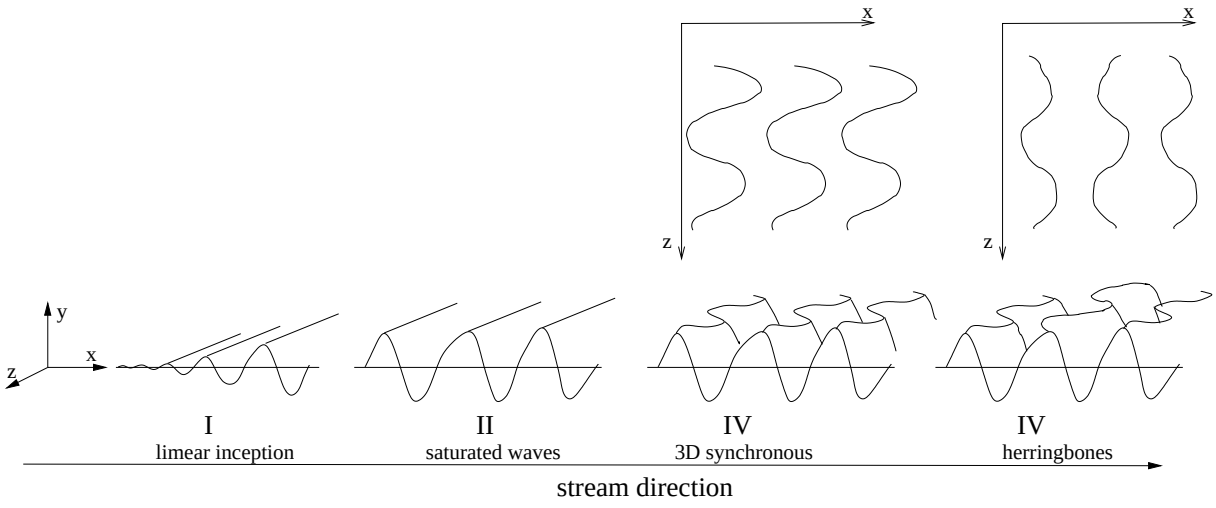

(a) high frequency

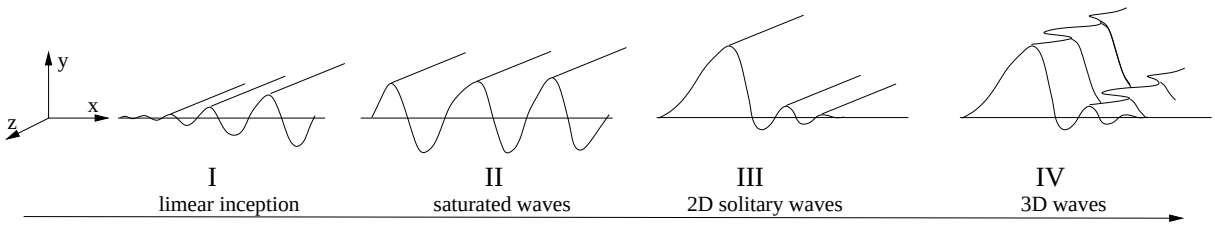

(b) low frequency

Figure 2.4: Schematic description of the spatial evolution of the film flows (from [59]).

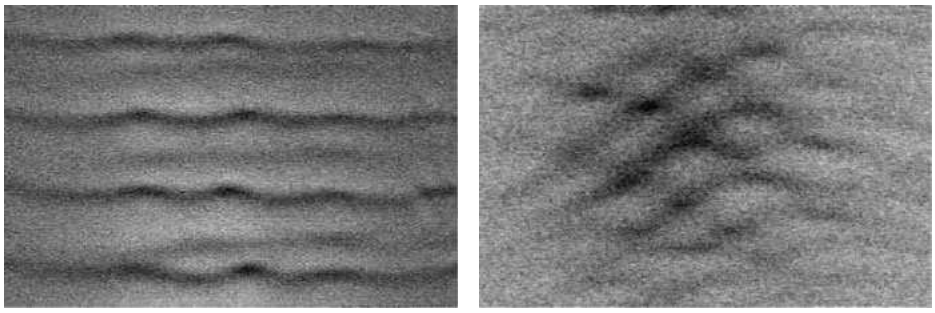

(a) (b)

Figure 2.5: (a) Synchronous instability; (b) subharmonic instability with herringbone pattern. From Émery & Brosse [42] and [59].

above the cut-off frequency the system is linearly stable (see in Fig. 2.4(a)). They belong to the γ_1 family following the terminology introduced by Chang [19, 20]. Two different scenarios are possible for the next evolution, first one can be referred to as a *synchronous instability* which is characterized by in-phase deformation of neighboring troughs in the spanwise direction, whereas the crests remain undisturbed. The second one is less observed, characterized by a phase shift between two successive crests which leads to *herringbone patterns*, characteristic of a spanwise modulation combined with a streamwise *subharmonic instability*, corresponding to a resonance between the frequency f of the two-dimensional traveling waves and its subharmonic $f/2$ (of Fig. 2.5). This instability triggers a doubling of the wavelength of the primary waves. At high enough forcing frequency, the flow becomes disordered before the onset of two-dimensional solitary waves because three-dimensional instabilities are stronger than two-dimensional, which explains the absence of region III in the corresponding picture (Fig. 2.4(a)). In Fig. 2.4(b), at low frequencies, the saturated waves triggered by the flat film primary instability experience a secondary instability which eventually leads to large amplitude two-dimensional solitary waves in the form of fast humps preceded by capillary ripples (region III). Such waves belong to the γ_2 family, following the terminology introduced by Chang [19, 20]. They are generally unstable to transverse perturbations, which leads to the last stage of secondary three-dimensional instabilities (region IV, see Fig. 2.6). Finally, at very low forcing frequencies, saturated γ_1 waves (region II) do not show up and the solitary-like wavetrains of the γ_2 family are directly generated by inlet forcing.

Depending on the flow regime, different levels of reduction can be used to simplify the governing equations, namely Navier–Stokes equations. Different approximations enable to perform a "gradient expansion" of the velocity and temperature fields and to subsequently obtain systems of equations of reduced dimensionality to model the dynamics of the flow.

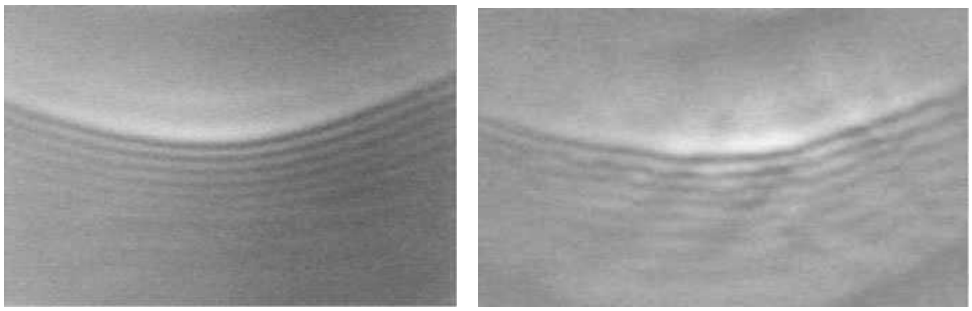

(a) (b)

Figure 2.6: (a) Quasi-two-dimensional solitary wave; (b) spanwise instability of a quasi-two-dimensional solitary wave. From Émery & Brosse [42] and [59].

2.3 Modeling attempts: a short review

In this section, my intention is to enlighten the modeling attempts by many scientists devoted to the falling film problem in last few decades. The classical modeling approach for falling film flow is the long-wave theory based on a gradient expansion of the governing equations with respect to a small parameter $\epsilon \sim |\partial_x h|/h \ll 1$, the so-called film parameter which measures the slow variations of the free surface in time and space. The theory typically leads to a single evolution equation for the film thickness h which is referred to as the Benney equation. The problem in isothermal case was first solved by Benney in 1966, later on by several other authors (see the reviews by Oron *et al.* [94] and Craster & Matar [30]). The Benney equation can be written as

$$\partial_t h + \frac{1}{3}\partial_x \left(h^3 + \frac{2}{5}\delta h^6 \partial_x h - \zeta h^3 \partial_x h + h^3 \partial_{xxx} h \right) = 0, \tag{2.1}$$

which describes the evolution of film thickness. Here, $\delta = 3Re/We^{\frac{1}{3}}$ is a reduced Reynolds number, $\zeta = \cot\beta We^{1/3}$ is the reduced slope, $Re = h_N^3/3$ and $We = \Gamma/h_N^2$ are the Reynolds and Weber numbers. Since this equation contains the film thickness h and its derivatives, is also called a *surface equation*. This scaling is inherent to the falling film problem in the region of moderate Reynolds numbers due to the separation of scales in the streamwise and cross-stream directions in this region that is in fact due to the strong effect of surface tension. It also makes apparent the balance among all forces, i.e., inertia, gravity, viscosity and surface tension, necessary to sustain strongly nonlinear waves.

Unfortunately, it is valid only close to the instability threshold and fails to reproduce the behavior of the film outside a close neighborhood of the threshold. The situation is not improved by pushing the gradient expansion to higher order, which leads to a more complicated equation with no better properties. The fundamental reason for the inability

of the Benney equation to describe nonlinear waves far from criticality (even though departure from the streamwise velocity distribution from the Nusselt flat film parabolic profile are small) is the slaving of all flow variables to the film thickness h. Benney equation has its own shortcoming, mainly it shows an unphysical behavior when $\delta > 1$ the drag-inertia regime as nicknamed by Ooshida [93]. In the drag-inertia regime, inertia plays a significant role, which is opposed to the drag-gravity regime (which corresponds to a balance between viscous drag on the wall and gravity acceleration) where inertia plays a perturbative role. It is precisely because inertia terms were considered as first-order perturbations in the gradient expansion parameter ϵ of the drag-gravity balance, which in turn corresponds to the Nusselt flat film flow, that the Benney equation can be derived.

Most of the models are based on an *in-depth averaging* of the original equations, i.e. averaging of the equations across the film, which require to introduce closure assumptions on the functional form of the dependence of the velocity on the film thickness. The procedure generally starts with a gradient expansion for the velocity field which can only be justified rigorously when inertia plays a weak/perturbative role, that is in the drag-gravity regime (δ less than unity). Following the long-wave/Benney equation approach, a nonlinear free-boundary problem is converted into a sequence of solvable problems. Hence the velocity field is obtained explicitly at each step in terms of functions of h but with amplitudes which are independent of h (e.g. to leading order, the amplitude of the velocity field contains the flow rate q). Contrary to the long-wave theory/Benney equation expansion where all variables are slaved to h, the averaging approach gives a higher level of flexibility to the velocity thus allowing it to have its own evolution. This is the fundamental difference between the averaging procedure and classical long-wave theory. Yet the velocity is described by a limited number of variables. The in-depth coherence of the flow is ensured by gravity and viscosity with inertia playing a perturbative role. The aim is to derive the simplest set of equations assuming small inertia effects that remain accurate when this assumption starts to be violated, i.e. as one proceeds from the drag-gravity to the drag-inertia regimes.

As a matter of fact, many models have been derived since the pioneering work of Kapitza [60]. Later on, Shkadov extended to non-stationary two-dimensional flows and then to three-dimensional ones by Demekhin & Shkadov [34]. In most of the cases found in literature, surface equations for film flows are based on the mass conservation equation (5.14) which is rewritten here for clarity

$$\partial_t h + \partial_x q = 0. \tag{2.2}$$

The Kapitza-Shkadov approximation leads to two coupled evolution equations for film thickness h and streamwise flow rate q. Considering boundary-layer equations at lowest order and assuming that the velocity profile is parabolic, Shkadov's model is obtained as follows,

$$\delta\partial_t q = h - 3\frac{q}{h^2} - \delta\left\{\frac{12}{5}\frac{q}{h}\partial_x q - \frac{6}{5}\frac{q^2}{h^2}\partial_x h\right\} - \zeta h\partial_x h + h\partial_{xxx} h = 0, \tag{2.3}$$

which is apparently free of finite-time blow-up but fails to give a quantitatively accurate description of the instability threshold. This model is not good enough to capture inertia correctly though inertia and surface tension are not considered small. Results for isothermal nonlinear waves far from criticality obtained from the Kapitza–Shkadov model are in quantitative agreement with the boundary layer [35] and full Navier-Stokes equations for moderate Reynolds numbers [36, 104, 119]. However, the Kapitza–Shkadov approach does not predict well neutral and critical conditions, except for large inclination angles. Indeed, it has been shown that for a vertical falling film, the Kapitza–Shkadov model gives the correct value for the critical Reynolds number, i.e., zero.

This shortcoming has been resolved by Ruyer-Quil & Manneville combining the gradient expansion with a "weighted residual" technique using polynomials as test functions [112, 113]. The resulting models are referred as weighted residual models. A Galerkin method, leads to a "first-order model" involving two coupled evolution equations for the film thickness h and the local flow rate q, much like the Kapitza-Shkadov model but with different numerical coefficients of the terms originating from inertia. The first-order model predicts the correct linear instability threshold for all inclination angles while at the same time it also predicts rather well the nonlinear flow features. This is a direct consequence of using a detailed representation of the velocity field accounting for its deviations from the semi-parabolic profile. A "second-order model" has also been developed that takes into account the second-order viscous effects. It involves four equations by allowing the corrections to the semi-parabolic velocity profile to evolve according to their own dynamics. Further, an approximation to this four-field model, a "simplified second-order model", has been proposed involving only two fields, which allows us to check easily the role played by the second-order viscous effects on wave profiles and stationary wave selection. The spatial evolution of the solutions of the simplified second-order model in the presence of noise or periodic forcing agrees rather well with both experiments and direct numerical simulations of the boundary layer equations.

The simplified second-order model proposed by Ruyer-Quil & Manneville [113] can be written as

$$\begin{aligned}\delta\partial_t q &= \frac{5}{6}h - \frac{5}{2}\frac{q}{h^2} - \delta\left\{\frac{17}{7}\frac{q}{h}\partial_x q - \frac{9}{7}\frac{q^2}{h^2}\partial_x h\right\} + \frac{5}{6}h\partial_{xxx}h - \frac{5}{6}\zeta h\partial_x h \\ &\quad +\eta\left[4\frac{q}{h^2}(\partial_x h)^2 - \frac{9}{2h}\partial_x q\partial_x h - 6\frac{q}{h}\partial_{xx}h + \frac{9}{2}\partial_{xx}q\right], \qquad (2.4)\end{aligned}$$

The terms within the square brackets are generated by the second-order contributions originating from the second-order term in the momentum equation and the tangential stress boundary condition. As such they include the effect of viscous dispersion that was lacking at first order. Hence, (2.2) and (2.4) will be referred to as the simplified second-order model (see in [59]). The models derived by Ruyer-Quil & Manneville are capable to capture the inertia effect in the drag-inertia regime for moderate Reynolds number. These models will be used in chapter 3 to provide some insight on the solitary wave solutions.

The results of these models will be compared with DNSs to explain the properties of solitary wave in drag-inertia regime ($\delta \gg 1$). In chapter 5 and 6, the weighted residual technique will be employed to deal with the non-Newtonian film flow problem.

Chapter 3

Solitary waves on a Newtonian falling film

During my thesis I had the opportunity to spend two months in Volos (January - February 2011). The material presented in this chapter is a part of collaborative work with the University of Thessaly, Volos under the direction of Prof. Vasilis Bontozoglou. This chapter is an extended version of a manuscript in preparation entitled "Extreme solitary waves down falling film flow" by S. Chakraborty, P.-K. Nguyen, C. Ruyer-Quil and V. Bontozoglou. My specific contribution to this work is to compute the solitary waves based on DNS and solutions to the models derived by Ruyer-Quil & Manneville [111, 112, 113, 114]. To this aim, I specifically modified some subroutines of the FORTRAN program developed in Volos and I computed the solutions to the models using Auto-07p software.

3.1 Introduction

Wave evolution on an inclined or vertical falling film is an open-flow hydrodynamic instability, which has attracted an extensive study since pioneering work of Kapitza and his son [61]. Interfacial waves on film flows has been known on one side to enhance heat and mass transfer rates in process equipment such as condensers, falling film evaporators, absorption columns, and two-phase flow reactors, and on the other side, they degrade the quality of films in coating processes. A brief review of some experimental and theoretical results are referred to the monographs by Alekseenko *et al.* [3], Chang [21], Craster & Matar [30], and Kalliadasis *et al.* [59] for a more detailed information of the relevant literature and results.

Much of the information available for the problem is based on experiments. From experimental observations, waves emerge first as short periodic, near sinusoidal waves in the inception region (near the inlet) and evolve into long solitary type waves, which are often preceded by one or more small capillary waves (or ripples). These solitary waves

might break up into spatially and temporally irregular three-dimensional waves further downstream. A technique introduced in the pioneering work of Kapitza & Kapitza [61] and subsequently adopted by many investigators [3, 70, 138, 144, 68] is to facilitate the observations of wave development by applying a constant-frequency disturbance at the inlet. In this way regular waves are produced, whose form depends to a large extent on the frequency of the forcing. These studies have demonstrated that high-frequency disturbances initially lead to saturated periodic waves, whereas low-frequency disturbances evolve directly into regularly-spaced solitary waves. The latter are characterized by large humps with steep wave fronts and gently sloping tails, preceded by front-running ripples (else called bow waves or precursor waves).

Other investigations have focused on waves that occur naturally, triggered by random noise [136, 56, 134, 16, 138, 144]. In that case, small-amplitude waves at the inception region generally correspond to the linearly most unstable mode, and initially evolve into a multi frequency, complex pattern. It has been demonstrated [70, 138] that, farther downstream, the film flows produced by either regular high-frequency forcing or by natural noise are eventually dominated by a small number of irregularly spaced solitary humps, which emerge through period-doubling and wave merging phenomena. The correlation of the celerity and the amplitude of solitary waves is documented in a recent experiment on vertical falling film covering a large range of fluid properties Kapitza number, Γ and flow rates Weber number, We by Meza & Balakotaiah [81].

Extensive theoretical efforts at the problem of film flow have centered on perturbation expansions in a small parameter proportional to the thickness-over-wavelength ratio (accompanied by various order-of-magnitude assumptions for the pertinent dimensionless numbers Re and We). Although natural wave structures resemble the three-dimensional waves with pronounced transverse variations, the waves travel downstream at a relatively constant speed without changing their shapes, suggesting that a local two-dimensional model is sufficient for describing these naturally occurring wave profiles. The purpose of these models is to obtain a simplified low-dimensional description of the film in terms of the stream wise coordinate (x) and time (t). They can be a single evolution equation [9, 21] for the local film thickness $h(x,t)$ or a pair of evolution equations for the local film thickness $h(x,t)$ and the local flow rate $q(x,t)$ [80, 126, 103, 84, 57, 20, 67, 66, 111, 112, 114, 123, 59], or a three-equation set based on a cubic stream function for the local film thickness $h(x,t)$, the local flow rate $q(x,t)$ and the local pressure $p(x,t)$, [86] and even up to a set of four equations [113].

Simplification of the Navier Stokes equations and analysis of the simplified models render the development of analytical expressions for predicting and correlating the behavior of wavy films. Benney [9] was credited for using a perturbation method to derive the first simplified model for describing the instantaneous amplitude of surface waves on liquid films. The model is commonly known as the long wave (LW) equation in the literature. A weakly nonlinear truncation of the long wave equation gives the Kuramoto Sivashinsky (KS) equation. Numerical studies of the KS equation by Sivashinsky &

Michelson [130] showed that solitary waves generated in a bounded domain with periodic boundary conditions travel at the same speed as predicted from the linear theory. Long-wave-type equations were also derived and analyzed by Frenkel [46, 47] for flows on cylindrical wires. Shkadov [126, 127] used the integral boundary layer (IBL) method with a self-similar velocity profile assumption to derive a two-equation model for describing the dynamics of large-amplitude waves. However, it was shown later that the Shkadov model does not give correctly the location of Hopf bifurcation in parameter space, a necessary condition for predicting periodic waves in a moving frame of reference. Alekseenko *et al.* [3] measured the local velocity components inside the waves and found that they are not self-similar but are close to the parabolic distribution. They also measured the wave growth rates, velocities, and amplitudes near inception. Trifonov & Tsvelodub [139] analyzed the Shkadov model and resolved the problem associated with it by using periodic boundary conditions. Although their numerical simulations showed reasonable agreement with experimental data (near the inception region) at low to moderate Reynolds numbers, the assumption of periodic boundary conditions was questionable. Applying the dynamic singularity theory, Chang [21, 23] derived quantitative correlations between the solitary wave amplitude, velocity, and wavelength and showed that the single frequency waves first appearing on the smooth film evolve into doubly periodic waves, which may then become chaotic just before the solitary wave limit is reached. Chang's work concentrated on the LW and the KS equation and was limited to small Reynolds numbers and high Kapitza (Weber) numbers for which the wave amplitude is very small. Further efforts to enrich the structure of the wave evolution process by retaining higher-order viscous terms and/or adding a third dimension did not result in significant improvement over simpler models [102, 20]. Using the boundary collocation method, Yu *et al.* [148] analyzed two models, namely the boundary layer(BL) model and the second-order boundary layer (SBL) model, which were capable of describing the dynamics of large-amplitude waves at high Reynolds numbers. Both models compared well with the linear stability results of the OS equation. The SBL model also included a pressure variation across the film and higher-order viscous terms, which were essential in predicting accurate wall shear stress. In the traveling coordinate, numerical integration of the BL and SBL models predicted large-amplitude waves with peak to substrate ratios of 3 to 4 and agreed well with experimental data. Although the numerical computations using these models were much simpler than the full Navier-Stokes equations, they were still too complicated for general analytical studies. The resulting approximate evolution equations for the film thickness admit stationary traveling solutions. They have been analyzed by modern bifurcation theory and have also been numerically scrutinized to yield a rich variety of solutions, including limit cycles, homoclinic orbits, and chaotic attractors [26, 102, 37, 139, 140, 141, 148].

Along the line with the need for a low-dimensional but accurate model, Ruyer-Quil & Manneville [111, 112, 113, 114] have systematically derived several low-dimensional models based on the weighted residual method and polynomial expansions. Their different models were gradually improved by including high-order viscous terms and by regular-

ization. Their most important contribution is a four-equation model which can take into account all characteristics of the full Navier Stokes equations by resolving on a high-order polynomial expansion and adding two independent local degrees of freedom to describe the evolution of finite amplitude waves for a realistic range of parameters.

Computational attempt on the film flow problem through direct computation based on the full Navier-Stokes equations are not very numerous. One attractive approach is the numerical integration of the time-dependent equations as an initial-value problem, because it captures the nonlinear, spatial evolution of a convective instability and is thus more amenable to a direct comparison with experiments. The earliest numerical study that has adopted such an approach is the extensive simulation of Ramaswamy *et al.* [104]. These authors have presented temporal stability results that identify a transition regime characterized by quasi periodic (instead of fully developed) waveforms, and have also computed the spatiotemporal evolution of inlet disturbances and compared their predicted free-surface profiles with the data of Liu & Gollub [70]. An extension of the above study is the study of solitary wave interaction using free outflow boundary condition [75, 77, 76] in order to ensure smooth exiting of nonlinear waves from the computational domain.

Due to the cost of the computations of unsteady waves computation, an alternative DNS can be used with the application of the periodic boundary conditions at the inlet and outlet of the flow field to capture the fully developed stationary wave. The pioneering work of Bach & Villadsen [6] was followed by few contributions [64, 50, 88, 119], which obtained good agreement with data of fully developed nonlinear waveforms. This formulation overcomes the problem of the outflow boundary condition but excludes by definition non-stationary dynamics and a periodic phenomena such as chaotic waves. On the contrary, periodic and fully developed solitary waves are recovered. Thus, the above studies permit comparisons with stationary solutions, derived from the aforementioned simplified forms of the Navier-Stokes equations based on long-wave expansion. However, characteristics of traveling wave was studied in part for short waves and at small Reynolds number, Re and information about solitary wave in the true solitary limit is not yet documented.

Even though most low-dimensional models predict similar behaviors close to the threshold, they exhibit differences from each other at intermediate and higher value of Reynolds number (or reduced Reynolds number δ), i.e. when inertia becomes significant. These differences have been noted initially by Ooshida [93] who noticed a drastic modification of the shape of solitary waves when δ becomes larger than 2. Ooshida nicknamed drag-gravity and drag-inertia regimes the two different regions ($\delta \ll 1$ and $\delta \gg 1$). In the drag-gravity region, inertia plays only a perturbative role, viscous drag and the gravity force being dominant. The wave front and tail have close typical lengths. In the drag-inertia regime, inertia become dominant and balance the viscous drag and gravity acceleration. At the front, the breaking of the wave prompted by inertia is arrested by surface tension, which generates a large number of capillary waves. These capillary waves accumulate because of the large scale separation between the length of the wave tails and the short wavelength of the capillary ripples. Based on two-equation models, Ruyer-Quil

& Manneville [114] have shown that the solitary-wave speed saturate to an asymptotic value as δ goes to infinity. Thus saturation is a consequence of the dissymetry between the front and back of the waves. At the back, viscous drag and gravity acceleration are balanced by inertia, surface tension being negligible. This saturation is parallel to the onset of roll waves, i.e., regularly varying section of laminar flow separated by shocks. As for roll wave, one is led to Thomas condition [137] that fixes the speed of the solitary wave as $\delta \to \infty$. In that limit, solitary waves have a very large amplitude and speed and we will refer to them as *extreme* solitary waves.

Crucial test of such models consists in the correct predictions of the properties (shape, wave speed and wave height) of solitary wave as a functions of the distance from the instability threshold. Motivated by this fact, our direct numerical simulation (DNS) work is based on the integration of the full two-dimensional Navier-Stokes equation by the finite element method with the application of periodic boundary conditions. The important point in this study is the use of a large enough length of computational domain in order that periodic waves approach asymptotically the solitary limit. It aims is two-fold, first, offering numerical predictions of the extreme solitary wave properties, then using these data to validate the different low-dimensional models found in literature. Among them, the four-equation model [113] is proved to have am excellent agreement to the DNS results and to be considered the most accurate available model for further theoretical and applied study perspectives.

This chapter is organized as follows: Problem formulation and finite-element implementation are outlined in §. 3.2. In §. 3.3, the fully-developed solitary wave is studied and its properties are characterized in terms of different parameters. Comparisons of results from DNS with the different low-dimensional model are made. Finally, the key properties of extreme solitary wave are summarized in the concluding section 3.6.

3.2 Problem formulation and Computational methodology

3.2.1 Governing equations

This study deals with liquid films flowing along an inclined plane under the action of gravity g with an angle β as sketched in Fig. 3.1. The flow is free of shear force at the gas-liquid interface. The solitary wave is further assumed to be fully developed and hence moves at a constant speed and with a constant shape. In this stationary state and in the co-moving reference frame, the solitary wave can be considered to move on a base substrate which is undisturbed far away from the main hump. If the solitary wave hump is placed at the middle point of a sufficiently large domain of length L, the liquid substrates near inflow and outflow regions are practically undisturbed and the flat Nusselt flow solution is retrieved so that the periodic boundary can be applied for these

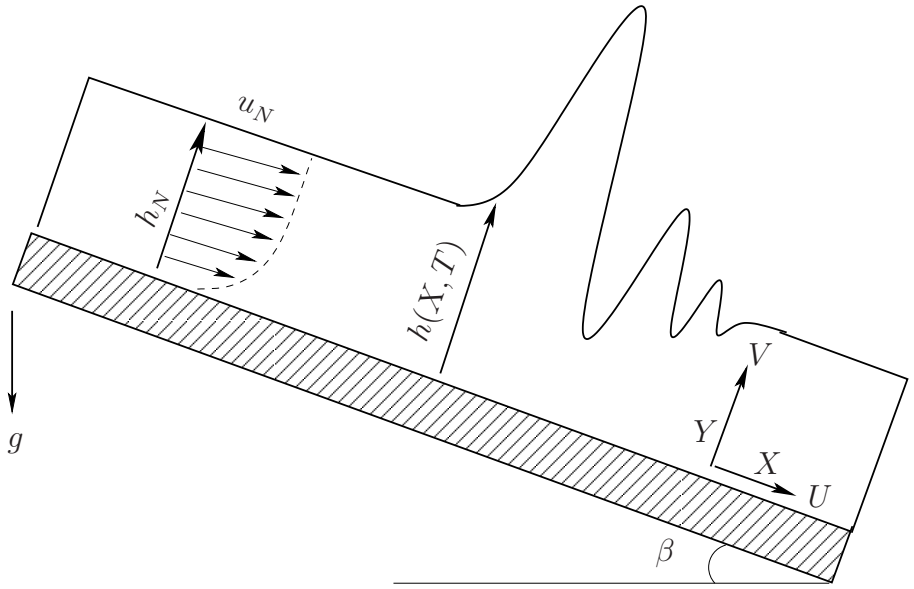

Figure 3.1: A sketch of the geometry for a Newtonian film flowing down an inclined plane.

two ends. The problem is modeled as two-dimensional in a Cartesian coordinate system, with the x-axis pointing in the mean flow direction and the y-axis across the film. The respective dimensional velocity components are u and v. The liquid is incompressible and Newtonian, with density ρ, dynamic viscosity μ, and surface tension σ. The primitive flow input is the volumetric flow rate Q and the location of the free surface is described at stationary state as $y = h(x)$. The dimensionless governing equations with kinematic condition at the free surface reads as

$$\nabla \underline{U} = 0\,, \tag{3.1a}$$

$$\frac{\partial \underline{U}}{\partial T} + \underline{U} \cdot \nabla \underline{U} = \nabla P + \frac{1}{Re} \nabla^2 \underline{U} + \frac{1}{Re \sin\beta} \underline{g}\,, \tag{3.1b}$$

$$\frac{\partial H}{\partial T} + U \frac{\partial H}{\partial X} - V = 0\,. \tag{3.1c}$$

The full Navier-Stokes equations governing the two-dimensional flow are non-dimensionalized using as characteristic scales the film thickness and the mean velocity

$$h_S = \left(\frac{3\mu Q}{\rho g \sin\beta} \right)^{1/3} \quad \text{and} \quad u_S = \frac{g h_S^2 \rho \sin\beta}{3\mu} \tag{3.2}$$

of the undisturbed substrate far away from the main hump transporting the flow rate Q along a planar wall. The resulting equations are formulated at stationary state in the

co-moving frame as follows, with capital letters indicating the respective dimensionless variables:

$$C = \nabla \cdot \underline{U} = 0, \tag{3.3}$$

$$M = -C\frac{\partial \underline{U}}{\partial X} + \underline{U} \cdot \nabla \underline{U} + \nabla P - \frac{1}{Re}\nabla^2 \underline{U} - \frac{3}{Re \sin\beta}\underline{g} = \underline{0}, \tag{3.4}$$

coupled with the kinematic equation for free surface evolution

$$K = -C\frac{\partial H}{\partial X} + U\frac{\partial H}{\partial X} - V = 0, \tag{3.5}$$

where the velocity vector is $\underline{U} = [U, V]^T$, and time derivatives is replaced by spatial derivatives in the co-moving frame, $\frac{\partial}{\partial T} = -C\frac{\partial}{\partial X}$. Moreover, we impose the no-slip and no-penetration boundary conditions at the wall,

$$U = V = 0, \tag{3.6}$$

and the dynamics boundary conditions at the free surface,

$$\underline{n} \cdot \underline{\underline{T}} = \Delta P\, \underline{n} + 3^{1/3}\, \Gamma\, Re^{-5/3}\, K\, \underline{n}. \tag{3.7}$$

In equation (3.7), $\underline{\underline{T}}$ is the stress tensor, $\underline{n}$ is the normal vector on the free surface and $K = \dfrac{H''}{(1+H'^2)^{3/2}}$ the surface curvature. We have 6 variables, two velocity components U and V, pressure P, free surface height H, pressure jump at a reference point in the liquid to the supposedly uniform gas pressure ΔP, and phase speed C. But so far it comes up with four equations: one from equation (3.3), two from Eqs. (3.4), and one from equation (3.5). Two additional equations need to be established. An additional condition can be obtained by imposing the phase of a steadily traveling wave by pinning the maximum height of solitary wave in the middle of domain (this is to avoid a degeneracy) without loss of generality,

$$H'(x = L/2) = 0, \tag{3.8}$$

Finally, another condition requires to set the thickness of undisturbed substrate far away from the main hump

$$H(x = 0) = 1. \tag{3.9}$$

The dimensionless parameters arising in the governing equations (3.4) are the Reynolds number

$$Re = \frac{\rho Q}{\mu} = \frac{\rho u_S h_S}{\mu}, \tag{3.10}$$

and the inclination angle, β of the planar wall to the horizontal plane, shown in the unit vector in the gravity direction $\underline{g} = [\sin\beta, -\cos\beta]^T$. The Kapitza number depending only on liquid properties, appears in equation (3.7),

$$\Gamma = \left(\frac{l_c}{l_v}\right)^2 . \tag{3.11}$$

The dimensional lengths entering into the above expressions are: viscous length, $l_v = (\nu^2/(g\sin\beta))^{1/3}$, capillary length, $l_c = (\sigma/(\rho g\sin\beta))^{1/2}$, and thickness of the undisturbed substrate, h_S, which is far away from main hump, and used as a characteristic scale length. In the definition of the Kapitza number, we have used the gravity acceleration in the flow direction $g\sin\beta$ as inferred by the definition of l_v and l_c. As a consequence, Γ depends not only on the liquid properties but also on the inclination angle β. It can be useful to introduce another definition of the Kapitza number, defined as

$$\Gamma^* = \Gamma(\sin\beta)^{1/3} = \frac{\sigma}{\rho\, g^{1/3}\nu^{4/3}}, \tag{3.12}$$

which is only dependent on the fluid properties.

Alternatively, three other dimensionless parameters, a reduced Reynolds number δ, a viscous dispersion number η, and reduced angle ζ) are often used in the low-dimensional model analysis [111, 112, 113], and falling film studies [59, 114, 123] and related to the three conventional parameters as follow.

$$\begin{aligned}
\delta &= (3Re)^{11/9}\Gamma^{-1/3} = \frac{h_s^{11/3}}{l_\nu^3 \quad l_c^{2/3}}\,, && (3.13)\\
\eta &= (3Re)^{4/9}\Gamma^{-2/3}\,, && (3.14)\\
\zeta &= \cot\beta(3Re)^{2/9}\Gamma^{-1/3}\,, && (3.15)\\
Fr^{-2} &= \frac{\cot\beta}{3Re} = \frac{\sqrt{gh_s\cos\beta}}{(3u_s)^2} = \frac{\zeta}{\delta}\,, && (3.16)\\
\text{and}\quad \Gamma &= \sigma/(\rho\nu^{4/3}(g\,\sin\beta)^{1/3}\,, && (3.17)
\end{aligned}$$

where in vertical case, $Fr^{-2} = 0$ and instability threshold, $Fr^{-2} = 2/5$. To make a comparison of solitary wave properties given by the low-dimensional models and DNS computation, we fix the Froude number $Fr^{-2} = 0$, two parameters δ and Γ are then varied. δ and Γ respectively measure the inertial effects and compare surface tension to viscous dispersion.

Using the Galerkin finite element method on a structured meshing, the system of governing equations is integrally weighted, particularly with bi-linear $\Psi^i(\xi,\eta)$ (i = 1, 9), bi-quadratic $\Phi^i(\xi,\eta)$ (i = 1, 9) , and quadratic basic functions $\Phi^i(\xi,\eta=1)$ (i = 1, 3) to produce respectively the residuals of the continuity equation, of the momentum equations,

and of the kinematic equation,

$$\iint_V C\,\Psi^i(\xi,\eta)\,dV = 0,$$
$$\iint_V M\,\Phi^i(\xi,\eta)\,dV = \underline{0},$$
$$\int_S K\,\Phi^i(\xi,\eta=1)\,dS = 0.$$

where ξ and η are element wise coordinates in each element of the computational domain. The flow field variables consisting of velocities U and V, pressure P, and free surface height H are also interpolated from nodal unknowns using these basic functions.

$$\underline{U} = \sum_{i=1,9} \underline{U}_i\,\Phi^i(\xi,\eta),$$
$$P = \sum_{i=1,4} P_i\,\Psi^i(\xi,\eta),$$
$$H = \sum_{i=1,3} H_i\,\Phi^i(\xi,\eta=1).$$

The element wise integration results in a discretised system of algebraic equations, which is solved by the Newton-Raphson iterative scheme, using a frontal technique.

The solitary wave resulting from the solution of the above system is typically characterized by:
(a) Wave height, H, which is measured at the peak of solitary wave, and scaled with the thickness of the undisturbed substrate (with X dependence, the same letter denotes the free surface height.)

$$H = \frac{h}{h_S} = h_m,$$

(b) Phase speed, C, which is a constant value of the stationary solitary wave in the co-moving frame, and scaled with the three times of the mean velocity of the undisturbed substrate.

$$C = \frac{c}{3\,u_S} = c.$$

3.2.2 Finite element formulation

The governing equations are partial non-linear differential equations that cannot be solved analytically. A numerical solution must be sought if theoretical prediction are desired. In this work the finite element method is used, often been derived from variational calculus, that has been established in the last ten years as a prominent method of

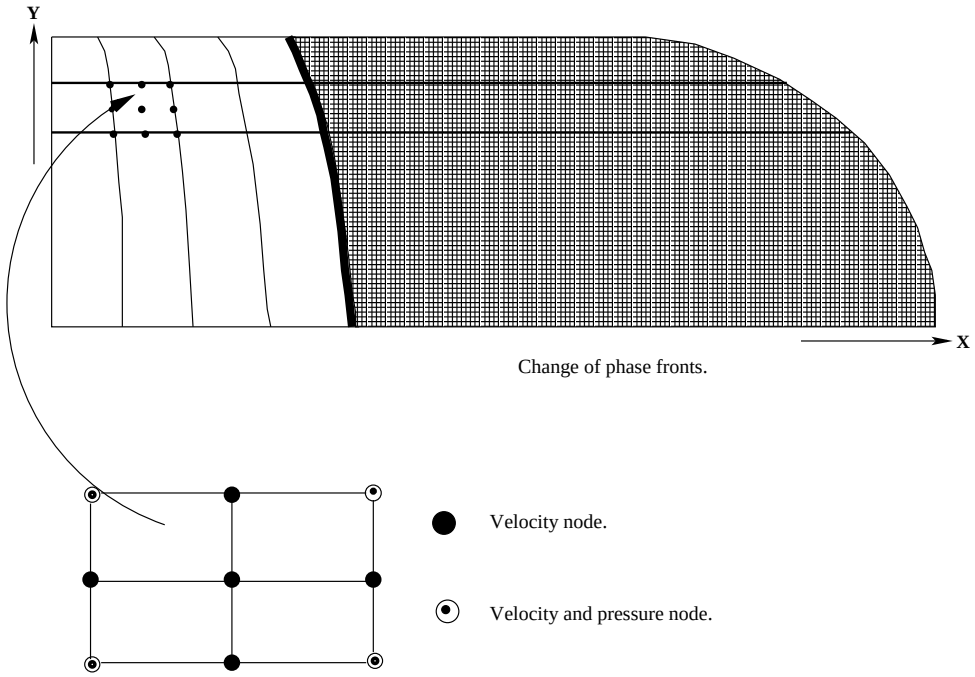

Figure 3.2: Sample finite element tessellation of a computational domain [75].

choice [31, 65, 92, 95, 118, 128] in transport phenomena. For this purpose, the computational domain is discretized into finite elements with often movable coordinates (X_i, Y_i) as shown in the Fig. 3.2.

The primary unknowns of the flow which are the velocities U_i and V_i, the pressure P_i along with the free surface unknowns H_i are expanded in terms of Galerkin basis functions,

$$U = \sum_{i=1}^{9} U_i \phi^i \,, \quad V = \sum_{i=1}^{9} V_i \phi^i \,, \quad P = \sum_{i=1}^{4} P_i \psi^i \,, \quad H = \sum_{i=1}^{3} H_i \phi^i \,,$$
$$X = \sum_{i=1}^{9} X_i \phi^i \,, \quad \text{and} \quad Y = \sum_{i=1}^{9} Y_i \phi^i \tag{3.18}$$

where ϕ^i are known biquadratic and ψ^i known bilinear basis functions over a prototype element shown in Fig. 3.3.

All elements of the computational domain are transformed into the standard biquadratic element of Fig. 3.3 by means of isoparametric transformations [133, 75].

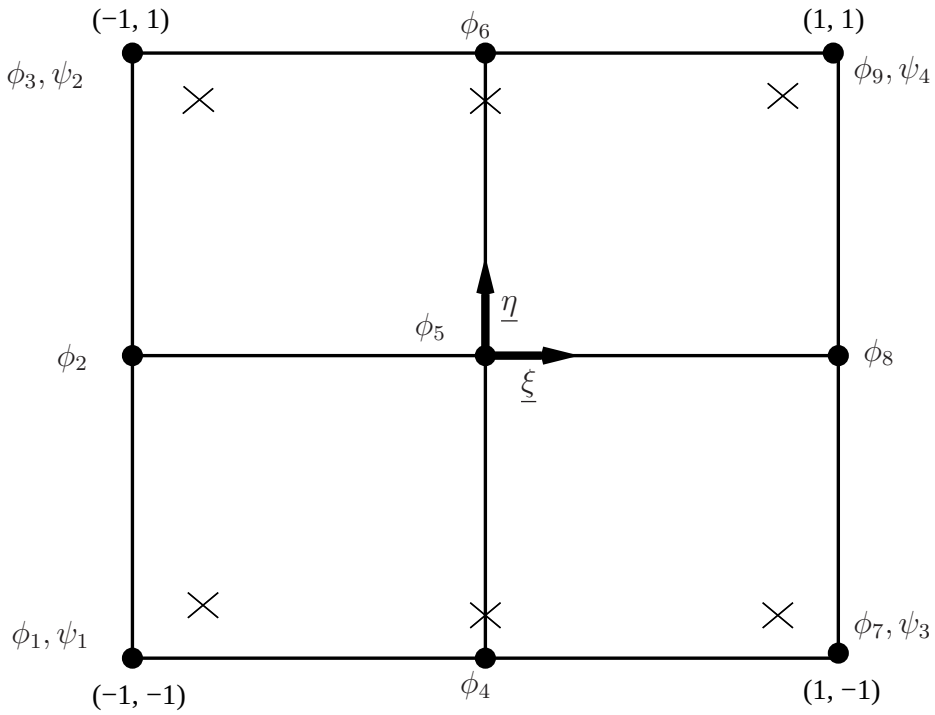

Figure 3.3: Isoparametic biquadratic element used for the computations throughout this work. Standard finite element with biquadratic, ϕ_i, and bilinear, ψ_i, basis functions and Gauss integration points $(0,0), (0,\pm 0.77), (\pm 0.77, 0), (\pm 0.77, \pm 0.77), (\mp 0.77, \pm 0.77)$ [75].

The biquadratic basis functions are:

$$\phi_1 = \frac{1}{4}\underline{\xi}(\underline{\xi}-1)\underline{\eta}(\underline{\eta}-1) \qquad \phi_5 = (1-\underline{\xi}^2)(1-\underline{\eta}^2)$$
$$\phi_2 = \frac{1}{2}\underline{\xi}(\underline{\xi}-1)(1-\underline{\eta}^2) \qquad \phi_6 = \frac{1}{2}(1-\underline{\xi}^2)\underline{\eta}(1+\underline{\eta})$$
$$\phi_3 = \frac{1}{4}\underline{\xi}(\underline{\xi}-1)\underline{\eta}(1+\underline{\eta}) \qquad \phi_7 = \frac{1}{4}\underline{\xi}(\underline{\xi}+1)\underline{\eta}(\underline{\eta}-1)$$
$$\phi_4 = \frac{1}{2}(1-\underline{\xi}^2)\underline{\eta}(\underline{\eta}-1) \qquad \phi_8 = \frac{1}{2}\underline{\xi}(\underline{\xi}+1)(1-\underline{\eta}^2)$$
$$\phi_9 = \frac{1}{4}\underline{\xi}(\underline{\xi}+1)\underline{\eta}(\underline{\eta}+1)$$

The bilinear basis functions are:

$$\psi_1 = \frac{1}{4}(1-\underline{\xi})(1-\underline{\eta}) \qquad \psi_3 = \frac{1}{4}(1+\underline{\xi})(1-\underline{\eta})$$
$$\psi_2 = \frac{1}{4}(1-\underline{\xi})(1+\underline{\eta}) \qquad \phi_4 = \frac{1}{4}(1+\underline{\xi})(1+\underline{\eta})$$

Isoparametric biquadratic element used for the computations throughout this work. The governing equations, weighted integrally with the basis functions, result in the following continuity, $\mathbb{R}^i{}_C$, momentum, $\mathbb{R}^i{}_M$, and kinematic, $\mathbb{R}^i{}_K$, residuals:

$$\mathbb{R}^i{}_C = \int_{\mathbf{V}} \nabla \cdot \underline{U}\psi^i d\mathbf{V} \tag{3.19}$$

$$\mathbb{R}^i{}_M = \int_{\mathbf{V}} \left[-C\frac{\partial \underline{U}}{\partial X} + \underline{U}\cdot\nabla\underline{U} - \nabla P + \frac{1}{Re}\nabla^2\underline{U} - \frac{1}{Re\sin\beta}\underline{g} \right] \phi^i d\mathbf{V} \tag{3.20}$$

$$\mathbb{R}^i{}_K = \int_S \left[-C\frac{\partial H}{\partial X} + U\frac{\partial H}{\partial X} - V \right] \phi^i dS \tag{3.21}$$

where the superscript i denotes the i-th node of the computational domain (Fig. 3.3) over which $\phi^i = 1$. Thus, the i-th residual equation corresponds to the i-th node where the unknown variables have values U_i, V_i, P_i, H_i, X_i, Y_i to be determined by solving the resulting algebraic system of equations (3.19), (3.20) and (3.21). Then the values of the variables elsewhere is computed by means of equation (3.18). Essential boundary conditions are applied by replacing the entire governing equations along the appropriate boundary nodes with the corresponding known values of the process variables. For confined flows, the equations (3.19) and (3.20) are integrated numerically by a nine-point Gaussian quadrature [18]. A system of nonlinear algebraic equation is obtained, which is solved with Newton-Raphson iteration [53], yielding directly the unknown process variables at the nodal positions of the computational domain and elsewhere by means of the equation (3.18). For free surface problem, the kinematic condition, equation (3.5), is

added to the governing equations in order to calculate the location of the free surface, H, which is expanded in terms of quadratic basis functions, $\phi(\underline{\xi}, \underline{\eta} = 1)$, simultaneously with the primary unknowns of the flow (U, V, and P) obtained from equations (3.3)-(3.4). These are the main features of ordinary Finite Element Methods where the position of the nodes of the computational domain is set .

3.2.3 Mesh clustering

Following the exponential mesh clustering technique given in the book of Hoffman and Chiang [51], the meshing of the 2D film flow domain is refined in the vicinity of the main hump of solitary wave in the streamwise direction. The clustering technique in the interior of domain is required. In particular, the mesh is clustered around the main hump and capillary ripples, and relaxed in the nearly flat substrate far away from the main hump. The following transformations are used

$$X = L\left\{1 + \frac{\sinh[\beta(\xi - A)]}{\sinh(\beta A)}\right\} \tag{3.22}$$

$$Y = H(X)\,\eta \tag{3.23}$$

where

$$A = \frac{1}{2\beta}\ln\left[\frac{1 + (e^{\beta} - 1)(D/L)}{1 + (e^{-\beta} - 1)(D/L)}\right] \tag{3.24}$$

In the equation (3.22), α is the clustering parameter in the range of $0 < \alpha < \infty$, and L the length of physical domain. Physical coordinate Y is scaled with the free surface height $H(X)$ in equation (3.23). In equation (3.24), D is the X coordinate where clustering is desired, in this case, it is the stream wise location of the maximum height which is pinned in the middle of domain, $D = L/2$. The isoparametric mapping from the physical domain to the rectangular computational domain is done by the transformations (3.22) and (3.23) where ξ and η (the same notation used also for the element wise coordinates in each element of computational domain) are the two coordinates of the computational domain in the range $0 < \xi < 1$, $0 < \eta < 1$ and with constant step sizes $\Delta\xi$ and $\Delta\eta$. In order to capture solitary wave properties in asymptotic limit, the domain length should be larger than thousand times of Nusselt flat substrate thickness. In this study, the domain length $L = 3000$ is sufficient to cover to a wide parametric range up to either a large flow rate $\delta = 20$ or to a very low viscous liquid of $\Gamma = 10^4$. Accordingly, the parameter α is defined such that the minimum space step ΔX_{min} should be much smaller than the scaled capillary length, i.e. $N_c\,\Delta X \leq l_c/h_s$, where a large factor $N_c = 512$ is empirically chosen because a small N_c may cause an overshoot or undershoot of solitary wave or a failure of numerical convergence due to low meshing resolution. To begin, the solitary wave is first computed at a small δ with highly clustering mesh intended

for following computation at higher δ. By parametric continuation, this mesh is fixed to compute waves at different parameters. It is not necessary to regenerate the mesh in each computing process, otherwise, the interpolation of nodal unknowns is needed and may cause significant deviation from the previous result and interrupt the continuation process.

3.3 DNS results for vertical wall

We first present our computations for a vertical wall, which is the most studied situation in literature. The reason of this choice is that the number of parameters reduces to δ and Γ only.

3.3.1 Solitary wave profile and characteristics

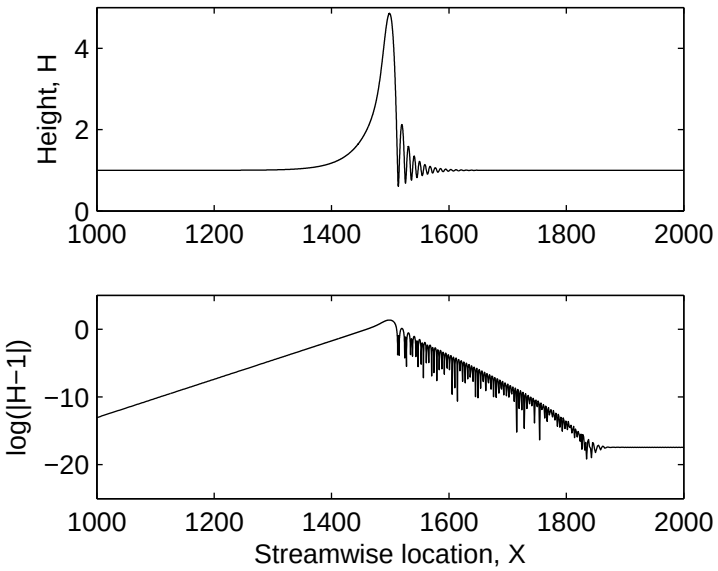

Figure 3.4: Free surface profile of extreme solitary wave and its exponential representation at $\delta = 4$, $\Gamma = 3400$, $Fr^{-2} = 0$, and computational domain length $L = 3000$, in which the nearly flat substrate far from the main hump is out of window.

In Fig. 3.4, the free surface profile shows an exponential growth upstream and oscillatory decay downstream of the main hump in the form of preceding ripples. Hence at a distance far away, the film flow is a nearly flat substrate both upstream and downstream. The main hump amplitude is determined in terms of parameters δ, Γ, Fr^{-2}, and saturated on a large-length domain, L, of one single wave, see Fig. 3.5. From numerical experience,

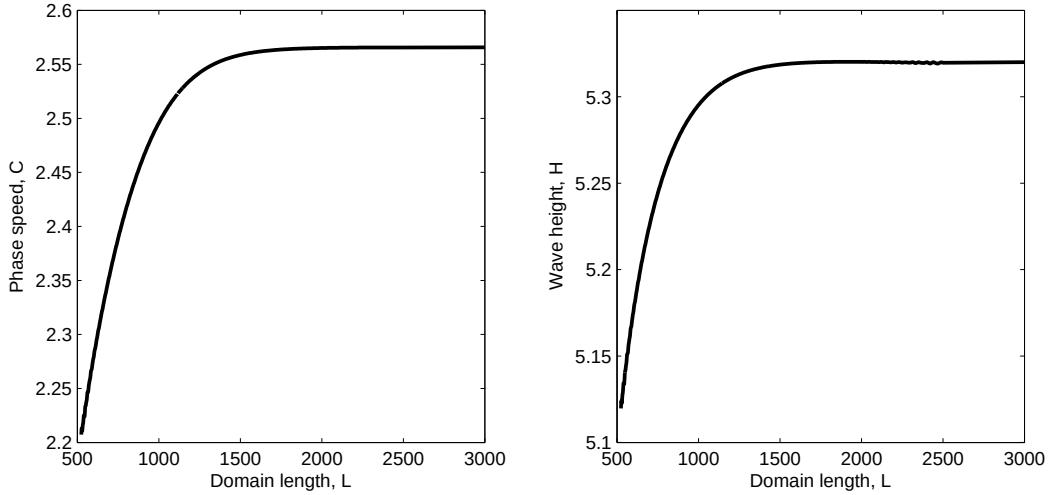

Figure 3.5: The convergence of extreme solitary wave properties in terms of domain length at $\delta = 10$, $\Gamma = 10^4$, and $Fr^{-2} = 0$ (vertical plane).

the dimensional domain length l should be hundreds to thousands times larger than (respectively proportional to the order magnitude of Kapitza number, $\Gamma \sim 10^0 \div 10^4$) the substrate thickness h_s, in order that solitary wave properties converge asymptotically to true solitary limit. However, the number of elements in the computational domain can be drastically reduced by the use of a clustering mesh around the main hump and the ripples, and a relaxed mesh in the nearly flat substrate part of the solitary wave. The clustering mesh is very useful to capture either a steep front of a solitary wave hump at small Kapitza number or an increasing number of tightly paced ripples in the drag-inertia regime (at medium to large reduced Reynolds number). Especially, a clustering grid effectively helps to resolve a zone of a very tall hump preceded by dense ripples at large Kapitza number Γ in order to avoid a numerical overshoot or undershoot of solitary wave peak. It is also noted that no solution can be provided when approaching to the limit condition where a parameter set of both small Kapitza and large reduced Reynolds number leads to extremely steep front of solitary wave.

3.3.2 Drag-gravity, transition, and drag-inertia regimes

Effect of flow inertia

In Fig. 3.6, it is observed that both the phase velocity and the wave height exhibit inflection points in the transition region, then maxima at intermediate values of δ, and finally a drop to a plateau at high enough δ. In particular, simulations and the above second-order model agree quantitatively in the drag-gravity regime and the transition

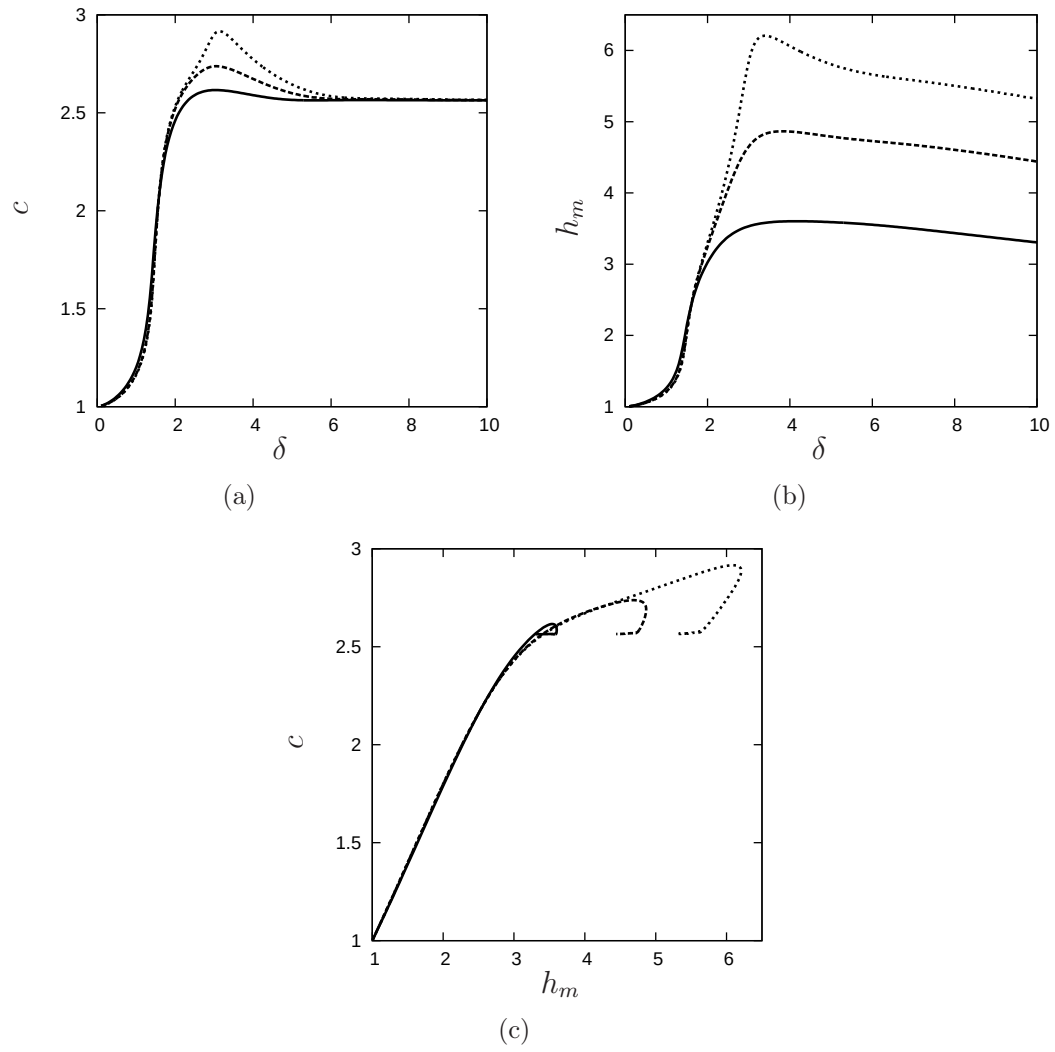

Figure 3.6: The extreme solitary wave properties interms of δ for different liquid properties $\Gamma = 193$ (solid line), $\Gamma = 3400$ (dashed line), $\Gamma = 10000$ (dotted line) flowing along a vertical wall $\beta = 90°$ and the third plot shows the phase space and the wave height of the solitary wave for different values of Kapitza numbers, $\Gamma = 193, 3400, 10000$.

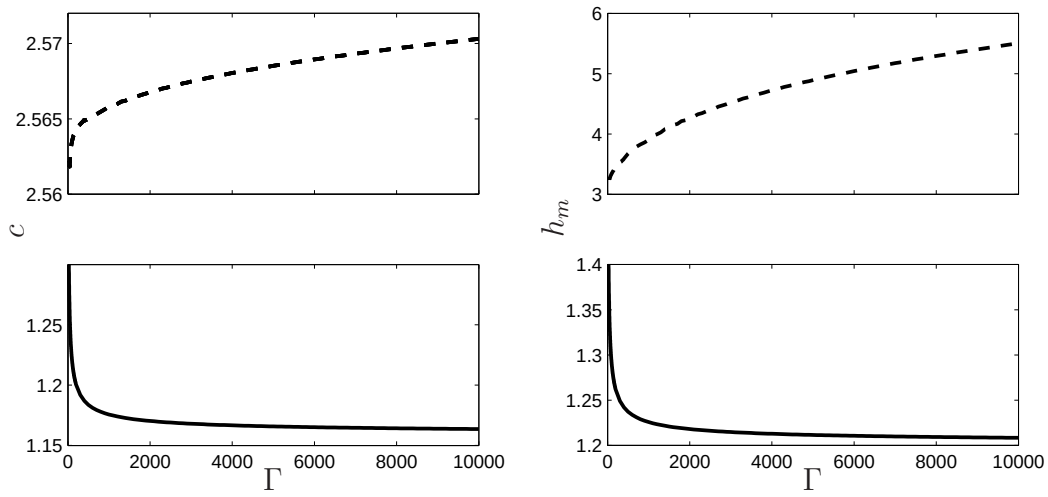

Figure 3.7: The extreme solitary wave properties in term of the Kapitza number Γ for flows in the drag-gravity regime, $\delta = 1$ (solid line in the lower pannel), and the drag-inertia regime, $\delta = 8$ (dash line in the upper pannel) along a vertical wall $\beta = 90°$.

region to the drag-inertia regime, but only qualitatively in the drag-inertia regime. The behavior deep in the drag-inertia regime is found to depend on Γ, which in the present simulations is varied in the range 200-10000. With increasing Γ, the maxima that occur at intermediate δ become steeper. However, whereas the high-δ limit of the phase velocity appears almost unaffected, that of the wave height increases roughly linearly with Γ, which underlines the stabilizing effect of viscous diffusion at low Kapitza numbers. It is observed that the maximum height does not necessarily occur at the same condition for the maximum phase speed. The latter is also found to drop to asymptotic value $c \approx 2.56$ in high δ limit. The phase plot shows the linear dependence of phase speed to the low-to-intermediate range of wave height. Then, the phase $h_m - c$ curves make similar-tie profile in the drag-inertia regime where phase speed is independent of Γ and the dimensionless wave height continuously drops down a gentle slope.

Effect of viscosity in the drag-gravity, and the drag-inertia regime

From Fig. 3.7, at high δ value in the drag-inertia regime, phase speed is almost unaffected by Kapitza number, but the wave height increases roughly linearly with Γ which underlines the stabilizing effect of viscous diffusion at low Γ.

In contrast, in the drag-gravity regime, when the inertia is less important and surface tension reaches a prominent role, it is observed that the wave height (and also the phase

speed) decreases with Kapitza number dictating a stabilizing effect of surface tension.

Flow reversal

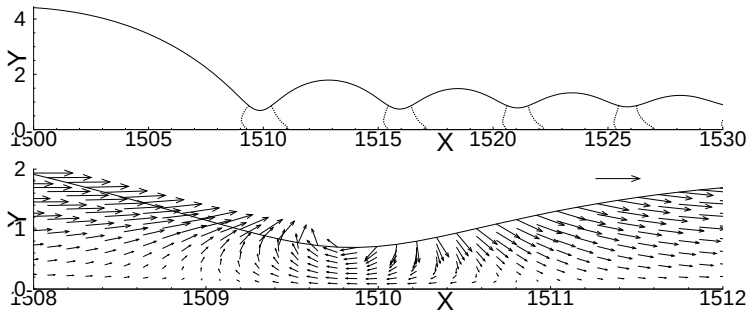

Figure 3.8: A close view of the reversal flow at high inertial regime, $\delta = 10$, for water with $\Gamma = 3400$ down a vertical wall. The upper panel plots the boundaries of flow reversal zone (in dashed lines), and the lower one depicts the velocity field (in vector) of one reversal zone in reference with the vector of the phase speed.

Flow reversal is studied for vertically falling film flows ($Fr^{-2} = 0$), as typically shown in Fig. 3.8, where dashed lines (in the upper panel) demarcate the boundaries (zero velocity) of the downward and upward flow zones. It should be clearly specified that the upward flow is not a recirculated one because there is no closed streamlines. The mechanism for this phenomenon can be explained by observing a velocity field of a typical flow reversal zone between the hump and the first ripple (on the lower panel). On the downwind side of the main hump or ripples, the velocity vectors point downward and to the wall ($U > 0, V < 0$), but on the upwind side, they gradually turn away from the wall ($U > 0, V > 0$), with a wall parallel direction at the peak of hump or ripples. In a high inertia flow, the pressure gradient becomes adverse to the flow direction and promotes the back flow [38, 39]. From Fig. 3.8, for example, the velocity ($U = 8.634650$) at the peak of the hump is larger than the phase speed ($3c = 7.694349$, the factor 3 is needed by rescaling with only h_s). However, the velocity U is only a local value and varies along the free surface. In particular, the liquid flow increases speed in downwind side and decreases speed in upwind side of the hump or ripples. It slowdowns to zero speed until a flow reversal occurs. In the flow reversal zone which takes place around capillary dimples, the local U component varies either increasingly or decreasingly by magnitude but take a reverse direction. The physical mechanism inside the flow is similar to the one on the free surface but with lower magnitude in approaching to the solid wall. It is observed that in high inertia flow there is no recirculation in the main hump or in the crest of ripples but rather several flow reversal zones immediately in front of the high and fast hump and ripples.

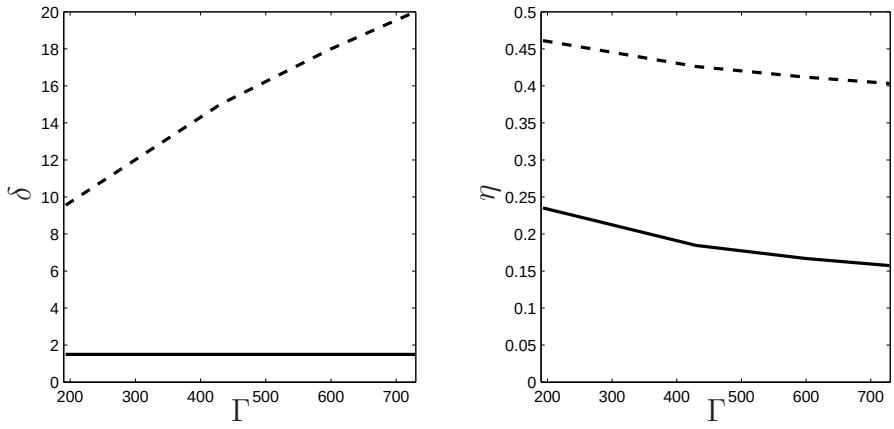

(a) (b)

Figure 3.9: A parametric map of the flow reversal down a vertical wall. (a) δ versus Γ, (b) η versus Γ, $Fr^{-2} = 0$. The occurrence of the back flow phenomenon is materialized by a lower boundary (solid line) and an upper boundary (dashed line). Here, $\delta_c = 0$ and $\eta_c = 0$.

At very low inertia with the wave height being very small, there is no flow reversal. However, its occurrence is not trivial because it is afterwards suppressed further in the higher inertia regime. A parametric map of flow reversal occurrence is necessarily shown in Fig. 3.9(a), where the flow reversal takes place in the zone between the two curves: one for the onset and the other for the suppression of flow reversal. An example for the water-glycerin solution with $\Gamma = 193$ shows the flow reversal emerges at $\delta = 1.5$, then survives in the higher range of inertia, and finally is suppressed beyond $\delta = 9.55$. It is observed that the appearance of flow reversal does not depend on liquids and emerges always at the same $\delta = 1.5$ but its survival and suppression delays to higher inertia for lower viscosity liquid (with large Γ^*). For water $\Gamma^* = 3400$, the suppression of flow reversal does not happen in the window of inertia up to $\delta = 20$. The last important remark is that the onset of flow reversal at $\delta = 1.5$ is a demarcation between the drag-gravity regime with low wave height and small phase speed to the drag-inertia regime with much larger pertinent characteristics. We may guess that the onset of the back flow phenomenon is related to the amplitude of the capillary ripples. Indeed, the adverse pressure gradient that slow down the flow up to the reversal point has a capillary origins [38]. The surface tension promotes a strong adverse pressure gradient from the humps to the nearby trough in the capillary region, gradient that can overcome the gravity acceleration. As a consequence, flow reversal will not be observed when the capillary waves are damped i.e., when the viscous dispersion effects become strong enough, which suggest that the disappearance of

flow reversal correspond to a critical constant value of the viscous dispersion parameter η_c. In Fig. 3.9(b) the onset of backflow is not observed in the capillary region for the vertical case at $Fr^{-2} = 0$.

3.4 Low-dimensional modeling

3.4.1 Models

Basically three low-dimensional models derived by Ruyer-Quil & Manneville [112] using a weighted residual technique are considered in this chapter. We have constructed the one-humped solitary wave solution to these models. Their properties are compared to the results from DNS in the drag-inertia regime ($\delta > 1$). Although these models shows similar behavior in the drag-gravity regime.

The modeling strategy is started with an expansion of the velocity field u in terms of the polynomial function. The first term taken of this expansion is the flat-film parabolic velocity profile. The first-order corrections to the parabolic velocity distribution is shown which could be described with the help of polynomials of higher degree [123]. Then Galerkin technique is used to ensure consistency up to $O(\epsilon^2)$. Finally, after some calculations, a system of four evolution equations is formed for four unknowns h, q, s_1 and s_2 (s_1 and s_2 are amplitudes of the departure of the velocity profile from the semi-parabolic Nusselt solution). It is referred as *full second order model* or *four-equation model* which is written in a vector form.

$$\begin{aligned}\delta\left\{\partial_t\mathbf{A}+\left(\frac{q\partial_x h}{h^2}\mathbf{M_h}+\frac{\partial_x q}{h}\mathbf{M_q}\right)\mathbf{A}+\frac{q}{h}\mathbf{M_A}\partial_x\mathbf{A}+\frac{h}{Fr^2}\partial_x h\mathbf{V_b}\right\}\\ =h\left(1+\partial_{xxx}h\right)\mathbf{V_b}-h^{-2}\mathbf{M_w}\mathbf{A}\end{aligned}\tag{3.25a}$$

where $\mathbf{A}=(q,s_1,s_2)$ is the amplitude vector and $\mathbf{M_h}$, $\mathbf{M_q}$, $\mathbf{M_A}$ and $\mathbf{V_b}$ are defined by

$$\mathbf{M_h} = \begin{bmatrix} -\frac{6}{5} & \frac{12}{5} & \frac{126}{65} \\ \frac{3}{35} & -\frac{108}{55} & \frac{5022}{5005} \\ 0 & \frac{4}{11} & -\frac{18}{11} \end{bmatrix} \quad \mathbf{M_q} = \begin{bmatrix} \frac{12}{5} & -\frac{12}{5} & -\frac{171}{65} \\ -\frac{1}{35} & \frac{103}{55} & -\frac{9657}{5005} \\ 0 & \frac{2}{33} & \frac{19}{11} \end{bmatrix} \tag{3.25b}$$

$$\mathbf{M_A} = \begin{bmatrix} 0 & -\frac{12}{5} & -\frac{1017}{455} \\ 0 & \frac{39}{55} & -\frac{10557}{10010} \\ 0 & -\frac{6}{55} & \frac{288}{385} \end{bmatrix} \quad \mathbf{M_w} = \begin{bmatrix} \frac{81}{28} & 33 & \frac{3069}{28} \\ \frac{3}{10} & \frac{126}{5} & \frac{126}{5} \\ \frac{13}{140} & \frac{39}{5} & \frac{11817}{140} \end{bmatrix} \quad \mathbf{V_b} = \begin{bmatrix} \frac{27}{28} \\ \frac{1}{10} \\ \frac{13}{420} \end{bmatrix} \tag{3.25c}$$

To deal with four-equation model is a difficult task, even if it is simpler for the corresponding study of the full Navier-Stokes problem, or boundary layer formulation, and to obtain a reliable two-field formulation consistent at $O(\epsilon^2)$ would be better. Setting s_1 ans s_2 to zero lowers the order of approximation. Then this procedure will leads to a simplified

averaged momentum equation, and the set of this equation with the mass conservation equation is called the *simplified model*. It can be written as

$$\partial_t h = -\partial_x q\,, \tag{3.26}$$

$$\begin{aligned}\delta\partial_t q = {} & \frac{5}{6}h - \frac{5}{2}\frac{q}{h^2} + \delta\left[\frac{9}{7}\frac{q^2}{h^2}\partial_x h - \frac{17}{7}\frac{q}{h}\partial_x q\right] - \frac{5}{6}\zeta h\partial_x h + \frac{5}{6}h\partial_{xxx}h \\ & + \eta\left[4\frac{q}{h^2}(\partial_x h)^2 - \frac{9}{2h}\partial_x q\partial_x h - 6\frac{q}{h}\partial_{xx}h + \frac{9}{2}\partial_{xx}q\right]\,.\end{aligned} \tag{3.27}$$

This model predicts the correct linear stability threshold. However, contrary to the gradient expansion of the four-equation model, the gradient expansion of (3.26) failed to reproduce the exact expression of the flow rate q as function of h at $O(\epsilon^2)$.

Later on Ruyer-Quil & Manneville have developed a two-equation model by following a procedure inspired by Ooshida's work using Padé approximation technique where second-order inertia terms are canceled. The set of evolution equations can be written as

$$\partial_t h = -\partial_x q\,, \tag{3.28}$$

$$\begin{aligned}\delta\partial_t q = {} & \delta\left[\frac{9}{7}\frac{q^2}{h^2}\partial_x h - \frac{17}{7}\frac{q}{h}\partial_x q\right] \\ & + \left\{\frac{5}{6}h - \frac{5}{2}\frac{q}{h^2} + \eta\left[4\frac{q}{h^2}(\partial_x h)^2 - \frac{9}{2h}\partial_x q\partial_x h - 6\frac{q}{h}\partial_{xx}h + \frac{9}{2}\partial_{xx}q\right]\right. \\ & \left. - \frac{5}{6}\zeta h\partial_x h + \frac{5}{6}h\partial_{xxx}h\right\}\left[1 - \frac{\delta}{70}q\partial_x h\right]^{-1}\,.\end{aligned} \tag{3.29}$$

which is known as *regularized model* [112, 123]. This set of equations is consistent at $O(\epsilon^2)$ and differs from the simplified model (3.26) through the addition of the Padé-like factor $\left[1 - \frac{\delta}{70}q\partial_x h\right]^{-1}$.

3.4.2 Asymptotes

Considering traveling wave solutions, i.e. waves that travel with a constant shape and speed c in their moving frame $\xi = x - c\,t$, the four-equation system (3.25) can be recast in a dynamical system of dimension five in a phase space spanned by h, $h' = dh/d\xi$, $h'' = d^2h/d\xi^2$, s_1 and s_2. Turning to the extreme solitary waves at large reduced Reynolds numbers, our computations show that, as for DNSs, solutions to the four-equation models present a slowly varying tail. From the DNSs, the tail length can be evaluated by finding the eigenvalues solutions to the Orr-Sommerfeld analysis. The eigenvalue λ_1, corresponding to the escape from the flat-film Nusselt solution $h = 1$ at the back of the waves, varies as δ^{-1} so that the length of the back tail $1/\lambda_1 \sim \delta$ is large. Focusing therefore on the back tail, let us introduce a slow variable $\tilde{\xi} = \xi/\delta$, the five-dimensional dynamical system

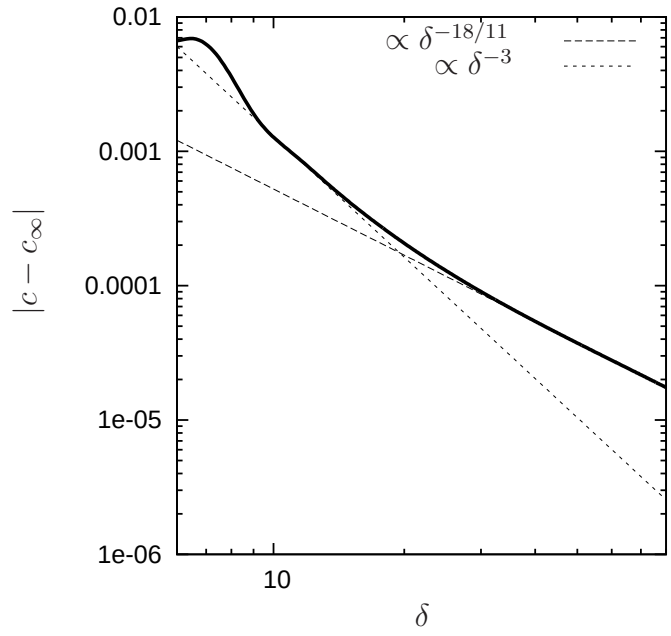

(a)

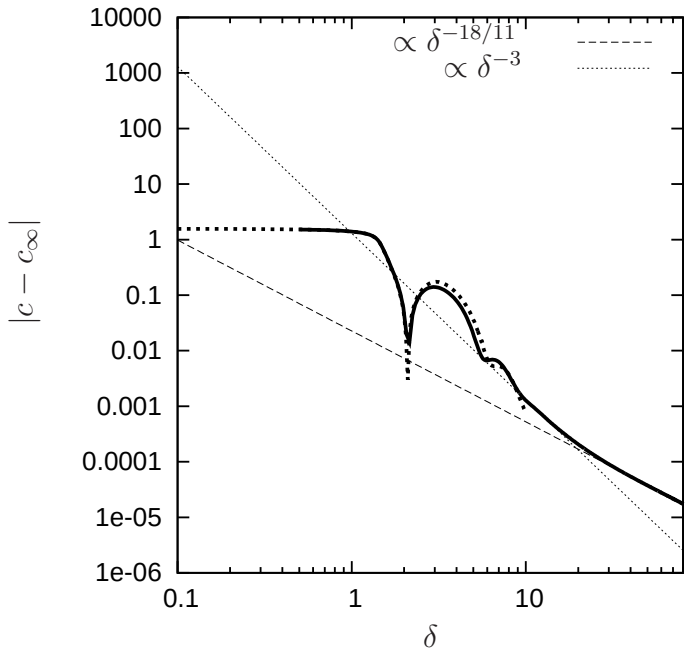

(b)

Figure 3.10: Comparison of convergence of the phase speed c to its asymptotic value c_∞ for the solutions to the four-equation model (3.25) (solid line) and DNS (thick dotted line) in a vertical plane $Fr^{-2} = 0$.

corresponding to (3.25) then reduces to a three-dimensional one

$$\mathbf{M}\frac{d\mathbf{X}}{d\tilde{\xi}} = \mathbf{B} + O\left(\eta/\delta^2, \delta^{-3}\right) \tag{3.30a}$$

where $\mathbf{X} = (h, s_1, s_2)^t$, $\mathbf{M} = [\mathbf{M}_i]$ is a matrix whose column vectors are denoted by $\mathbf{M}_i$. The vectors $\mathbf{M}_i$ and $\mathbf{B}$ are given below

$$\mathbf{M}_1 = \begin{bmatrix} -c^2 + \frac{27}{28}\frac{h}{Fr^2} + c\left(\frac{12}{5}\frac{q}{h} - \frac{12}{5}\frac{s_1}{h} - \frac{171}{65}\frac{s_2}{h}\right) + \frac{q}{h^2}\left(\frac{12}{5}s_1 + \frac{126}{65}s_2\right) - \frac{6}{5}\frac{q^2}{h^2} \\ c\left(-\frac{1}{35}\frac{q}{h} + \frac{103}{55}\frac{s_1}{h} - \frac{9657}{5005}\frac{s_2}{h}\right) + \frac{q}{h^2}\left(-\frac{108}{55}s_1 + \frac{5022}{5005}s_2\right) + \frac{3}{35}\frac{q^2}{h^2} \\ c\left(+\frac{2}{33}\frac{s_1}{h} + \frac{19}{11}\frac{s_2}{h}\right) + \frac{q}{h^2}\left(\frac{4}{11}s_1 - \frac{18}{11}s_2\right) \end{bmatrix} \tag{3.30b}$$

$$\mathbf{M}_2 = \begin{bmatrix} -\frac{12}{5}\frac{q}{h} \\ \frac{39}{55}\frac{q}{h} - c \\ -\frac{6}{55}\frac{q}{h} \end{bmatrix} \qquad \mathbf{M}_3 = \begin{bmatrix} -\frac{1017}{455}\frac{q}{h} \\ -\frac{10557}{10010}\frac{q}{h} \\ \frac{288}{385}\frac{q}{h} - c \end{bmatrix} \tag{3.30c}$$

$$\mathbf{B} = \begin{bmatrix} \frac{27}{28}h - \frac{81}{28}\frac{q}{h^2} - 33\frac{s_1}{h^2} - \frac{3069}{28}\frac{s_2}{h^2} \\ \frac{1}{10}h - \frac{3}{10}\frac{q}{h^2} - \frac{126}{5}\frac{s_1+s_2}{h^2} \\ \frac{13}{420}h - \frac{13}{140}\frac{q}{h^2} - \frac{39}{5}\frac{s_1}{h^2} - \frac{11817}{140}\frac{s_2}{h^2} \end{bmatrix} \tag{3.30d}$$

The shape of the back tail of the waves is determined, in the region of the fixed point, by the eigenvector $\mathbf{X}_1$ corresponding to the smallest eigenvalue λ_1 solutions to the stability problem of the fixed point. Numerical computations of $\mathbf{X}_1$ show that, for all cases of interest, this eigenvector is nearly aligned with the unit vector $(1, 0, 0)^t$. We can therefore approximate the flow corresponding to the back tail of the waves by setting $s_1 = s_2 = 0$ in (3.30) which leads to a single ordinary equation

$$\left[c - c_{d+}(h, u)\right]\left[c - c_{d-}(h, u)\right]\frac{dh}{d\tilde{\xi}} = \frac{27}{28}\frac{(3u - h^2)}{h} \tag{3.31}$$

where $u = q/h$ is the local mean flow velocity and

$$c_{d\pm}(h, u) = \frac{6}{5}u \pm \frac{1}{10}\sqrt{\frac{3}{7}}\sqrt{56u^2 + 225\frac{h}{Fr^2}} \tag{3.32}$$

are the speed of linear dynamic wave speeds traveling on a uniform film of height h and averaged speed $u = c + q_0/h$ [115, 117]. The r.h.s. of equation (3.31) corresponds to the balance of viscous drag and gravity acceleration, its zeros thus coincide with the locations of the fixed points in the phase space which are given by $h_{\mathrm{I}} = 1$ and $h_{\mathrm{II}} = -1/2 + \sqrt{3(c - 1/4)}$. Consequently, as the homoclinic orbit the level $h = h_{\mathrm{II}}$ corresponds to a maximum if the l.h.s. of (3.31) does not go to zero simultaneously, the resulting orbit being an heteroclinic orbit connecting the two fixed points.As a consequence, the construction of a one-loop homoclinic orbit then requires that the location of the second fixed point coincide with the location of a critical layer $h = h_c$ at which the phase speed

of the wave is equal to the speed of the linear dynamic waves $c_{d\pm}(h,u)$. The asymptotic speed of the waves is thus given by the solution to

$$h_c(c,Fr^2) = h_{\rm II}(c) \tag{3.33}$$

which is nothing but the Thomas condition derived in the context of the mathematical treatment of periodic bores, or roll waves consisting in regular sections of laminar flows connected by hydraulic jumps [137, 72]. Solving (3.33) gives

$$c_\infty(Fr^{-2}) = 1+\frac{1}{168\sqrt{\Delta}}\left(168+2\Delta\sqrt{\frac{42(56-405Fr^{-2})-196(\Delta-9)\sqrt{\Delta}}{\sqrt{\Delta}}}\right) \tag{3.34a}$$

$$\Delta = 3+\left(\frac{2}{7\Upsilon}\right)^{1/3}(14-405Fr^{-2})+\frac{\Upsilon^{1/3}}{2\times 14^{2/3}} \tag{3.34b}$$

$$\begin{aligned}\Upsilon = {} & 14112+10935Fr^{-2}(135Fr^{-2}-56)\\ & +5^{1/2}\left\{39337984+1215Fr^{-2}\left[-2809856\right.\right.\\ & \left.\left.+81Fr^{-2}(834176Fr^{-2}(-5264+6561Fr^{-2}))\right]\right\}^{1/2}\end{aligned} \tag{3.34c}$$

For a vertical plane ($Fr^{-2}=0$), (3.34) simplifies into

$$c_\infty(0) = 1+\frac{1}{\sqrt{6}}\sqrt{\frac{1}{2}+\sqrt{\frac{2}{3}}} \approx 2.55564 \tag{3.35}$$

which is in good agreement with the numerical computations (up to the two first digits after the decimal point).

Now, considering that s_1 and s_2 are small but not negligible, we can expect from the previous analysis that the homoclinic orbit departing from the fixed point $h_{\rm I}=1$ must encounter a critical surface in the phase space at which the system (3.30) is not invertible, i.e. $\det\mathbf{M}=0$. On the critical surface, the column vectors $\mathbf{M}_i$ are linearly dependent and thus $\mathbf{M}d\mathbf{X}/d\tilde{\xi}$ is a linear combination of $\mathbf{M}_2$ and $\mathbf{M}_3$ which yields $\mathcal{D}\equiv\det[\mathbf{B},\mathbf{M}_2,\mathbf{M}_3] = O\left(\eta/\delta^2,\delta^{-3}\right)$. Denoting by $\mathbf{X}_c$ the first point of intersection of the homoclinic orbit with the critical surface and denoting by $\mathbf{X}_\infty$ its location in the limit $\delta\to\infty$, we have $\partial_{\mathbf{X}}\mathcal{D}\cdot(\mathbf{X}_c-\mathbf{X}_\infty) = O\left(\eta/\delta^2,\delta^{-3}\right)$. Since one-humped homoclinic orbits are solutions to a nonlinear eigen problem for the phase speed c, $|\mathbf{X}_c-\mathbf{X}_\infty|\propto c-c_\infty$ and we thus get

$$c-c_\infty = O\left(\eta/\delta^2,\delta^{-3}\right)\ . \tag{3.36}$$

Surface tension effects on the shape of the tails of extreme solitary wave is responsible for the $O(\delta^3)$ terms at the r.h.s. of (3.36), whereas $O(\eta/\delta^2)$ terms come from streamwise viscous diffusion. Since $\eta/\delta^2 = 1/(3Re)^2\Gamma^{-6/11}\delta^{-18/11}$ varies as $\delta^{-18/11}$ for a given Kapitza number, we expect that the convergence of c to its asymptotic value c_∞ is driven by

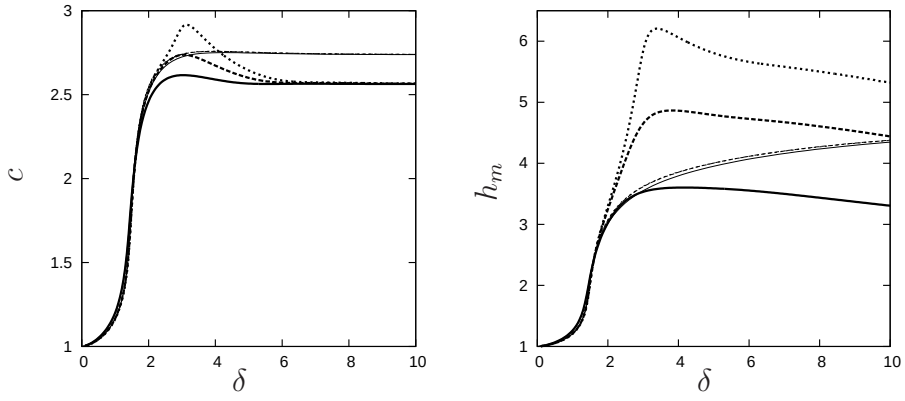

(a) (b)

Figure 3.11: **DNS - Simplified model** The phase speed c and the amplitude h_m of the single hump solitary waves as functions of the reduced Reynolds number δ of simplified model where the thick-solid line, thick-dashed line, thick-dotted line corresponds to the result from code and thin-solid line, thin-dashed line, thin-dotted line corresponds to the result of the model for different Kapitza numbers, $\Gamma = 193$ (water-glycerin solution), $\Gamma = 3400$ (water), $\Gamma = 10000$ respectively.

viscous diffusion terms and not by surface tension. From our numerical computations of the one-humped solitary-wave solutions to (3.25), we have performed a fit of the phase speed of the wave assuming that the distance to c_∞ varies as $\propto \delta^{-18/11}$ at large values of δ. The result is illustrated in Fig. 3.10. We thus get $c_\infty(F^{-2} = 0) \approx 2.56403$.

3.4.3 Comparison of DNS with the results of low-dimensional models

In Fig. 3.11 the numerical predictions, the phase speed c and the amplitude h_m, of the simplified model are shown in terms of the reduced Reynolds number δ and validated with the DNS results. These curves given by the simplified model almost coincide even for different liquids on a whole range of δ, in disagreement with DNSs in the drag-inertia regime, where the wave height is affected by the viscosity of liquids. Even if the regularized model can capture some differences of wave heights in terms of different liquids, its predictions deviate significantly from the prediction of the DNS, as shown by the c and h_m curves in Fig. 3.12. Finally, the predictions given by the four-equation full second-order model show a commencing agreement with the DNS results for a large range of liquids, even though some differences may arise as expected for extremely high Kapitza number at

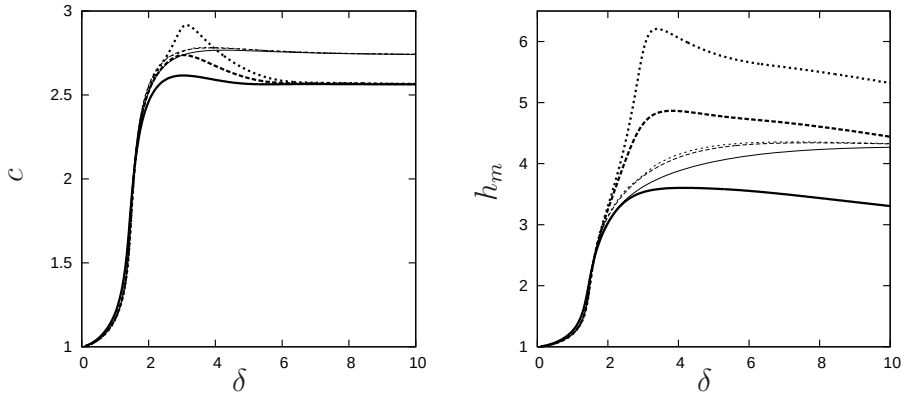

(a) (b)

Figure 3.12: **DNS - Regularized model** The phase speed c and the amplitude h_m of the single hump solitary waves as functions of the reduced Reynolds number δ of regularized model where the thick-solid line, thick-dashed line, thick-dotted line corresponds to the result from code and thin-solid line, thin-dashed line, thin-dotted line corresponds to the result of the model for different Kapitza numbers, $\Gamma = 193$ (water-glycerin solution), $\Gamma = 3400$ (water), $\Gamma = 10000$ respectively.

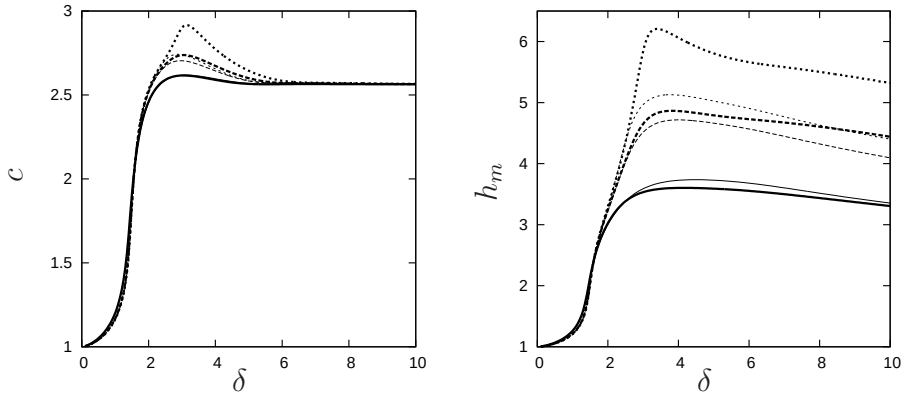

(a) (b)

Figure 3.13: **DNS - Full second order model** The phase speed c and the amplitude h_m of the single hump solitary waves as functions of the reduced Reynolds number δ of full second order model where the thick-solid line, thick-dashed line, thick-dotted line corresponds to the result from code and thin-solid line, thin-dashed line, thin-dotted line corresponds to the result of the model for different Kapitza numbers, $\Gamma = 193$ (water-glycerin solution), $\Gamma = 3400$ (water), $\Gamma = 10000$ respectively.

$\Gamma = 10000$, see Fig. 3.13. These are unique characteristics of the full second-order model by Ruyer-Quil & Manneville [113], whereas all other models predict either a monotonic increase or a monotonic, asymptotic limit.

3.5 Shape of the solitary wave

The front and back of solitary waves can be approximated by exponentials as $h = 1 + \Re(Ae^{\lambda\xi})$ and $q = \frac{1}{3} + \Re(Be^{\lambda\xi})$. Determining λ is tantamount to solve the Orr-Sommerfeld eigenvalue problem for the values of the phase speed c corresponds to the solitary wave branch of solutions. In Fig. 3.14, 3.15 and 3.16, we solved the Orr-Sommerfeld eigenvalue problem and calculated the eigenvalues at the tail and at the front of the solitary wave which reflect the characteristic of their shape. Fig. 3.14 shows the real eigenvalue λ_1 corresponding to the unstable manifold and the imaginary part of the complex conjugate eigenvalues associated with the stable manifold for the single-hump solitary wave solutions of the full second order model as a function of δ and $1/\lambda_1$ provides a measure of the characteristic scale of the upstream tail of a solitary wave. Let us define $l_{tail} = 1/\lambda_1$. On the other hand $1/\lambda_{2i}$ is a measure of the characteristic scale of the radiation oscillations (the oscillations at the front correspond to the balance between the inertia and the surface tension) in front of the solitary hump. It is indicated that $1/\lambda_{2i}$ varies as $\delta^{1/2}$ for both $\delta \lesssim 1$ and $\delta > 1$ so that the characteristic scale of the radiation oscillations varies as $\delta^{-1/2}$. This scale increases up to $\delta = 1$ and decreases as δ increases from 1. It is also indicated that for $\delta \lesssim 1$, λ_1 varies as $\delta^{1/2}$ so that l_{tail} varies as $\delta^{-1/2}$ which is the same with the characteristic scale of the radiation oscillations at the front, a direct consequence of the absence of separation of scales between the front and the back of the wave for $\delta \lesssim 1$. On the other hand, for $\delta > 1$, λ_1 varies like $1/\delta$ so that l_{tail} varies like δ and increases as δ increases. Also, the sum of the three eigen values vanishes when $\eta = 0$, thus at $\Gamma = \infty$, so that $\lambda_{2r} \approx -\lambda_1/2$ and the characteristic length of the envelope of the radiation oscillations at the front varies like the scale l_{tail} at the back and increases as δ increases, whereas at the same time the characteristic length of the radiation oscillations decreases (due to the $\delta^{-1/2}$ -dependence). As a consequence, the number of radiation oscillations increases as δ increases. The same operation done on the low dimensional models gives tail lengths $1/\lambda_1$, $1/\lambda_{2r}$ and oscillation rate λ_{2i} that are compared to DNSs in Fig. 3.14 to Fig. 3.18. It is observed from the Fig. 3.14, that the shape of wave is well captured by the four-equation full second order model. Considering wave front, λ_{2r} seems quite distant from DNS results. This can be explained by the fact that the amplitude of capillary waves is incommensurate with the crest of the wave. The interpolation can thus be biased. By contrary, the frequency of the capillary waves (imaginary part) seems best to approach the theoretical analytical results. This result only valid for full second order model but if we observed the figures of the calculation of eigen values for other models seems far from the theoretical analytical result. The results of eigen values at the back and the front of

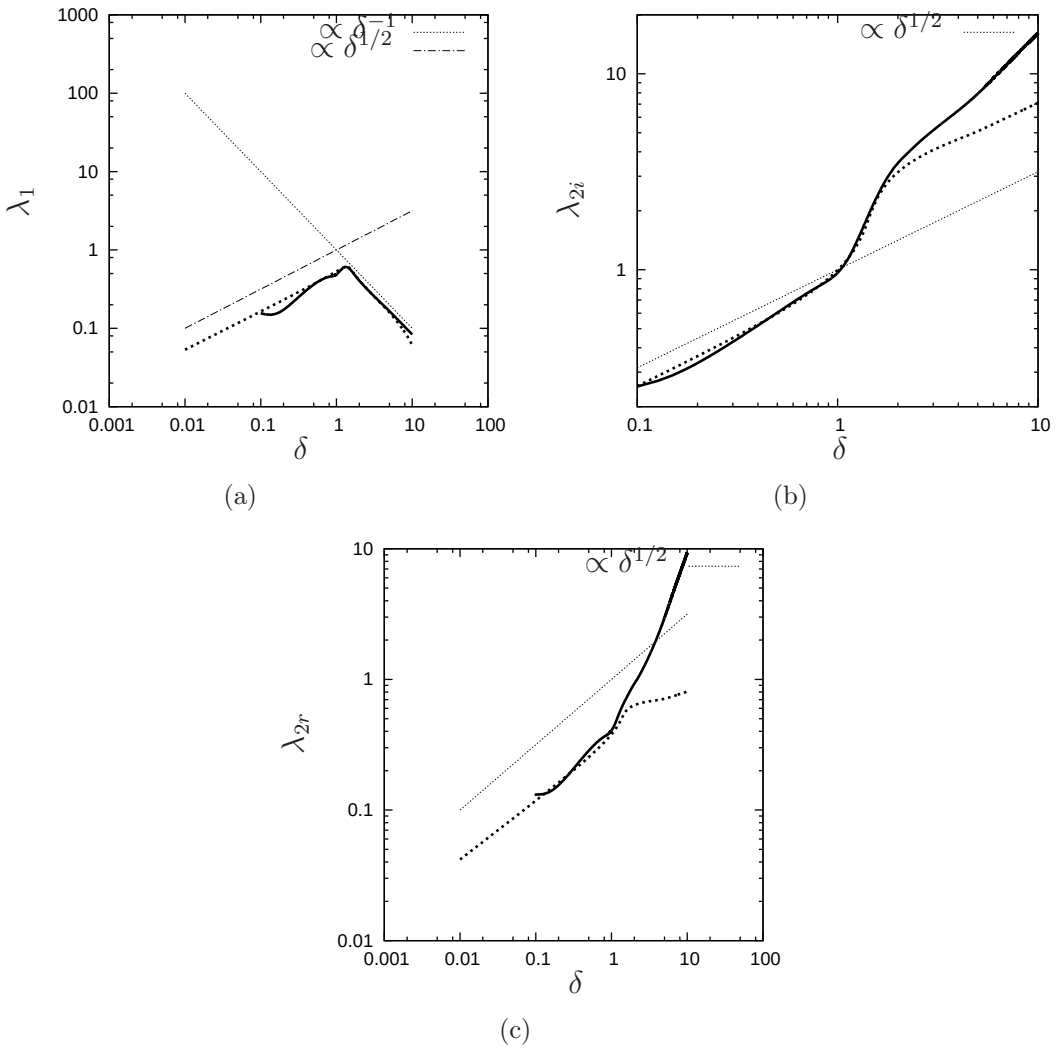

Figure 3.14: **DNS - Full second order model ($\Gamma = 193$).** a) real eigenvalue λ_1 where thin-dotted line refers δ^{-1} and dashed-dotted line refers $\delta^{1/2}$; (b) and (c) complex eigenvalues λ_{2i} and λ_{2r} where thin-dotted line refers $\delta^{1/2}$ calculated at the back and front of the solitary wave as a function of δ, shows comparison of the full second order model (thick-dotted line) with DNS(solid line).

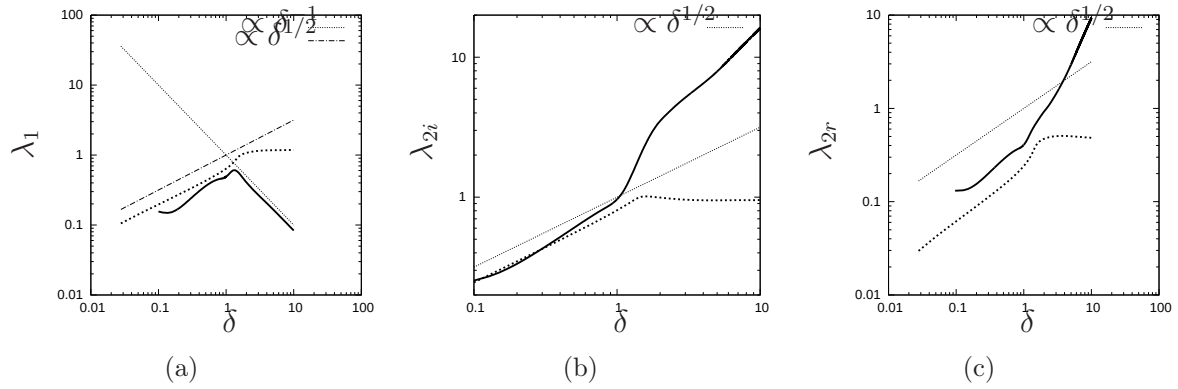

(a) (b) (c)

Figure 3.15: **DNS - Simplified model ($\Gamma = 193$).** a) real eigenvalue λ_1 where thin-dotted line refers δ^{-1} and dashed-dotted line refers $\delta^{1/2}$; (b) and (c) complex eigenvalues λ_{2i} and λ_{2r} where thin-dotted line refers $\delta^{1/2}$ calculated at the back and front of the solitary wave as a function of δ, shows comparison of the simplified model(thick-dotted line) with DNS(solid line).

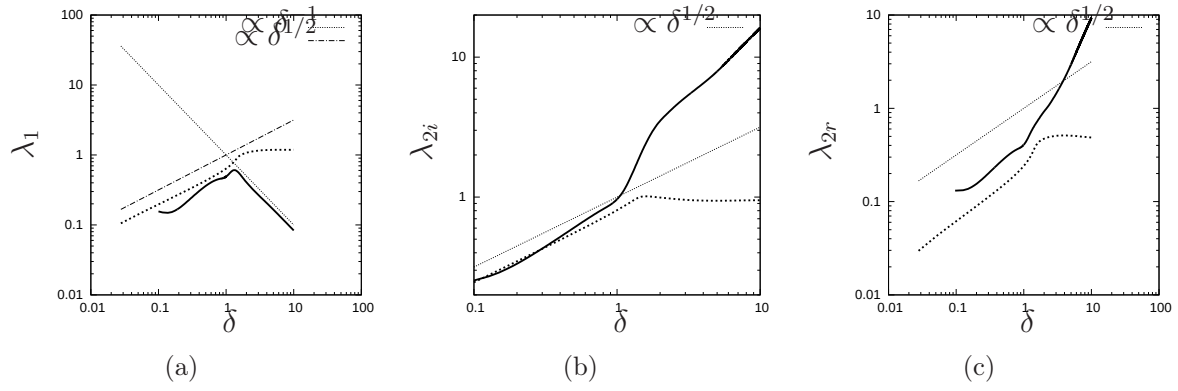

(a) (b) (c)

Figure 3.16: **DNS - Regularized model ($\Gamma = 193$).** a) real eigenvalue λ_1 where thin-dotted line refers δ^{-1} and dashed-dotted line refers $\delta^{1/2}$; (b) and (c) complex eigenvalues λ_{2i} and λ_{2r} where thin-dotted line refers $\delta^{1/2}$ calculated at the back and front of the solitary wave as a function of δ, shows comparison of the regularized model(thick-dotted line) with DNS(solid line).

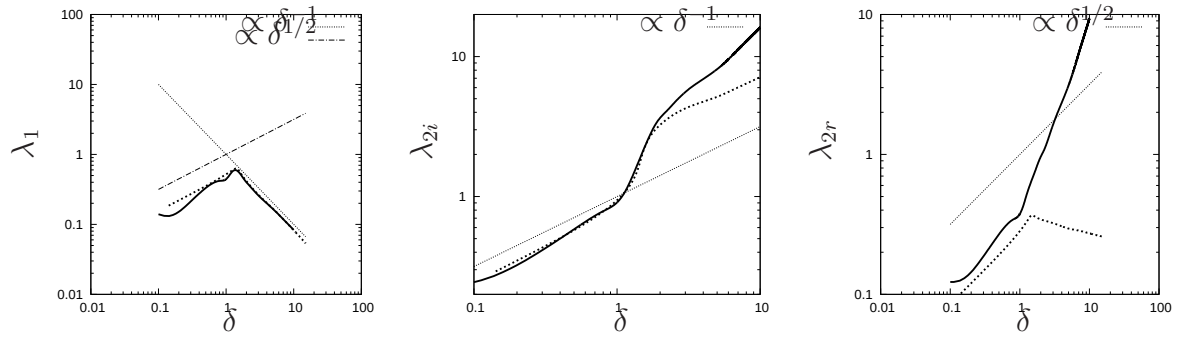

(a) (b) (c)

Figure 3.17: **DNS - Full second order model ($\Gamma = 3400$).** a) real eigenvalue λ_1 where thin-dotted line refers δ^{-1} and dashed-dotted line refers $\delta^{1/2}$; (b) and (c) complex eigenvalues λ_{2i} and λ_{2r} where thin-dotted line refers $\delta^{1/2}$ calculated at the back and front of the solitary wave as a function of δ, shows comparison of the full second order model(thick-dotted line) with DNS(solid line).

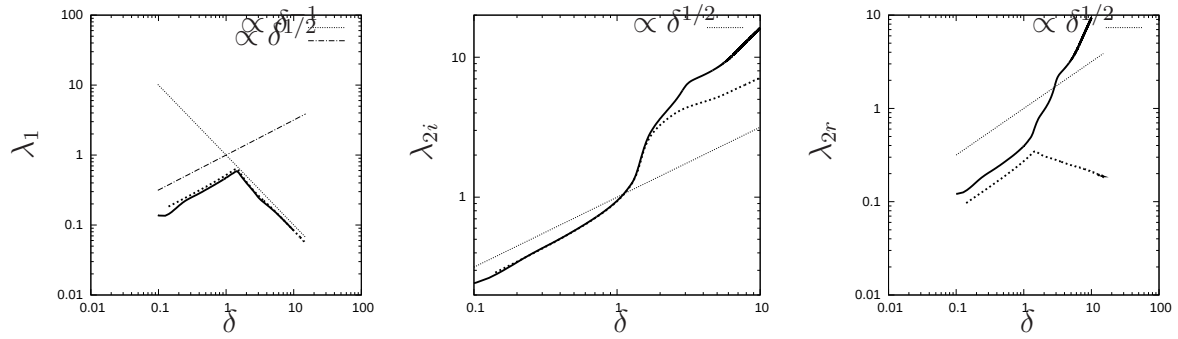

(a) (b) (c)

Figure 3.18: **DNS - Full second order model ($\Gamma = 10000$).** a) real eigenvalue λ_1 where thin-dotted line refers δ^{-1} and dashed-dotted line refers $\delta^{1/2}$; (b) and (c) complex eigenvalues λ_{2i} and λ_{2r} where thin-dotted line refers $\delta^{1/2}$ calculated at the back and front of the solitary wave as a function of δ, shows comparison of the full second order model(thick-dotted line) with DNS(solid line) for $\Gamma = 10000$.

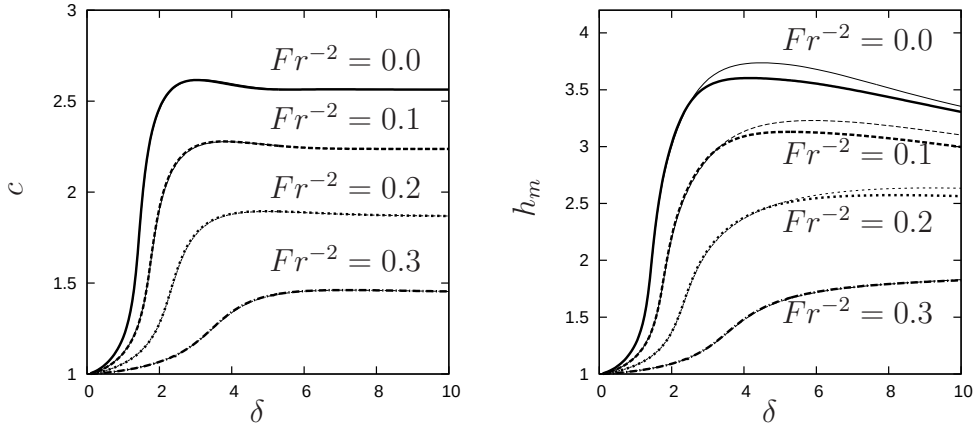

Figure 3.19: The phase speed a) and the wave height b) with respect to the reduced Reynolds number δ of one hump solitary wave for vertical wall ($1/Fr^2 = 0.0$) and inclined walls ($1/Fr^2 = 0.1, 0.2, 0.3$) where the thick-(solid, dashed, dotted, dash-dotted) line corresponds to the result of DNS and thin-(solid, dashed, dotted, dash-dotted) line corresponds to the result of the full second order model for $\Gamma^* = 193$

the solitary waves profile for full second order model by Ruyer-Quil & Manneville [113] for different values of Kapitza number, $\Gamma = 3400$ and $\Gamma = 10000$ are shown in the Fig. 3.17 and Fig. 3.18 respectively.

3.5.1 Effect of Froude number to solitary wave properties

Now, extreme solitary waves are studied for film flow not only along vertical wall but also along inclined wall. Inertia and gravity can be compared in terms of the Froude number Fr, which compares the speed of "kinematic wave" $3u_s$ (linear waves in the limit $k \to 0$), and the speed of " surface gravity waves". Written in terms of the Froude number, the critical threshold of long wave instability, $Re_c = \frac{5}{6}\cot\beta$, that reads $Fr_c^{-2} = 2/5$. If the value of Fr^{-2} varies in the unstable range from zero for vertical wall to the critical threshold, $Fr^{-2} = 0 \div 0.4$, the solitary wave properties can be shown for the liquid of water-glycerin with $\Gamma^* = 193$ in Fig. 3.19 where Γ^* depending only on liquid properties. It is observed that for the same δ, the phase speed and wave height get smaller when approaching the instability threshold or the critical Froude number. The DNS result also confirms the linear stability theory that there is no more wave above the threshold $Fr_c^{-2} = 2/5$. At the other end of the range, speed and amplitude reach their largest values for a flow along vertical wall, $Fr^{-2} = 0$. Again, it is observed that the results given by the

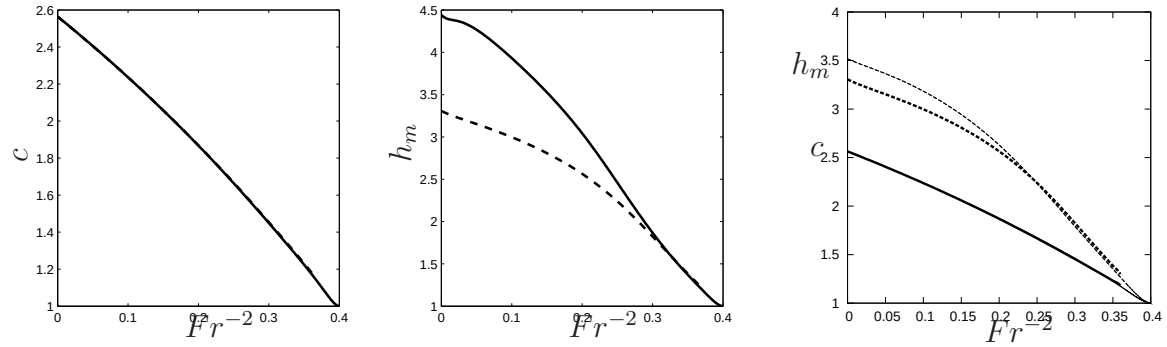

(a) (b) (c)

Figure 3.20: (a) and (b) represents the results from DNS for the extreme solitary wave properties in terms of $(1/Fr^2)$ in the drag-inertia regime at $\delta = 10$ where dashed line refers $\Gamma^* = 193$ and solid line refers $\Gamma^* = 3400$. (c) thick-solid line and thick-dashed line refers the result of DNS is compared to the full second order model results which is represented by thin-solid and thin-dashed line for $\Gamma^* = 193$ at $\delta = 10$.

full second order model are in excellent agreement with the DNS results, see Fig. 3.19. Moreover the wave height of solitary wave is observed to not depend on liquids up to a distance from the critical threshold $Fr^{-2} = 0.4$, and departures are more significant in smaller Fr^{-2} range, as shown in Fig. 3.20 for two liquids: water-glycerin, and pure water $\Gamma^* = 3400$ when all other physical parameters δ and Fr are kept the same. On the other hand, the c curves appear to be insensitive to liquids properties, and nearly linearly proportional to $Fr^{-2} - Fr_c^{-2}$ from the criticality.

Noting the high δ limit of the same Fr curve, the phase speed appears to approach asymptotic value irrespective of flow rate whereas the wave height shows a slight dependence on the δ.

3.6 Summary and Conclusion

Derivation of simplified models, based on long-wave expansions, for the description of liquid film flow has a long history marked by classical results such as the one-equation model of Benney and the two-equation model of Shkadov. A crucial test of such models is the correct prediction of the properties (shape, maximum height, phase velocity) of solitary waves as a function of the distance from the instability threshold. The latter is usually quantified in terms of the reduced Reynolds number, δ, where the Reynolds number is defined in terms of the undisturbed film thickness and mean velocity, $Re = u_s h_s/\nu$,

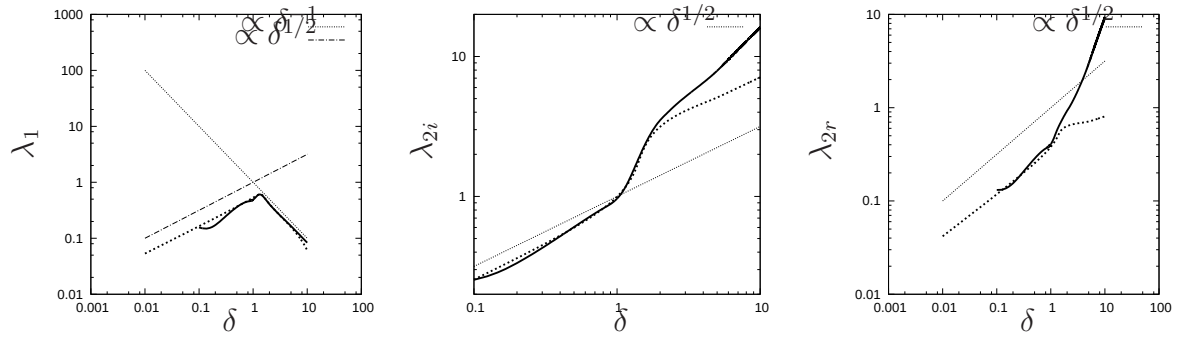

(a) (b) (c)

Figure 3.21: a) real eigenvalue λ_1 where thin-dotted line refers δ^{-1} and dashed-dotted line refers $\delta^{1/2}$; (b) and (c) complex eigenvalues λ_{2i} and λ_{2r} where thin-dotted line refers $\delta^{1/2}$ shows comparison of the full second order model(thick-dotted line) with DNS(solid line) at $\underline{Fr^{-2} = 0.0}$ for $\Gamma^* = 193$.

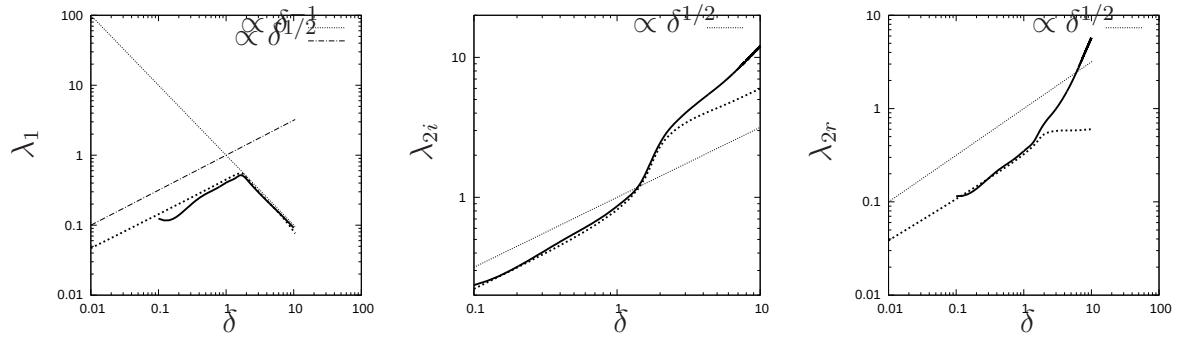

(a) (b) (c)

Figure 3.22: a) real eigenvalue λ_1 where thin-dotted line refers δ^{-1} and dashed-dotted line refers $\delta^{1/2}$; (b) and (c) complex eigenvalues λ_{2i} and λ_{2r} where thin-dotted line refers $\delta^{1/2}$ shows comparison of the full second order model(thick-dotted line) with DNS(solid line) at $\underline{Fr^{-2} = 0.1}$ for $\Gamma^* = 193$.

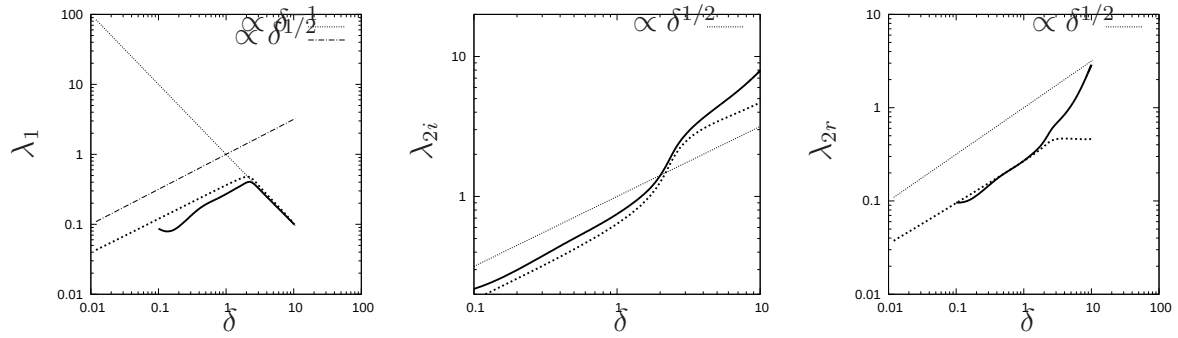

(a) (b) (c)

Figure 3.23: a) real eigenvalue λ_1 where thin-dotted line refers δ^{-1} and dashed-dotted line refers $\delta^{1/2}$; (b) and (c) complex eigenvalues λ_{2i} and λ_{2r} where thin-dotted line refers $\delta^{1/2}$ shows comparison of the full second order model(thick-dotted line) with DNS(solid line) at $\underline{Fr^{-2} = 0.2}$ for $\Gamma^* = 193$.

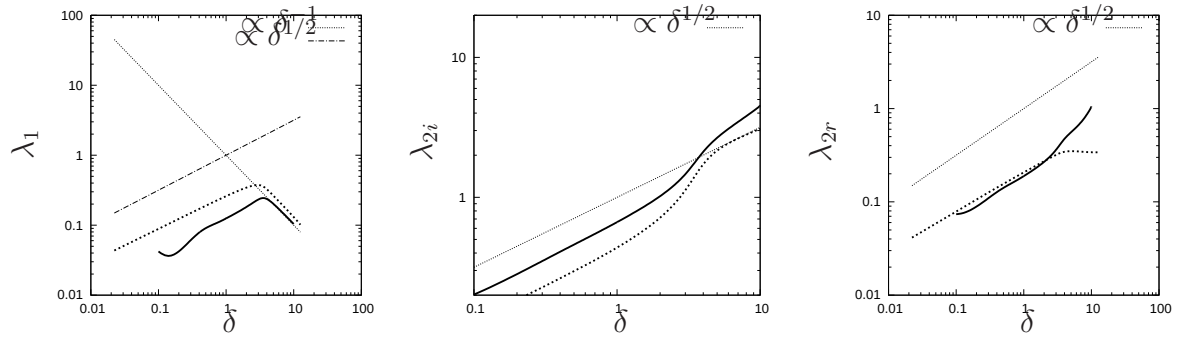

(a) (b) (c)

Figure 3.24: a) real eigenvalue λ_1 where thin-dotted line refers δ^{-1} and dashed-dotted line refers $\delta^{1/2}$; (b) and (c) complex eigenvalues λ_{2i} and λ_{2r} where thin-dotted line refers $\delta^{1/2}$ shows comparison of the full second order model(thick-dotted line) with DNS(solid line) at $\underline{Fr^{-2} = 0.3}$ for $\Gamma^* = 193$.

and the Kapitza number, Γ, contains only physical properties and compares capillary and viscous diffusive effects. Considering a vertical wall and assuming negligible streamwise viscous diffusion effects, i.e. large Kapitza numbers, δ is the only independent parameter of the rescaled equations. It is recalled that, though most models predict similar behavior close to the threshold (onset of drag-gravity regime), they exhibit large differences from each other at intermediate and large values of δ, i.e. when inertia becomes significant (transition region and drag-inertia regime). Thus, rigorous simulations emerge as the only means to resolve this issue. The present work computes accurately the properties of stationary, traveling wave by solving the Navier-Stokes equation by a finite-element technique, implemented with periodic boundary conditions and strong mesh refinement in the vicinity of the solitary wave. Solitary-like waves are derived by considering a long enough computational domain. However, it is shown that lengths of the order of 10^3 times the film thickness are necessary for the properties of the wave to converge asymptotically to the true solitary limit with accuracy less than 10^{-3}. Both the phase velocity and the wave height exhibit inflection points in the transition region, then maxima at intermediate values of δ, and finally a drop to a plateau at high enough δ. These are unique characteristics of the full second-order model by Ruyer-Quil & Manneville, whereas all other models predict either a monotonic increase or a monotonic, asymptotic limit. In particular, simulations and the above second-order model agree quantitatively in the drag-gravity regime and the transition region to the drag-inertia regime, but only qualitatively in the drag-inertia regime. The behavior deep in the drag-inertia regime is found to depend on Γ, which in the present simulations is varied in the range 200-10000. With increasing Γ, the maxima that occur at intermediate δ become steeper. However, whereas the high-δ limit of the phase velocity appears almost unaffected, that of the wave height increases roughly linearly with Γ, which underlines the stabilizing effect of viscous diffusion at low Kapitza numbers.

Chapter 4

Rheology of Non-Newtonian Fluids

4.1 Introduction

Rheology is the study of the flow and deformation of all forms of material. The main interest in rheology science is to analyze and describe the behavior of relevant materials. I simply started with the definition of Newtonian fluid which has a simple linear relation between stress and strain-rate characterized by a constant viscosity. A simple equation to describe Newtonian fluid behavior is $\tau = \mu\dot{\gamma}$ where τ is the shear stress, μ is the fluid viscosity and $\dot{\gamma} = du/dy$ is the strain rate which generally coincides with the velocity gradient perpendicular to the direction of shear. In common terms, this means that the fluid continues to flow, regardless of the forces acting on it. For example, water is Newtonian, because it continues to exemplify fluid properties no matter how fast it is stirred or mixed. Other examples may be aqueous solutions, emulsions. Apart from some annoyingly common fluids such as air and water, virtually no fluid is actually Newtonian. The objective of this chapter is to introduce the different kinds of non-Newtonian flow characteristics and their characterizations; and to illustrate the frequent and wide occurrence of non-Newtonian fluid behaviors in a diverse range of applications, both in nature and in technology.

A non-Newtonian fluid is a fluid whose viscosity is variable based on applied stress or force. The properties of non-Newtonian fluid flows are not described by a single constant value of viscosity. Non-Newtonian fluids arise in virtually every environment. Typical examples within our own bodies are blood and mucus. Many polymer solutions and molten polymers are non-Newtonian fluids, as are many commonly found substances such as lava, snow, suspensions of clay, mud slurries, toothpaste, ketchup, starch suspensions, paint, shampoo, molten rubber and emulsions. In a non-Newtonian fluid, the relation between the shear stress and the strain rate is nonlinear, and can even be time-dependent. Therefore, a constant coefficient of viscosity cannot be defined. The simplest possible deviation from the Newtonian fluid behavior occurs when the simple shear data $\tau - \dot{\gamma}$

does not pass through the origin and/or does not result into a linear relationship between τ and $\dot{\gamma}$. Conversely, the apparent viscosity, defined as $\tau/\dot{\gamma}$, is not constant and is a function of τ or $\dot{\gamma}$. Indeed, under appropriate circumstances, the apparent viscosity of certain materials is not only a function of flow conditions (geometry, shear rate, etc.), but it also depends on the kinematic history of the fluid element under consideration. It is convenient, though arbitrary (and probably unscientific too), to group such materials into the following categories:

- Systems for which the value of $\dot{\gamma}$ at a point within the fluid is determined only by the current value of τ at that point; these substances are variously known as purely viscous, inelastic, time-independent or generalized Newtonian fluids (GNF),
- Systems for which the relation between τ and $\dot{\gamma}$ shows further dependence on the duration of shearing and kinematic history; these are called time-dependent fluids, and finally,
- Systems which exhibit a blend of viscous fluid behavior and of elastic solid-like behavior. For instance, this class of materials shows partial elastic recovery, recoil, creep, etc. Accordingly, these are called visco-elastic or elasto-viscous fluids.

In fact, all fluids are non-Newtonian on an appropriate time-scale, though for many common fluids such as air and water the time-scale is extremely short. When the time-scale of a flow t_f is much less than the relaxation time t_r of an elasto-viscous material, elastic effects dominate. This typically happens when there are abrupt changes in flow geometry. When on the other hand t_f is much greater than t_r elastic effects relax quickly for viscous effects to dominate. This typically happens when there are no abrupt changes in flow geometry. The ratio of t_f to t_r is a dimensionless number of particular significance in the study of flow of non-Newtonian fluids which is called the Deborah Number. If the Deborah number is small, elastic effects can be neglected and the non-Newtonian fluid can be treated as a purely viscous material, albeit with a non-constant viscosity. For Newtonian fluids, the viscosity is independent of the speed at which the fluid is caused to move. However, for non-Newtonian fluids, the viscosity can change by many orders of magnitude as the speed (velocity gradient) changes.

The mass and linear momentum conservation equations which govern the flow of any fluid are respectively [106]:

$$\frac{\partial \rho}{\partial t} + \nabla \cdot (\rho \mathbf{u}) = 0\,, \tag{4.1}$$

$$\rho \frac{\partial \rho}{\partial t} + \rho \mathbf{u} \cdot \nabla \mathbf{u} = \rho \mathbf{g} - \nabla p + \nabla \cdot \tau\,. \tag{4.2}$$

where ρ denotes the density of the fluid, $\mathbf{u}$ velocity, p pressure, τ stress tensor, g gravitation acceleration and t time. Notice that it is assumed that τ is a symmetrical tensor,

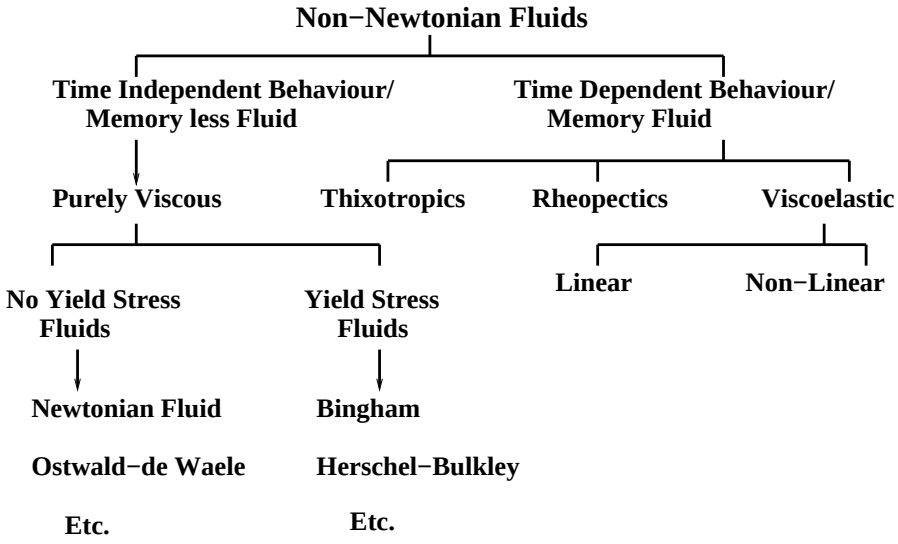

Figure 4.1: Rheological tree of non-Newtonian fluids.

thus ensuring that angular momentum is conserved. Determination of the flow of any fluid requires solution of these conservation equations, subject to appropriate boundary and initial conditions, together with constitutive equations for the fluid. It is in the constitutive equations that the nature of a given fluid is manifested. The science devoted to obtaining suitable constitutive equations for description of the behavior of non-Newtonian fluids is called rheology.

For a given material (fluid, solid, soft solid) the rheological behavior can be expressed mathematically trough a relation (constitutive equation) between two of its specific physical quantities. A constitutive equation relates the applied stresses (τ), or forces to strains, to the rate of deformations ($\dot{\gamma}$). Therefore, any decent analysis requires the knowledge and understanding of some fundamental concepts like viscosity, elasticity, viscoelasticity, stress, strain. Generally, practical processes consist of complex fluid flows that are difficult to analyze and describe analytically. Accordingly, the simple motions (like simple shear or extensional flow) are being used to determine rheological properties of fluids and soft solids, a common method being the approximation of experimental data obtained with different constitutive functions describing material behavior. When modeling a flow through a constitutive equation one important aspect is how the model parameters should be determined so that they may be suitable to be used in the process. So far no constitutive model has been proposed which is able to describe the fluid behavior in every possible flow fields. Therefore, any constitutive model has an area of performance within which the specified flow field may be explained satisfactory. Standard constitutive equations in literature are usually applied to some simple kinds of flows.

Fig. 4.1 shows a general classification of non-Newtonian fluids. As noted earlier, the

aforementioned classification scheme is quite arbitrary, though convenient, because most real materials often display a combination of two or even all these types of features under appropriate circumstances. For instance, it is not uncommon for a polymer melt to show time-independent (shear-thinning) and time-dependent behavior simultaneously and for a china clay (kaolin) suspension to exhibit a combination of shear-thinning and shear-thickening features at certain concentrations and/or at appropriate shear rates.

The important constitutive equation for fluid mechanics is the one relating the stress in the fluid to the kinematics of the motion (that is, the velocity, the derivatives of the velocity with respect to position, and the time history of the velocity). Generalized Newtonian fluids consist in a class of non-Newtonian fluids defined by the following constitutive equation. They form the first branch of the rheological tree displayed in Fig. 4.1 (time-independent behavior).

$$\tau_{ij} = \mu(\dot{\gamma})\dot{\gamma}_{ij} \tag{4.3}$$

where $\dot{\gamma} = \sqrt{\dot{\gamma}_{ij}\dot{\gamma}_{ij}/2}$ and $\dot{\gamma}_{ij} = (\partial_i u_j + \partial_j u_i)$ are called the rate of strain tensor, and $\mu(\dot{\gamma})$ is the viscosity as a function of the rate of strain. Here, u_i is the ith component of the velocity vector, and the i are the position coordinates. The generalized Newtonian fluid constitutive equation is not capable of describing viscoelasticity or any effects of normal stress differences.

4.2 Generalized Newtonian Fluid

Each type of generalized Newtonian fluid behavior, i.e., shear-thinning, shear-thickening and visco-plastic fluids, is now dealt with more detail in this section. Fig. 4.2, shows qualitatively the flow curves of different types of generalized Newtonian fluid.

4.2.1 Shear-thinning fluid

A fluid is shear-thinning when the apparent viscosity μ(defined as $\tau/\dot{\gamma}$) decreases with the stress rate. This is also known as pseudoplastic. In daily life, a paper pulp in water, latex paint, ice, blood, syrup, molasses, etc. are examples of this kind of fluids. In polymeric systems (melts and solutions), at low shear rates, the apparent viscosity approaches to a Newtonian plateau where the viscosity is independent of shear rate (zero shear viscosity, μ_0).

$$\lim_{\dot{\gamma}\to 0} \frac{\tau}{\dot{\gamma}} = \mu_0 \,. \tag{4.4}$$

Furthermore, only polymer solutions also exhibit a similar plateau at very high shear rates (infinite shear viscosity, μ_∞), i.e.,

$$\lim_{\dot{\gamma}\to \infty} \frac{\tau}{\dot{\gamma}} = \mu_\infty \,. \tag{4.5}$$

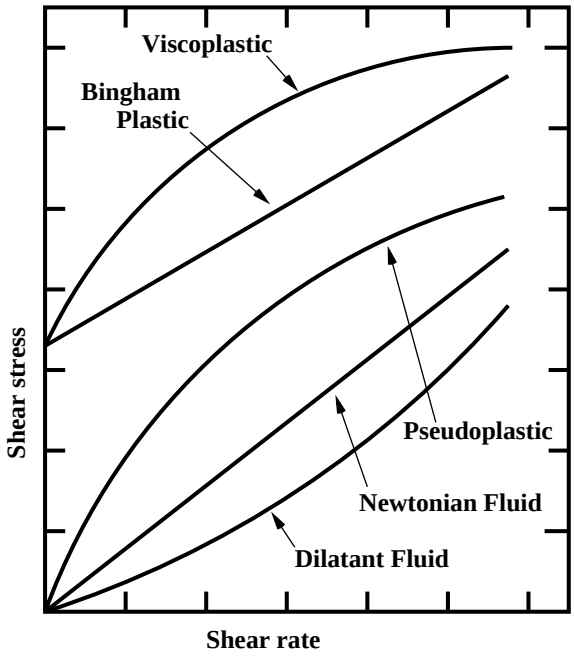

Figure 4.2: Summary of the different types of generalized Newtonian fluids.

Typically, the viscosity μ of these fluids is given as a function of the rate of strain $\dot{\gamma}$. A simple and widely used constitutive equation for this type of fluid is the Carreau fluid,

$$\mu = \mu_\infty + (\mu_0 - \mu_\infty)[1 + (\lambda_r \dot{\gamma})^2]^{(n-1)/2} \tag{4.6}$$

This model involves four parameters: μ_0, the viscosity at very small shear rates, μ_∞, the viscosity at very large shear rates; λ_r, which describes the shear rate at which the curve begins to decrease; and n, which determines the rate at which viscosity decreases. Fig. 4.3 shows the viscosity for a fluid that is shear-thinning (that is, the viscosity decreases as the shear rate increases, $n < 1$, and μ_0 is greater than μ_∞). For other non-Newtonian fluids, the viscosity might increase as the shear rate increases (shear-thickening fluids, for which n is greater than one and μ_0 is less than μ_∞).

4.2.2 Shear-thickening fluid

A shear thickening fluid (also known as dilatant) is a fluid in which apparent viscosity increases with the strain rate. This behavior is generally encountered in suspension. It is only one type of deviation from Newton's Law, and it is controlled by such factors as particle size, shape, and distribution. This can readily be seen with a mixture of cornstarch and water. This class of fluids is similar to pseudo-plastic (shear-thinning) systems in that it shows no yield stress, but its apparent viscosity increases with the increasing shear rate

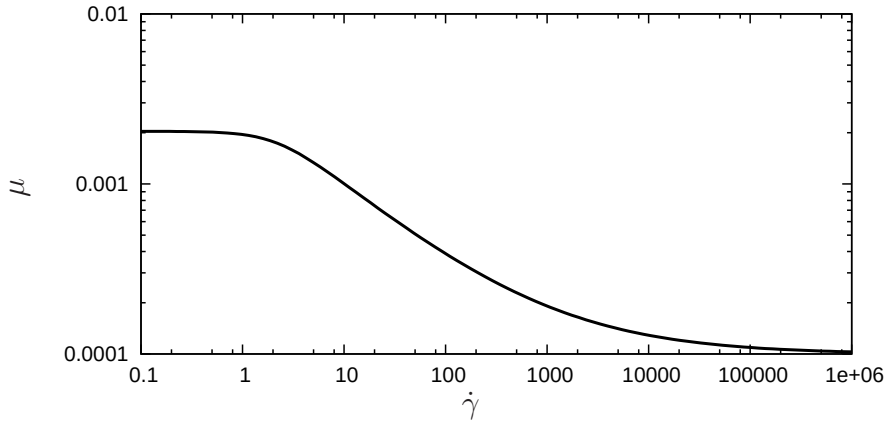

Figure 4.3: Typical dependence of the viscosity (μ) on shear rate ($\dot{\gamma}$) for a non-Newtonian fluid. The functional from shown is called the Carreau model.

and hence the name shear-thickening. Originally, this type of behavior was observed in concentrated suspensions, and one can qualitatively explain it as follows: at rest, the voidage of the suspension is minimum and the liquid present in the sample is sufficient to fill the voids completely. At low shearing levels, the liquid lubricates the motion of each particle past another thereby minimizing solid–solid friction. Consequently, the resulting stresses are small. At high shear rates, however, the mixture expands (dilates) slightly (similar to that seen in sand dunes) so that the available liquid is no longer sufficient to fill the increased void space and to prevent direct solid–solid contacts (and friction). This leads to the development of much larger shear stresses than that seen in a pre-dilated sample at low shear rates. This mechanism causes the apparent viscosity μ to rise rapidly with the increasing rate of shear. Of the time-independent fluids, this sub-class has generated very little interest and hence very few reliable data are available. Indeed, until up to about early 1980s, this type of flow behavior was considered to be rare, but, however, with the recent growing interest in the handling and processing of systems with high solids loadings, it is no longer. Typical examples of fluids showing shear-thickening behavior include thick suspensions and pastes of kaolin, TiO_2 and corn flour in water.

4.2.3 Power Law or Ostwald de Waele Equation

A power-law fluid, or the Ostwald–de Waele relationship, is the simplest type of generalized Newtonian fluid for which the shear stress, τ, is given by

$$\tau = m\dot{\gamma}^n \,, \tag{4.7}$$

where m is the flow consistency index, $\dot{\gamma}$ is the shear rate or the velocity gradient perpendicular to the plane of shear and n is the flow behavior index. The currently available

limited information (mostly restricted simple shear) suggests that it is possible to approximate $\tau - \dot{\gamma}$ data for these systems also by the power law model (4.7), with the power-law index (n) taking on values greater than unity. Notwithstanding the lack of rheological data on such systems, it is not yet possible to say with confidence whether these materials also display limiting viscosities in the limits of $\dot{\gamma} \to 0$ and $\dot{\gamma} \to \infty$.

The quantity

$$\mu_{\text{eff}} = m\dot{\gamma}^{n-1}\,, \tag{4.8}$$

represents an apparent or effective viscosity as a function of the shear rate. Also known as the Ostwald–de Waele power law, this mathematical relationship is useful because of its simplicity, but only approximately describes the behavior of a real generalized Newtonian fluid. For example, if $n < 1$, the power law predicts that the effective viscosity, μ_{eff}, would decrease with increasing shear rate, $\dot{\gamma}$ indefinitely, requiring a fluid with infinite viscosity at rest and zero viscosity as the shear rate approaches infinity, but a real fluid has both a minimum and a maximum effective viscosity that depend on the concentration and molecular weight of the polymer, etc. If $n = 1$ it will show the Newtonian behavior and the consistency is just the viscosity. However, if $n > 1$, the viscosity increases with the amount of shearing, and the fluid has a shear-thickening behavior. Therefore, the power-law is only a good description of fluid behavior across the range of shear rates to which the coefficients were fitted. In these equations, m and n are two empirical curve-fitting parameters.

4.2.4 Viscoplastic fluids

This type of non-Newtonian fluid behavior is characterized by the existence of a threshold stress (called yield stress or apparent yield stress, τ_0), which must be exceeded for the fluid to deform (shear) or flow. Conversely, such a substance will behave like an elastic solid (or flow en masse like a rigid body) when the externally applied stress is less than the yield stress, τ_0. Of course, once the magnitude of the external yield stress exceeds the value of τ_0 , the fluid may exhibit Newtonian behavior (constant value of μ) or shear-thinning characteristics, i.e., $\mu(\dot{\gamma})$. It therefore stands to reason that, in the absence of surface tension effects, such a material will not level out under gravity to form an absolutely flat free surface. Quantitatively, this type of behavior can be hypothesized as follows: such a substance at rest consists of three-dimensional structures of sufficient rigidity to resist any external stress less than $|\tau_0|$ and therefore offers an enormous resistance to flow, albeit it still might deform elastically. For stress levels above $|\tau_0|$, however, the structure breaks down and the substance behaves like a viscous material. In some cases, the build-up and breakdown of structure has been found to be reversible, i.e., the substance may regain its (initial or somewhat lower) value of the yield stress following a long period of rest. A fluid with a linear flow for $|\tau| > |\tau_0|$ is called a Bingham plastic fluid, and is characterized by a constant value of viscosity μ_B. A Bingham plastic

is a viscoplastic material that behaves as a rigid body at low stresses but flows as a viscous fluid at high stress. A common example is mayonnaise and toothpaste, which will not be extruded until a certain pressure is applied to the tube. It then is pushed out as a solid plug. The material is rigid for shear stress $|\tau|$, less than a critical value $|\tau_0|$. Once the critical shear stress (or "yield stress") is exceeded, the material flows in such a way that the shear rate, $\dot{\gamma}$, is directly proportional to the amount by which the applied shear stress exceeds the yield stress. Thus, in one-dimensional shear, the Bingham model is written as:

$$\begin{aligned} \tau &= {\tau_0}^B + \mu_B \dot{\gamma} \qquad |\tau| > |{\tau_0}^B|\,, \\ \dot{\gamma} &= 0 \qquad |\tau| < |{\tau_0}^B|\,, \end{aligned} \tag{4.9}$$

The physical reason for this behavior is that the liquid contains particles (e.g. clay) or large molecules (e.g. polymers) which have some kind of interaction, creating a weak solid structure, formerly known as a false body, and a certain amount of stress is required to break this structure. Once the structure has been broken, the particles move with the liquid under viscous forces. If the stress is removed, the particles associate again.

On the other hand, a visco-plastic material showing shear-thinning behavior at stress levels exceeding $|\tau_0|$ is known as a yield-pseudoplastic fluid, and its behavior is frequently approximated by the so-called Herschel–Bulkley fluid model written for 1-D shear flow as follows:

$$\begin{aligned} \tau &= {\tau_0}^H + \mu(\dot{\gamma})^n \qquad |\tau| > |{\tau_0}^H|\,, \\ \dot{\gamma} &= 0 \qquad |\tau| < |{\tau_0}^H|\,, \end{aligned} \tag{4.10}$$

Probably the most popular model that incorporates both shear thinning or shear thickening and a yield stress is the Herschel–Bulkley model, where τ_0 is the yield stress. With $n \neq 1$, the Herschel–Bulkley model allows also for shear thinning or thickening beyond yielding.

Typical examples of yield-stress fluids include blood, yogurt, melt chocolate, tomato ketchup, cosmetics, nail paint, foams, suspensions, etc. In geophysical context, wet snow exhibits a yield-pseudoplastic behavior. Debris flows in mountainous area consists in concentrated suspensions of clay and sand that also exhibit a pseudo-plastic behavior. Finally, it is appropriate to mention here that it has long been a matter of debate and discussion in the literature whether a true yield stress exists or not. In experimental view, the yield stress in terms of a transition from solid-like behavior to fluid-like behavior which manifests itself in terms of an abrupt decrease in viscosity (by several orders of magnitude in many substances) over an extremely narrow range of shear rate. Evidently, the answer to the question whether a substance has a yield stress or not seems to be closely related to the choice of a time scale of observation. In spite of this fundamental difficulty, the notion of an apparent yield stress is of considerable value in the context of engineering

applications, especially for product development and design in food, pharmaceutical and health care sectors. A large number of industrial and geophysical problems involve the spreading of viscoplastic fluids under gravity over horizontal and inclined surfaces or within a channel, including certain emplacements of concrete and lava; and the flow viscoplastic fluid can come to rest under the action of the yield stress.

4.3 Viscoelastic fluids

The aim of this section is to show how the ideas of viscosity and elasticity can be combined to derive a single constitutive equation describing the viscoelastic effects of viscoelastic liquids. Viscoelastic fluid is a fluid that behaves like a solid and as well as viscous behavior. The rheological response of viscoelastic fluids is quite complex, including combination of viscous and elastic effects. Many materials initially shows viscous behavior when some shear is applied and then 'relax' to elastic behavior. Perhaps the most striking behavior of non-Newtonian fluids is a consequence of their viscoelasticity. Elastic solids can be thought of as having perfect memory. If they are deformed through the action of a force, they return to their original shape when the force is removed. This happens when a rubber ball bounces, the ball is deformed as it hits a surface, but the rubber remembers its undeformed spherical shape. Recovery of the shape causes the ball to bounce back. In contrast, Newtonian fluids have no memory; when a force is removed, they retain their condition at the time the force is removed (or continue moving as the result of inertia). When a Newtonian fluid is dropped onto a surface, it does not bounce. Some non-Newtonian fluids are viscoelastic in the sense that they have fading memory. If a force is removed shortly after it is applied, the fluid will remember its undeformed shape and return towards it. However, if the force is applied on the fluid for a long time, the fluid will eventually forget its undeformed shape. If a sample of a non-Newtonian fluid is dropped onto a surface, it will bounce like a ball. However, if the fluid is simply placed on the surface, it will flow smoothly. Viscoelasticity is frequently the cause of many of the secondary flows that are observed for non-Newtonian fluids. It has elastic nature and it will regain back when applied stress is removed. Viscous fluids, like honey, resist shear flow and strain linearly with time when a stress is applied. Viscoelastic fluids have elements of both of these properties and, as such, exhibit time dependent strain.

The generalized Newtonian fluid model does not incorporate any elastic effects whatsoever, and so is inappropriate for such flows. Instead, it is usually necessary to introduce the strains as well as strain rates into the constitutive law. This is apparent from the constitutive law must take in the extreme limits: an incompressible linear elastic material has a stress that is proportional to the strain, whereas a Newtonian fluid has a stress proportional to the rate of strain. Thus, for a general viscoelastic fluid, the constitutive law takes the form of an evolution equation. The appearance of time evolution terms in the rheology relation reflects the relaxational character of the fluid stresses, and leads to

the notion of a characteristic relaxation timescale.

One standard experiment is to apply instantaneously a shear at the surface of a sample material. If the material is linearly elastic the resulting stress is zero before the application of the shear, and constant immediately afterwards. On the other hand, if the material is a Newtonian fluid, the stress is infinite at the instant the stress is applied, but thereafter is zero. Thus elastic and viscous responses are markedly different, and many real materials have elements of both types of response. A viscoelastic material will have an initially large stress due to the viscous component, but the stress then decreases over the relaxation time to a constant value arising due to the intrinsic elasticity. The simplest constitutive equation that is capable of describing viscoelasticity is the Maxwell model.

If It be assumed that the relation between the deviatoric stress and the strain rates is purely linear, then a general constitutive law can be stated as

$$\tau_{ij} = \int_{-\infty}^{t} G(t-\tau)\dot{\gamma}_{ij}(\tau)d\tau\,, \tag{4.11}$$

Here, $G(t)$ is called the relaxation function, and builds in the elastic and viscous behavior. Implicitly, the shape of the function $G(t)$ determines the characteristic relaxation timescale (or timescales if there are more than one). The relaxation time is important because it characterizes whether viscoelasticity is likely to be important within an experimental or observational timescale. Many fluids, particularly those in industrial situations containing polymers or emulsion droplets, exhibit both elastic and viscous responses on an experimental or observational timescale.

For a Newtonian fluid, $G(t) = \mu\delta(t)$ and relaxation is immediate. If the relaxation time is denoted by λ_r then the simplest viscoelastic model, the Maxwell model, has $G(t) = \mu\exp(-t/\lambda_r)/\lambda_r$ and the integral relation above can be recast in the form of a differential constitutive relation,

$$\tau_{ij} + \lambda_r\dot{\tau}_{ij} = \mu\dot{\gamma}\,. \tag{4.12}$$

In the Maxwell model, expresses the stresses as time integrals over the history of the velocity derivatives, where G (the shear modulus) and λ_r (the relaxation time) are material-dependent constants, and the time integral extends over all past time. It is straightforward to see how the Maxwell model incorporates the memory of the fluid; the stresses at the current time depend on the velocity derivatives at past times, and the memory fades because of the exponential that becomes smaller at more distant past times. For smaller values of λ_r the memory fades more rapidly, and for larger values of λ_r the fluid behaves more elastically.

Much can be achieved with this simple extension to the Newtonian constitutive model, and in many circumstances, particularly if one wishes to investigate whether viscoelasticity can be important, this linear theory suffices. Extensions to multiple relaxation times with a sequence of relaxation functions are also straightforward.

Unfortunately, the Maxwell model (4.12) has at least one major failing– it is not frame indifferent (objective). That is, if a moving coordinate frame change, the equations are also changed. One crude, effective and ad-hoc cure is to replace the time derivatives in (4.12) with more complicated operators that build in the convection, rotation and stretching of the fluid motion. These operators, called either Oldroyd or Jaumann derivatives, render the equations frame indifferent; in usual tensor notation, the Oldroyd (upper convected) derivative, $\overset{\triangledown}{\tau}$, for a tensor τ is

$$\overset{\triangledown}{\tau} = \partial_t \tau + \mathbf{v}\nabla\tau - \tau\nabla\mathbf{v}^{\mathbf{T}} - \nabla\mathbf{v}\tau \tag{4.13}$$

These derivatives involve the local fluid motion, and so substantially complicate the constitutive law, and therefore computations using them. Although Balmforth & Craster [7] introduced these derivatives as a mathematical device to improve the linear model.

4.4 Elasto-viscoplastic fluids

A fluid which displays simultaneous elastic, viscous and plastic behaviors is referred to as elastoviscoplastic or EVP. The Herschel-Bulkley rheological fluid model includes viscosity and plasticity. In this classical model, under the yield stress the material is strictly rigid. Complementing this model by including an elastic behavior under the yield stress leads to a description of elastoviscoplastic (EVP) materials such as suspensions or liquid foams. Many industrial materials, such as filled polymers, polymer gels, thickeners, foodstuffs, cosmetics, concentrated mineral suspensions, electro-rheological and magneto-rheological fluids behave rheologically in a manner that varies between elastic solid and viscous liquid depending upon the processing conditions. The existence of a "yield stress" is traditionally recognized to be responsible for the complicated transition between classical solid-like and liquid-like behavior.

Saramito [120, 121] and Benito *et al.* [11] derived (independently) tensorial elasto-viscoplastic models that combine viscoelastic and viscoplastic properties. They satisfy the second law of thermodynamics and match the behavior of elasto-viscoplastic materials such as foams and emulsions: elastic solid before yielding and viscoelastic flow after yielding. The elasto-viscoplastic model presented by Saramito [121] is simple enough to allow for the numerical resolution of the associated partial differential equations even in intricate two-dimensional (Cheddadi *et al.* [27]) and three-dimensional geometries and is thus suitable for practical and industrial purposes. It is written as

$$\frac{1}{G}\overset{\triangledown}{\tau} + \max\left(0, \frac{|\tau| - \tau_0}{K|\tau|^n}\right)^{\frac{1}{n}} \tau - \dot{\gamma} = 0 \tag{4.14}$$

where $\overset{\triangledown}{\tau}$ is defined in equations (4.13), and G is the elastic modulus and K is a consistency

parameter. When $1/G = 0$ we obtain the Herschel–Bulkley model.

$$\tau = K|\dot{\gamma}|^{n-1}\dot{\gamma} + \tau_0 \frac{\dot{\gamma}}{|\dot{\gamma}|} \qquad \text{when} \qquad |\dot{\gamma}| > 0 \tag{4.15a}$$

$$|\tau| < \tau_0 \qquad \text{when} \qquad |\dot{\gamma}| = 0 \tag{4.15b}$$

Conversely, when $n = 1$ and $\tau_0 = 0$, we obtain the Oldroyd-B model,

$$\frac{1}{G}\overset{\triangledown}{\tau} + \tau = K\dot{\gamma}\,. \tag{4.16}$$

Finally, when both $1/G = 0$, $\tau_0 = 0$ and $n = 1$, the Newtonian behavior is recovered.

4.5 Summary and Conclusion

There is a wide range of rheological models available for non-Newtonian fluids. I have simply focused on the most popular ones. Now, having set the framework of non-Newtonian fluids, I consider the simplest case of generalized Newtonian falling film problem modeled by a power-law in Chapter 5, showing the effects of shear-thinning and shear-thickening fluid close to threshold. In Chapter 6, I introduce the effect of the yield stress at the free surface using Saramito's model for elasto-viscoplastic fluid that combines both the Oldroyd viscoelastic model and the Hershel-Bulkley viscoplastic model with a power-law index $n > 0$.

Chapter 5

Generalized Newtonian fluid

This chapter is an extended version of a published paper "Wavy regime of a power-law film flow" by C. Ruyer-Quil, S. Chakraborty and B. S. Dandapat, *Journal of Fluid Mechanics*, vol. 692, pp. 220-256, published on January 2012. My specific contribution to this work is to perform linear stability analysis with Orr-sommerfeld problem and compute the nonlinear traveling wave solution by using Gerris and Auto-07p software.

5.1 Introduction

Mud flows are frequently encountered in mountainous regions, especially after torrential rains, and often exhibit a series of breaking waves (roll waves). These type of waves can also be observed as an event following volcano eruptions. A report on roll waves can be found in extensive references quoted by Ng & Mei [85]. The roll waves which occur in inclined open channels are important in drainage problems and have received an extensive treatment in turbulent regime by Jeffreys [55], Dressler [41], Boudlal & Liapidevskii [13], among others, and for a laminar sheet flow by considering the flow with quadratic distribution of velocity profile [4, 17, 58, 14]. The discontinuous waves play an important role in engineering and geophysical processes. Roll waves consist of a periodic pattern of bores separated by continuous profiles of free boundary. The transition from uniform flow to intermittent flow regime is usually tackled by resorting to stability theory. When it is perturbed, a steady flow becomes unstable, if certain criteria are satisfied, and evolves towards wave breaking. Dressler has been the first, who gave the analytical solution for such waves in open channel flows. Based on long wave approximation, Dressler's theory of roll waves was extended in [85] to a shallow layer of fluid mud, which has been modeled as a power law fluid. It has been shown, particularly, that if the fluid is highly non-Newtonian, very long waves may still exist even if the corresponding uniform flow is stable to infinitesimal perturbations.

The space time evolution of a Newtonian liquid film flowing down an inclined plane

exhibits a very rich phenomenology which has attracted a considerable number of studies since Kapitza's experiments in the years 1940s [60]. This is a classical example of a convective primary instability [15] giving way to a sequence of secondary instabilities ending with teardrop-shape large-amplitude solitary waves (see e.g. [4, 25, 59] for a review of this complex phenomenology). There is still a renewed interest for falling film wavy dynamics and, in particular to its spatio-temporal disordered state of solitary waves in interaction, which is an example of weak turbulence organized by dissipative structures [79]. The experiments by Liu & Gollub, Vlachogiannis & Bontozoglou [70, 143] have evidenced coalescence and repulsion events between waves resulting into a decrease of the number of solitary waves with the distance at inlet. This coarsening dynamics have been numerically investigated by Chang *et al.* [22].

In comparison to the Newtonian case, far less studies have been devoted to generalized Newtonian film flows for which the effective viscosity $\mu_{\text{eff}}(\dot{\gamma})$ is a function of the strain rate $\dot{\gamma}$. Yet, because of the simplicity of the Ostwald-de Waele power-law model

$$\mu_{\text{eff}}(\dot{\gamma}) = \mu_n \dot{\gamma}^{n-1}\,, \tag{5.1}$$

shear-thinning falling films have recently been the subject of a consequential interest (see e.g. [32, 33, 129, 5, 44]). These studies are based on the shallow-water averaging of the primitive equations, also often referred to as the integral boundary layer formulation in the context of falling films [25]. A scale separation is assumed in the streamwise and cross-stream directions, the free surface being deformed on a length scale that is much larger than the film thickness, which enables the introduction of a small film parameter ϵ. The continuity and momentum equations are integrated in depth and form a closed system of equations for the film thickness h and the local flow rate q once a closure hypothesis, generally a self-similar velocity distribution, is made. Amaouche *et al.* [5] and Fernández-Nieto *et al.* [44] have corrected the Kármán-Polhausen averaged momentum equation derived by Hwang *et al.* [52] and Ng & Mei [85] and formulated two-equation models that are consistent up to order ϵ. This consistency enabled them to correctly capture the instability threshold obtained by Ng & Mei, Miladinova *et al.* [85, 82].

The two-equation models derived by Amaouche *et al.* [5] and Fernández-Nieto *et al.* [44] are consistent at $O(\epsilon)$ but do not account for $O(\epsilon^2)$ effects such as streamwise viscous diffusion, which is known to affect wave-to-wave interaction processes and thus the wave dynamics for Newtonian film flows [62, 63, 101]. In this chapter, a modeling attempt of power-law falling film flows including second-order viscous diffusion terms in a consistent way is presented. To account for streamwise viscous diffusion, the effective viscosity $\mu_{\text{eff}}(\dot{\gamma})$ and its derivative $d\mu_{\text{eff}}/d\dot{\gamma}$ must be computed at the free surface, where the strain rate $\dot{\gamma}$ goes to zero for an unperturbed interface. In the case of the power law (5.1) either $\mu_{\text{eff}}(0)$ or $d\mu_{\text{eff}}/d\dot{\gamma}(0)$, or both, are undefined for $n < 3$ which corresponds to most shear-thinning and shear-thickening fluids. This calls for a regularization at zero strain rate of the power law (5.1) which is here accounted for by introducing a Newtonian plateau at low strain rates.

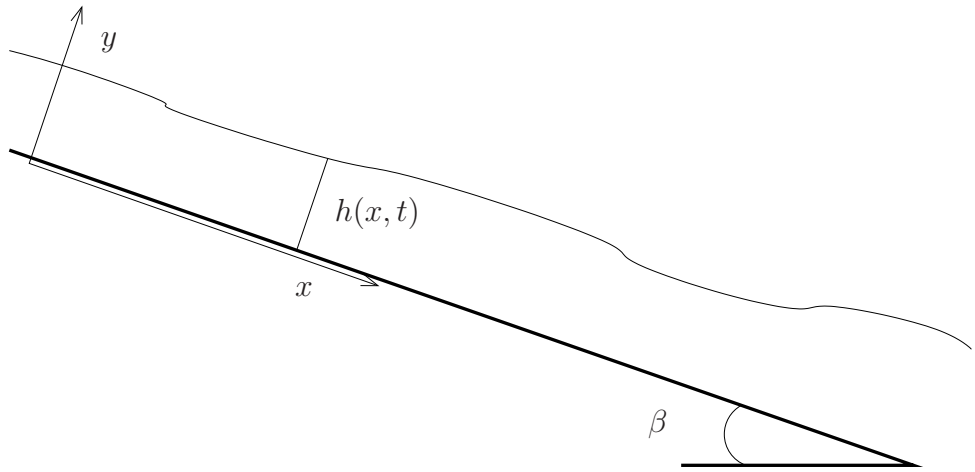

Figure 5.1: A sketch of the geometry for a power-law film flowing down an inclined plane.

This chapter is organized as follows: Section 5.2 presents the governing equations. The weighted-residual modeling approach is detailed in § 5.3 and § 5.4. The linear stability of the base flow is discussed in § 6.5. Nonlinear traveling waves are obtained and compared to direct numerical simulations in § 5.6. The conditional stability of a shear-thinning film is considered in § 5.8. Section 5.9 concludes the present study.

5.2 Governing equations

We consider a power-law fluid flowing down an inclined plane under the action of gravity as sketched in Fig. 5.1. The flow is assumed to be incompressible and the fluid properties, density ρ, surface tension σ, viscosity μ_n and power-law index n are constant. The angle of inclination β and the gravity acceleration g are also constant. The dimensional governing equations read

$$\partial_x u + \partial_y v = 0\,, \tag{5.2a}$$

$$\rho\left(\partial_t u + u\partial_x u + v\partial_y u\right) = -\partial_x p + \rho g \sin\beta + \partial_x \tau_{xx} + \partial_y \tau_{xy}\,, \tag{5.2b}$$

$$\rho\left(\partial_t v + u\partial_x v + v\partial_y v\right) = -\partial_y p - \rho g \cos\beta + \partial_x \tau_{yx} + \partial_y \tau_{yy}\,, \tag{5.2c}$$

$$\text{where} \qquad \tau_{ij} = 2\mu_{\text{eff}} D_{ij} \tag{5.2d}$$

Here $\mathbf{u} = u\mathbf{i} + v\mathbf{j}$ is the velocity field, $D_{ij} = (\partial_i u_j + \partial_j u_i)/2$ is the rate of strain tensor, $\dot\gamma = \sqrt{2D_{kl}D_{kl}}$ is the strain rate, and μ_{eff} is an effective viscosity which is a function of the strain rate $\dot\gamma$. Strain to shear relation (5.1) is the Ostwald-de Waele mathematical modeling of pseudoplastic or shear-thinning fluids ($n < 1$) and dilatant or shear-thickening fluids ($n > 1$). The system of equations is completed by the boundary conditions at the

free surface $y = h$

$$\left[1 - (\partial_x h)^2\right] \tau_{xy} + \partial_x h \left(\tau_{yy} - \tau_{xx}\right) = 0 \,, \tag{5.3a}$$

$$p_a - p + \frac{\tau_{xx}(\partial_x h)^2 - 2\tau_{xy}\partial_x h + \tau_{yy}}{1 + (\partial_x h)^2} = \frac{\sigma \partial_{xx} h}{\left[1 + (\partial_x h)^2\right]^{3/2}} \,, \tag{5.3b}$$

$$\partial_t h + u \partial_x h = v \,, \tag{5.3c}$$

and at the wall $y = 0$

$$u = v = 0 \,. \tag{5.3d}$$

The length scale is the uniform film thickness $\bar{h}_{\rm N}$. The velocity scale V is defined by balancing viscous friction $\propto \mu_n V^n \bar{h}_{\rm N}^{-(n+1)}$ and streamwise gravity acceleration $\propto \rho g \sin\beta$ which gives

$$V = \left(\frac{\rho g \bar{h}_{\rm N}^{n+1} \sin\beta}{\mu_n}\right)^{1/n} \tag{5.4}$$

such that the Froude number $Fr = V/\sqrt{g\bar{h}_{\rm N}\cos\beta}$, which compares the characteristic speed of the flow with the speed of the gravity waves propagating at the interface, and the Reynolds number

$$Re = \frac{\rho V^{2-n} \bar{h}_{\rm N}^n}{\mu_n} = \left[(\mu_n/\rho)^{-2} \left(g \sin\beta\right)^{2-n} \bar{h}_{\rm N}^{n+2}\right]^{1/n} \tag{5.5}$$

are related by the relation $Re/\cot\beta = Fr^2$. Finally, let us note that the Reynolds number can also be written $Re = (\bar{h}_{\rm N}/l_\nu)^{(n+2)/n}$ where $l_\nu = (\mu_n/\rho)^{2/(n+2)} \left(g\sin\beta\right)^{(n-2)/(n+2)}$ is the length scale corresponding to the balance of gravity acceleration and viscous drag. We may also rewrite the velocity scale V as

$$V = \frac{l_\nu}{t_\nu}\left(\frac{\bar{h}_{\rm N}}{l_\nu}\right)^{\frac{n+1}{n}} \qquad \text{where} \qquad t_\nu = \left(\frac{\mu_n}{\rho}\right)^{\frac{1}{n+2}} \left(g\sin\beta\right)^{-\frac{2}{n+2}} \tag{5.6}$$

t_ν is the time scale corresponding to the balance of viscosity and gravity acceleration.

With the above choice of scales, the dimensionless equations thus read

$$\partial_x u + \partial_y v = 0 \,, \tag{5.7a}$$

$$Re\left(\partial_t u + u\partial_x u + v\partial_y u\right) = -\partial_x p + 1 + \partial_x \tau_{xx} + \partial_y \tau_{xy} \,, \tag{5.7b}$$

$$Re\left(\partial_t v + u\partial_x v + v\partial_y v\right) = -\partial_y p - \cot\beta + \partial_x \tau_{yx} + \partial_y \tau_{yy} \,, \tag{5.7c}$$

with boundary conditions

$$\left[1 - (\partial_x h)^2\right] \tau_{xy} + \partial_x h \left(\tau_{yy} - \tau_{xx}\right) = 0 \,, \tag{5.7d}$$

$$-p + \frac{\tau_{xx}(\partial_x h)^2 - 2\tau_{xy}\partial_x h + \tau_{yy}}{1 + (\partial_x h)^2} = We \frac{\partial_{xx} h}{\left[1 + (\partial_x h)^2\right]^{3/2}} \,, \tag{5.7e}$$

the kinematic condition (5.3c) and the no-slip condition (5.3d) at the wall. The Weber number is defined by $We = \sigma/(\rho g \sin\beta \bar{h}_{\rm N}^2)$. Finally, surface tension, gravity and viscous drag can be compared by the Kapitza number

$$\Gamma = (l_c/l_\nu)^2 = (\sigma/\rho)(\mu_n/\rho)^{-4/(n+2)}(g\sin\beta)^{(2-3n)/(n+2)}\,, \tag{5.8}$$

where $l_c = \sqrt{[\sigma/(\rho g \sin\beta)]}$ is the capillary length. The Weber and Kapitza numbers are related one to the other by the relation $We = \Gamma(l_\nu/\bar{h}_{\rm N})^2$.

5.3 Low-dimensional formulation

Let us assume (i) slow space and time evolutions $\partial_{x,t} \sim \epsilon$ where $\epsilon \ll 1$ is a formal film parameter, (ii) surface deformations induce order-ϵ corrections of the velocity profile from the flat-film solution. Otherwise stated, assumption (ii) implies that viscosity is strong enough to ensure the cross-stream coherence of the flow which should be verified for small to moderate Reynolds numbers.

With the help of the continuity equation, assumption (i) implies that the cross-stream velocity $v = -\int_0^y \partial_x u\, dy = O(\epsilon)$ so that the cross-stream momentum balance reads

$$\partial_y p = -\cot\beta + \partial_x \tau_{yx} + \partial_y \tau_{yy} + O(\epsilon^2) \tag{5.9}$$

$$\begin{aligned}
\tau_{yx} &= (\partial_y u + \partial_x v)\left[2\left(\partial_x u\right)^2 + \left(\partial_y u + \partial_x v\right)^2 + 2\left(\partial_y v\right)^2\right]^{(n-1)/2} \\
&= \partial_y u\left|\partial_y u\right|^{n-1} + n\left|\partial_y u\right|^{n-1}\partial_x v + 2(n-1)\partial_y u\left|\partial_y u\right|^{n-3}\left(\partial_x u\right)^2 + O(\epsilon^4)
\end{aligned}$$

$$\begin{aligned}
\tau_{xx} &= 2\partial_x u\left[2\left(\partial_x u\right)^2 + \left(\partial_y u + \partial_x v\right)^2 + 2\left(\partial_y v\right)^2\right]^{(n-1)/2} \\
&= 2\partial_x u\left|\partial_y u\right|^{n-1} + O(\epsilon^3)
\end{aligned}$$

$$\begin{aligned}
\tau_{yy} &= 2\partial_y v\left[2\left(\partial_x u\right)^2 + \left(\partial_y u + \partial_x v\right)^2 + 2\left(\partial_y v\right)^2\right]^{(n-1)/2} \\
&= 2\partial_y v\left|\partial_y u\right|^{n-1} + O(\epsilon^3)
\end{aligned}$$

and therefore

$$\partial_y p = -\cot\beta + \partial_x\left[\partial_y u\left|\partial_y u\right|^{n-1}\right] + 2\partial_y\left[\partial_y v\left|\partial_y u\right|^{n-1}\right] + O(\epsilon^2)\,. \tag{5.10}$$

From the continuity of the tangential stress at the free surface, $\tau_{xy}|_h = O(\epsilon^2)$ and the Laplace law simplifies into

$$p|_h = -2\partial_x u|_h\left|(\partial_y u|_h)\right|^{n-1} - We\,\partial_{xx} h + O(\epsilon^2)\,. \tag{5.11}$$

After integration of the truncated cross-stream momentum balance, the pressure distribution reads

$$p = \cot\beta(h-y) - We\partial_{xx}h - \int_y^h \partial_x\left[\partial_y u\,|\partial_y u|^{n-1}\right] dy - 2\partial_x u\,|\partial_y u|^{n-1} + O(\epsilon^2)\,. \quad (5.12)$$

Substitution of this expression for the pressure distribution in the streamwise momentum balance thus gives

$$\begin{aligned} Re\,(\partial_t u + u\partial_x u + v\partial_y u) = 1 &+ \partial_y\left[\partial_y u\,|\partial_y u|^{n-1}\right] - \cot\beta\partial_x h + We\partial_{xxx}h \\ &+\partial_y\left[n\,|\partial_y u|^{n-1}\,\partial_x v + 2(n-1)\partial_y u\,|\partial_y u|^{n-3}\,(\partial_x u)^2\right] \\ &+4\partial_x\left[|\partial_y u|^{n-1}\,\partial_x u\right] + \partial_x\left\{\int_y^h \partial_x\left[\partial_y u\,|\partial_y u|^{n-1}\right] dy\right\} \end{aligned} \quad (5.13a)$$

where the effective viscosity has been Taylor expanded as

$$\dot\gamma^{n-1} = |\partial_y u|^{n-1} + 2(n-1)(\partial_x u)^2|\partial_y u|^{n-3} + (n-1)|\partial_y u|^{n-3}\partial_y u\partial_x v + O(\epsilon^4)\,. \quad (5.13b)$$

Equation (5.13a) is completed by the tangential stress balance at the free surface truncated at order ϵ^2

$$\partial_y u\,|\partial_y u|^{n-1} = -n\,|\partial_y u|^{n-1}\,\partial_x v - 2(n-1)\partial_y u\,|\partial_y u|^{n-3}\,(\partial_x u)^2 + 4\partial_x u\,|\partial_y u|^{n-1}\,\partial_x h\,, \quad (5.13c)$$

the no-slip condition (5.3d) at the wall and the kinematic condition (5.3c).

In spite of the elimination of the pressure, solving the boundary-layer equations (5.13) remain a formidable task. A further simplification can be achieved by taking advantage of the strong coherence of the velocity distribution across the fluid layer, in which case the velocity field can be assumed to be slaved to a limited number of unknowns functions of time t and location x on the plane. The first of these effective degrees of freedom is necessarily the film thickness $h(x,t)$, for which an evolution equation is easily obtained after integration of the continuity equation

$$\partial_t h + \partial_x q = 0\,, \quad (5.14)$$

where $q = \int_0^h u\,dy$ is the local flow rate. Equation (5.14) expresses the mass conservation equation. In all cases found in literature, surface equations are obtained using a closure assumption $q = Q(h)$ manifesting the complete slaving of the dynamics of the film to the evolution of the free surface.

Using Benney expansion of the velocity field $u = u_0 + u_1$ assuming $Re = O(1)$, one obtains at order ϵ^0:

$$u_0 = \frac{n}{n+1}h^{(n+1)/n}\left[1 - \left(1 - \frac{y}{h}\right)^{(n+1)/n}\right] = a_0 f_0(\bar y) \quad (5.15)$$

where $\bar{y} \equiv y/h$, $f_0(\bar{y}) \equiv \frac{n}{n+1}\left[1-(1-\bar{y})^{(n+1)/n}\right]$ and $a_0 \equiv h^{(n+1)/n}$. u_0 corresponds to the velocity distribution under a film of constant thickness h, which we shall refer to as the Nusselt solution. Integration across the fluid layer gives

$$q_0 = \int_0^h u_0\, dy = \frac{n}{2n+1} h^{(2n+1)/n} \tag{5.16}$$

which corresponds to the relation between the film thickness and the flow rate for the Nusselt solution. This relation gives the film thickness as function of the inlet flow rate:

$$\bar{h}_{\rm N} = \left[\frac{\mu_n}{\rho g \sin\beta}\left(\frac{2n+1}{n}\bar{q}_{\rm N}\right)^n\right]^{1/(2n+1)} . \tag{5.17}$$

Substitution of (5.16) into the mass balance (5.14) leads to a kinematic-wave equation [146]:

$$\partial_t h + h^{(n+1)/n}\partial_x h = 0\,, \tag{5.18}$$

which governs the propagation of free surface deformations when the velocity field is slaved to the film thickness through the mass balance (5.14) or, equivalently the kinematic boundary condition (5.3c). Infinitesimal waves $|h-1| \ll 1$ thus propagate at speed unity and the velocity scale V given by (5.4) is the dimensional speed of the linear kinematic waves in the long-wavelength limit. V is also related to the speed average of the Nusselt solution since from (5.16) we get $\bar{q}_{\rm N}/\bar{h}_{\rm N} = nV/(2n+1)$.

Similarly, one obtains for the order-ϵ correction to the flow rate:

$$q_1 = \frac{1}{6n^2+7n+2} h^{(2n+1)/n}\left[2Re\, h^{(n+2)/n} + (3n+2)\left(-\cot\beta\,\partial_x h + We\,\partial_{xxx} h\right)\,.\right] \tag{5.19}$$

The threshold of the instability is given by Ng & Mei, Miladinova *et al.* [85, 82]

$$Re = Re_c = \frac{3n+2}{2}\cot\beta \qquad \text{or} \qquad Fr^2 = \frac{3n+2}{2} \tag{5.20}$$

The slaving of the velocity to the free surface evolution is verified only at small values of the Reynolds numbers Re. At moderate Reynolds number, some additional degrees of freedom must be added to capture the dynamics of the film, which can be done by projecting the velocity field on a set of chosen test functions. This closure assumption is generally reduced to the postulate of a self-similar profile [52, 32, 129]:

$$u = u_s(x,y,t) \equiv \frac{q(x,t)}{\phi_0 h(x,t)} f_0(y/h(x,t))\,, \tag{5.21}$$

where

$$\phi_0 = \int_0^1 f_0(\bar{y}) d\bar{y} = n/(2n+1)\,. \tag{5.22}$$

We avoid this restrictive closure (5.21) which is known to lead to an incorrect prediction of the instability threshold [85]. However, since the mass conservation equation (5.14) is exact, we stick to the derivation of a low-dimensional model consisting of two evolution equation for the film thickness h and the local flow rate q. Considering that assumption (ii) holds, i.e. that the velocity distribution across the fluid layer is never far from the flat-film solution, which enables to separate the streamwise velocity into $u = u^{(0)} + u^{(1)}$ where $u^{(0)} = a_0(x,t)f_0(\bar{y})$ and $u^{(1)}$ are at least order ϵ terms induced by the free surface deformations. The amplitude a_0 is related to the flow rate through its definition

$$a_0 = \frac{1}{\phi_0 h}\left(q - \int_0^h u^{(1)}\, dy\right) . \tag{5.23}$$

$u^{(1)}$ is an order-ϵ term, its integral is again $O(\epsilon)$ and it is possible to write instead

$$u = u_s(x,y,t) + \tilde{u}^{(1)} \tag{5.24}$$

where $u_s = O(1)$ is defined in (5.21) and $\tilde{u}^{(1)} = O(\epsilon)$ with the gauge condition $\int_0^h \tilde{u}^{(1)}\, dy = 0$.

We see that assumption (ii) expressed by (5.24), less restrictive than the classical assumption of a self-similar profile (5.21) is sufficient to enable the formulation of a coherent model at order ϵ. However, since $\partial_y u_s|_{y=h} = 0$, the Taylor expansion (5.13b) becomes invalid whenever $n < 3$ and my derivation procedure is strictly valid in the case $n \geq 3$.

Substitution of (5.24) into the boundary-layer equation truncated at order ϵ leads to

$$\begin{aligned} Re\left(\partial_t u_s + u_s\partial_x u_s + v_s\partial_y u_s\right) &= 1 + \partial_y\left[\partial_y u_s\left|\partial_y u_s\right|^{n-1}\right] - \cot\beta\partial_x h + We\partial_{xxx}h \\ &\quad + \partial_y\left[n\left|\partial_y u_s\right|^{n-1}\partial_y\tilde{u}^{(1)}\right] , \end{aligned} \tag{5.25}$$

where $v_s = -\int_0^y \partial_x u_s dy$ refers to the normal component of the velocity field. The last part of (5.25) can be rewritten

$$\partial_y\left[n\left|\partial_y u_s\right|^{n-1}\partial_y\tilde{u}^{(1)}\right] = \left|q/(\phi_0 h^2)\right|^{n-1}\partial_y\left[n(f_0')^{n-1}\partial_y\tilde{u}^{(1)}\right] = \left|q/(\phi_0)\right|^{n-1} h^{-2n}\,\mathcal{L}\tilde{u}^{(1)}$$

where $\mathcal{L}$ is the linear operator $\mathcal{L} \equiv \partial_{\bar{y}}\left[n(f_0')^{n-1}\partial_{\bar{y}}\cdot\right]$. From (5.25) an evolution equation for q can be obtained by averaging. Let us introduce a weighting function $w(\bar{y})$ and the scalar product $\langle\cdot|\cdot\rangle = \int_0^h \cdot dy$. We then have to evaluate $\langle\mathcal{L}\tilde{u}^{(1)}|w\rangle = \langle\tilde{u}^{(1)}|\mathcal{L}^+ w\rangle$ where $\mathcal{L}^+$ is the adjoint operator to $\mathcal{L}$. We can then make use of the zero mean flow condition on $\tilde{u}^{(1)}$, i.e. $\int_0^h \tilde{u}^{(1)}dy = \langle\tilde{u}^{(1)}|1\rangle = 0$, and select w such that $\mathcal{L}^+ w = cst$

Imposing boundary conditions to the weighting functions w similar to the boundary conditions truncated at order ϵ, i.e. $w(0) = 0$ and $w'(1) = 0$, a straightforward integration by part shows that $\langle\mathcal{L}\tilde{u}^{(1)}|w\rangle = \langle\tilde{u}^{(1)}|\mathcal{L}w\rangle$ and therefore that the operator $\mathcal{L}$ is self-adjoint. We show in Appendix A.1 that the solution to $\mathcal{L}w = cst$ is proportional to f_0 as a consequence of the self-similarity of the constant-thickness solution u_0. We led to the

conclusion that an integral momentum balance coherent at order ϵ can be obtained by averaging and using the weight $w = f_0$ corresponding to the Galerkin weighted residual method.

Substitution of the ansatz (5.24) into the second-order order momentum balance, averaging with weight $f_0(\bar{y})$ and making use of the tangential stress balance (5.13c) to evaluate $\left(\partial_y u \left|\partial_y u\right|^{n-1}\right)\big|_h$ then gives

$$
\begin{aligned}
&Re \int_0^h f_0(\bar{y}) \left(\partial_t u_s + u_s \partial_x u_s + v_s \partial_y u_s\right) dy + \mathcal{R}^{in,(2)} = \\
&\phi_0 h \left(1 - \cot\beta \partial_x h + We \partial_{xxx} h\right) - \frac{q|q|^{n-1}}{(\phi_0 h^2)^n} \int_0^1 (f_0')^{n+1} d\bar{y} \\
&- \int_0^h \frac{f_0'(\bar{y})}{h} \left[n \left|\partial_y u_s\right|^{n-1} \partial_x v_s + 2(n-1) \partial_y u_s \left|\partial_y u_s\right|^{n-3} \left(\partial_x u_s\right)^2\right] dy \\
&+ \int_0^h f_0(\bar{y}) \left\{\partial_x \left(\int_y^h \partial_x \left[\partial_y u_s \left|\partial_y u_s\right|^{n-1}\right] dy\right) + 4 \partial_x \left[\left|\partial_y u_s\right|^{n-1} \partial_x u_s\right]\right\} dy \,,
\end{aligned}
\tag{5.26}
$$

where $\mathcal{R}^{in,(2)}$ stands for the second-order inertial terms generated by the departure $\tilde{u}^{(1)}$ of the velocity profile from the flat-film solution u_s. As will be verified later on, these terms do not contribute to the determination of the instability threshold and we dropped them out.

After some algebra using the definition of u_s in (5.21) and the equivalence $\partial_t h = -\partial_x q$, we obtain:

$$
\begin{aligned}
Re \partial_t q \;=\; & Re \left[-F(n) \frac{q}{h} \partial_x q + G(n) \frac{q^2}{h^2} \partial_x h\right] + I(n) \left[h \left(1 - \cot\beta \partial_x h + We \partial_{xxx} h\right) - \frac{q|q|^{n-1}}{(\phi_0 h^2)^n}\right] \\
& + \left[\frac{|q|}{\phi_0 (h^2)}\right]^{n-1} \times \left[J(n) \frac{q}{h^2} (\partial_x h)^2 - K(n) \frac{\partial_x q \partial_x h}{h} - L(n) \frac{q}{h} \partial_{xx} h \right. \\
& \left. + M(n) \partial_{xx} q + N(n) \frac{(\partial_x q)^2}{q}\right] ,
\end{aligned}
\tag{5.27}
$$

where coefficients F, G, I, J, K, L, M and N are function of the power-law index n given

below.

$$F(n) = \frac{11n+6}{4n+3}, \tag{5.28a}$$

$$G(n) = \frac{6n+3}{4n+3}, \tag{5.28b}$$

$$I(n) = = \frac{3n+2}{2(2n+1)}, \tag{5.28c}$$

$$J(n) = \frac{(3n+2)(8n^4+24n^3-8n^2-n+1)}{6n(2n-1)(4n+1)}, \tag{5.28d}$$

$$K(n) = \frac{(2n+1)(2n+7)(3n+2)}{6(4n+1)}, \tag{5.28e}$$

$$L(n) = \frac{(2n+1)(3n+2)(12n^3+36n^2+n-1)}{6n(2n-1)(3n+1)(4n+1)}, \tag{5.28f}$$

$$M(n) = \frac{(2n+1)(2n+7)(3n+2)}{6(4n+1)(2n-1)}, \tag{5.28g}$$

$$N(n) = \frac{(2n+1)(n-1)(2n+7)(3n+2)}{12(2n-1)(4n+1)}. \tag{5.28h}$$

Truncated at first order, i.e. when J, K, L, M and N are all set to zero, the obtained averaged momentum equation is identical to the one derived by Amaouche *et al.* [5].

In the Newtonian case $n = 1$, the averaged momentum equation obtained by Ruyer-Quil & Manneville [112] is also recovered

$$\begin{aligned} Re\partial_t q = {} & Re\left[-\frac{17}{7}\frac{q}{h}\partial_x q + \frac{9}{7}\frac{q^2}{h^2}\partial_x h\right] + \frac{5}{6}\left[h\left(1-\cot\beta\partial_x h + We\partial_{xxx}h\right) - 3\frac{q}{h^2}\right] \\ & \left[4\frac{q}{h^2}(\partial_x h)^2 - \frac{9}{2}\frac{\partial_x q\partial_x h}{h} - 6\frac{q}{h}\partial_{xx}h + \frac{9}{2}\partial_{xx}q\right]. \end{aligned} \tag{5.29}$$

The momentum balance (5.27) is consistent at order ϵ and consistently accounts for viscous effects up to $O(\epsilon^2)$. Our procedure is strictly valid only for $n \geq 3$, a situation that arises from my will to account for the second-order streamwise viscous diffusion effects. Yet, we note that the second-order viscous terms found in the residual (5.27) remain bounded as long as $n \leq 2$ and the second-order viscous terms of (5.27) therefore may diverge only when $n < 2$ and q goes to zero as it is sometimes observed in the Newtonian case at the front of large-amplitude solitary waves [78, 138, 38]. Moreover, the expressions of the coefficients (5.28) remain bounded as long as $n > 1/2$, which reflects the fact that $\int_0^1 (f_0')^{n-1} d\bar{y}$ remains bounded for $n > 1/2$. Finally, truncation at first order (by setting J, K, L, M and N to zero) gives an averaged momentum equation that is usable for any values of n in spite of the singularity of the apparent viscosity at the free surface [44]. Thus, we conclude to the regularizing advantage of the averaging process.

5.4 Beyond: a Newtonian-power-law model

The fact that we end up with a formulation (5.14), (5.27) and (5.28) that is limited to a certain range of possible values of the index n is not surprising when the linear stability of the Nusselt solution (5.15) is considered. Indeed, the effective viscosity of a power-law fluid (see equation (5.1)) diverges when the shear rate $\dot{\gamma}$ goes to zero which is precisely the case at the free surface of the film. As a consequence and for a shear-thinning fluid ($n < 1$), a flat interface becomes a rigid boundary and infinitesimal perturbations around the base flow solution (5.15) cannot deform the interface, which is an essential ingredient of the instability mechanism of a falling film [131]. Indeed, the transfer of energy from the base flow to the perturbations is enabled by the deformation of the free interface.

There are different solutions to this problem. The first one is probably to consider that the interface is already deformed as in the pseudo-plug theory introduced by Balmforth & Liu [8] to consider viscoplastic flows that are modeled by the Herschel-Buckley law. Rheological measurements of solutions of semi-flexible rod-like polymer, e.g. xanthan solutions, show evidence of yield stresses at high concentrations [145, 132]. However, in the case of dilute xanthan solutions, yield stresses are not observed but shear viscosity measurements show the presence of a first Newtonian plateau at low strain rate [12, 110]. A second solution to the divergence of the viscosity for the power-law model is therefore a regularization at low shear rate to recover the Newtonian behavior in that limit. This is the spirit of a three-parameter Carreau law:

$$\mu_{\text{eff}}(\dot{\gamma}) = \mu_0 \left[1 + (\dot{\gamma}/\dot{\gamma}_c)^2\right]^{(n-1)/2} . \tag{5.30}$$

However, using (5.30) forbids the base flow from being determined analytically and one can instead introduce a Newtonian plateau:

$$\mu_{\text{eff}}(\dot{\gamma}) = \mu_n \dot{\gamma}^{n-1} \quad \text{for} \quad \dot{\gamma} > \dot{\gamma}_c \,, \tag{5.31a}$$

$$\mu_{\text{eff}}(\dot{\gamma}) = \mu_0 \quad \text{for} \quad \dot{\gamma} \leq \dot{\gamma}_c \,. \tag{5.31b}$$

The continuity of the shear stress at $\dot{\gamma} = \dot{\gamma}_c$ requires $\mu_n \dot{\gamma}_c^{n-1} = \mu_0$. The Carreau law (5.30) and the Newtonian-plateau model (5.31a) are related one to another by $1/\dot{\gamma}_c$. For example, Fig. 5.2 shows the comparison of Ostwald-de Waele model with a Newtonian plateau, and Carreau law for shear-thinning ($n < 1$) and shear-thickening fluid ($n > 1$). Table 5.1 presents reasonable values of the zero strain viscosity μ_0 and the critical strain rate $\dot{\gamma}_c$ separating Newtonian and non-Newtonian behavior of shear-thinning xanthan dilute solutions. Those values are taken from [12, 69, 125]. Noteworthy is that dilute xanthan solutions do not present yield stresses [28]. The surface tension of xanthan solutions is assumed here to remain close to that of pure water $\sigma = 65$ mN/m [125]. Conversely, table 5.2 presents the properties of three typical shear-thickening solutions of cornstarch in ethylene glycol. The dynamic viscosity μ_0 of the Newtonian plateau is assumed to correspond to the solvent viscosity. Removing dimensions with the help of

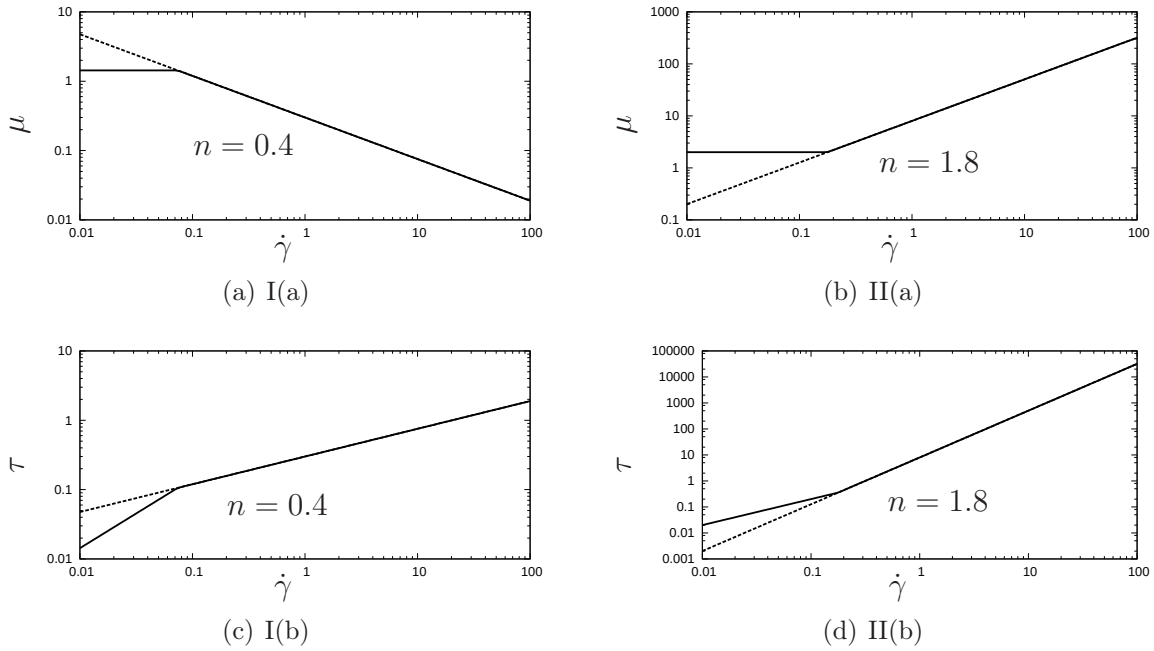

(a) I(a) (b) II(a)

(c) I(b) (d) II(b)

Figure 5.2: Ostwald-de Waele model (solid line) with a Newtonian plateau and Carreau law (dash line) for Shear-thinning fluid (I(a) and (b)), $n = 0.4$ and Shear-thickening fluid (II(a) and (b)), $n = 1.8$.

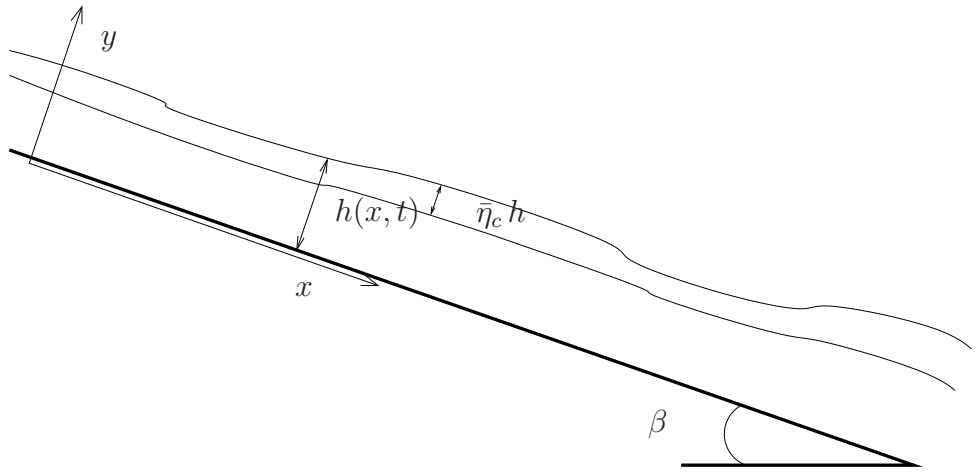

Figure 5.3: Sketch of a powerlaw fluid falling film with a Newtonian layer close to the free surface.

Set number	Concentration	μ_n (Pa.s^n)	n	μ_0 (Pa.s)	$\dot{\gamma}_c$ (s^{-1})	$\dot{\gamma}_c t_\nu$	Γ
1.	500 ppm	0.04062	0.607	0.08	0.18	1.8×10^{-3}	378
2.	1500 ppm	0.3592	0.40	1.43	0.1	1.7×10^{-3}	48.7
3.	2500 ppm	0.9913	0.34	7.16	0.05	1.2×10^{-3}	13.0

Table 5.1: Parameters from rheological measurements of xanthan gum solutions in water. Surface tension and density are $\sigma = 65$ mN/m and $\rho = 995$ kg/m^3. Values of the Kapitza number are computed for a moderate inclination $\beta = 15°$. Set 1 corresponds to data from [12, 69]. Sets 2 and 3 refer to the fluids studied by Seevaratnam [125].

Set number	Concentration	μ_n (Pa.s^n)	n	μ_0 (Pa.s)	$\dot{\gamma}_c$ (s^{-1})	$\dot{\gamma}_c t_\nu$	Γ
4.	33 %	8	1.3	0.016	10^{-9}	1.3×10^{-10}	0.01
5.	35 %	6	1.55	0.016	2.1×10^{-5}	2.8×10^{-6}	0.0077
6.	38 %	1.8	2.4	0.016	0.034	5.2×10^{-3}	0.005

Table 5.2: Parameters from rheological measurements of cornstarch dispersions in ethylene glycol [48]. Surface tension and density are $\sigma = 48$ mN/m and $\rho = 1113$ kg/m^3. The viscosity μ_0 of the Newtonian plateau is assumed to correspond to the solvent viscosity. Values of the Kapitza number are computed for a moderate inclination $\beta = 15°$.

the film thickness and the characteristic velocity V defined in (5.4) gives

$$\mu_{\text{eff}}(\dot\gamma) = \dot\gamma^{n-1} \quad \text{for} \quad \dot\gamma > s \tag{5.32a}$$
$$\mu_{\text{eff}}(\dot\gamma) = r \quad \text{for} \quad \dot\gamma \le s \tag{5.32b}$$

where the dimensionless threshold s and dimensionless maximum effective viscosity r are defined by $s = \dot\gamma_c \bar h_{\text{N}}/V$ and $r = s^{n-1}$. The dimensionless Carreau law equivalent to the Newtonian plateau model (5.32) reads

$$\mu_{\text{eff}}(\dot\gamma) = \left(s^2 + \dot\gamma^2\right)^{(n-1)/2} . \tag{5.33}$$

The advantage of the Newtonian plateau formulation (5.32) over the Carreau law (5.33) lies in the presence of an analytical solution for the base flow of constant film thickness h:

$$u_0 = h^{(n+1)/n} f_0(\bar y) \quad \text{for} \quad \bar y < 1 - \bar\eta_c \tag{5.34a}$$
$$u_0 = h^{(n+1)/n} f_0(1-\bar\eta_c) + s^{n+1}\, g_0[(\bar y + \bar\eta_c - 1)/\bar\eta_c] \quad \text{for} \quad \bar y > 1 - \bar\eta_c\,, \tag{5.34b}$$

where $f_0(\bar y) = n/(n+1)\left[1-(1-\bar y)^{(n+1)/n}\right]$, $g_0(\bar y) = \bar y - (1/2)\bar y^2$ and $\bar\eta_c = s^n/h$ is the fraction of the film thickness for which the fluid is Newtonian. From the uniform-thickness solution (5.34) we obtain $\partial_y u_0|_{y=0} = 1$ and the dimensional rate of strain at the wall is thus $V/\bar h_{\text{N}}$ for the base flow. Therefore, the dimensionless group r can be interpreted as the ratio $r = \mu_0/\mu_w$ of the shear viscosities $\mu_0 = \mu_n(\dot\gamma_c)^{n-1}$ and $\mu_w = \mu_n(V/\bar h_{\text{N}})^{n-1}$ at the free surface and at the wall for the corresponding base flow Nusselt solution. The Newtonian-plateau model (5.32) thus introduces a fake interface at $y = h(1-\bar\eta_c)$ separating a power-law region and a Newtonian layer at the free surface. This is reminiscent of the pseudo-plug theory developed by [8, 44], although in that case the fake interface has a different physical meaning and separates a plastic upper layer from a fluid layer underneath.

In the case of the three shear-thinning xanthan solutions whose properties are listed in Table 5.1, the approximation of a thin Newtonian layer ($\bar\eta_c \ll 1$) and a large viscosity ratio ($r \gg 1$) is well verified. Fig. 5.4 presents the relative thickness s^n of the Newtonian layer and the viscosity ratio r for the Nusselt film solution (5.34) at two inclinations ($\beta = 15°$ and $85°$) and for the three studied xanthan solutions when the Reynolds number is varied in the interval $[Re_c, 100]$. The instability threshold Re_c is here approximated by the formula (5.20) which corresponds to the Ostwald-de Waele power-law model (5.1). In each case, the viscosity at the free surface is at least one order of magnitude larger than at the wall and the Newtonian layer at the free surface has a thickness that is at least one order of magnitude smaller than the total thickness of the film. Turning to the cornstarch suspensions (see table 5.2) the Newtonian surface layer is very thin and the viscosity ratio is very small, s^n and r being less than 2×10^{-6} and 5×10^{-4}, respectively for Re in the range $[Re_c, 100]$ and $\beta = 15°$ or $85°$. Then we conclude that a thin Newtonian

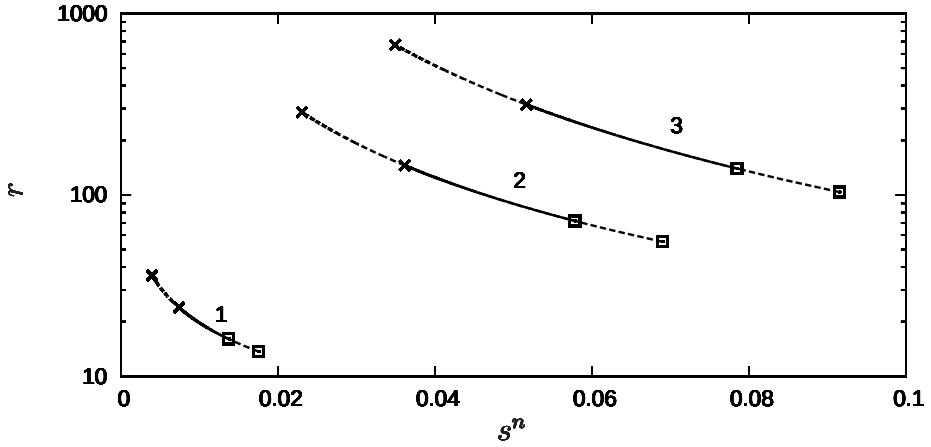

Figure 5.4: Ranges of dimensionless maximum viscosity $r = s^{n-1}$ and relative thickness s^n of the Newtonian surface layer attained for the Nusselt solution of uniform thickness (5.34) when the Reynolds number is varied between Re_c and 100. Solid (dashed) lines refer to $\beta = 15°$ ($\beta = 85°$). Labels refer to the shear-thinning dilute xanthan solutions whose properties are listed in table 5.1. Crosses (squares) correspond to $Re = 100$ ($Re = Re_c$).

layer at the free surface ($\bar{\eta}_c \ll 1$) can be assumed for typical shear-thinning and shear-thickening fluids, an assumption that will be useful to drastically simplify the derivation of the integral models that we detail below.

Finally, let us note that, although not strictly equivalent, the two models (5.33) and (5.32) of generalized Newtonian fluids will be shown to lead to close results in the linear and nonlinear regimes whenever $s \ll 1$ and we shall consider them equivalent to my analysis in the limit $s \to 0$ (see § 5.4.1). We first adapt the approach adopted for the power-law fluid case in § 5.3 by postulating that the velocity distribution is never far from the flat-film profile (5.34b). This can be expressed by

$$u = u_s + \tilde{u}^{(1)} \qquad \text{where :} \tag{5.35a}$$

$$u_s = \bar{u} f_0(\bar{y}) \quad \text{for} \quad \bar{y} \leq 1 - \bar{\eta}_c \tag{5.35b}$$

$$u_s = \bar{u}\left[f_0(1-\bar{\eta}_c) + \bar{\eta}_c{}^{(n+1)/n}\, g_0[(\bar{y}+\bar{\eta}_c-1)/\bar{\eta}_c]\right] \qquad \text{for} \quad \bar{y} \geq 1-\bar{\eta}_c\,, \tag{5.35c}$$

and $\bar{\eta}_c$ is the local relative thickness of the Newtonian layer at the free surface.

The definition of the velocity distribution u_s is based on the local film thickness $h(x,t)$ and a local velocity scale $\bar{u}(x,t)$ that can be related to the rate of strain at the wall $\dot{\gamma}_{(y=0)} = \bar{u}/h + O(\epsilon)$. $\tilde{u}^{(1)}$ accounts for the order-ϵ deviations of the velocity profile induced by the deformation of the free surface. We can also include in $\tilde{u}^{(1)}$ the $O(\epsilon)$ corrections of

the relation between the flow rate $q = \int_0^h u\,dy$, h and $\bar{u}$ provided by the flat-film profile

$$q = \frac{3n + (1-n)\bar{\eta}_c^{(2n+1)/n}}{6n+3} h\bar{u} \equiv \phi(\bar{\eta}_c) h\bar{u}\,, \tag{5.36}$$

so that $\int_0^h \tilde{u}^{(1)}\,dy = 0$ is assumed without any restrictions.

The local thickness $\bar{\eta}_c$ of the Newtonian layer is defined by $\dot{\gamma}(\bar{y} = 1 - \bar{\eta}_c) = s$, which reads at order ϵ^2

$$s^2 = \left\{4\left(\partial_x u_s\right)^2 + \left[\partial_y u_s + \partial_x v_s\right]^2\right\}_{\bar{y}=1-\bar{\eta}_c}. \tag{5.37}$$

In the limit $\bar{\eta}_c \ll 1$, (5.37) can be further simplified to give

$$s^2 = \frac{4n^2}{(1+n)^2}(\partial_x \bar{u})^2 + {\bar{\eta}_c}^{2/n}\frac{\bar{u}^2}{h^2}\,. \tag{5.38}$$

Therefore, the Newtonian layer disappears locally if

$$|\partial_x \bar{u}| > \frac{n+1}{2n} s\,. \tag{5.39}$$

Though formally of different orders with respect to the film parameter ϵ, we cannot neglect $(\partial_x u)^2$ in the computation of the strain rate $\dot{\gamma}$. Since $\partial_y u$ becomes small close to the free surface, the viscosity at the free surface is then governed by the value of the streamwise derivative $\partial_x u|_{y=h}$ for a thin or vanishing Newtonian layer.

The formulation of an averaged momentum balance in terms of q and h is made difficult by the impossibility to inverse (5.37) and (5.36) to express $\bar{u}$ as function of h and q. We thus aim at a a three-equation model for the unknowns h, $\bar{\eta}_c$ and $\bar{u}$ made of the (exact) mass conservation equation (5.14), (5.37) and an evolution equation for $\bar{u}$.

A boundary-layer momentum balance consistent at order ϵ^2 can be obtained following a procedure similar to the derivation of (5.13a). Integration of the cross-stream momentum balance gives the pressure distribution at order ϵ:

$$\text{if } y > y_c\,, \quad p = \cot\beta(h-y) - We\partial_{xx}h - r\left[\partial_x u|_h + \partial_x u\right]\,, \tag{5.40a}$$

$$\begin{aligned}\text{if } y \le y_c\,, \quad p &= \cot\beta(h-y) - We\partial_{xx}h - r\left[\partial_x u|_h + \partial_x u|_{y_{c+}}\right] + 2r\partial_x u|_{y_{c-}} \\ &\quad -2\partial_x u{\dot{\gamma}_0}^{n-1} - \int_y^{y_c} \partial_x\left[\partial_y u{\dot{\gamma}_0}^{n-1}\right] dy\,,\end{aligned} \tag{5.40b}$$

where $y_c = h(1-\bar{\eta}_c)$ defines the location of the fake interface separating the Newtonian and power-law layers and $\dot{\gamma}_0 = \sqrt{(\partial_y u)^2 + 4(\partial_x u)^2}$. Note that $\partial_y u$ and $\partial_x u$ must be taken of the same order of magnitude in the expression of the strain rate.

Substitution of (5.40) into the streamwise momentum balance gives

$$Re\left(\partial_t u + u\partial_x u + v\partial_y u\right) = 1 + \partial_y \tau_{xy}^{(0)} + \mathcal{D}^{(2)} - \cot\beta\partial_x h + We\partial_{xxx}h \tag{5.41a}$$

where the definition of the lowest-order rate of strain $\tau_{xy}^{(0)}$ and of the second-order viscous terms $\mathcal{D}^{(2)}$ depend on whether the flow is Newtonian or non-Newtonian. For $y > y_c$ they read

$$\tau_{xy}^{(0)} = r\partial_y u \quad \text{and} \quad \mathcal{D}^{(2)} = 2r\partial_{xx}u + r\partial_x\left[\partial_x u|_h\right] \tag{5.41b}$$

whereas for $y \leq y_c$ we have

$$\begin{aligned}
\tau_{xy}^{(0)} &= \partial_y u \dot\gamma_0^{n-1}\,, \\
\mathcal{D}^{(2)} &= \partial_y\left[\partial_x v\left(\dot\gamma_0^{n-1} + (n-1)(\partial_y u)^2\dot\gamma_0^{n-3}\right)\right] + 4\partial_x\left[\partial_x u \dot\gamma_0{}^{n-1}\right] \\
&\quad + \partial_x\left\{\int_y^{y_c}\partial_x\left[\partial_y u\dot\gamma_0{}^{n-1}\right]dy\right\} - 2\partial_x\left[r\partial_x u|_{y_c-}\right] \\
&\quad + r\partial_x\left[\partial_x u|_{y_c+} + \partial_x u|_h\right]\,,
\end{aligned} \tag{5.41c}$$

Equation (5.41a) completed by the no-slip condition $u = v = 0$ at the wall and the tangential stress continuity at the free surface $y = h$ truncated at order ϵ^2:

$$\partial_y u = 4\partial_x h\partial_x u - \partial_x v\,. \tag{5.41d}$$

As for the derivation of the averaged momentum balances (5.27) for a power-law fluid, the weight w must be chosen so that the viscous drag term

$$\int_0^{y_c} w(\bar y)\partial_y\left[n|\partial_y u_s|^{n-1}\partial_y\tilde u^{(1)}\right]dy + \int_{y_c}^h rw(\bar y)\partial_{yy}\tilde u^{(1)}dy \equiv \frac{1}{h}\left|\frac{\bar u}{h}\right|^{n-1}\langle\mathcal{L}_{\bar\eta_c}\tilde u^{(1)}|w\rangle + O(\epsilon^2) \tag{5.42}$$

is $O(\epsilon^2)$. The linear operator is an extension of the operator $\mathcal{L}$ introduced in § 5.3 and $\mathcal{L}_{\bar\eta_c}$ is defined by

$$\mathcal{L}_{\bar\eta_c} = \partial_{\bar y}\left[n(f_0')^{n-1}\partial_{\bar y}\cdot\right] \qquad \text{if} \quad 0 \leqslant \bar y \leqslant \bar\eta_c\,, \qquad \text{and} \quad \mathcal{L}_{\bar\eta_c} = \bar\eta_c{}^{(n-1)/n}\partial_{\bar y\bar y}\cdot \qquad \text{otherwise}\,, \tag{5.43}$$

where the thickness of the Newtonian layer is estimated by $\bar\eta_c = (sh/\bar u)^n + O(\epsilon^2)$. The deviations $\tilde u^{(1)}$ of the velocity field verify the no-slip condition $\tilde u^{(1)}|_{\bar y=0} = 0$ at the wall, $\partial_{\bar y}\tilde u^{(1)}|_{\bar y=1} = 0$ at the interface and

$$n\partial_{\bar y}\tilde u^{(1)}|_{\bar y=\bar y_{c-}} = \bar\eta_c{}^{(n-1)/n}\partial_{\bar y}\tilde u^{(1)}|_{\bar y=\bar y_{c+}} \tag{5.44}$$

where $\bar y_c = 1 - \bar\eta_c$, which is a consequence of the continuity of the rate of stress at the fake interface:

$$|\partial_y u|^{n-1}\partial_y u|_{\bar y=\bar y_{c-}} + O(\epsilon^2) = r\partial_y u|_{\bar y=\bar y_{c+}}\,. \tag{5.45}$$

Two integrations by part of (5.42) show that the linear operator $\mathcal{L}_{\bar\eta_c}$ is self-adjoint. To make use of the definition of the flow rate q, which implied the gauging condition $\int_0^h u^{(1)}dy = 0$, the weight function w must be solution to $\mathcal{L}_{\bar\eta_c} = cst$ which gives

$$\begin{aligned}
&\text{if } y < y_c\,, \quad w(\bar y) &&= f_0(\bar y)\,, \\
&\text{if } y \geqslant y_c\,, \quad w(\bar y) &&= f_0(1-\bar\eta_c) + n\bar\eta_c{}^{(n+1)/n}\,g_0[(\bar y + \bar\eta_c - 1)/\bar\eta_c]\,.
\end{aligned} \tag{5.46a}$$

Noteworthy is that the weight w is not proportional to the velocity profile u_s defined in (5.35). The adopted weighted residual method is therefore slightly different from the Galerkin method for which $w \propto u_s$. This discrepancy is an effect of the non-linearity of the strain to stress relationship which introduces a factor n.

We next proceed to the averaging of the boundary-layer equations (5.41) with appropriate weights (5.46). To compute the viscous terms appearing in the boundary-layer formulation (5.41c), we expand the non-linear constitutive equation:

$$\dot{\gamma_0}^{n-1} = |\partial_y u|^{n-1} + 2(n-1)(\partial_x u)^2 |\partial_y u|^{n-3} + O(\epsilon^4)\,, \tag{5.47}$$

and replace r with $\dot{\gamma_0}^{n-1}|_{y=h(1-\bar{\eta}_c)}$.

After some tedious algebra, the resulting averaged momentum equation (5.41) reads

$$\begin{aligned}\partial_t \bar{u} \;=\; & -Re\left[\tilde{G}\frac{\bar{u}^2}{h}\partial_x h + \tilde{F}\bar{u}\partial_x \bar{u}\right] + \tilde{I}\left(1 - \cot\beta\partial_x h + We\partial_{xxx}h - \frac{\bar{u}|\bar{u}|^{n-1}}{h^{n+1}}\right) \\ & + \tilde{J}\frac{\bar{u}}{h^2}(\partial_x h)^2 + \tilde{K}\frac{\partial_x \bar{u}\partial_x h}{h} + \tilde{L}\frac{\bar{u}}{h}\partial_{xx}h + \tilde{M}\partial_{xx}\bar{u} + \tilde{N}\frac{(\partial_x \bar{u})^2}{\bar{u}}\,.\end{aligned}$$

The coefficients $\tilde{F}$ to $\tilde{N}$ of the averaged momentum balance (5.48) are explicit, but cumbersome, functions of the power-law index n and of the relative thickness $\bar{\eta}_c$ of the Newtonian layer. We give in appendix A.3 the full expressions of the coefficients $\tilde{F}$, $\tilde{G}$, $\tilde{I}$ of the terms of orders ϵ^0 and ϵ which will be needed to determine the value of the critical Reynolds number at onset. The system (5.14), (5.37) and (5.48) is consistent up to order ϵ and accurately accounts for second-order viscous terms. As stated in the introduction, the derivation of the (5.48) has required a regularization of the power law (5.1) for $n < 3$ in order to compute both $\mu_{\text{eff}}(0)$ and $d\mu_{\text{eff}}/d\dot{\gamma}(0)$ in the Taylor expansion (5.47).

5.4.1 Shear-thinning film ($n < 1$) in the limit of vanishing Newtonian layer

The system of equations (5.14), (5.37) and (5.48) is still formidable to solve, mainly because of the dependence of the coefficients (A.2) on the relative thickness $\bar{\eta}_c$ of the Newtonian layer, which is in turn a nonlinear function of h, $\bar{u}$ and their derivatives. For this reason, we further simplify the formulation by retaining the asymptotic behavior of the coefficients when the Newtonian layer is very thin ($\bar{\eta}_c \to 0$).

In this limit, the expressions of the eight coefficients $\tilde{F},\ldots,\tilde{N}$ simplify to

$$\tilde{F} \sim \frac{n(7n+3)}{(4n+3)(2n+1)}, \tag{5.48a}$$

$$\tilde{G} \sim \frac{n^2}{(4n+3)(2n+1)}, \tag{5.48b}$$

$$\tilde{I} \sim \frac{3n+2}{2n}, \tag{5.48c}$$

$$\tilde{J} \sim \frac{(3n+2)\left[n(2n-3)(n+3)-2\right]}{12n(4n+1)}\left[\frac{|\bar{u}|}{h}\right]^{n-1}, \tag{5.48d}$$

$$\tilde{K} \sim \frac{n(n-1)(3n+2)}{(n+1)^2}\left[\bar{\eta_c}^{1/n}\frac{|\bar{u}|}{h}\right]^{n-1} \tag{5.48e}$$

$$\tilde{L} \sim \tilde{K}/2 \tag{5.48f}$$

$$\tilde{M} \sim -\frac{(n-1)(3n+2)}{2(n+1)}\left[\bar{\eta_c}^{1/n}\frac{|\bar{u}|}{h}\right]^{n-1}, \tag{5.48g}$$

$$\tilde{N} \sim \frac{(n-1)(2n+1)(2n+7)(3n+2)}{12(2n-1)(4n+1)}\left[\frac{|\bar{u}|}{h}\right]^{n-1}, \tag{5.48h}$$

$$\tag{5.48i}$$

where we used the relation (5.38) to eliminate the maximum viscosity $r = s^{n-1}$:

$$r = \left(\frac{\bar{\eta_c}^{1/n}|\bar{u}|}{h}\right)^{n-3}\left[\frac{\bar{\eta_c}^{2/n}\bar{u}^2}{h^2} + \frac{2n^2(n-1)}{(n+1)^2}(\partial_x\bar{u})^2\right] + O(\epsilon^2) \tag{5.49}$$

Finally, we note that $\phi_0 = \phi(0) = n/(2n+1)$ and we can substitute $q/(\phi_0 h)$ for $\bar{u}$ in the limit $\bar{\eta_c} \to 0$. We finally obtain:

$$\begin{aligned} Re\partial_t q &= Re\left[-F(n)\frac{q}{h}\partial_x q + G(n)\frac{q^2}{h^2}\partial_x h\right] + I(n)\left[h\left(1-\cot\beta\partial_x h + We\partial_{xxx}h\right) - \frac{q|q|^{n-1}}{(\phi_0 h^2)^n}\right] \\ &\quad + r\left[J_0(n)\frac{q}{h^2}(\partial_x h)^2 - K_0(n)\frac{\partial_x q\partial_x h}{h} - L_0(n)\frac{q}{h}\partial_{xx}h + M_0(n)\partial_{xx}q\right]. \end{aligned} \tag{5.50}$$

Coefficients $F(n)$, $G(n)$, $I(n)$, J_0, K_0, L_0, M_0 are also functions of the power-law index n whose expressions are given below:

$$F = \frac{11n+6}{4n+3}, \qquad G = \frac{6n+3}{4n+3}, \qquad I = \frac{3n+2}{2(2n+1)}, \tag{5.51a}$$

$$K_0 = J_0 = -\frac{(n-1)(2n+1)(3n+2)}{(n+1)^2}, \tag{5.51b}$$

$$L_0 = K_0/2, \qquad M_0 = -\frac{(n-1)(3n+2)}{2(n+1)}. \tag{5.51c}$$

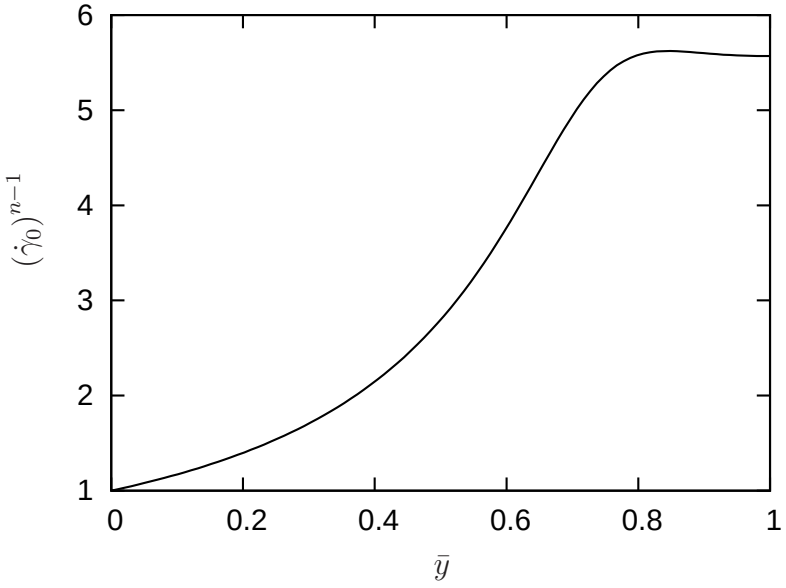

Figure 5.5: Example of viscosity distribution computed using $n = 0.4$, $\bar{u}/h = 1$, $\partial_x h = 0.1$ and $\partial_x \bar{u} = 0.1$.

The limit of a very thin Newtonian layer implies that the strain-rate threshold s also goes to zero. Since we made use of the Taylor expansion (5.47) to obtain (5.48), $\epsilon = O(s)$ and the momentum averaged equation (5.48) completed with (5.48) is formally only relevant to describe weakly nonlinear waves in the vicinity of the instability threshold.

Yet, (5.50) takes into account the contribution of the effective viscosity $\mu_{\text{eff}}(y = h)$ at the free surface. For non-infinitesimal deformations, the strain rate at the free surface can rapidly exceeds s, the Newtonian viscous layer disappears and $\mu_{\text{eff}}(y = h)$ is much below its maximum r. Let us reconsider the distribution of effective viscosity inside the film. Whenever q is non zero and the gradient of h and q fulfill the long-wave assumption, the viscosity distribution can be approached using the Nusselt base flow as

$$(\dot{\gamma})^{n-1} \approx \left[(\partial_y u_s)^2 + 4(\partial_x u_s)^2\right]^{(n-1)/2} \tag{5.52}$$

whose maximum is again nearly reached at the free surface. Fig. 5.5 presents an example of the effective viscosity distribution μ_{eff} corresponding to (5.52) with $\bar{\eta}_c = 0$, $\bar{u}/h = 1$, $\partial_x h = 0.1$ and $\partial_x \bar{u} = 0.1$. Apart from a nearly constant plateau close to the free surface, the effective viscosity decreases rapidly. We lead to the previous case of a power-law fluid with a thin Newtonian layer at the free surface where the ratio of free-surface to wall viscosities is now given by $\mu_{\text{eff}}(y = h)$. The averaged momentum equation (5.50) can therefore easily be extended to account for the disappearance of the Newtonian layer when the effective viscosity $\mu_{\text{eff}}(y = h)$ at the free surface is substituted for r. We thus

obtain a coherent formulation accounting for streamwise viscous diffusion in the proper limit within the long-wave assumption, for which the maximum of effective viscosity is reached at the free surface. We therefore retain only the leading contribution of the free surface viscosity to the second-order terms with two drawbacks: (i) Second-order viscous effects are dropped out in the limit $n \to 1$ as $J_0(1) = K_0(1) = L_0(1) = M_0(1) = 0$. (ii) These effects are underestimated whenever the maximum of effective viscosity is not reached at the free surface but in the bulk of the film. Indeed, there are evidence that the maximum of effective viscosity can sometimes be located at the wall. Dietze *et al.* and Dietze *et al.* [38, 39] have pointed out the onset of backflow phenomena at the minimum thickness of large amplitude solitary waves running on Newtonian falling films. These backflow phenomena are accompanied by the occurrence of separation points at the wall where the strain rate necessarily goes to zero. In the case of shear-thinning fluids, the effective viscosity would be maximum at the wall close to the locations of the separation points.

To remedy to these drawbacks, one would have to identify the leading order contributions of the bulk and wall regions to the streamwise viscous diffusion terms in the averaged momentum equation (5.48), a very difficult task to achieve because of its complexity. A simple but *ad hoc* way to proceed is to estimate the effective viscosity in the bulk region from its value at the wall $\mu_{\text{eff}}(y=0) \approx [|q|/(\phi_0 h^2)]^{n-1} = h^{(n-1)/n} + O(\epsilon)$, assume a constant viscosity within the layer and compute the $O(\epsilon^2)$ viscous contribution to the averaged momentum equation. The contribution of the bulk region of the flow to the streamwise viscous diffusion terms are evaluated by assuming a constant viscosity μ_{eff}. The second-order boundary-layer equations then read [112]:

$$\begin{aligned} Re\left(\partial_t u + u\partial_x u + v\partial_y u\right) &= \mu_{\text{eff}}\left[\partial_{yy}u + 2\partial_{xx}u + \partial_x\left(\partial_x u|_h\right)\right] \\ &\quad +1 - \cot\beta\partial_x h + We\partial_{xxx}h\,, \end{aligned} \tag{5.53a}$$

completed by the tangential stress balance at the free surface

$$\partial_y u|_h = 4\partial_x h\partial_x u|_h - \partial_x v|_h\,, \tag{5.53b}$$

the kinematic condition (5.3c) and the no-slip condition (5.3d) at the wall.

Considering the self-similar velocity profile (5.21) and averaging the momentum balance (5.53a) with the weight f_0 then leads to

$$\begin{aligned} Re\int_0^h f_0(\bar{y})\left(\partial_t u_s + u_s\partial_x u_s + v_s\partial_y u_s\right)dy = \mu_{\text{eff}}\Bigg\{ & f_0(1)\left[4\partial_x h\partial_x u_s|_h - \partial_x v_s|_h\right] \\ & \int_0^h f_0''(\bar{y})u_s + f_0(\bar{y})\left[2\partial_{xx}u_s + \partial_x\left(\partial_x u_s|_h\right)\right]dy\Bigg\}\,. \end{aligned} \tag{5.54}$$

We then obtain the following averaged momentum equation

$$\begin{aligned} Re\partial_t q &= Re\left[-F(n)\,\frac{q}{h}\partial_x q + G(n)\,\frac{q^2}{h^2}\partial_x h\right] + I(n)\left[h\left(1-\cot\beta\partial_x h + We\partial_{xxx}h\right) - \frac{q|q|^{n-1}}{(\phi_0 h^2)^n}\right] \\ &+ r(h,q)\left[J_0(n)\frac{q}{h^2}\left(\partial_x h\right)^2 - K_0(n)\frac{\partial_x q\partial_x h}{h} - L_0(n)\frac{q}{h}\partial_{xx}h + M_0(n)\partial_{xx}q\right] \\ &+ h^{(n-1)/n}\left[J_w(n)\frac{q}{h^2}\left(\partial_x h\right)^2 - K_w(n)\frac{\partial_x q\partial_x h}{h} - L_w(n)\frac{q}{h}\partial_{xx}h + M_w(n)\partial_{xx}q\right]. \end{aligned} \tag{5.55}$$

where $I_w = (2n+1)/(n+2)$ and J_w, K_w, L_w and M_w are defined by

$$J_w = \frac{3n^2+13n+8}{(n+2)(n+1)}, \qquad K_w = M_w = \frac{5n+4}{n+1}, \tag{5.56a}$$

$$L_w = \frac{17n^2+23n+8}{2(n+1)^2}, \tag{5.56b}$$

and $r(h,q)$ stands for the evaluation of the effective viscosity at the free surface $\mu_{\text{eff}}(y=h)$ from the model variables h and q:

$$r(h,q) \equiv \left[s^2 + \partial_x v_s^2 + 4(\partial_x u_s)^2\right]^{(n-1)/2}\Big|_{y=h} \tag{5.57a}$$

where

$$\begin{aligned} \partial_x v_s^2 + 4(\partial_x u_s)^2\big|_{y=h} &= \left[\frac{2(2n+1)}{n+1}\partial_x\left(\frac{q}{h}\right)\right]^2 + \left\{\frac{2n+1}{n+1}\left[-2\frac{\partial_x h\partial_x q}{h}\right.\right. \\ &\left.\left. + q\left(2\frac{\left(\partial_x h\right)^2}{h^2} - \frac{\partial_{xx}h}{h}\right)\right] + \partial_{xx}q\right\}^2. \end{aligned} \tag{5.57b}$$

We have considered as equivalent the assumption (5.32) of a Newtonian plateau and the Carreau law (5.33) to express the effective viscosity $r(h,q)$. Our computations show that this assumption is reasonable in the limit of a vanishing Newtonian layer $\bar{\eta}_c \ll 1$ (see § 5.5.1 and § 5.6.3). We note that the $O(\epsilon^2)$ term $\partial_x v_s$ has been kept in the expression of the strain rate at the free surface. Indeed, retaining only the dominant term $4\left(\partial_x u_s|_{y=h}\right)^2 \propto \left[\partial_x(q/h)\right]^2$ implies that the effective viscosity spuriously reaches local maxima at crests and troughs of traveling waves since q is a function of h in that case (cf. section 5.6).

The averaged momentum equation (5.55) retains the contribution to streamwise viscous diffusion from the free surface (second row) and from the bulk (third row). In the Newtonian limit $n \to 1$, the averaged momentum equation obtained by [112] is recovered

$$\begin{aligned} Re\partial_t q &= Re\left[-\frac{17}{7}\,\frac{q}{h}\partial_x q + \frac{9}{7}\,\frac{q^2}{h^2}\partial_x h\right] + \frac{5}{6}\left[h\left(1-\cot\beta\partial_x h + We\partial_{xxx}h\right) - 3\frac{q}{h^2}\right] \\ &+ 4\frac{q}{h^2}(\partial_x h)^2 - \frac{9}{2}\frac{\partial_x q\partial_x h}{h} - 6\frac{q}{h}\partial_{xx}h + \frac{9}{2}\partial_{xx}q\,. \end{aligned} \tag{5.58}$$

The averaged momentum balance (5.55) accounts for the rapid decrease of the effective viscosity $\mu_{\text{eff}}(y = h)$ when the interface is disturbed. Consistency is achieved up to $O(\epsilon)$ for inertial terms and up to $O(\epsilon^2)$ for the contribution of the surface effective viscosity to the streamwise diffusion terms. The contribution of the bulk to the streamwise viscous diffusion terms is evaluated in an *ad hoc* way but ensures consistency with the Newtonian case in the limit $n \to 1$.

Truncated at order ϵ, i.e. when the second and third rows are omitted, (5.55) is identical to the momentum balance derived by Amaouche [5]. Similarly to [85], Amaouche *et al.* used the power-law constitutive equation (5.1) without regularization of the effective viscosity at zero strain rate. As a matter of fact, the divergence of the effective viscosity does not affect the boundary-layer momentum balance (5.41) when truncated at first order. Indeed at $O(\epsilon)$, viscous contribution comes only through the stress τ_{xy} which remains bounded. As a consequence, a regularization of the effective viscosity at low strain rate becomes necessary only when streamwise viscous effects are accounted for.

5.4.2 Shear-thickening film ($n > 1$) in the limit of vanishing Newtonian layer

Now, turning to the shear-thickening case, the expressions of the coefficients of (5.48) simplify to the following expressions for $1 < n < 3$ are

$$\tilde{J} \sim \tilde{K} \sim \frac{(3n+2)[n(2n-3)(n+3)-2]}{12n(4n+1)} \left[\frac{|\bar{u}|}{h}\right]^{n-1} \tag{5.59a}$$

$$\tilde{L} \sim -\frac{(2n+1)(3n+2)(3n^2+8n+1)}{6n(3n+1)(4n+1)} \left[\frac{|\bar{u}|}{h}\right]^{n-1}, \tag{5.59b}$$

$$\tilde{M} \sim \frac{(2n+1)(2n+7)(3n+2)}{6(2n-1)(4n+1)} \left[\frac{|\bar{u}|}{h}\right]^{n-1}, \tag{5.59c}$$

$$\tilde{N} \sim \frac{(n-1)(2n+1)(2n+7)(3n+2)}{12(2n-1)(4n+1)} \left[\frac{|\bar{u}|}{h}\right]^{n-1}, \tag{5.59d}$$

For a shear-thickening fluid, the Newtonian layer at the free surface corresponds to a minimum of viscosity $r = s^{n-1}$ that goes to zero in the limit $s \to 0$. The averaged momentum equation thus reduces to

$$\begin{aligned} Re\partial_t q = Re\left[-F(n)\frac{q}{h}\partial_x q + G(n)\frac{q^2}{h^2}\partial_x h\right] + I(n)\left[h\left(1 - \cot\beta\partial_x h + We\partial_{xxx}h\right) - \frac{q|q|^{n-1}}{(\phi_0 h^2)^n}\right] \\ + \left[\frac{|q|}{\phi_0 h^2}\right]^{n-1} \times \left[J_1(n)\frac{q}{h^2}(\partial_x h)^2 - K_1(n)\frac{\partial_x q \partial_x h}{h} - L(n)\frac{q}{h}\partial_{xx}h + M(n)\partial_{xx}q\right], \end{aligned} \tag{5.60}$$

where L and M are defined in (5.28). The set of coefficients is completed by

$$J_1 = -\frac{(2n+1)(2n+7)(3n+2)}{3(2n-1)(4n+1)}, \tag{5.61a}$$

$$K_1 = -\frac{(3n+2)(4n^4-12n^3-85n^2-23n+2)}{12n(2n-1)(4n+1)}, \tag{5.61b}$$

$$L_1 = \frac{(2n+1)(3n+2)(12n^3+36n^2+n-1)}{6n(2n-1)(3n+1)(4n+1)}, \tag{5.61c}$$

$$M_1 = \frac{(2n+1)(2n+7)(3n+2)}{6(4n+1)(2n-1)}. \tag{5.61d}$$

In the Newtonian limit $n \to 1$, the averaged momentum equation (5.58) derived by Ruyer-Quil & Manneville [112] is recovered but for the coefficients of the streamwise viscous diffusion terms $(q(\partial_x h)^2/h^2$ and $\partial_x q \partial_x h/h$ as $K_1(1) = 19/2$ and $J_1(1) = 9$. We note that these terms are nonlinear and do not contribute to the linear stability analysis of the Nusselt base flow so that the dispersion relations of the model (5.14), (5.60) and (5.14), (5.58) coincide when $n = 1$. The above discrepancy is a consequence of the Taylor expansion (5.47) of the effective viscosity ${\dot\gamma_0}^{n-1}$ which becomes invalid as $\partial_y u_s|_{y=h}$ goes to zero for $n = 1$. Yet, the assumption of a vanishing Newtonian layer, necessary to derive (5.60), is obviously not compatible with the Newtonian limit $n \to 1$ and a full agreement of (5.60) with (5.58) is therefore not expected.

Whenever the power law index $n \geq 2$, the averaged momentum equation (5.27) and (5.60) do not either coincide. We note that it is again an effect of the divergence of the Taylor expansion (5.47) as $\partial_y u_s|_{y=h}$ goes to zero. However, (5.27) and (5.60) differ only through second-order viscous nonlinear terms which do not contribute to the linear stability analysis of the flow.

5.5 Linear stability analysis

5.5.1 Orr-Sommerfeld analysis

In this section, we consider the linear stability of the Nusselt uniform film solution. We first linearize the governing equations (5.7) with a fluid modeled by a power-law and a Newtonian behavior at low rate of strain (5.31). We thus perturb the basic state (5.34) with $h = 1$:

$$\text{if } y < 1 - s^n\,,\ U(y) = f_0(y)$$

$$\text{otherwise} \quad U(y) = f_0(1-s^n) + s^{n+1} g_0\left[s^{-n}(y+s^n-1)\right], \tag{5.62a}$$

$$P(y) = \cot\beta(1-y). \tag{5.62b}$$

We introduce a stream function and proceed to a decomposition on normal modes:

$$\begin{aligned} u &= U + \Re\left(\psi'(y)e^{\mathrm{i}k(x-ct)}\right), \qquad v = \Re\left(-\mathrm{i}k\psi(y)e^{\mathrm{i}k(x-ct)}\right), \\ h_i &= 1 - s^n + \Re\left(f_i e^{\mathrm{i}k(x-ct)}\right), \end{aligned}$$

where k and c are the wavenumber and phase speed, respectively, and $\Re$ stands for the real part; h_i refers to the position of the fake interface separating the Newtonian and non-Newtonian regions of the flow. We thus obtain a Orr-Sommerfeld problem,

$$\begin{aligned} \text{if } y < 1-s^n, \quad \mathrm{i}kRe\left[(U-c)(D^2-k^2)\psi - \psi U''\right] &= \left(D^2+k^2\right)\left[n(U')^{n-1}\left(D^2+k^2\right)\psi\right] \\ &\quad -4k^2 D\left[(U')^{n-1}D\psi\right], \qquad (5.63a) \\ \text{otherwise}, \quad \mathrm{i}kRe\left[(U-c)(D^2-k^2)\psi - \psi U''\right] &= r\left(D^2-k^2\right)^2\psi, \qquad (5.63b) \end{aligned}$$

where $D \equiv d/dy$ and again $r = s^{n-1}$ is the ratio of the viscosity at the free surface and at the wall. The system of equations (5.63) is completed by the boundary conditions at the wall and at the interface,

$$\begin{aligned} \psi(0) = \psi'(0) &= 0, \qquad (5.63c) \\ k^2\psi(1) + \psi''(1) + U''(1)\frac{\psi(1)}{c-U(1)} &= 0, \qquad (5.63d) \\ \frac{\psi(1)}{c-U(1)}\left(Wek^3 + \cot\beta k\right) + kRe[U(1)-c]\psi'(1) & \\ +\mathrm{i}r\left[\psi'''(1) - 3k^2\psi'(1)\right] &= 0, \qquad (5.63e) \end{aligned}$$

The amplitude of the deformation of the fake interface is given by

$$f_i = ns^{n-1}(k^2\psi|_{y_{c-}} + \psi''|_{y_{c-}}), \qquad (5.63f)$$

where $y_c = 1 - s^n$ refers to the location of the interface for the base flow. The continuity of the velocity implies the continuity of ψ and ψ' at $y = y_c$. Writing the continuity of stresses at the fake interface finally leads to

$$\begin{aligned} \psi''|_{y_{c+}} &= \left[n\psi'' + (n-1)k^2\psi\right]|_{y_{c-}}, \qquad (5.63g) \\ s^n\left[\psi'''\right]|_{y_{c+}} &= \left\{s^n\left[n\psi''' + (n-1)k^2\psi'\right] - (n-1)\left[\psi'' + k^2\psi\right]\right\}|_{y_{c-}} \qquad (5.63h) \end{aligned}$$

at the fake interface $y_c = 1 - s^n$.

We solve systems (5.63) by continuation using AUTO07P software [40]. We obtain the spatial long-wave mode (k complex and ω real) starting from its analytical solution at $k = 0$. We first present the result obtained for the three shear-thinning fluids whose properties are detailed in table 5.1. Fig. 5.6(a) shows the behavior of the spatial growth rate $-k_i = -\Im(k)$ as function of the wavenumber $k_r = \Re(k)$. The Reynolds number

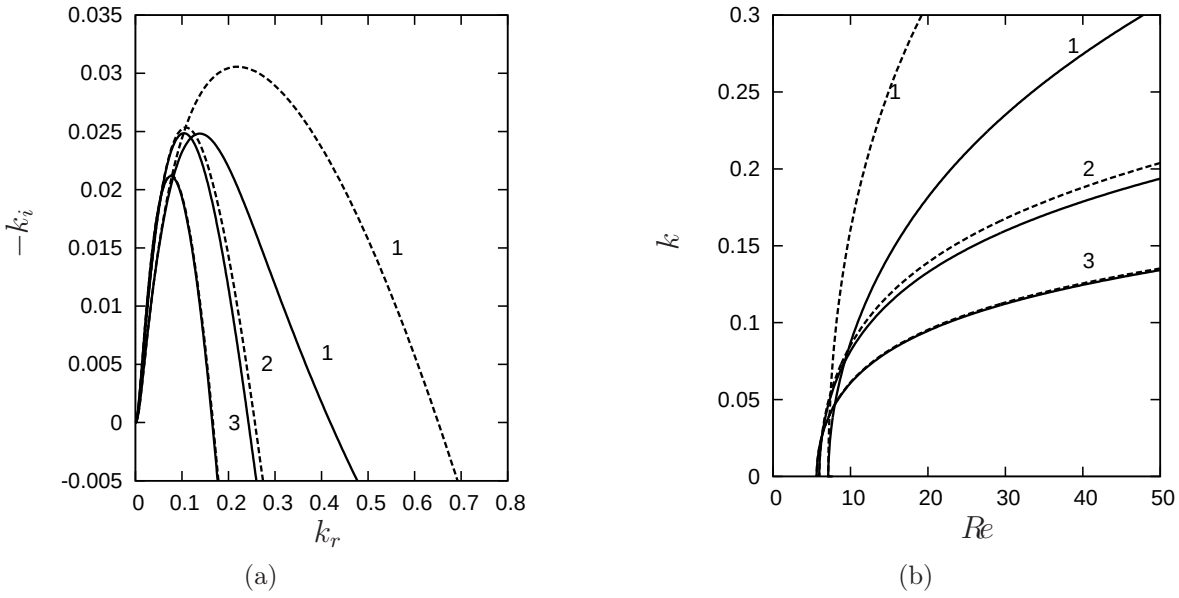

(a) (b)

Figure 5.6: (a) Spatial growth rate $-k_i$ versus wavenumber k_r at $Re = 100$. (b) Marginal stability curves in the plane (Re, k). Inclination angle is $\beta = 15°$. Labels refer to shear-thinning xanthan gum solutions (cf.Table 5.1). Solid lines refer to the solutions to the Orr-Sommerfeld problem (5.63). Dashed lines correspond to the solutions when surface tension is not taken into account ($We = 0$).

is chosen large ($Re = 100$) and the inclination moderate ($\beta = 15°$). Similarly to the Newtonian case [15], the range of unstable wavenumber extend from zero to the cut-off wavenumber k_c. Fig. 5.6(b) presents the marginal stability curve, i.e. cut-off wavenumber k_c versus Reynolds number Re. As the concentration of xanthan gum increases from 500 ppm (set 1) to 2500 ppm (set 3), the instability threshold is displaced to lower values of the critical Reynolds number whereas the range of unstable wave numbers is decreased. Shear-thinning effects therefore enhance the primary instability close to threshold [83], but also tend to stabilize the base flow far from threshold. We have compared the Orr-Sommerfeld analyses with ($We \neq 0$) and without surface tension ($We = 0$). Differences are important for set 1 but hardly noticeable for the fluid sets 2 and 3, in which case the cut-off wavenumber is determined by the balance of inertia and viscous damping. For shear-thinning fluid, viscosity is maximal at the free surface and a competition of surface tension and viscous damping at the free surface can be evaluated by computing the Kapitza number Γ_0 based on the the maximum viscosity μ_0 of the fluid:

$$\Gamma_0 = (l_c/l_{\mu_0})^2 = (\sigma/\rho)(\mu_0/\rho)^{-4/3}(g\sin\beta)^{-1/3} \quad \text{where} \quad l_{\mu_0} = (\mu_0/\rho)^{2/3}\,(g\sin\beta)^{-1/3} \tag{5.64}$$

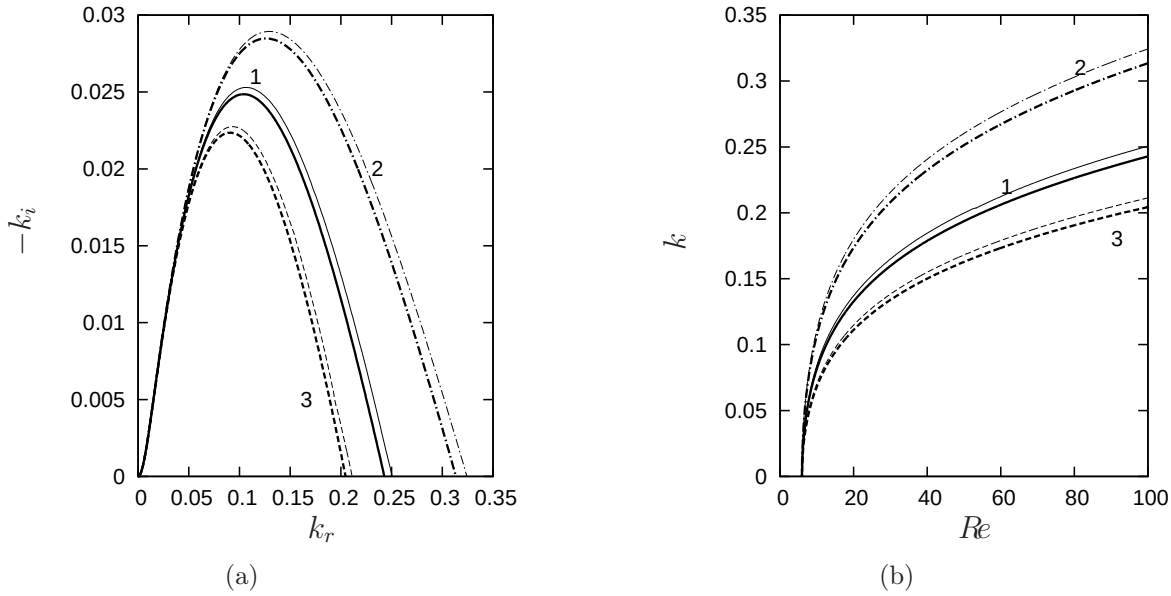

(a) (b)

Figure 5.7: Spatial linear stability analysis based on the Orr-Sommerfeld problem (5.63). (a) Spatial growth rate $-k_i$ versus wavenumber k_r at $Re = 100$. (b) Marginal stability curves in the plane (Re, k). Inclination angle is $\beta = 15°$. Fluid properties correspond to a shear-thinning xanthan gum solution of concentration 1500 ppm (Set 2 in Table 5.1). Labeled lines 1,2 and 3 refer to $\dot{\gamma}_c = 0.1$ s^{-1}, 1 s^{-1} and 0.02 s^{-1} respectively.

is the length at which viscosity μ_0 balances streamwise gravity acceleration. From the data in 5.1, we get $\Gamma_0 = 8.8$ for a 500 ppm xanthan solution (set 1) and equal to $\Gamma_0 = 0.19$ and 0.02 respectively for the two more concentrated solutions corresponding to sets 2 and 3, which explains that for the concentrated xanthan solutions surface tension effects are rather weak in comparison with the wave damping by the viscosity of the fluid at the free surface. Fig. 5.7 compares the marginal stability conditions and spatial growth rate for given fluid properties, flow rate and inclination angle, when the threshold $\dot{\gamma}_c$ separating the shear-thinning and the Newtonian behavior of the fluid. As expected, both the location of the marginal stability curve in the plane (Re, k_r) and the spatial growth rate $-k_i$ varies significantly with $\dot{\gamma}_c$ which underlines the damping role of the viscosity at the free surface on the linear stability of the Nusselt film. We therefore conclude that for sufficiently small power-law index ($n = 0.4$ for Set 2 and $n = 0.34$ for Set 3), the marginal stability conditions and thus the range of unstable wave numbers are governed by the viscous damping of short waves in the Newtonian layer below the interface, a mechanism which is more effective than surface tension and the viscous momentum diffusion in the bulk of

the film.

We have compared the results of the spatial stability analysis obtained with the Newtonian-plateau regularization (5.32) to the ones from the Carreau law (5.33) (see Appendix A.4). The two analyses lead to close results as illustrated in Fig. 5.7. We have checked that it is also the case for the fluid properties listed in table 5.1 and the range of parameters $[Re_c,\, Re]$ for $\beta = 15°$ and $85°$ for which the thickness of the Newtonian layer is small ($s^n \ll 1$). We thus conclude that the results of my linear stability analysis do not depend on the peculiar choice of regularization of the power law (5.1) at low strain rate.

Turning to the shear-thickening cornstarch solutions, we present the spatial growth rate $-k_i$ versus wavenumber k_r at $Re = 100$ and the marginal stability curves in the plane $(Re,\, k)$ in Fig. 5.8. Labels 4, 5 and 6 refer to the parameter sets given in table 5.2. As the concentration of the cornstarch solution is raised from 33 % (set 4) to 38 % (set 6), the instability threshold is displaced to larger values of the critical Reynolds number whereas the range of unstable wavenumber increases. Conversely to what is observed for shear-thinning fluids, shear-thickening effects stabilize the base flow close to the instability threshold but are destabilizing farther from threshold. The results presented in Fig. 5.8 are not noticeably modified whenever surface tension in neglected ($We = 0$) or the critical strain rate is raised up to $\dot\gamma_c = 1\ \mathrm{s}^{-1}$, which shows that the range of unstable wave numbers is determined by the effective viscosity of the non-Newtonian bulk region and not by the significantly lower viscosity of the Newtonian layer at the free surface or surface tension effects.

5.5.2 Whitham wave hierarchy

Turning to the stability analysis of the low-dimensional model (5.14), (5.38), (5.48) and (5.36) leads to the dispersion relation

$$\begin{aligned} n\tilde I(c-1) + rk^2\left\{c\,\tilde M + n\tilde L(2\phi-1) + \tilde M\,[n-2(n+1)\phi]\right\} \\ -\mathrm{i}kRe\left\{\left[c^2 - c(\tilde F - n + 2(n+1)\phi)) + n\tilde G(2\phi-1) + \tilde F(2(n+1)\phi - n)\right]\right. \\ \left. + n\tilde I\left(Fr^{-2} + \frac{We}{Re}k^2\right)(2\phi-1)\right\} \;=\; 0 \end{aligned} \tag{5.65}$$

where ϕ is a function of the relative thickness $\bar\eta_c$ of the Newtonian layer and is defined in (5.36). The coefficients $\tilde I$, $\tilde F$, $\tilde G$, $\tilde L$, $\tilde M$ and ϕ are computed for the base state relative thickness $\bar\eta_c = s^n$.

The dispersion relation(5.65) corresponds to a wave hierarchy situation considered by [146] and can be recast in the canonical form:

$$c - c_k(k) - \mathrm{i}kRe\,[c - c_{d-}(k)]\,[c - c_{d+}(k)] = 0\,. \tag{5.66}$$

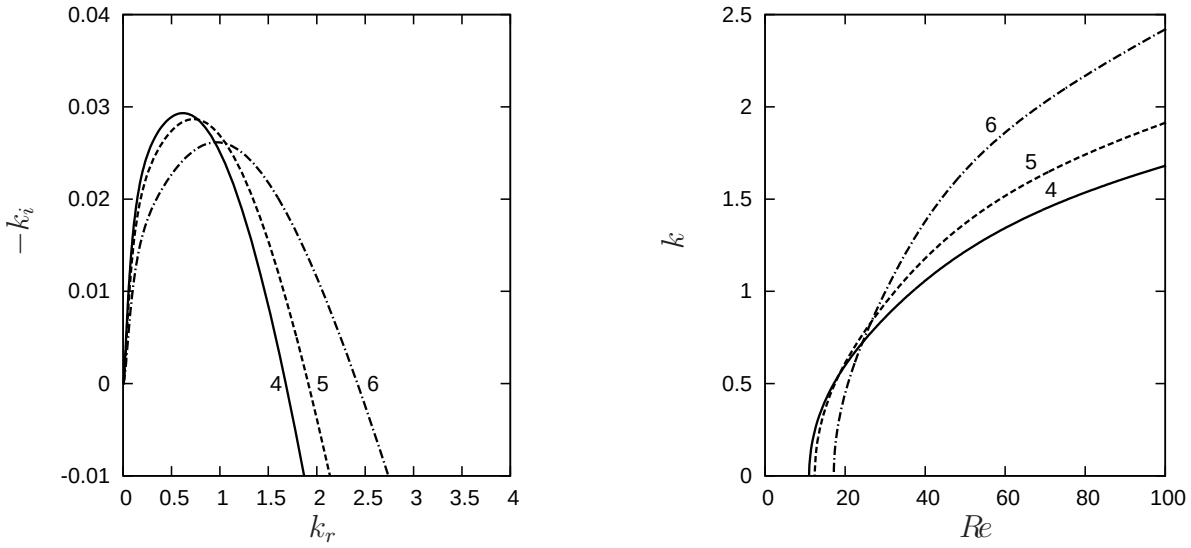

Figure 5.8: Spatial linear stability analysis based on the Orr-Sommerfeld problem (5.63). (a) Spatial growth rate $-k_i$ versus wavenumber k_r at $Re = 100$. (b) Marginal stability curves in the plane (Re, k). Inclination angle is $\beta = 15°$. Fluid properties correspond to the shear-thickening cornstarch solutions whose properties are listed in table 5.2.

Each dispersion relation of the form (5.66) can be split into two parts with a $\pi/2$ phase shift, each part corresponding to a different kind of wave. The dispersion relation of the first kind of waves is obtained by taking the limit $Re \to 0$. In this limit, the velocity field and thus the flow rate q are utterly slaved to the evolution of the film thickness h and waves of the first kind are governed by the mass balance (5.14) or equivalently the kinematic boundary condition (5.3c). These kinematic waves result from the kinematic response of the free surface to a perturbation and propagate at speed

$$c_k = \frac{n\tilde{I} + rk^2\left\{n\tilde{L}(1-2\phi) + \tilde{M}\left[2(1+n)\phi - n\right]\right\}}{n\tilde{I} + rk^2 M}\,. \tag{5.67}$$

In the limit $k \to 0$ we recover $c_k = 1$ which in dimensional units corresponds to the velocity scale V as already noticed in § 5.3. Let us stress that the dependence of c_k on the wavenumber k arises from the viscous diffusion of the momentum in the direction of the flow. This viscous dispersion effect was first noted in [115].

In contrast, waves of the second kind correspond to the limit $Re \to \infty$. These dynamic waves are the responses of the film to the variation in momentum, hydrostatic pressure and surface tension (for bounded Froude number and ratios We/Re) which are induced by deformations of the free surface. They propagate at speeds

$$c_{d\pm} = \frac{1}{2}\left(\tilde{F} - n + 2(n+1)\phi \pm \sqrt{\Delta}\right)\,, \tag{5.68}$$

$$\text{with} \quad \Delta = [\tilde{F} - n + 2(n+1)\phi]^2 + 4\{[n - 2(n+1)\phi]\tilde{F} + n(1-2\phi)\tilde{G}\} + 4n(1-2\phi)\tilde{I}\tilde{Fr}^{-2}\,, \tag{5.69}$$

where the coefficients are again computed at $\bar{\eta}_c = s^n$ and $\tilde{Fr}^{-2}(k^2) = (\cot\beta + Wek^2)/Re$. Dispersion of dynamic waves is induced by surface tension.
Considering real wave numbers, the temporal stability condition of the base state can be written in terms of the speeds c_k and $c_{d\pm}$ of the kinematic and dynamic waves [146]:

$$c_{d-} \leqslant c_k \leqslant c_{d+} \tag{5.70}$$

which is schematically illustrated in Fig. 5.9. The base state is marginally stable if $c_{d-} = c_k$ or $c_{d+} = c_k$. In my case, only the latter condition can be achieved. The instability threshold arises at $k = 0$ which reflects the long-wave nature of the instability and leads to

$$Fr^2 = \frac{Re}{\cot\beta} = \frac{n\tilde{I}}{(n+1)(1-\tilde{F}) - n\tilde{G}}\,. \tag{5.71}$$

We present in Fig. 5.10 the variations of the critical Froude number with respect to the relative thickness s^n of Newtonian layer for the base flow for the shear-thinning and shear-thickening fluids reported in table 5.1 and 5.2. The expression (5.71) is compared to the

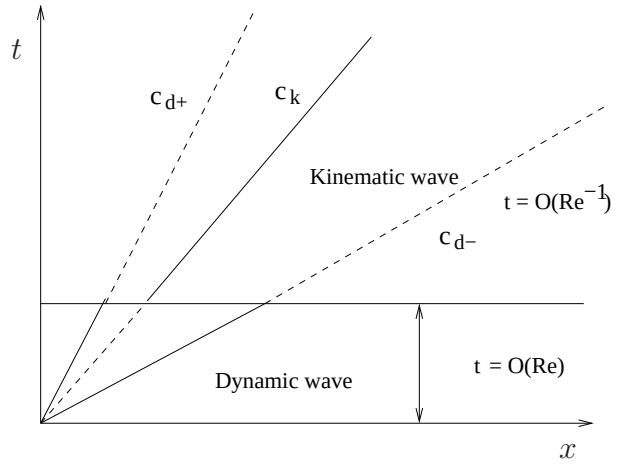

Figure 5.9: Sketch of the spatio-temporal diagram of primary instability.

threshold obtained by solving numerically the Orr-Sommerfeld problem. For all tested values of s^n and n a remarkable agreement is achieved. As for Newtonian film flows this agreement is related to the consistency of the modeling approach at order ϵ [112]. We have completed Fig. 5.10 with the values of the Froude number at the instability threshold given by the solution to the Orr-Sommerfeld problem (A.4) when the Carreau constitutive equation (5.33) is assumed. Whenever the Newtonian layer s^n is less than 0.2, the solutions to the Orr-Sommerfeld problem when the regularization of the effective viscosity at small strain rate is given by (5.33) or (5.32) give close results.

The effect of the Ostwald-de Waele model on the stability of the uniform film Nusselt solution can be found by comparing kinematic and dynamic wave speeds. We have plotted in Fig. 5.11 the minimum of the fastest dynamic wave speed c_{d+} which is reached in the limit $\tilde{Fr}^{-2} \to 0$ corresponding to a vertical wall and a null wavenumber. The largest is the interval between the minimum of c_{d+} and c_k, the smallest is the threshold Fr^2 of the instability. Since the minimum of c_{d+} is always smaller than one, which is the dimensionless value of c_k for $k = 0$, lowering (increasing) the minimum of c_{d+} is destabilizing (stabilizing). The decrease of the instability threshold observed for a shear-thinning fluid ($n < 1$) in Fig. 5.10 is therefore made clear by the drop of the minimum of the fastest dynamic wave velocity observed in Fig. 5.11. The same analysis applies conversely for a shear-thickening fluid ($n > 1$). Fig. 5.11 has been completed with the fluid velocity at the interface i.e. $u_i = u|_{y=1}$ for the Nusselt base flow $h = 1$ (5.34). Interestingly, u_i stays close to the minimum of c_{d+} whatever are the values of n and s^n. Therefore, the variations of the interval between c_{d+} and c_k follow closely the variations of the interval between c_k and the velocity of the fluid at the interface (which is also the maximum velocity of the base flow). As noted by [131], the ability of kinematic waves to move faster than any fluid particles in the key ingredient of the instability mechanism of a falling liquid film. There

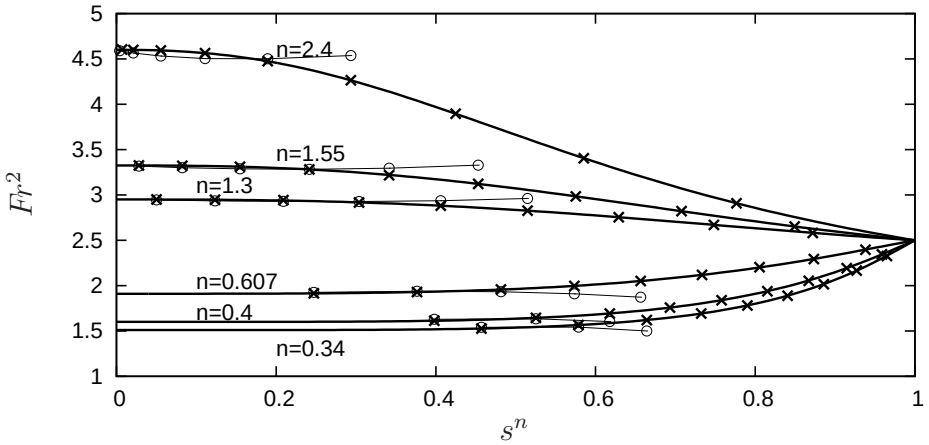

Figure 5.10: Critical Froude number $Fr^2 = Re/\cot\beta$ as function of the relative thickness s^n of the Newtonian layer for the different values of the power-law index n. The solid lines correspond to (5.71) and crosses refer to the numerical solutions to the Orr-Sommerfeld problem (5.63).

is a direct correlation between the movement of the threshold Fr^2 in Fig. 5.10 and the variation of the velocity at the interface u_i depicted in Fig. 5.11. The smaller the power-law index n and the thinnest is the Newtonian layer, the smaller is the minimum of c_{d+} and thus the instability threshold Fr^2 [109, 83]. The weak dependence of the maximum velocity of the base flow u_i and the speed c_{d+} of the fast dynamic waves on the thickness s^n of the Newtonian layer for s^n lower than 0.2 makes clear the similar trend observed for the critical Froude number.

5.5.3 Limit of a vanishing Newtonian layer

Now we turn to the simplified models (5.14), (5.55) and (5.14), (5.60) obtained in § 5.4 in the limit of thin Newtonian layers at the free surface ($s^n \to 0$).

For a shear-thinning fluid the dispersion relation of model (5.14), (5.55) can be recast in the canonical form (5.66) where the kinematic wave speed now reads

$$c_k = \frac{n}{n+1} + \frac{1}{1+n+(1-n)rk^2} \tag{5.72}$$

so that $c_k = 1$ when the viscous dispersive effect vanishes ($r \to 0$). The dynamic wave

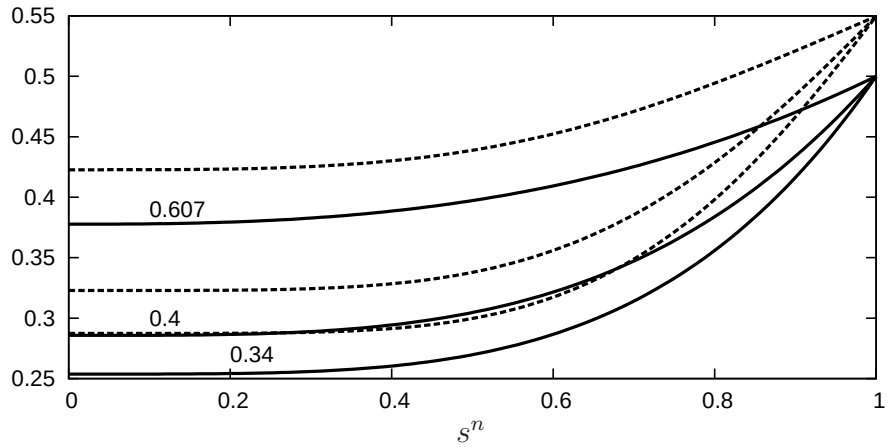

(a) $n = 0.34$, 0.4 and 0.607

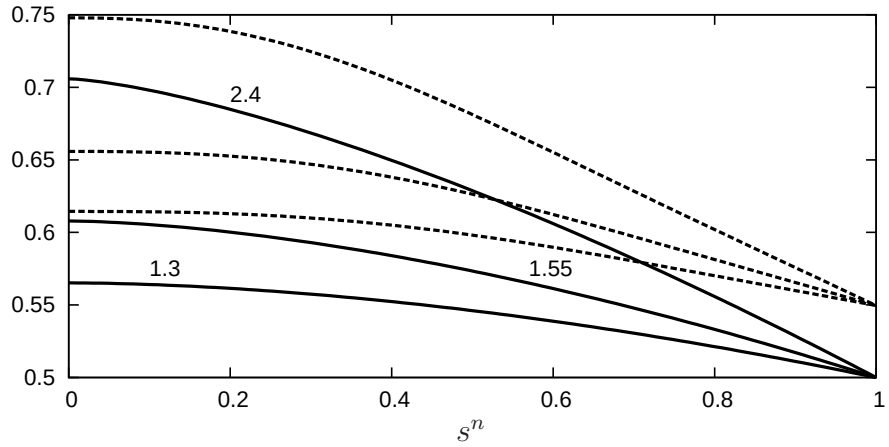

(b) $n = 1.3$, 1.55 and 2.4

Figure 5.11: Velocity at the free surface u_i (solid lines) and dynamic wave speed c_{d+} in the limit $\tilde{Fr}^{-2} \to 0$ (dashed lines).

speed reads

$$\begin{aligned} c_{d\pm} &= \frac{1}{2}\phi_0\left(F \pm \sqrt{\Delta}\right), \\ \text{with} \quad \Delta &= F^2 - 4G + \frac{I}{\phi_0^2 \tilde{Fr}^2}. \end{aligned} \tag{5.73}$$

where again $\phi_0 = \phi(0) = n/(2n+1)$.

Turning to a shear-thickening fluid, the dispersion relation of the two-equation model (5.14), (5.60) again admits the canonical form (5.66) where kinematic-wave speed is given by

$$c_k = \frac{nI + \phi_0^2 L k^2}{nI + \phi_0 M k^2} \tag{5.74}$$

and dynamic-wave speeds remain given by (5.73). For both models (5.14), (5.55) and (5.14), (5.60), the marginal stability condition $c_k = c_{d+}$ leads to the correct expression (5.20) of the instability threshold.

We compare in Figs. 5.12 and 5.13 the marginal stability curves obtained with the two-equation models (5.14), (5.55) and (5.14), (5.60) with the reference results from the Orr-Sommerfeld stability analysis. A good agreement is obtained for each shear-thinning and shear-thickening fluid properties listed in tables 5.1 and 5.2. More precisely, the instability threshold is very well captured for each tested set of parameters although we assume a negligible thickness of the Newtonian layer at the free surface ($s^n \to 0$). The very weak dependence of the instability threshold on the thickness s^n of the Newtonian layer for s^n lower than 0.2 observed in Fig. 5.10 does explain this remarkable agreement. Note that a better agreement is observed the models and the Orr-Sommerfeld analysis is achieved in the case of shear-thinning fluids than for shear-thickening fluids. Considering that the hypothesis $s^n \ll 1$ is far better achieved in the latter case than in the former ones, this observed discrepancy must be related to the long-wave assumption sustaining the derivation of the models. Since the cut-off wave numbers are smaller in the shear-thinning case, which reflects the stabilizing contribution of streamwise viscous diffusion at the free surface layer, the long-wave assumption is more easily verified in that case which explains the observed better agreement with the Orr-Sommerfeld analysis. As for the Orr-Sommerfeld analysis, we note that the spatial stability analysis of the shear-thinning model (5.14), (5.55) is strongly dependent on the viscosity contrast r between the wall and the free surface. Indeed setting r to zero provides much larger values of the cut-off wavenumber and spatial growth rate as illustrated in Fig. 5.14. Conversely, we have not noticed significant differences for the stability of a uniform film of shear-thickening fluid based on the weighted-residual approach when the Newtonian layer viscosity is taken into account or not ($r = 0$). We can now make use of the two-wave hierarchy framework to interpret the displacement with respect to n of the marginal stability curves presented in Figs. (5.6), (5.8), (5.12) and (5.13) in terms of the variations of the kinematic and

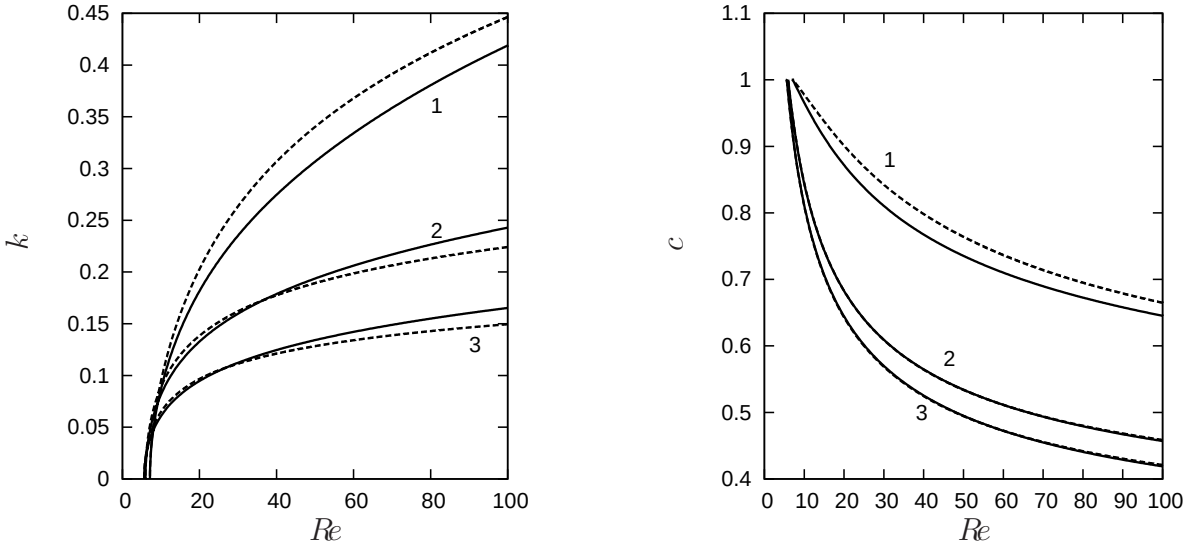

Figure 5.12: (a) Cut-off wavenumber k_c versus Reynolds number Re. (b) Phase speed c at marginal conditions versus Re. Inclination angle is $\beta = 15°$. Labels refer to the shear-thinning xanthan gum solutions whose properties are listed in table 5.1. Solid and dashed lines stand for the solutions to the Orr-Sommerfeld problem (5.63) and to the dispersion relation of (5.14), (5.55) respectively.

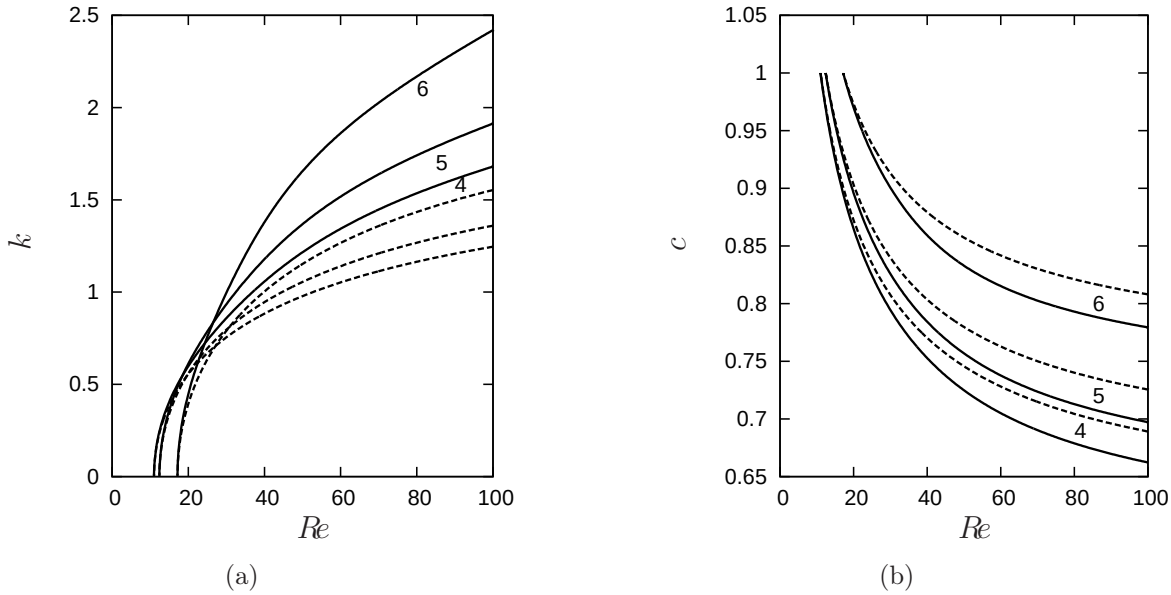

Figure 5.13: (a) Cut-off wavenumber k_c versus Reynolds number Re. (b) Phase speed c at marginal conditions versus Re. Inclination angle is $\beta = 15°$. Labels refer to the shear-thickening cornstarch solutions whose properties are given in table 5.2. Solid and dashed lines stand for the solutions to the Orr-Sommerfeld problem (5.63) and to the dispersion relation of (5.14), (5.60) respectively.

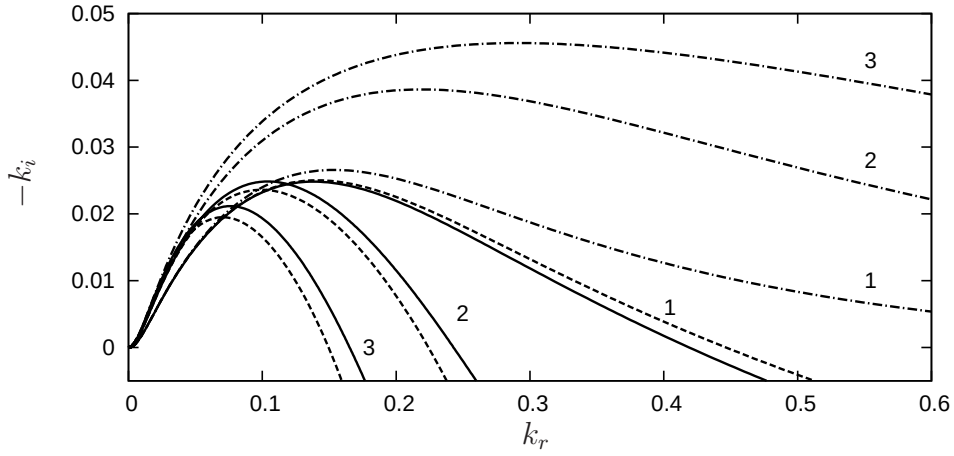

Figure 5.14: Spatial growth rate $-k_i$ versus wavenumber k_r. Inclination angle is $\beta = 15°$. Labels refer to the shear-thinning fluids whose properties are listed in table 5.1. Solid and dashed lines correspond to the solutions to the Orr-Sommerfeld problem (5.63) and to the dispersion relation of (5.14), (5.55). Dashed-dotted lines stand for the solution to (5.14), (5.55) when viscous dispersion is neglected ($r \to 0$ or equivalently $L_0 = M_0 = 0$).

dynamic wave speeds. In the shear-thinning case, the movement with respect to n of the curves $c_k(rk^2)$ and $c_{d+}(\tilde{Fr}^2)$ governed by equations (5.72) and (5.73) are illustrated in Fig. 5.15. Lowering the power-law index enhances the stabilizing decrease of the kinematic wave speed by the streamwise viscous diffusion as observed in panel a. Since the speed of kinematic waves is not affected at low values of k, this effect becomes significant only when k is large that is far from the instability threshold. The reduction of dynamic wave speed c_{d+} conversely contributes to maintain the gap between speeds of dynamic and kinematic waves. The downward movement of the curve $c_{d+}(\tilde{Fr}^2)$ is thus accompanied by a shift to the left of the crossing with the horizontal axis $c_{d+} = 1$ signaling a decrease of the instability threshold $Fr_c^2 = Re_c/\cot\beta$ in agreement with Fig. 5.10. Conversely, for shear-thickening fluids, the movement of the curves $c_k(k^2)$ and $c_{d+}(\tilde{Fr}^2)$ as depicted in Fig. 5.16 indicate that increasing n is destabilizing by augmenting the speed of kinematic waves but also stabilizing by raising simultaneously the speed if dynamic waves. The crossing of the curves $c_{d+}(\tilde{Fr}^2)$ with $c_{d+} = 1$ being displaced to the right in Fig. 5.16(b), the instability is triggered at larger values of the critical Froude number Fr_c^2 again in agreement with what is observed in Fig. 5.10. The destabilizing increase of the speed of kinematic waves becomes significant only at large wavenumber whereas the stabilizing decrease of the dynamic wave speed occurs even at $k = 0$ which explains the stabilization of the base flow close to threshold and its destabilization further from threshold by shear-

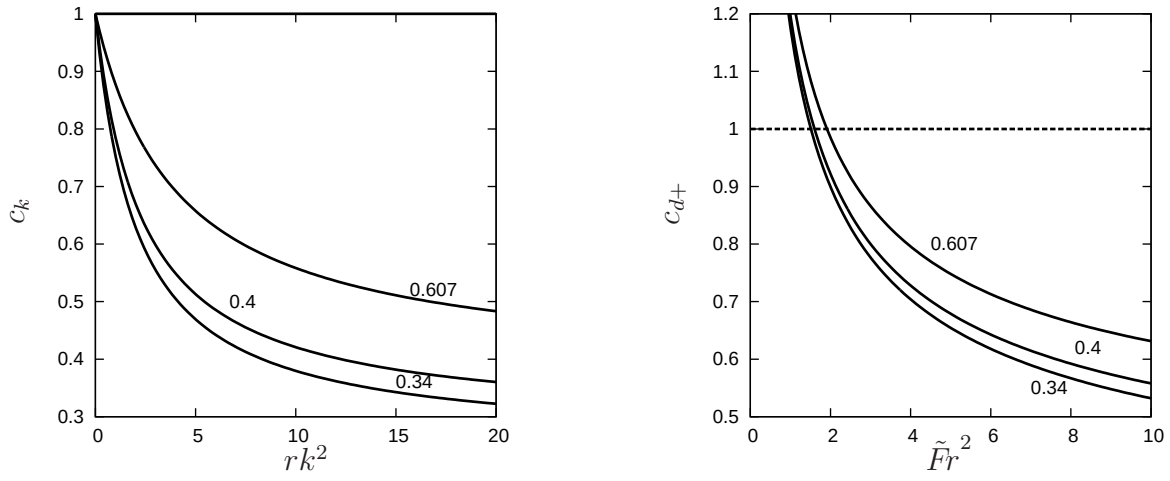

(a) (b)

Figure 5.15: (a) kinematic wave speed c_k as function of rk^2 and (b) dynamic wave speed c_{d+} as function of $\tilde{Fr}^2$ for shear-thinning fluids ($n = 0.607$, $n = 0.4$ and $n = 0.34$).

thickening effects.

5.6 Traveling waves

5.6.1 Fixed points

In this section we consider the nonlinear solutions to the simplified models (5.14), (5.55) and (5.14), (5.60) such as traveling waves propagating at constant speed c. In the a frame of reference moving with the speed of the waves, $\xi = x - ct$, the flow is stationary and partial differential equations are converted into ordinary differential equations which we solved by continuation using AUTO07P software [40]. The mass balance (5.14) being integrated once gives

$$q - ch \equiv q_0 \,, \tag{5.75}$$

where q_0 is the rate at which the fluid flows under the waves. Denoting by primes the differentiations with respect to the moving coordinate ξ ,the averaged momentum balances (5.48), (5.55) and (5.60) can then be recast into the form $h''' = f(h, h', h'')$, where f is a function of the thickness h, its first and second derivatives and the parameters Re, We, $\cot\beta$, n and c. We thus end up with a dynamical system of dimension three in the phase space spanned by h, h' and h''. Fixed points of this dynamical system satisfy $h' = h'' = 0$

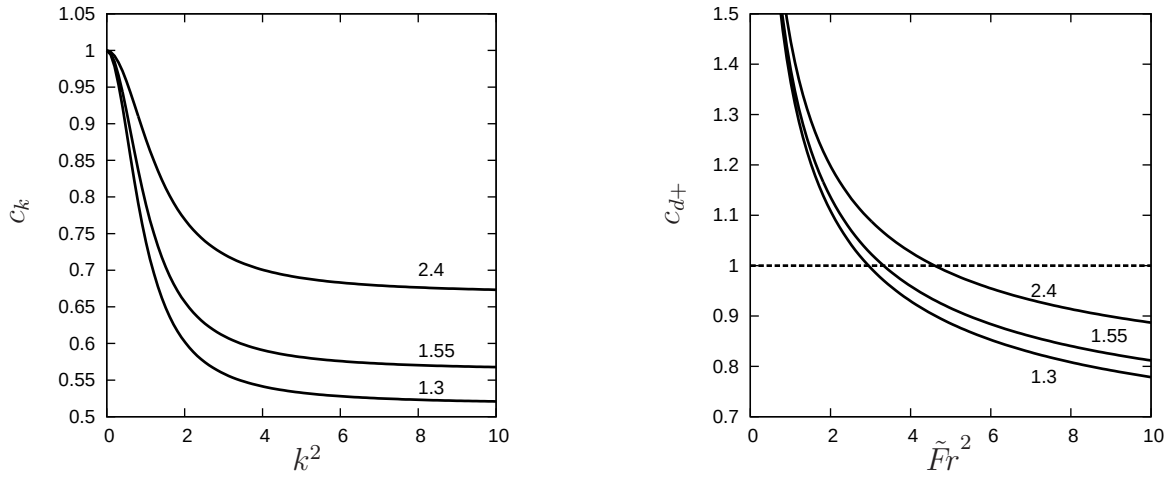

(a) (b)

Figure 5.16: (a) kinematic wave speed c_k as function of k^2 and (b) dynamic wave speed c_{d+} as function of $\tilde{Fr}^2$ for shear-thickening fluids ($n = 1.3$, $n = 1.55$ and $n = 2.4$).

and

$$\frac{n}{2n+1}h^{\frac{2n+1}{n}} - ch = q_0\,. \tag{5.76}$$

where we made use of $\phi_0 = n/(2n+1)$. The constant q_0 may be determined by demanding $h = 1$ to be solution to (5.76) which gives:

$$q_0 = \frac{n}{2n+1} - c\,. \tag{5.77}$$

In addition to the imposed solution $h = 1$, there is one more real positive solution to (5.76) with (5.77) and two fixed points $\mathbf{U_I} = (1, 0, 0)^t$ and $\mathbf{U_{II}} = (h_{\rm II}, 0, 0)^t$ are found. Their positions are displayed in Fig. 5.17(a) as functions of the wave speed c and power index n. As expected, the two fixed points coincide at $c = 1$ where the traveling-wave speed equals the speed of the kinematic waves in the zero-wavenumber limit. In the limit $n = 1$, we recover the expression $h_{\rm II} = -1/2 + \sqrt{3(c - 1/4)}$ corresponding to an inclined plane [103]. The position $h_{\rm II}$ of the second fixed point can be compared to the corresponding solution to (5.14), (5.37) and (5.48). For $h' = h'' = h''' = \bar{u}' = \bar{u}'' = 0$, (5.37) simplifies into $\bar{\eta}_c = s^n/h$ if $s^n/h < 1$, $\bar{\eta}_c = 1$ otherwise. We thus obtain

$$\begin{aligned} \phi(s^n/h)h^{\frac{2n+1}{n}} - ch &= q_0 \qquad \text{if} \qquad s^n/h < 1\,, \\ r\frac{h^3}{3} - ch &= q_0 \qquad \text{otherwise} \end{aligned} \tag{5.78}$$

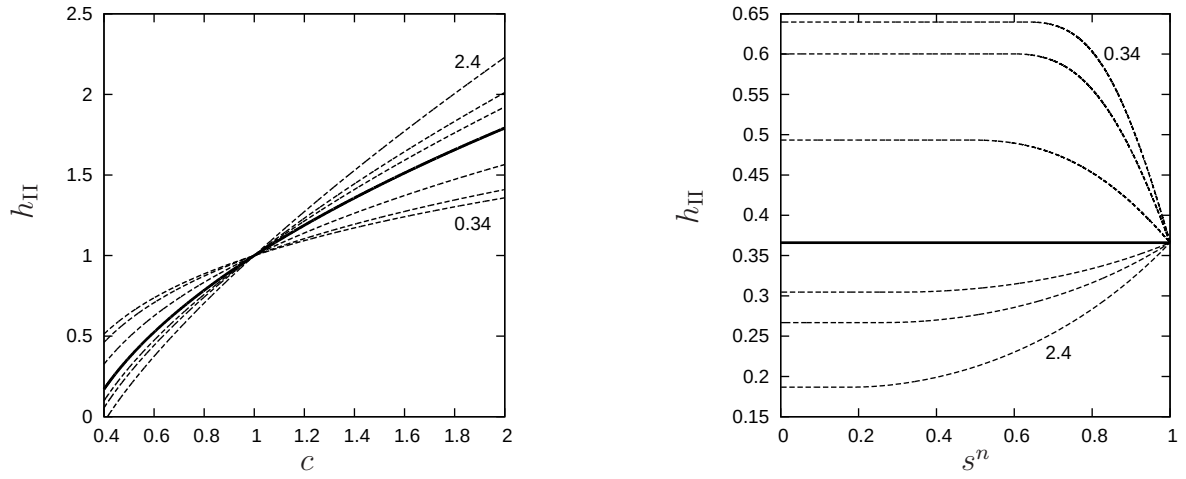

(a) $s^n \to 0$ (b) $c = 0.5$

Figure 5.17: Position of the second fixed point $\mathbf{U_{II}}$. (a) $h_{\rm II}$ as function of the wave speed c in the limit $s^n \to 0$. (b) as function of s^n for $c = 0.5$. The solid line refers to the Newtonian case $n = 1$. Dashed lines correspond to $n = 0.34$, 0.4, 0.607, 1.3, 1.55 and 2.4. The labels stand for the extreme values taken for n.

where q_0 is determined by demanding that $h = 1$ is solution. The solutions to (5.78) for $c = 0.5$ are displayed in Fig. 5.17(b). The location $h_{\rm II}$ of the second fixed point varies weakly for $s^n < 0.3$. A similar trend is found for other values of the the phase speed c. This observation again supports the idea that the assumption of a negligible Newtonian layer ($s^n \to 0$), necessary to derive (5.55) and (5.60), can be extended up to $s^n \approx 0.3$.

5.6.2 Bifurcation diagrams

As an alternative to the request that $h = 1$ is solution, the flow rate q_0 in the moving frame can be adjusted by demanding that the average thickness $\langle h \rangle = \lambda^{-1} \int_0^\lambda h \, d\xi$ or the average flow rate $\langle q \rangle$ remain constant. Here $\lambda = 2\pi/k$ refers to the wavelength. The constraint $\langle h \rangle = 1$ is related to time-dependent computations with spatial periodic conditions for which the mass of simulated liquid in the computational domain remains constant as time is passing by. The fluid leaving the numerical domain being re-injected at inlet, the flow is closed and the constraint $\langle h \rangle = 1$ is referred to as the closed-flow condition. Conversely, the constraint $\langle q \rangle = \phi_0$, corresponds to the experimental response to a time periodic forcing at inlet. Indeed, integration in time of the mass balance (5.14) gives $\partial_x \langle q \rangle = 0$ such that the time average flow rate remains equal to its value at inlet. The constraint $\langle q \rangle = \phi_0$ will be referred to as the open-flow condition [122].

Considering first shear-thinning fluids, we have reported in Fig. 5.18 the bifurcation diagrams in the plane wavenumber versus speed of the traveling wave branches of solutions to (5.14), (5.55) for the fluid properties of the three xanthan gum aqueous solutions reported in table 5.1, a moderate inclination angle $\beta = 15^\circ$ and $Re = 20$. The closed-flow integral constraint $\langle h \rangle = 1$ has been enforced.

For the most dilute solution (panel a), a first branch of slow-wave solutions arises from the marginal stability condition $k = k_c$ through a Hopf bifurcation. Several secondary branches are found through period doubling of this first branch. One bifurcates at $k \approx 0.55k_c$ and terminates into fast waves. Following [20], we denote by γ_1 the principal branch of slow waves and by γ_2 the secondary branch of fast waves. The other secondary waves bifurcating from the principal γ_1 branch are slow.

Traveling waves correspond to limit cycles in the phase space that terminate into homoclinic trajectories connecting h_1 to itself as their lengths are augmented. These trajectories correspond to small-wavenumber solitary-like wavetrains. Fig. 5.19 presents the shapes of slow γ_1 and fast γ_2 waves at low wave numbers. The γ_1 waves are made of a trough followed by capillary ripples (panel a) whereas γ_2 are one-humped waves preceded by capillary ripples (panel b). The wrinkling of the solution branches in the k-versus-c diagram in Fig. 5.18(a) and the onset of numerous secondary branches are consequences of the interaction between the typical length of the capillary ripples preceding or following the waves and the wavelength. For the more condensed xanthan gum solutions in water (parameter sets 2 and 3), we observed a much simpler bifurcation diagram (see Fig. 5.18(b)). A unique branch of traveling-wave solutions bifurcate from the Nusselt solutions through a Hopf bifurcation. Secondary bifurcations through period doubling were not found. The shapes of γ_2 solitary-like waves are displayed in Fig. 5.20. The number and amplitude of the capillary ripples preceding the main hump of the waves are considerably reduced because of the efficient damping of short waves by viscosity. This efficient damping of capillary waves is responsible for the drastic simplification of the bifurcation diagram in Fig. 5.18(b) when compared with Fig. 5.18(a). For each bifurcation diagram displayed in Fig. 5.18, traveling-wave solutions are found at k larger than the cut-off wavenumber k_c which corresponds to a stable Nusselt uniform film flow. Traveling waves therefore bifurcate subcriticaly from the Nusselt solution. The range of subcritical wave numbers $[k_{\rm sub}, k_c]$ for which traveling waves coexist with a stable Nusselt solution tend to increase as the power-law index n is lowered. The onset of subcriticality is here related to the large viscosity ratio r between the wall and the free surface. Linear waves are efficiently damped by the free surface viscosity and the cut-off wavenumber is determined by this effect (see Fig. 5.14 and its discussion in § 5.5.3). Finite-amplitude disturbances may survive to viscous damping by removing the Newtonian layer and thus significantly lower the viscosity at the free surface.

Turning to shear-thickening fluids ($n > 1$), Fig. 5.21 presents the bifurcation diagrams obtained with model (5.14), (5.60) for the cornstarch solutions whose properties are listed in table 5.2. The closed-flow constraint $\langle h \rangle = 1$ is again enforced. For each set of fluid

γ_1

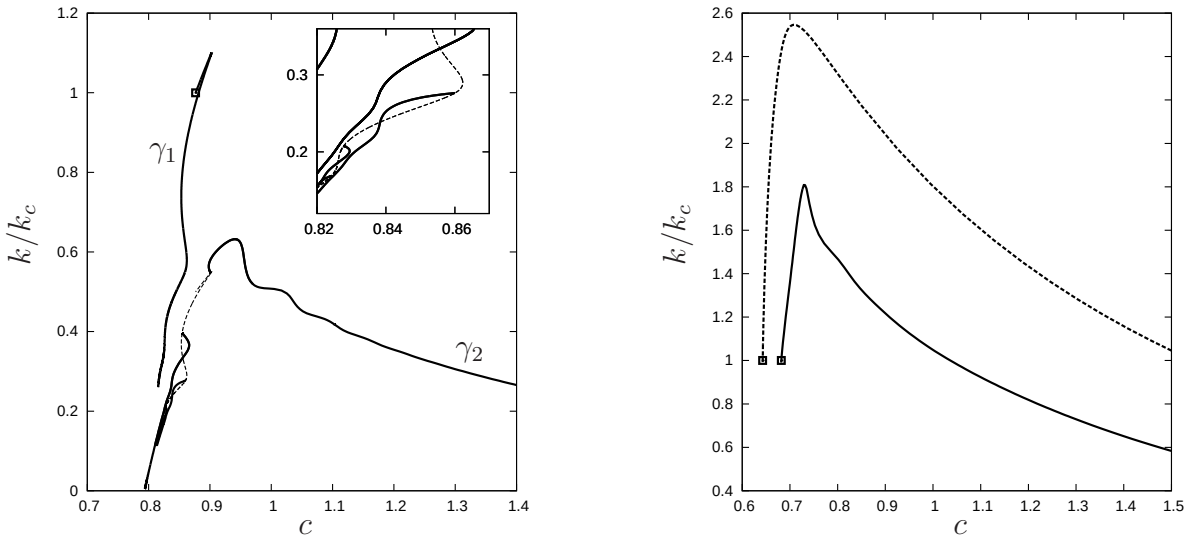

Figure 5.18: Speed c of traveling-wave solutions as a function of the wavenumber k/k_c normalized by the cut-off wavenumber k_c. Hopf bifurcation at k equal to the cut-off wavenumber k_c is indicated by squares. Filled squares refer to period-doubling bifurcations. Dotted (dashed-dotted) lines refer to the locus of solutions made of two or four γ_1 waves. $Re = 20$, $\beta = 15°$. (a) 500 ppm shear-thinning xanthan solution in water (set 1 in table 5.1); (b) solid and dashed lines refer to 1500 ppm and to 2500 ppm xanthan solutions: set 2 and 3 in table 5.1.

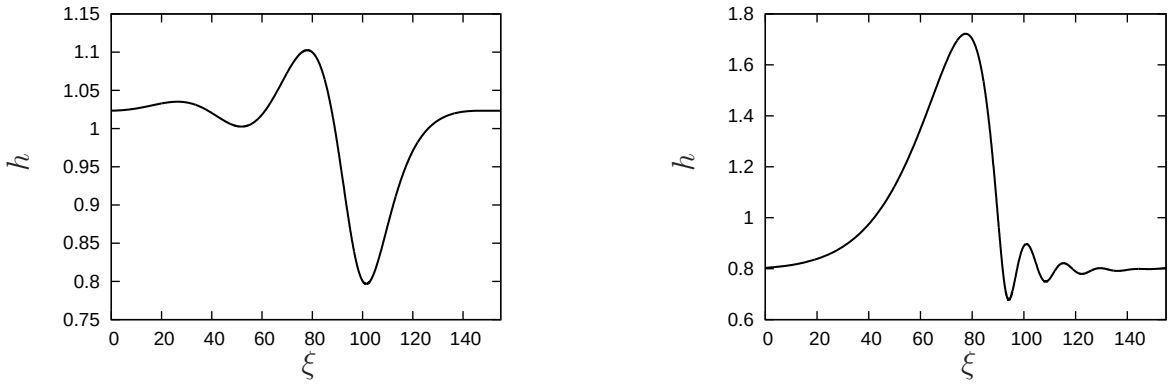

(a) γ_1 wave, $c = 0.819016$ (b) γ_2 wave, $c = 1.31315$

Figure 5.19: Traveling wave profiles. 500 ppm shear thinning xanthan gum solution (set 1 in table 5.1), $R = 20$, $\beta = 15°$, $k = k_c/3$ ($n = 0.607$).

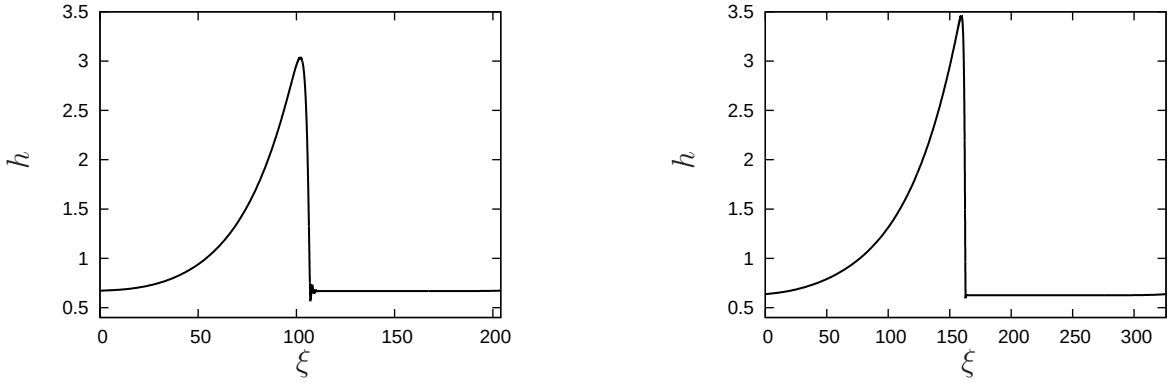

(a) Set 2 ($n = 0.40$, $r = 97$), $c = 2.59392$ (b) Set 3 ($n = 0.34$, $r = 200$), $c = 3.58155$

Figure 5.20: γ_2 wave profiles. Shear-thinning xanthan-gum solutions (see table 5.1), $R = 20$, $\beta = 15°$ and $k = k_c/5$.

properties, the Kapitza number Γ is small and capillary waves are effectively damped by viscous effects so that (i) no capillary ripples are observable at the front of the nearly solitary waves at small wavenumber and (ii) no secondary branches have been found to emerge from the principal one through period-doubling bifurcations. Contrary to shear-thinning fluids, traveling wave solutions are found only when the Nusselt base flow solution is unstable and the Hopf bifurcation corresponds to a supercritical situation.

5.6.3 Comparisons to direct numerical simulations

Direct numerical simulations (DNSs) of the primitive set of equations (5.7) have been performed implementing periodic boundary conditions. Initial conditions correspond to the Nusselt flat-film solution to which a small disturbance has been added. At the final stage of the computation, nonlinear saturated traveling waves are observed that can be compared with the traveling-wave solutions to the models (5.14), (5.55) and (5.14), (5.60) with the closed-flow condition $\langle h \rangle = 1$.

Gerris software developed by [99, 100] enables to implement the Ostwald-de Waele power-law with a Newtonian plateau (5.31) and has been used extensively for this purpose [1]. Gerris uses a multilevel Poisson solver, an approximate projection method and a second-order accurate upwind scheme to discretized advection terms. Variable spatial resolution is enabled by a quadtree adaptive refinement method. Interfacial flow phenomena are captured by means of a generalized Volume of Fluid scheme which allows mesh refinement along the interface. Gerris software and the numerical procedure that we have followed are detailed in § 5.7

Refinement of the mesh to the deepest available level is imposed at the free surface in order to accurately capture the instability of the film. A typical mesh grid is presented in Fig. 5.22. Gerris automatically adapts the mesh in order to capture velocity variations as is observable at the liquid-solid interface. Considering first shear-thickening cornstarch solutions (cf. table 5.2), the free surface elevations corresponding to the final time of my DNSs are displayed in Fig. 5.23. A striking agreement is obtained with the results to the weighted-residual model (5.14), (5.60). The amplitude and speed of the waves are also faithfully captured (see table 5.3). However, for the largest tested numerical domains, either my DNSs do not lead to permanent waves or wave breaking phenomena are observed.

Fig. 5.23(c) shows the wave profile corresponding to the final stage of my simulation for the most concentrated cornstarch solution (set 6). Although a large amplitude front propagates with a nearly constant speed and shape, small disturbances are continuously generated and superposed to it. Whether these disturbances are physically relevant or result from the numerical scheme and the VOF method is a difficult question considering the large viscosity ratio at the gas-liquid interface. The weighted-residual model (5.14),

[1] Gerris is a GPL licensed program that freely downloadable from `http://gfs.sourceforge.net`

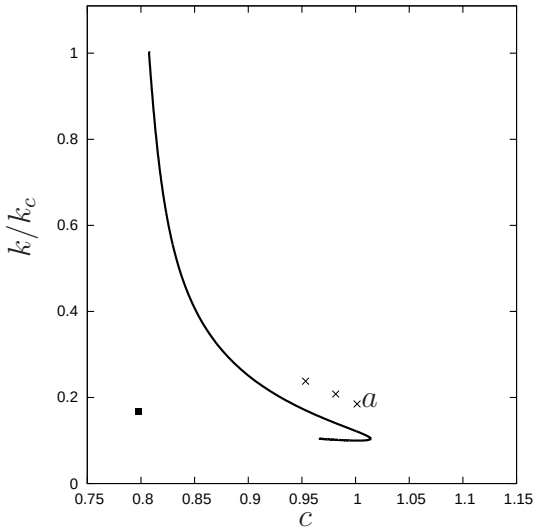

(a) Set 4, $n = 1.3$

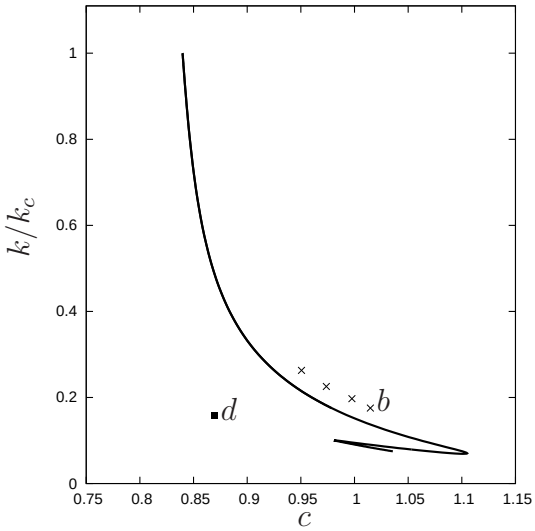

(b) Set 5, $n = 1.55$

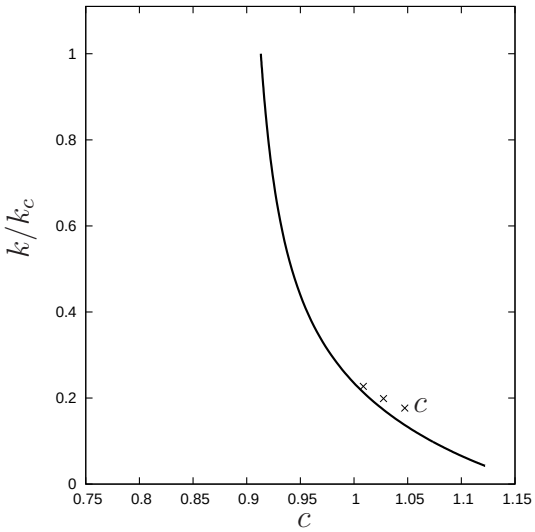

(c) Set 6, $n = 2.4$

Figure 5.21: Speed c of traveling-wave solutions as a function of the wavenumber k. Solid line refers to model (5.14), (5.60), crosses and square refers the phase speed of the wave before and after breaking respectively of DNS result from Gerris software. $Re = 30$, $\beta = 15°$. The fluid properties of the shear-thickening cornstarch solutions are given in table 5.2. Labels a, b, c and d refer to the wave profiles displayed in Fig. 5.23.

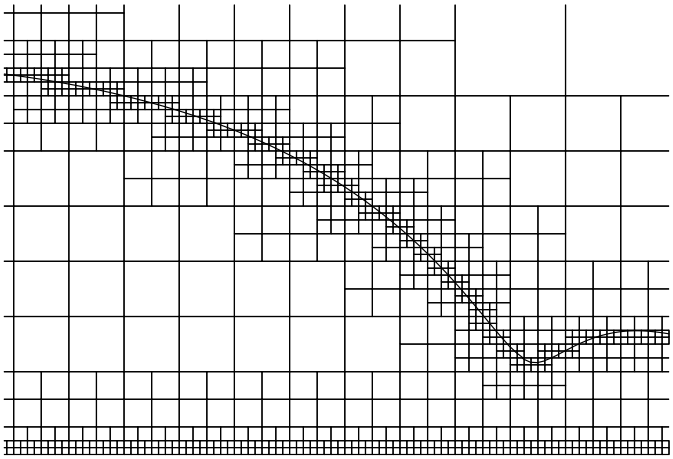

Figure 5.22: detail of the mesh grid at the end of one Gerris run showing the dynamic refinement at the interface. The number of cells in the total grid is 15971. $Re = 100$, $\beta = 15°$, $\lambda = 80$, fluid properties correspond to shear-thinning 1500 ppm xanthan gum solution (Set 2 in table 5.1). The entire wave profile is displayed in Fig. 5.24(d)

(5.60) does not capture well the amplitude of the nearly permanent traveling-wave. Yet, the speed of the traveling-wave solutions to the model are in remarkable agreement with the nearly constant speed of the front in the DNSs as can be observed in Fig. 5.21(c).

For the less concentrated cornstarch solutions (sets 4 and 5), wave breaking have been observed for the largest tested domains. A snapshot of the free surface elevation just before the wave breaks is presented in Fig. 5.23(d) and compared with the traveling wave solution to the weighted-residual model with the same periodicity. If the wave breaking phenomenon cannot be reproduced by the model, it is however clear that the wave shape and amplitude predicted by the model are in excellent agreement with the DNSs. The speeds of the fronts, computed immediately before the breaking of the waves take place, are indicated by filled squares in Figs. 5.21(a) and 5.21(b). Curiously, the onset of the wave breaking phenomenon is accompanied by a reduction of the wave speed, a trend that is reproduced by the traveling wave solutions to the weighted-residual model as the wavenumber k is lowered. Turning to shear-thinning xanthan gum solutions in water (cf. table 5.1) the profiles of the traveling waves obtained at the end of the DNSs are presented in Fig. 5.24. The waves systematically present capillary ripples preceding the main hump in spite of the very large ratio r of the free surface to wall effective viscosities. Their shapes are similar to the solitary waves observed experimentally for Newtonian fluids [70, 25]. If the amplitude of the waves are comparable for the three tested sets of fluid properties, the phase speed tends to be larger for the most concentrated xanthan solution (set 3) corresponding to the lowest value of the power-law index ($n = 0.34$). This

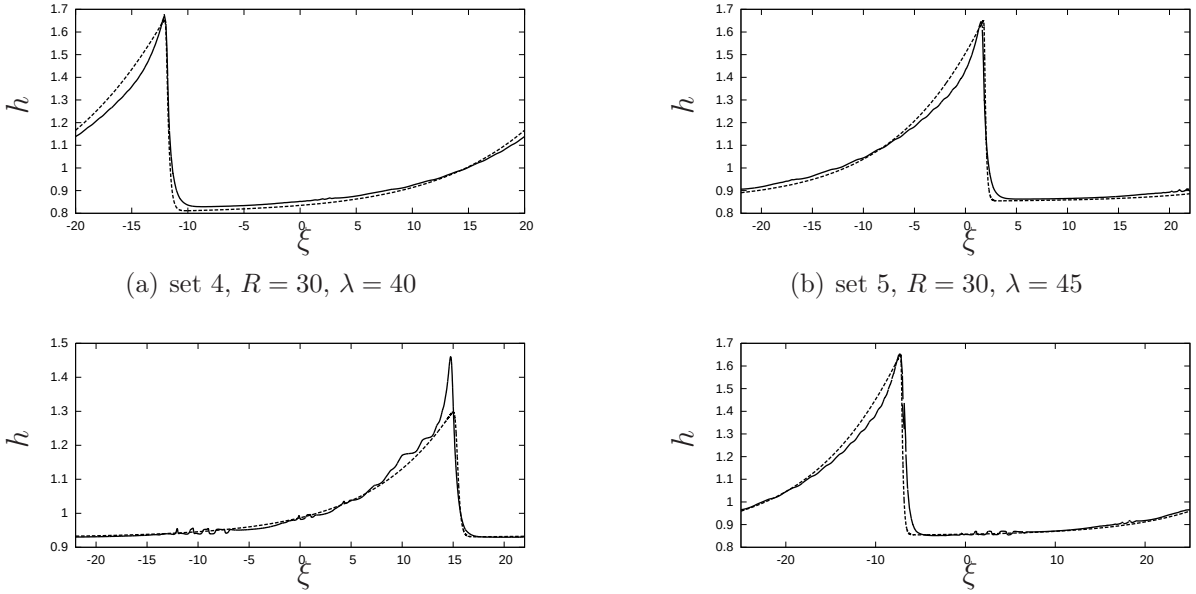

(a) set 4, $R = 30$, $\lambda = 40$

(b) set 5, $R = 30$, $\lambda = 45$

(c) set 6, $R = 30$, $\lambda = 45$

(d) set 5, $R = 30$, $\lambda = 50$

Figure 5.23: Traveling wave profiles for the shear-thickening fluids ($n > 1$) whose properties are listed in table 5.2. Solid lines refer to the DNS results from Gerris software, whereas dashed lines refer to the solutions to model (5.14), (5.60).

Fluid	Re	λ	c		h_m	
			Gerris	model	Gerris	model
Set 4	30	40	0.98	0.92	1.68	1.65
Set 5	30	45	1.01	1.00	1.65	1.65

Table 5.3: Phase speed c and maximum height h_m of traveling wave solutions with $\langle h \rangle = 1$. Fluid properties correspond to a shear-thickening cornstarch dispersion in ethylene glycol and to a 15° inclination angle (Table 5.2).

Fluid	Re	λ	c			h_m		
			DNS	DNS(CL)	model	DNS	DNS(CL)	model
Set 1	50	60	0.86	0.86	0.88	1.65	1.65	1.60
–	100	80	0.81	0.82	0.87	2.19	2.19	1.94
Set 2	50	60	0.92	0.92	1.03	2.07	2.07	1.96
–	100	80	0.76	0.76	0.96	2.20	2.20	2.22
Set 3	50	60	0.93	0.92	1.14	2.02	2.01	2.09
–	100	80	0.75	0.75	1.05	2.07	2.06	2.28

Table 5.4: Phase speed c and maximum height h_m of traveling wave solutions with $\langle h \rangle = 1$. Fluid properties correspond to shear-thinning dilute solutions of xanthan gum and to a 15° inclination angle (see table 5.1). 'DNS' and 'DNS(CL)' refer to the results from Gerris using the Newtonian-plateau constitutive equations (5.32) and (5.33) respectively.

can be understood from the relative positions of the fixed points displayed in Fig. 5.17(a). For $h_{\mathrm{II}} > h_{\mathrm{I}}$, which corresponds to the positive humps of the γ_2 waves, we note that an augmentation of the phase speed c is necessary to conserve a given distance $h_{\mathrm{II}} - h_{\mathrm{I}}$ between the fixed points when the power-law index n is lowered. The amplitude of the waves being related to the distance $h_{\mathrm{II}} - h_{\mathrm{I}}$, large amplitude γ_2 waves travel faster as n decreases.

Shapes, speeds and amplitudes are compared with the predictions of the weighted residual model (5.14), (5.55) in Fig. 5.24 and table 5.4. Good agreement is obtained for the shape and amplitude. However, the model tends to overestimate the speed of the waves. A drawback that is more pronounced for concentrated xanthan gum solution for which the power-law index is already rather low ($n = 0.34$). We note that the nonlinear dependence of the effective viscosity (5.57) on the gradients of q and h is necessary to reproduce the capillary waves observed in the DNSs. Solutions to the two-equation model (5.14), (5.50) with a constant effective free surface viscosity r do no present capillary ripples.

Fig. 5.25 presents the distribution of the strain rate under the solitary-like waves whose profiles are shown in Figs. 5.24(a) and 5.24(c). We limit ourself to consider the capillary region at the front of the main hump where the free surface is the steepest. Parameters correspond to the same Reynolds number, inclination and wavelength but different xanthan-gum solutions. The more dilute one, set 1 in table 5.1 with $n = 0.607$ is less shear-thinning that the other one, set 2 with $n = 0.4$. From the results of the DNSs, the local maxima of the strain rate are located either at the wall or at the free surface.

Global maxima of the strain rate, maxima along the wall and along the free surface are compared in table 5.5. For the most dilute xanthan gum solution (set 1 with $n = 0.607$), the shear rate is maximum at the wall at a location that is close to the maximum elevation

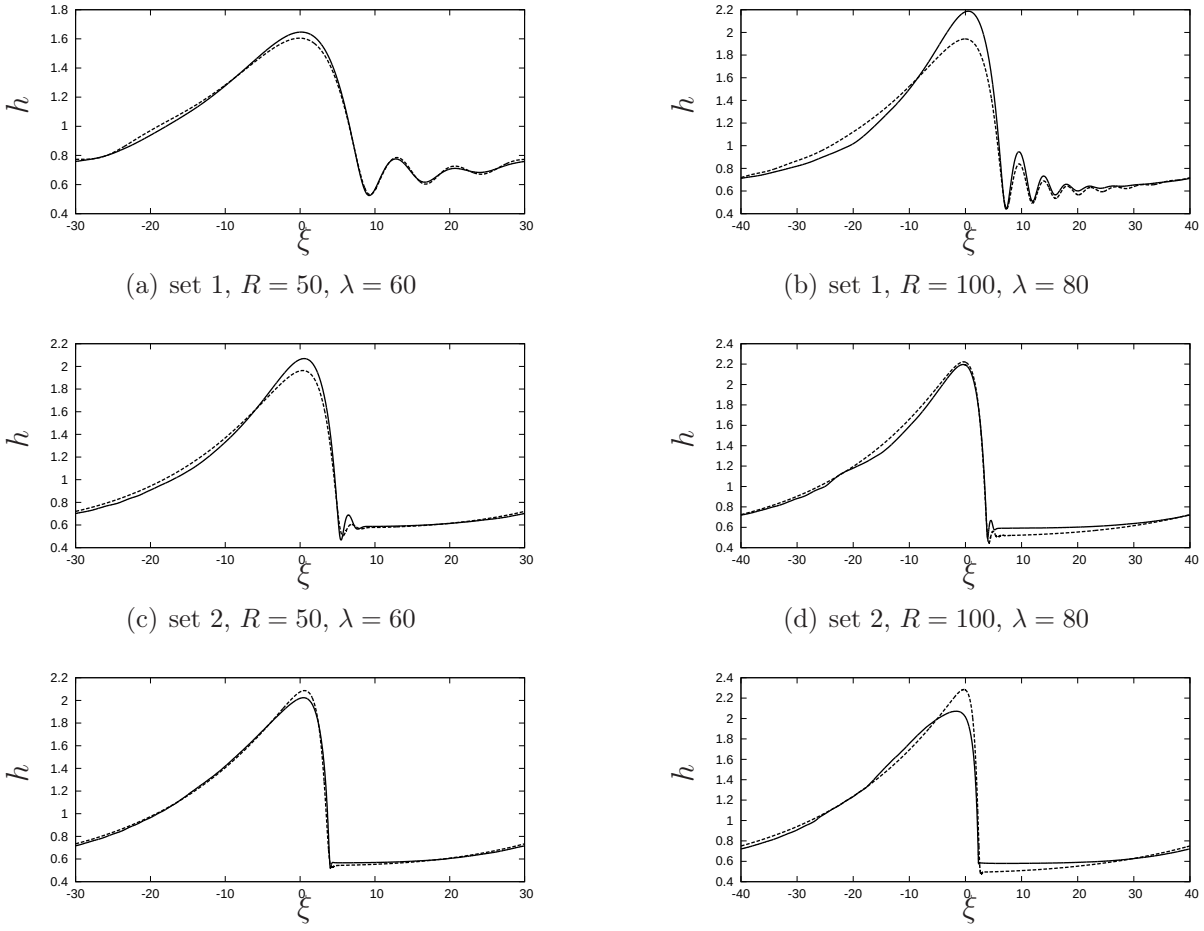

(a) set 1, $R = 50$, $\lambda = 60$

(b) set 1, $R = 100$, $\lambda = 80$

(c) set 2, $R = 50$, $\lambda = 60$

(d) set 2, $R = 100$, $\lambda = 80$

(e) set 3, $R = 50$, $\lambda = 60$

(f) set 3, $R = 100$, $\lambda = 80$

Figure 5.24: Travelling wave profiles for shear-thinning xanthan gum solutions in water (see table 5.1). Solid lines refer to the DNS results from Gerris software, whereas dashed lines refer to the solutions to model (5.14), (5.55).

	Set 1 ($n = 0.607$)				Set 2 ($n = 0.4$)			
	$\dot{\gamma}_{\max}$	$\max(\dot{\gamma}_{y=0})$	$\max(\dot{\gamma}_{y=h})$	$\Gamma_\star$	$\dot{\gamma}_{\max}$	$\max(\dot{\gamma}_{y=0})$	$\max(\dot{\gamma}_{y=h})$	$\Gamma_\star$
Gerris	1.6	1.6	0.8	470	4.5	1.8	4.5	380
Model	1.2	1.2	0.6		2.0	2.0	1.6	

Table 5.5: Maxima of the strain rate $\dot{\gamma}$, global, at the wall and at the free surface corresponding to Fig. 5.25. 'Gerris' refers to the final stage of DNSs performed with Gerris software, whereas 'Model' stands for the traveling solutions to (5.14), (5.55). $\beta = 15°$, $Re = 50$ and $\lambda = 60$. $\Gamma_\star$ is the Kapitza number corresponding to the viscosity minimum at the free surface, i.e. $\Gamma_\star = \Gamma_0(s/\max(\dot{\gamma}_{y=h}))^{4(n-1)/3}$.

of the free surface as suggested by the leading order term of the gradient expansion $\dot{\gamma} = |\partial_y u_s| + O(\epsilon)$ whose maximum $|q/(\phi_0 h^2)| = h^{1/n} + O(\epsilon)$ is reached at the wall under the crest of the wave. Instead, for the less dilute solution (set 2 with $n = 0.4$), the global maximum of the strain rate is reached at the free surface at a point where the gradient of the thickness is the largest, which suggests that the long-wave approximation is not well verified at the front of the wave. Indeed, the front of the wave quite steep and the assumption $\partial_x h \ll 1$ does not hold there. In that region, viscous diffusion and surface tension effects can be compared by computing the Kapitza number based on the minimum of viscosity at the free surface, i.e. $\Gamma_\star = \Gamma_0(s/\max(\dot{\gamma}_{y=h}))^{4(n-1)/3}$. In each case, $\Gamma_\star$ is found to be large which implies that the breaking of the wave is arrested by surface tension and shows that the observed ripples have indeed a capillary origin.

Fig. 5.25 and table 5.5 have been completed with the corresponding results from the weighted-residual model (5.14), (5.55). The strain rate distribution has been computed from the self-similar velocity profile (5.21). In both cases, the model slightly underestimates the amplitude of the capillary ripples and predicts smaller values of the maxima of the strain rate. However, the locations of the local minima and maxima predicted with the model are in remarkable agreement with the strain rate distributions found by DNS. For the 500 ppm solution (set 1, $n = 0.607$), a convincing agreement is obtained, whereas for the more concentrated 1500 ppm solution (set 2, $n = 0.4$) the model fails to locate at the free surface the maximum of the strain rate. We note that in the latter situation the long-wave approximation starts to be violated.

5.7 DNS with Gerris

In this section, we give detail on the numerical procedure we have followed to produce DNSs. These details have been found in Gerris documentation. Interested reader can find further information in [99] and [100]. To solve the powerlaw problem numerically,

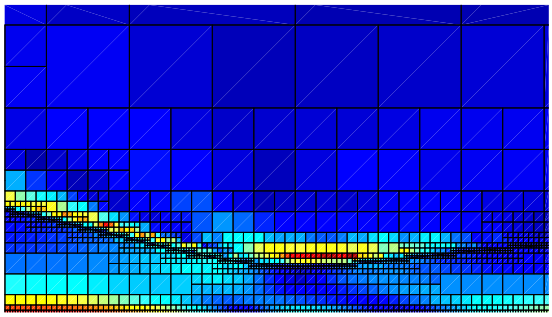

(a) DNS

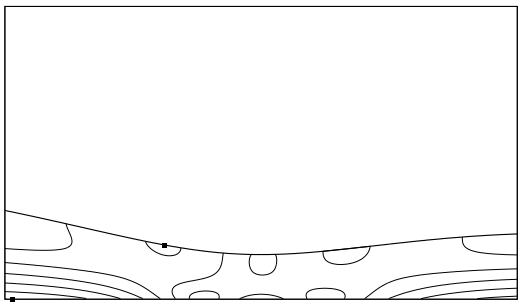

(b) model (5.14), (5.55)

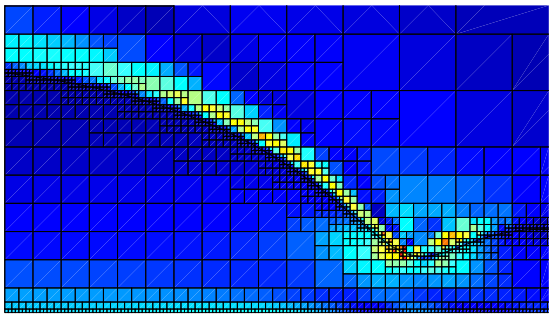

(c) DNS

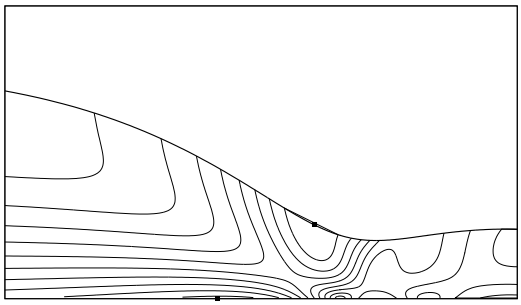

(d) model (5.14), (5.55)

Figure 5.25: Distribution of the strain rate $\dot{\gamma}$ under the waves whose profiles are shown in Figs. 5.24(a) and 5.24(c). Left: results from DNS. Dark blue (red) regions correspond to the minimum (maximum) of $\dot{\gamma}$. Right: isocontours of the strain rate corresponding to the weighted-residual model (5.14), (5.55). The location of the maxima of $\dot{\gamma}$ at the wall and at the free surface are depicted by squares.

the computer code Gerris, free software under the GNU General Public License 1.2, uses a type 'finite volumes' to solve a system of Navier-Stokes or Euler for incompressible fluids, with an adaptive mesh of the computational domain, and an approach such as 'Volume of Fluid' to represent the interface between two fluids. In computational fluid dynamics, the volume of fluid method (VOF method) is a numerical technique for tracking and locating the free surface (or fluid-fluid interface). It belongs to the class of Eulerian methods which are characterized by a mesh that is either stationary or is moving in a certain prescribed manner to accommodate the evolving shape of the interface. As such, VOF is an advection scheme, a numerical recipe that allows the programmer to track the shape and position of the interface, but it is not a standalone flow solving algorithm. The Navier-Stokes equations describing the motion of the flow have to be solved separately. The Volume of Fluid method is based on earlier Marker-and-Cell (MAC) methods. First accounts of what is now known as VOF have been given by Noh and Woodward [87], where fraction function C (see in § 5.7.1) appeared, although first publication was by Hirt and Nichols [49]. Since, VOF method surpassed MAC by lowering computer storage requirements, it quickly became popular. First implementations of VOF suffered from imperfect interface description, which was later remedied by introducing a Piecewise-Linear Interface Calculation (PLIC) scheme. Using VOF with PLIC is a contemporary standard, used in number of computer codes e.g. Gerris Flow Solver (http://gfs.sourceforge.net), including commercial ones as ANSYS Fluent.

5.7.1 Method of monitoring interface

The numerical method can be stored in the class of methods for monitoring of interfaces called Eulerian, i.e., using a fixed mesh on which the interface moves freely(see Fig. 5.26). In fact, a cell calculation can be crossed by the interface and consequently occupied the two fluids. The characterization of interfaces leads to a breakdown of eulerian methods, Gerris ranks in the methods known as tracking volume, and more particularly, 'Volume of Fluid' (VOF) methods. In this type of method, one of the two fluids is marked with a volume fraction C a calculation cell:

$$\frac{\partial C}{\partial t} + \nabla \cdot (C\mathbf{v}) = 0 \tag{5.79}$$

where $\mathbf{v}$ is the velocity of the fluid (see Fig. 5.26, 2D representation). The method is based on the idea of so-called fraction function C. It is defined as the integral of fluid's characteristic function in the control volume (namely, volume of a computational grid cell). Basically, when the cell is empty, with no traced fluid inside, the value of C is zero; when the cell is full, $C = 1$; and when the interface cuts the cell, then $0 < C < 1$. C is a continuous function, its value jumps from 0 to 1 when the argument moves into interior of traced phase. Gerris belongs to a sub-classification of these methods VOF, those that provide a reconstruction interface, i.e., a location of this interface, mesh by mesh, to from

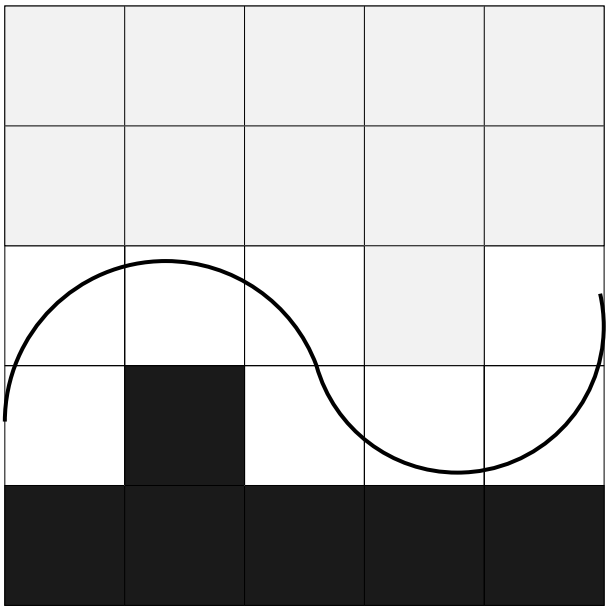

Figure 5.26: Example of an interface on a fixed mesh. The white region shows the interface separating two fluids like liquid(fluid 1, represents the dark region) and gas(fluid 2, represents the gray region). The cell contains liquid, then volume fraction $C = 1$, otherwise $C = 0$ and the interface included the cells, there $0 < C < 1$.

the value of C and the vector normal to the interface ∇C while ensuring the conservation the mass of each fluid. It is noted that these methods require VOF, in order to prevents oscillations related to sudden change from C to cross the interface (eddy currents). In the case of incompressible fluid flow and Newtonian (viscous or not), the system under consideration is a closed system of three equations (one equation for conservation of mass and two equations of conservation of momentum) with three unknowns ($u(x, y, t)$, $v(x, y, t)$ and $p(x, y, t)$) for a two-dimensional problem. The interface tracking method involves $C(x, t)$. The change in C is directly related to the displacement of the interface. The numerical solution of equations of the model of the Navier-Stokes implies a discretization in time and space. Gerris used 'Finite Volume' method for this type of calculation. Here, second order of the time discretization scheme is used. As an example, for such a scheme, the approximate value of the time derivative a variable ϕ can be written, to from a Taylor expansion to first order:

$$\begin{aligned}\phi(x, t + \Delta t) &= \phi(x, t) + \Delta t\frac{\partial \phi}{\partial t} + \frac{1}{2}\Delta t^2\frac{\partial^2 \phi}{\partial t^2} + O(\Delta t^3)\\ \phi(x, t - \Delta t) &= \phi(x, t) - \Delta t\frac{\partial \phi}{\partial t} + \frac{1}{2}\Delta t^2\frac{\partial^2 \phi}{\partial t^2} + O(\Delta t^3)\end{aligned}$$

From difference of the two equations, one can obtain:

$$\frac{\partial \phi}{\partial t} = \frac{\phi(x, t + \Delta t) - \phi(x, t - \Delta t)}{2\Delta t} + O(\Delta t^2)$$

Numerically, an iteration Δt characterizes time t^n to time t^{n+1}. Hence, it can be written as $\Delta t = t^{n+1} - t^n$ and $\left(\frac{\partial \phi}{\partial t}\right)^n = \frac{\phi^{n+1} - \phi^{n-1}}{2\Delta t}$.
Gerris uses a condition of dynamic stability, denoted CFL(Courant-Friedrich-Levy) to adjust the time step in the velocity of the fluid, given that Δx is set at the beginning of resolution. This condition comes from the stability study of advection equation: $CFL = \mid c \mid \frac{\Delta t}{\Delta x}$. By imposing $CFL \leqslant \frac{1}{2}$, it limits the time step as follows:

$$\mid c \mid \frac{\Delta t}{\Delta x} \leqslant \frac{1}{2} \qquad \Leftrightarrow \quad \Delta t \leqslant \frac{\Delta x}{2 \mid c \mid}$$

For example, if $min \mid c \mid \geqslant 1$ where c is the speed of the physical phenomenon (thus $max\frac{1}{|c|} \leqslant 1$), then $\Delta t \leqslant \frac{\Delta x}{2}$. As for time, Gerris uses a discretization scheme for space of order 2, i.e.,

$$\frac{\partial \phi}{\partial x} = \frac{\phi(x + \Delta x, t) - \phi(x - \Delta x, t)}{2\Delta x} + O(\Delta x^2)$$

Numerically, Δx characterizes an iteration space of the abscissa x_j to x_{j+1}. Hence, it can be written as $\Delta x = x_{j+1} - x_j$ and $\left(\frac{\partial \phi}{\partial x}\right)_j = \frac{\phi_{j+1} - \phi_{j-1}}{2\Delta x}$.
In the same way, an approximate value of the second derivative of ϕ obtained with a

Taylor expansion to second order:

$$\begin{aligned}\phi(x+\Delta x,t) &= \phi(x,t)+\Delta x\frac{\partial\phi}{\partial x}+\frac{(\Delta x)^2}{2}\frac{\partial^2\phi}{\partial x^2}+\frac{(\Delta x)^3}{8}\frac{\partial^3\phi}{\partial x^3}+O((\Delta x)^4)\\ \phi(x-\Delta x,t) &= \phi(x,t)-\Delta x\frac{\partial\phi}{\partial x}+\frac{(\Delta x)^2}{2}\frac{\partial^2\phi}{\partial x^2}-\frac{(\Delta x)^3}{8}\frac{\partial^3\phi}{\partial x^3}+O((\Delta x)^4)\end{aligned}$$

Summing these above two equations, one obtains:

$$\frac{\partial^2\phi}{\partial x^2}=\frac{\phi(x+\Delta x,t)-2\phi(x,t)+\phi(x-\Delta x,t)}{(\Delta x)^2}+O((\Delta x)^2)$$

which gives: $\left(\frac{\partial^2\phi}{\partial x^2}\right)_j=\frac{\phi_{j+1}-2\phi_j+\phi_{j-1}}{(\Delta x)^2}$.
Now, it is important to present the steps of calculating the velocity and pressure. In solving the Navier-Stokes system, there is no explicit equation for calculating the pressure. The difficulty lies in determining the pressure, while respecting the incompressibility condition expressed by the equation of conservation of mass.
The conservation equation of motion in vector form is:

$$\partial_t\mathbf{v}+\mathbf{v}\cdot\nabla\mathbf{v}=-\frac{1}{\rho}\nabla p+\nu\Delta^2\mathbf{v}+\mathbf{g}$$

Consider a finite difference scheme of order 1 and then it comes:

$$\frac{\mathbf{v}_{n+1}-\mathbf{v}_n}{\Delta t}+\frac{1}{\rho}(\nabla p)_n=-(\mathbf{v}\cdot\nabla\mathbf{v})_n+\nu(\Delta^2\mathbf{v})_n+\mathbf{g}$$

One has to solve in a first approximation $\mathbf{v}_*$ such that:

$$\frac{\mathbf{v}_*-\mathbf{v}_n}{\Delta t}=-(\mathbf{v}\cdot\nabla\mathbf{v})_n+\nu(\Delta^2\mathbf{v})_n+\mathbf{g} \tag{5.80}$$

$$\text{with}\quad \frac{\mathbf{v}_{n+1}}{\Delta t}+\frac{1}{\rho}(\nabla p)_n=\frac{\mathbf{v}_*}{\Delta t} \tag{5.81}$$

By adopting at $t=0$, an initial velocity profile $\mathbf{v}_0$ as $\nabla\cdot\mathbf{v}_0=0$, one can calculate $\mathbf{v}_*$ for all t. But, it is necessary to calculate the pressure before $\mathbf{v}_{n+1}$ can be found. Knowing that $\nabla\cdot\mathbf{v}_{n+1}=0$, equation 5.81 can be written as:

$$\frac{1}{\rho}(\nabla^2 p)_n=\frac{\nabla\cdot\mathbf{v}_*}{\Delta t}$$

This equation is a Poisson equation which provides the pressure, in accordance with the normal component of boundary conditions. By solving this equation, one can solve the equation (5.81) while respecting the kinematic condition. The computational domain is discretized into a finite number of cells (or control volumes), associated with each point

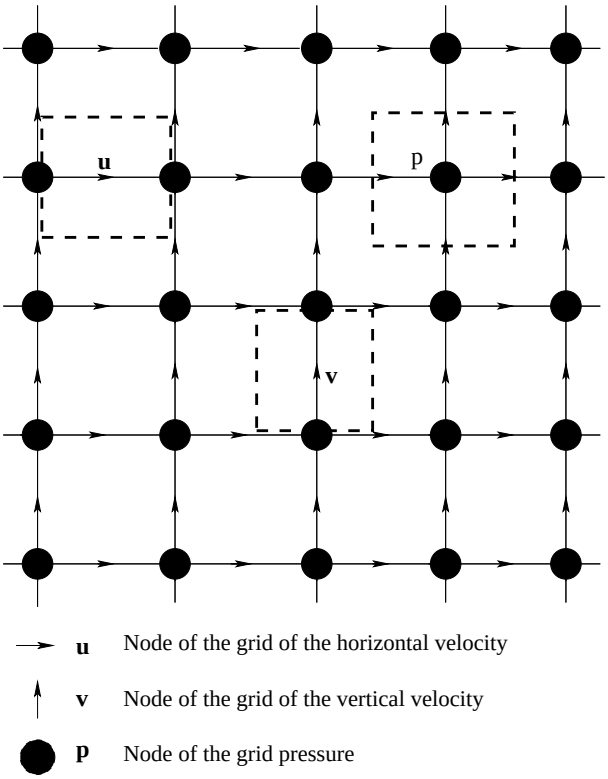

Figure 5.27: Schematic diagram of staggered grid.

of the mesh. The equations are integrated on each of the volumes control, focusing on the points of the mesh. The velocity components are calculated on the side mesh, while the scalar (pressure, volume fraction) are the nodes of the mesh. For this, the computational domain is discretized on two types of grids, one for pressure, the other for the velocity components (see Fig. 5.27). The two types of grids are shifted. Scalar variables (pressure, volume fraction) are calculated on the main grid, called grid pressure. From this grid, a grid is constructed to shifted in each direction in space for the grid velocity. The structure of the staggered mesh facilitates the calculation of the pressure gradient and divergence of velocity. This avoids some pressure oscillations observed for non-staggered grids. In Gerris, it is possible to impose a condition of Dirichlet or Neuman at the edges of the computational domain. Inserting a solid (regardless of its geometry) within the area by default Gerris imposes a Dirichlet condition.

5.7.2 Adaptive mesh refinement

In Gerris, the strategy of meshing is to divide the computational domain into a number of meshes defined at the initialization step, on the basis of the finite volume method. However, this subdivision is not homogeneous, Fig. 5.28 gives an example in two space dimensions, this type of division called 'quadtree division' where the original domain is divided into four sub-areas, subdomain in the lower left is itself divided into four sub-domain and so on. The user has the option initially to refine the area differently according to the regions of interest. Gerris simulation is not yet well resolved therefore it could be always change the `GfsRefine6` line to something bigger but it would not make really good use of the quadtree approach implemented in Gerris (see Appendix A.5). A code using a simple regular Cartesian grid approach would be faster and would produce the same results. Instead one can use *dynamic adaptive mesh refinement*, where the quadtree structure of the discretization is used to adaptively follow the small structures of the flow, thus concentrating the computational effort on the area where it is most needed.

The simplest possible way to refine the initial root cell is to use the syntax `Refine 6`. This means to tell the program that we want to keep refining the cell tree (by dividing each cell in four children cells (in 2D, eight in 3D)) until the level of the cell is equal to five. The level of the root cell is zero, the level of all its children cells is one and so on recursively. After this refinement process completes a regular Cartesian grid is created with $2^6 = 64$ cells in each dimension on the finest level (6).

This is done using yet another object class: `Adapt`. Various criteria can be used to determine where refinement is needed. In practice, each criterion will be defined through a different object derived from `Adapt`. If several `Adapt` objects are specified in the same simulation file, refinement will occur whenever at least one of the criteria is verified. For example, a simple criterion is used which is based on the local value of the vorticity. A

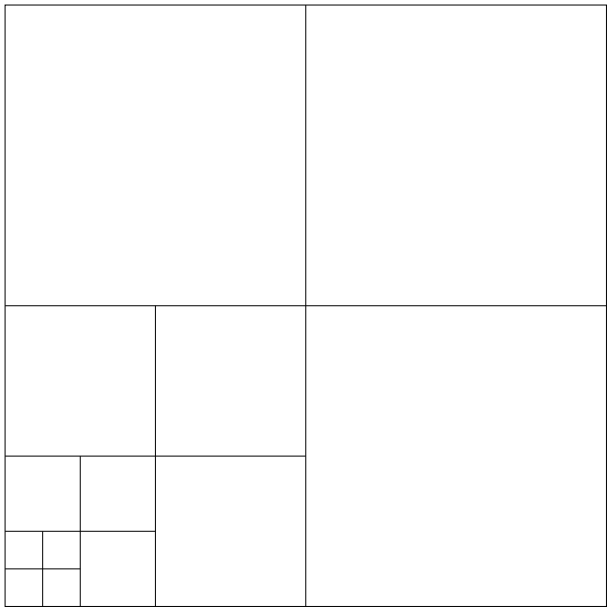

Figure 5.28: Type of adaptive mesh 'quadtree'.

cell will be refined whenever

$$\frac{|\nabla \times v|\Delta x}{max|v|} > s\,,$$

where Δx is the size of the cell and s is a user-defined threshold which can be interpreted as the maximum angular deviation (caused by the local vorticity) of a particle traveling at speed $max|v|$ across the cell. This criterion is implemented by the `AdaptVorticity` object. The syntax for an `AdaptVorticity` which is defined as the norm of the local vorticity vector multiplied by the cell size and divided by the maximum of the velocity norm over the whole domain, is written in the simulation file as

```
AdaptVorticity { istep = 1 } { maxlevel = LEVEL cmax = 1 }
```

This means we want to refine dynamically the mesh through the `AdaptVorticity` object applied every time step `{istep=1}` . The threshold s (`cmax` :The maximum cell cost allowed. If the number of cells is smaller than the maximum allowed and the cost of a cell is larger than this value, the cell will be refined) is set to 1 and `maxlevel` (The maximum number of refinement levels) which is set to 11 in the given simulation program in A.5.

This method is more adaptive dynamically, indeed, the tool can adapt the mesh during the execution of code, when a condition defined by the user is satisfied. In this strategy of cutting, we are discussing about 'deep level' mesh, which is the finest cut of the computational domain. For a level m for example, the computational domain is divided into

$2^m \times 2^m$ theoretically cells, 2^m intervals and $2^m + 1$ abscissa. A computational domain of length L, we get $\Delta x = \frac{L}{2^m}$ and any abscissa can be written $x_i = i\Delta x$.

It is noted that a computational domain of length L in Gerris is a square whose abscissa and ordinates are in the range $\left[-\frac{L}{2}, +\frac{L}{2}\right]$. The mesh used the term adaptive, optimizes the computation time by reducing the number of cells. Take an example of gravity flow, the discretization of the part of the domain does not contain the fluid can be neglected. In three-dimensional space, the computational domain is divided theoretically into $2^m \times 2^m \times 2^m$ cells. The meshing strategy is similar to the case of two space dimensions and subdivision of a cell increases from 4 in 2D to 8 in 3D. The refinement rules are the same.

5.7.3 Description of simulations

The code implements the case of a periodic flow in a bounded square computational domain ($L = 60, 80$):

- the free surface height h initially set to 1,
- this interface is assessed a sinusoidal perturbation of small amplitude and wavelength λ equal to the length L of the field, resulting in deformation of a periodic wave,
- the amount of liquid leaving the computational domain is fed back as input to it.

This has the effect of imposing a condition suitable for a periodic flow, which is that any variable X of the flow satisfies: $X \mid_{x=-\frac{L}{2}} = X \mid_{x=\frac{L}{2}} \forall t$. This condition indicates that: $\langle h \rangle_x = 1 \ \forall t$. Indeed, define the average in space (on the x-axis) of any variable X as:

$$\langle X \rangle_x = \frac{1}{L} \int_{-\frac{L}{2}}^{\frac{L}{2}} X dx$$

Applied to the kinematic equation of the height (5.14), one obtains

$$\frac{1}{L} \int_{-\frac{L}{2}}^{\frac{L}{2}} \partial_t h dx + \frac{1}{L} \left(q \mid_{-\frac{L}{2}} - q \mid_{\frac{L}{2}} \right) = 0.$$

However, in a periodic flow, we have: $X \mid_{x=-\frac{L}{2}} = X \mid_{x=\frac{L}{2}} \forall t$. Therefore, it becomes:

$$\frac{1}{L} \int_{-\frac{L}{2}}^{\frac{L}{2}} \partial_t h dx = 0, \quad \forall t \quad \Leftrightarrow \quad \partial_t \langle h \rangle_x = 0, \quad \forall t$$

Hence, one can conclude that the average height of the film is constant $\forall t$, thus equal to its original height at $t = 0$, whether $\langle h \rangle_x = 1$ This condition is a necessary condition

in the case of a periodic flow, so in the numerical solution of the gravity flow and the fulfillment of this condition will be monitored in order to evaluate the accuracy of the simulations.

An input file of Gerris consists of three parts (see Appendix A.5 for an example of Gerris program solving a gravity flow):

- the body of the program that matches the resolution of the system, `GfsSimulation` solves the Navier-Stokes and Poisson equation for the calculation of the pressure,
- boxes that correspond to the area of the domain: `GfsBox` to define the boundary conditions at the edge,
- edges that define the link between the boxes, `GfsGEdge`, which allows, in particular, to connect the output of the last box with the entrance of the first (regular flow).

These blocks can be preceded by the definition of constants, variables or global functions called 'macros' to be interpreted in blocks (variable replaced by its value) beginning of the program. It includes:

- characteristics of the fluid: Re, We (`BOND`), ρ (continuous function of a value for the liquid 1 and 1/100 for gas)r (`RATIO`),(see in Section 5.2 and 5.4),
- data of the physical problem: β, `RADIUS`,
- numerical parameters: `LENGTH`, m.

Gerris defines its own physical parameters:

- the length of the domain: L is initial of the `LENGTH`,
- gravity: g, by default equal to 1,
- the specific volume 'alpha': $\frac{1}{\rho}$.

Gerris also requires the characterization of a T interface, with a radius of curvature and a function 'Position' ($y = T(x,t)$ in 2D). This interface must be initially perturbed by a periodic function (to meet the conditions for a periodic flow). The gravitational acceleration of the fluid is accounted for by introducing body forces:

- $F_x = 1$,
- $F_y = -B = -cot\beta$, where β is the angle in radians.

These forces apply only to the liquid. The program was finally completed with technical functions to define:

- in terms of flow `Solid`,
- the depth level default mesh in the domain `Refine`, in terms of `RefineSolid`,
- adaptation of the mesh, running, moving with the movement of the interface `AdaptFunction`,
- adaptation of the mesh, running, moving with the vorticity `AdaptVorticity`,
- numerical results and graphics `OutputScalarNorm`, `OutputScalarSum`, `OutputSimulation`.

The results of numerical simulations provide data and measures that will ultimately allow us to calculate the characteristics of a solitary wave (measures observable at the crest of the wave):

- the phase velocity,
- the maximum amplitude,

for a range of higher Reynolds numbers. In the description of the numerical experiment, we noted that at the end of a simulation, the wave was saturated and stationary in its repository moving. It is identified after watching this stationarity, when we have all the data and measures, we averaged in time in order to smooth the approximation errors.

The initial height of the substrate is fixed at $h = 1$ in a domain of length $L = 60, 80$. Every time t^n, for no pre-defined time and small enough ($\Delta t = 5$) each resolution provides us with the average height: $\langle h \rangle^n = \frac{1}{L} \sum_{i=-\frac{L}{2}}^{\frac{L}{2}} {h_i}^n$ where ${h_i}^n$ is the height of the interface at the point x_i at time t^n for $i \in \left[-\frac{L}{2}, +\frac{L}{2}\right]$ (there $h_i = h(x_i) = h(i\Delta x)$). We perform an average $\langle h \rangle$ on k successive time steps ($k = 5$) in order to smooth errors related to the displacement of the wave on the mesh studied, and thus the variation induced the digital representation. Then, $t = n$ to $n + k$, we get the average height:
$\langle h \rangle = \frac{1}{k} \sum_n^{n+k} \langle h \rangle^n$ ($\langle h \rangle$ average height on k time step).

When there is a stabilization (or saturation) of the solitary wave (either a given time t^n), the ridge provides us with two features that we wish to study:

- the phase velocity on the surface: $c^{n+1} = \frac{({x_i}^{max})^{n+1} - ({x_i}^{max})^n}{t^{n+1} - t^n}$ where $({x_i}^{max})^n$ and $({x_i}^{max})^{n+1}$ are the abscissa, time t^n and t^{n+1}, for $i \in \left[-\frac{L}{2}, +\frac{L}{2}\right]$,
- the maximum amplitude of the wave: $\| h \|_\infty^n = max \mid {h_i}^n \mid$ where ${h_i}^n$ denotes, as before, the height of the interface x_i at time t^n for $i \in \left[-\frac{L}{2}, +\frac{L}{2}\right]$ (note: $({x_i}^{max})^n$ the abscissa of $max \mid {h_i}^n \mid$).

As with the above measures, we want to smooth the values over several successive time steps. It is, for $t = n$ to $n + k$:
the average phase velocity: $\langle c \rangle = \frac{1}{k-1} \sum_{n+1}^{n+k} \langle c \rangle^n$
the average maximum amplitude: $\langle \| h \|_\infty \rangle = \frac{1}{k} \sum_{n}^{n+k} \langle \| h \|_\infty \rangle^n$.

It must be noted that, by default, Gerris does not introduce parameters. The equations are written dimensionally so that for instance the Reynolds number is $1/\nu$, where ν is the viscosity implemented by the user. Thus, we introduced $F_x = 1$ and $h = 1$, initially which fixes the length scale as $L = \bar{h}_{\mathrm{N}}$ (uniform thickness of the film) and the time scale is such that $\frac{L}{T^2} = g \sin\beta \quad \Rightarrow T = \sqrt{\frac{\bar{h}_{\mathrm{N}}}{g \sin\beta}}$. Now we need to specify the initial conditions which is a particular type of event happening only once and before any other type of event, they are all derived from the same parent object `GfsInit`. After some algebra, the initial velocity profile (see Section 5.3) is given by

$$\begin{aligned} \text{if } y < 1\,, \quad u(y) &= \frac{n}{n+1} \left[1 - (1-y)^{(n+1/n)}\right] \sqrt{Re}\,, \\ \text{if } y \geqslant 1\,, \quad u(y) &= \frac{n}{n+1} \sqrt{Re}\,. \end{aligned}$$

The velocity field is just chosen to be continuous at the free surface, the gas velocity being uniform and equal to the velocity at the liquid free surface. This trick enables to avoid spurous instabilities promoted by a shear at the interface. We add these above lines to the simulation file 'filmst.gfs' (see in Appendix A.5):

```
 Init {} {
    U = {
      y = y - RADIUS;
if (y < 1.)
  return (N/(N+1.))*(1.- exp((N+1.)*log(1- y)/N))*sqrt(REYNOLDS);
else
  return sqrt(REYNOLDS)*N/(N+1.);
        }
    }
```

By default, the density ρ is unity and the molecular viscosity μ is zero (i.e. there is no explicit viscous term in the momentum equation). But it does not mean that there is no viscosity at all however, because in my scheme we explain about the effective viscosity which is a function of $\dot{\gamma}$ (see in Section 5.4) and write the syntax in the simulation file (see Appendix A.5) as

```
  SourceViscosity {} {
    double mu, mumax;
    double m;
    mu = exp (-0.5*N*log (REYNOLDS)) ;
    mumax = RATIO/sqrt(REYNOLDS) ;
    if (D2 > 0.)
         m = mu*exp ((N - 1.)*log (sqrt(2.)*D2));
    else
         m = mumax;
    return RHO(T)*MIN(m, mumax);
    } {
# Crank-Nicholson does not converge for these cases, we need backward Euler
# (beta = 0.5 -> Crank-Nicholson, beta = 1 -> backward Euler)
    beta = 1
  }
```

where $\dot{\gamma}$ is mentioned as `(sqrt(2.)*D2)`.

It is necessary to allow the time to compute the numerical solutions. Since, the falling film problem is not an easy task because in long wave instability with large aspect ratio of waves, long time needed to develop the instability. Accuracy is needed at the free surface to capture the instability mechanism and large computational time to see the development of waves (small growth rate), are also has monitor the mass $\langle h \rangle$ that must be conserved over large number of time steps. In Gerris, the command `GfsTime` defines the physical and the computational time (number of time steps performed). By default both the physical time and the time step number are zero when the program starts and both end time and end step values are infinite. But the keyword `GfsOutput`is used to control any action which needs to be performed at a given time during a simulation. Therefore, the syntax is `OutputSimulation` which writes the whole simulation. For example,

```
OutputSimulation { step = 5 } sim-%lf.gfs
```

which means that we will write into a file "sim-%lf.gfs" every 5 of physical time starting from 0, where %lf means (long) floating-point number replaced with the current physical time.

5.8 Conditional stability of shear-thinning film flows

In section 5.6.2, we have seen that traveling waves may be found for shear-thinning fluids even if the Nusselt flat-film solution is linearly stable. Since infinitesimal perturbations are then damped, we conclude with a conditional stability of the Nusselt solution.

DNSs of the temporal response of the film to an initial perturbation of the form $h(x,0) = 1 + A\cos(kx)$ have been performed to test the conditional stability of the film. As in § 5.6.3, periodic boundary conditions have been implemented. Fig. 5.29 reports the amplitude $h_{\max} - h_{\min}$ of the waves observed at the final stage of the simulations. DNS results are compared with the corresponding bifurcation diagrams of the traveling-wave solutions to the model (5.14), (5.55) (the speed of these waves is already reported in Fig. 5.18(b)). At a given wavenumber, larger than the linear cut-off wavenumber k_c but smaller than a limiting values k_{sub}, we expect to find three solutions. For $k > k_{\text{sub}}$, only the Nusselt flat-film solution is found. In the range $[k_c, k_{\text{sub}}]$ the largest-amplitude traveling wave and the Nusselt flat-film solutions should be stable, whereas the smallest-amplitude traveling wave is presumed to be unstable. In most of my DNSs, traveling waves are found to emerge from a transient growth or decay. As expected, at small amplitude, the initial disturbance relaxes to the linearly stable flat-film solution, whereas at sufficiently large amplitude, traveling waves are found. Interestingly, the estimation of k_{sub} from DNS is in remarkable agreement with the bifurcation diagram from the weighted-residual model. We therefore conclude that the model (5.14), (5.55) accurately capture the conditional stability of the Nusselt film solution. Some DNSs indicated by double circles in Fig. 5.29, leads to temporally periodic waves whose amplitude oscillate in time. This kind of wave is also observable in the DNSs of Newtonian falling films performed by [104]. They are observed only in few cases and within a quite narrow band of amplitudes A of the initial perturbation. We presume that these waves result from the instability of the low-amplitude traveling-wave solutions, which otherwise are not observable. The use of periodic boundary conditions enables to limit the computational domain to the size of the waves and thus to drastically reduce the cost of DNSs. An immediate drawback is that we investigate the temporal response of the film whereas experimental conditions correspond to the spatial response of the film to periodic forcing at inlet. However, the weighted-residual model (5.14), (5.55) accurately captures the conditional stability of the film and drastically reduces the cost of the simulations of extended spatial domains. We therefore investigate the spatial response of the film to a periodic excitation at frequency f within the frame of equations (5.14) and (5.55).

Fig. 5.30(a) presents the amplitude $h_{\max} - h_{\min}$ versus the frequency f of the principal branch of traveling-wave solutions for a xanthan gum solution (parameter set 2 in table 5.1), $Re = 100$ and a moderate inclination angle $\beta = 15°$. The integral constraint $\langle q \rangle = \phi_0$ has been enforced in order to enable comparisons with the wavetrains emerging from the time-dependent simulations of the spatial response of the film to a periodic excitation at frequency f [122].

Traveling waves emerges at the cut-off frequency f_c from the Nusselt solution ($h_{\max} - h_{\min} = 0$). The control parameter being f, a saddle-node bifurcation is observed at the frequency f_{sub}. Monitoring f_c and f_{sub} in the plane (f, Re) gives the stability diagram displayed in Fig. 5.30(b). Below the cut-off frequency f_c, the flat film is unconditionally unstable, whereas unconditional stability is expected above f_{sub}. Whenever f lies in the

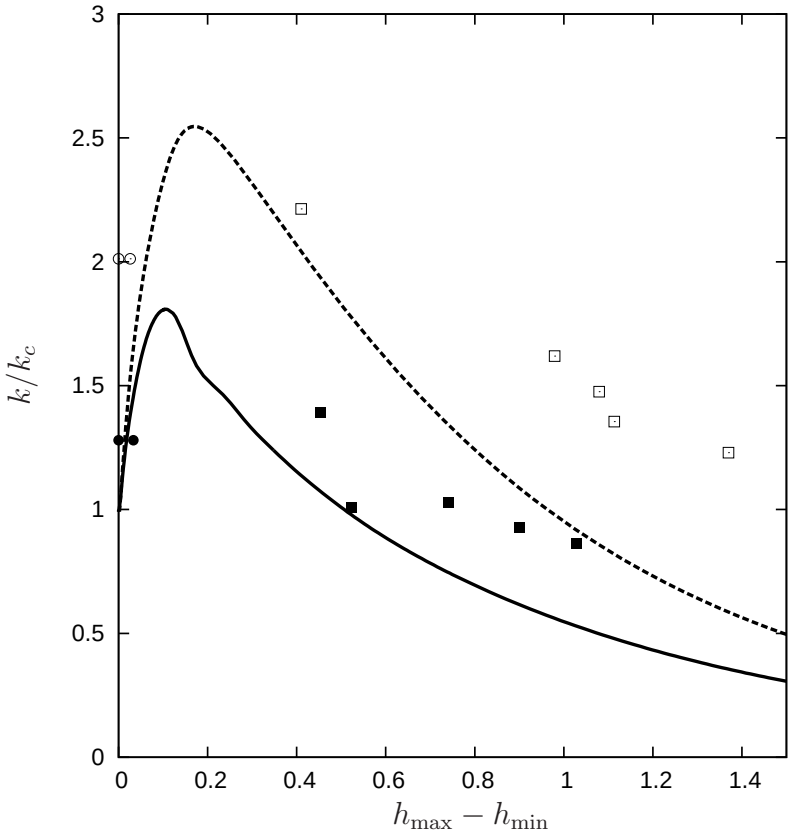

Figure 5.29: Amplitude of the waves obtained at the final stage of DNSs. Parameters correspond to shear-thinning xanthan gum, $Re = 20$, $\beta = 15°$. Black and white squares stand for the traveling-wave solutions for parameter sets 2 and 3 respectively. The range of amplitudes achieved for time-periodic solutions is indicated by double circles. Solid and dashed lines refer to the traveling-wave solutions to (5.14), (5.55) for sets 2 and 3 respectively.

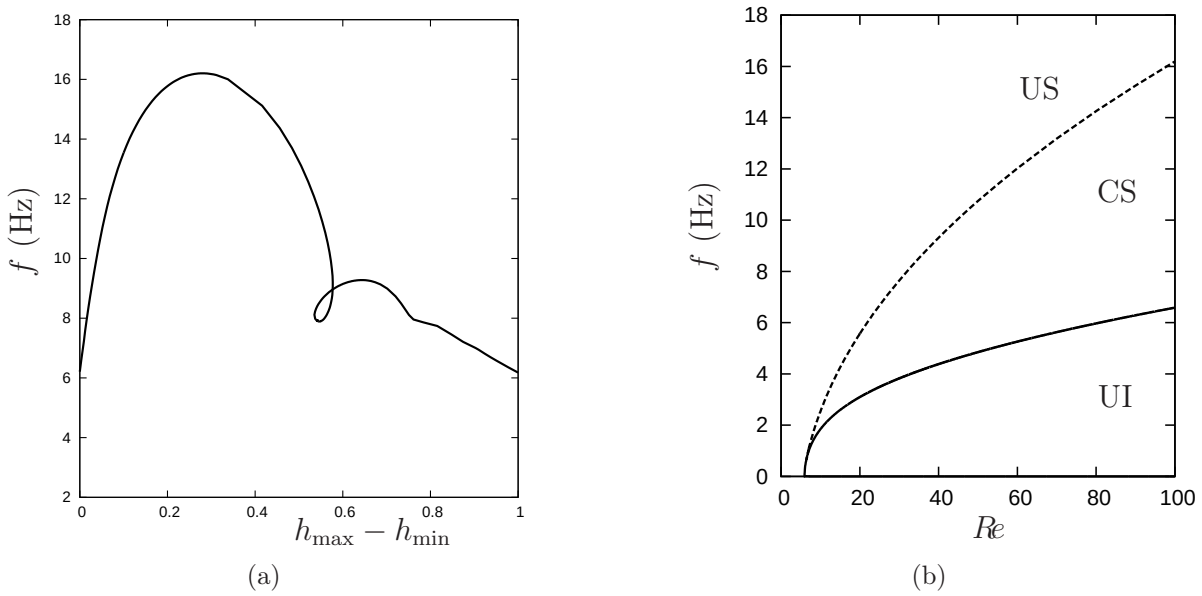

Figure 5.30: (a) Amplitude ($h_{\max} - h_{\min}$) versus frequency at $Re = 100$ showing the subcritical onset of traveling waves when frequency is varied from the cut-off frequency f_c. (b) Stability diagram in the plane (R, f). Solid and dashed lines refers to the marginal stability curve and to the locus of a saddle-node bifurcation f_{sub}. The unconditionally and conditionally stable regions are labeled 'US' and 'CS' respectively. The unconditional instability region is labeled 'UI'. Inclination angle is $\beta = 15°$, other parameters correspond to a shear-thinning xanthan gum solution (Set 2 in Table 5.1). Traveling wave solutions have been computed enforcing the open-flow condition ($\langle q \rangle = \phi_0$).

interval $[f_c,\ f_{\text{sub}}]$, a conditional stability is anticipated. The spatial response of the flat film to a periodic excitation at inlet then depends on the amplitude of the perturbation. We next simulate the response in space and time of the Nusselt flat-film solution to a periodic forcing at inlet. We have imposed a sinusoidal disturbance on the inlet flow rate $q(0,t) = \phi_0[1 + A\cos(2\pi f t)]$. Chosen properties correspond to a 1500 ppm xanthan gum solution (parameter set 2 in table 5.1), $Re = 100$ and $\beta = 15°$ which corresponds to the traveling wave branch drawn in Fig. 5.30(a). The chosen dimensional forcing frequency $f = 14$ Hz lies in the range $[6.5, 16]$ bounded by f_c and f_{sub}. At low values of the forcing amplitude A, the inlet signal is attenuated as it travels downstream. After A reaches a certain threshold, inlet perturbations are amplified downstream and give way to regular trains of traveling waves whose temporal periodicity agrees with the inlet forcing frequency. Fig. 5.31 presents snapshots of the film thickness at two amplitudes $A = 0.08$

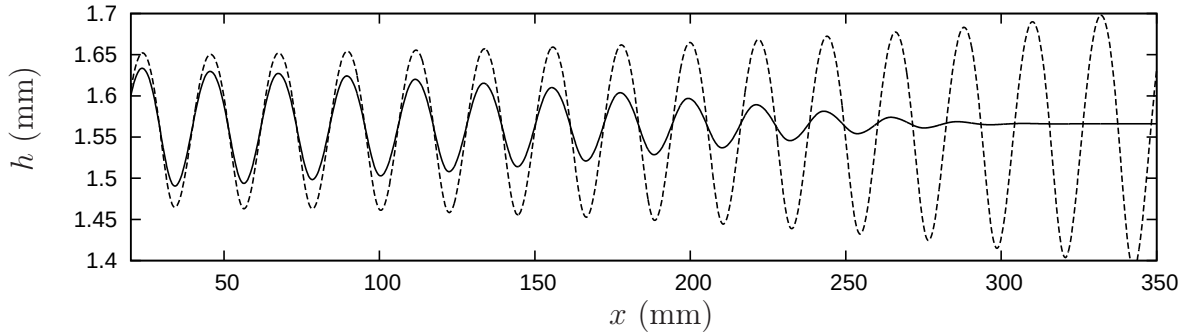

Figure 5.31: Snapshots of the free-surface elevation showing the response of the film to a forcing at inlet with two forcing amplitudes. The simulation is based on model (5.14), (5.55). The fluid is a xanthan gum solution (set 2 in table 5.1 with $n = 0.4$). $Re = 100$, $\beta = 15^\circ$ and the forcing frequency is $f = 14$ Hz. Solid and dashed lines refer to forcing amplitudes $A = 0.08$ and $A = 0.1$ respectively.

and $A = 0.1$ chosen slightly below and above the threshold. The damping of the signal for $A = 0.08$ and its amplification for $A = 0.1$ are clearly visible. We have rerun my simulations with the addition of a small amount of noise to the inlet periodic forcing. The spatio-temporal diagram displayed in Fig. 5.32(a) gives an illustration of the evolution of the wave pattern in time and space. The regular wavetrain that emerges at the forcing frequency close to inlet is quickly disorganized by secondary instabilities, even if the amplitude $A = 0.4$ of the forcing signal is already quite large. The primary wavetrain is disrupted by the onset of larger waves which accelerate and capture the smaller waves ahead of them. A series of coalescence events then occurs which drastically reduces the wave density. Fig. 5.32(b) presents a snapshot of the film thickness at the end of the simulation showing the entire numerical domain. At the downstream end of the flow, large-amplitude solitary waves in interaction organize the disordered state of the flow. The resulting wave dynamics is qualitatively similar to the observation of noise-driven dynamics of a Newtonian falling film [20, 70, 78].

5.9 Summary and conclusion

The evolution of a power-law laminar film flow has been modeled within the frame of the lubrication approximation by means of the weighted residual approach. The derived models are made of the exact mass balance (5.14) and an averaged momentum equation, which form a set of two coupled evolution equations for the film thickness h and the flow rate q, or equivalently a local velocity amplitude $\bar{u}$. The models consistently account

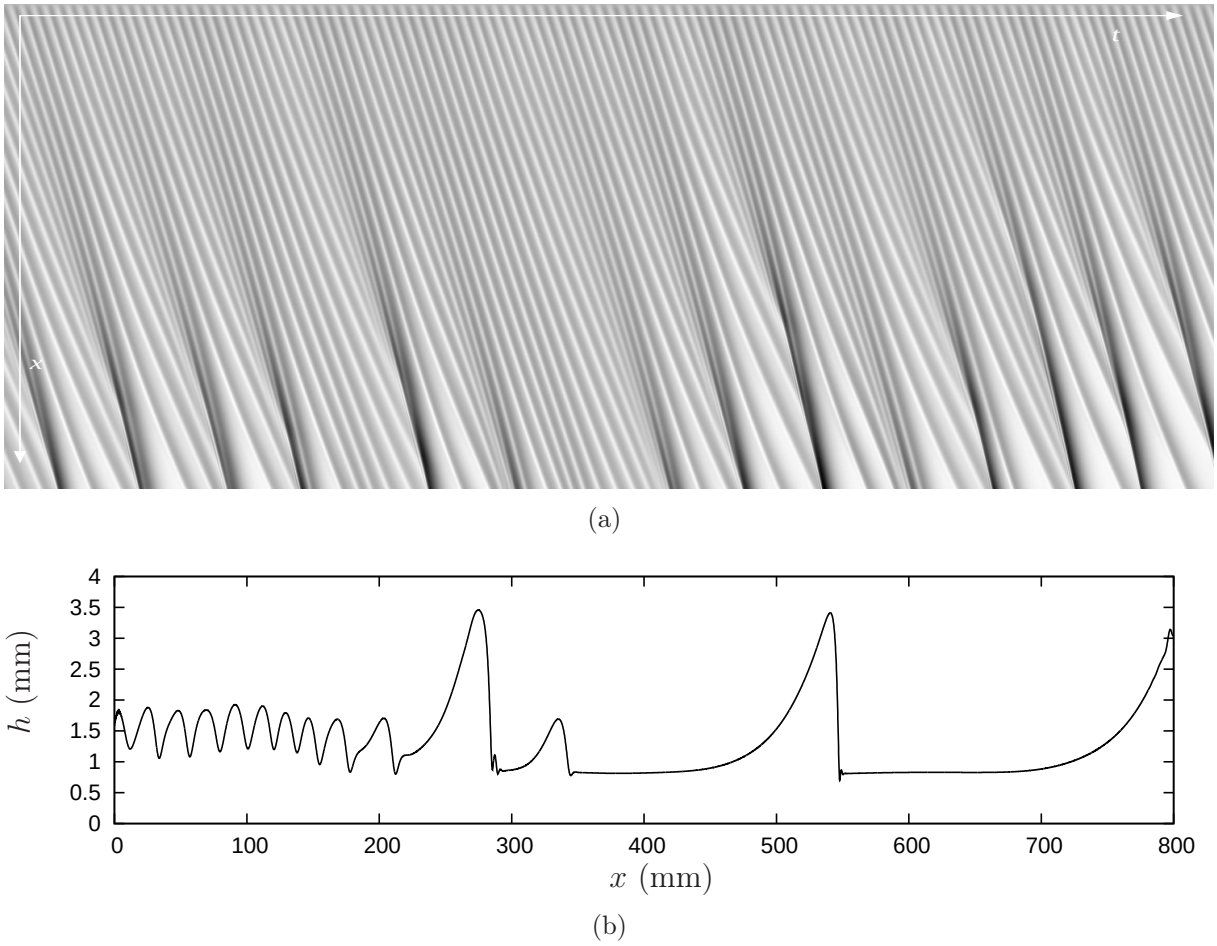

Figure 5.32: Simulation of the response of the film to a forcing at inlet with a small amount of noise. The simulation is based on model (5.14), (5.55). The fluid is a xanthan gum solution (set 2 in table 5.1 with $n = 0.4$). $Re = 100$, $\beta = 15°$. The forcing frequency and amplitude are $f = 14$ Hz and $A = 0.4$. (a) Spatio-temporal diagram. Light (dark) regions correspond to small (large) elevations. Vertical and horizontal ranges are 7.5 s and 0.3 m, respectively. (b) Snapshot of the free-surface elevation at the end of the simulation.

for inertial terms up to $O(\epsilon)$ and to viscous diffusion terms up to $O(\epsilon^2)$. This choice has enabled us to limit the number of degrees of freedom to only two and to limit the complexity of the different averaged momentum equations. It is possible to extent the present analysis to account for second-order inertia terms but at the cost of an increased complexity [112, 123]. We expect these terms to play an important role when three-dimensional wave dynamics are considered.

Consistency at first order of inertial terms is necessary to adequately capture the onset of the instability, whereas consistency at second order of the viscous terms enables to accurately account for the damping of the short waves by streamwise viscous diffusion. Owing of the unphysical divergence of the effective viscosity of power-law fluids as the strain rate goes to zero, it is not possible to consistently account for the streamwise viscous diffusion. To avoid this difficulty, we introduce a bound to the effective viscosity and a Newtonian plateau at low strain rate, or equivalently a Carreau law, and divide the flow into a Newtonian layer at the free surface and a non-Newtonian bulk separated by a fake interface. The relative thickness $\bar{\eta}_c$ of Newtonian layer and the local flow rate q are slaved to the h and $\bar{u}$ by the implicit relations (5.37) and (5.36). Application of the weighted residual approach leads to the evolution equation (5.48) whose coefficients are functions of $\bar{\eta}_c$. The two-equation model (5.14), (5.48) is thus formidable to solve. A drastic simplification is obtained in the limit $\bar{\eta}_c \to 0$ but at the cost of two different formulations (5.55) and (5.60) of the averaged momentum equation for shear-thinning fluids ($n < 1$) and shear-thickening fluids ($n > 1$) respectively. The momentum balance (5.55) accounts for the contributions of the free surface and wall regions to the viscous streamwise diffusion terms. It is consistent with the averaged momentum equation (5.58) previously derived in the Newtonian case in the limit $n \to 1$. In the case of equation (5.60), (5.58) is not recovered as n goes to one. Yet, the dispersion relations corresponding to the linear stability of the Nusselt flow, and obtained from (5.60) and (5.58), coincide at $n = 1$. We note that a full agreement is not required as the limit of a vanishing Newtonian layer at the free surface is not compatible with the limit $n \to 1$.

The two-equation models (5.14), (5.55) and (5.14), (5.60) have been validated in the linear and nonlinear regimes by means of comparisons with the solutions of the primitive set of equations (5.2), (5.3) and (5.31). A remarkable agreement with the Orr-Sommerfeld stability analysis has been obtained. In particular, the instability threshold is accurately recovered. Comparisons to the DNSs of two-phase flows demonstrate that the models correctly predicts the speed, amplitude and shape of large-amplitude nearly solitary waves. In particular, the details of the capillary ripples, the capillary shock region, preceding the main humps are captured correctly.

We have compared the results of Orr-Sommerfeld analyses and DNSs with the only continuous Newtonian plateau constitutive law (5.32) and with the smooth Carreau law (5.33). Whenever the thickness of the Newtonian layer is small ($s^n \ll 1$), which is indeed the case for the fluids we have considered in my study, the two constitutive laws give very similar results. This gives us confidence that the results of my study are not dependent

on a particular regularization at low strain rate of the power law (5.1).

Our linear stability analysis shows that the threshold of the long-wave instability is weakly dependent on the relative thickness s^n of the Newtonian layer at the free surface. The smaller the power-law index n and the thinner the Newtonian layer, the smaller the critical Froude number is. For shear-thinning fluids ($n < 1$) and low-power-law indices, the range of unstable wavenumbers is governed by the balance of inertia to streamwise viscous diffusion at the free surface, surface tension and the contribution of the bulk to viscous diffusion being negligible. Instead, in the case of shear-thickening fluids ($n > 1$), viscous diffusion at the free surface is negligible and the range of unstable wavenumbers is governed by the effective viscosity of the non-Newtonian bulk layer. The influence of viscoplasticity on the primary instability is shown to be nontrivial. Instead of the destabilization (stabilization) of the base flow close to threshold in the case of shear-thinning (shear-thickening) fluids, an unexpected reverse behavior is observed further from threshold when the viscous damping of short waves becomes dominant. The excellent agreement between the stability analyses based on the primitive equations and the two-equation weighted-residual models enables to comprehend these observations within the framework of Whitham hierarchies. The effect of shear-thinning (shear-thickening) on the stability threshold is a consequence of the acceleration (deceleration) of the kinematic waves with respect to the fluid velocity at the interface. Farther from threshold, shear-thinning (shear-thickening) enhances (slows down) the deceleration of kinematic waves by viscous dispersion which stabilize (destabilize) the base flow.

Our study of nonlinear waves focuses on the one-humped large-amplitude solitary waves that are well known to organize the dynamics of a Newtonian film [4]. For shear-thickening fluids, surface tension is a weak effect as compared to viscous diffusion ($\Gamma \ll 1$) and traveling waves do not present the capillary ripples observed on shear-thinning and Newtonian films. Shear thinning accelerates solitary waves and promotes a subcritical onset of traveling waves at larger wavenumber than the linear cut-off wavenumber k_c. A conditional stability of the base flow is thus observed, the film being able to respond to a periodic forcing at inlet at $k > k_c$ if the amplitude of the perturbations is large enough. This phenomenon results from the removal of the Newtonian layer, the reduction of the effective viscosity at the free surface and therefore the attenuation of the damping of short waves. Comparisons with DNSs show that this phenomenon is accurately captured by the weighted-residual model (5.14), (5.55). Spatio-temporal simulations reveal that trains of short waves excited at larger frequencies than the cut-off frequency are quickly disrupted by secondary instabilities which lead to a disordered state organized around solitary waves in interaction. The spatio-temporal dynamics of this disordered state is then amenable to a coherent-structure theory in which the flow is discretized into particle-like solitary waves. Wave-to-wave interaction of solitary waves in Newtonian flows have been recently investigated by Pradas [101] who pointed out the role of viscous dispersion effects. An extension of the theory by Pradas *et al.* to shear-thinning film flows is currently under way.

A natural application of the present modeling effort is the study of roll waves in overland shallow flows which remain laminar and where clay suspensions present shear-thinning properties. For such flows, the onset of nonlinear waves in conditions for which the base flow is linearly stable have also been observed by [85, 98]. Yet, these studies do not correctly predict the instability threshold, a drawback which prevents quantitative comparisons with experimental data. The remarkable agreement of the solutions to the weighted-residual models with DNS suggests that a quantitative representation of the roll wave dynamics might be achieved within the frame of shallow-water equations similar to (5.14), (5.55).

Chapter 6

Viscoplastic falling film

In this chapter, I present a preliminary study of a viscoplastic falling film based on the elasto-viscoplastic constitutive relation introduced by Saramito [121]. The aim of this work is to extend the pseudo-plug theory formulated by Balmforth & Liu [8] to deal with viscoplastic films at the moderate values of the Reynolds number.

6.1 Introduction

Balmforth & Liu [8] considered the stability of a viscoplastic fluid layer flowing on an inclined plane under the action of gravity. Their concern was the onset of roll waves that are observable in mud surges. As a consequence they did not consider surface tension nor streamwise viscous effects. Indeed, the structure of the shock separating each gradually varying laminar regions of the flow is governed by the details of the turbulent flow in the 'roll'. For that reason, their approach was truncated at first order in the film parameter. Balmforth & Liu showed that an unyielded plug region laying at the top of a uniform film forms a lid which forbids the instability to occur. However, as soon as the free surface is deformed, the plug starts to yield and the instability is possible which assumes that normal stresses appears instantly in the plug region so that the second invariant of the stress can exceed the yield stress. In other words, small but finite amplitude perturbations of the free surface are sufficient to trigger the instability and viscosplastic film flows should be conditionally unstable. Moreover, in order to describe the dynamics of a viscoplastic film, surface tension and streamwise viscous diffusion must be accounted for. Balmforth & Liu considered a viscoplastic fluid modelled by the Herschel and Bulkley law

$$\tau = K|\dot{\gamma}|^{n-1}\dot{\gamma} + \tau_0 \frac{\dot{\gamma}}{|\dot{\gamma}|} \qquad \text{when} \qquad |\dot{\gamma}| > 0 \tag{6.1a}$$

$$|\tau| < \tau_0 \qquad \text{when} \qquad |\dot{\gamma}| = 0 \tag{6.1b}$$

where τ and $\dot{\gamma}$ are the stress and rate of strain tensors, τ_0 is the yield stress and $|\dot{\gamma}|$ is the second invariant of the rate of strain. Equation (6.1) can be rewritten as [121]

$$\dot{\gamma} = \max\left(0, \frac{|\tau| - \tau_0}{K|\tau|^n}\right)^{\frac{1}{n}} \tau \equiv \kappa_n(|\tau|)\tau \tag{6.2}$$

The viscosity of a viscoplastic fluid modelled by (6.1) is undefined in the unyielded region and diverges at zero strain rate. In order to take into account viscous effects at the interface and to capture the conditional stability of the film, one has to describe how the unyielded plug region is deformed which demands to include the elasticity of the solid-like behavior of the fluid into the constitutive equation. Recently, Saramito [121] has proposed an extension of the Herschel-Bulkley law (6.1) including the viscoelastic properties of the fluid:

$$\frac{1}{G}\overset{\triangledown}{\tau} + \kappa_n(|\tau_d|)\tau - \dot{\gamma} = 0 \tag{6.3}$$

where G is th elastic modulus, $\tau_d = \tau - \frac{1}{N}tr(\tau)I$ denotes the deviatoric part of τ and

$$\overset{\triangledown}{\tau} = \partial_t\tau + \mathbf{v}\nabla\tau - \tau\nabla\mathbf{v}^T - \nabla\mathbf{v}\tau \tag{6.4}$$

is the upper convected time derivative of the stress tensor τ. I propose to extend the pseudo-plug theory by Balmforth and Liu using the constitutive equation (6.3).

6.2 Governing equations

I consider a viscoplastic fluid flowing down an inclined plane under the action of gravity as sketched in figure 6.1. The flow is assumed to be incompressible and the fluid properties, density ρ and surface tension σ are constant. The angle of inclination β and the gravity acceleration g are also constant. Dimensional quantities will be referred to with a bar decoration. The length scale is the uniform film thickness $\bar{h}_{\mathrm{N}}$. The velocity scale is defined by the free surface velocity of the base flow, denoted by $\bar{V}_{\mathrm{N}}$. With the above choice of scales, the dimensionless equations read

$$\partial_x u + \partial_y v = 0\,, \tag{6.5a}$$

$$Re\,(\partial_t u + u\partial_x u + v\partial_y u) = -\partial_x p + \Lambda + \partial_x\tau_{xx} + \partial_y\tau_{xy}\,, \tag{6.5b}$$

$$Re\,(\partial_t v + u\partial_x v + v\partial_y v) = -\partial_y p - \Lambda\cot\beta + \partial_x\tau_{xy} + \partial_y\tau_{yy}\,, \tag{6.5c}$$

$$\begin{aligned} De\,(\partial_t\tau_{xx} + u\partial_x\tau_{xx} + v\partial_y\tau_{xx} - 2\tau_{xx}\partial_x u - 2\tau_{xy}\partial_y u) & \\ +\kappa_{Bi}(|\tau_d|)\tau_{xx} - 2\partial_x u &= 0\,, \end{aligned} \tag{6.5d}$$

$$\begin{aligned} De\,(\partial_t\tau_{yy} + u\partial_x\tau_{yy} + v\partial_y\tau_{yy} - 2\tau_{xy}\partial_x v + 2\tau_{yy}\partial_x u) & \\ +\kappa_{Bi}(|\tau_d|)\tau_{yy} + 2\partial_x u &= 0\,, \end{aligned} \tag{6.5e}$$

$$\begin{aligned} De\,(\partial_t\tau_{xy} + u\partial_x\tau_{xy} + v\partial_y\tau_{xy} - \tau_{xx}\partial_x v - \tau_{yy}\partial_y u) & \\ +\kappa_{Bi}(|\tau_d|)\tau_{xy} - \partial_y u - \partial_x v &= 0\,, \end{aligned} \tag{6.5f}$$

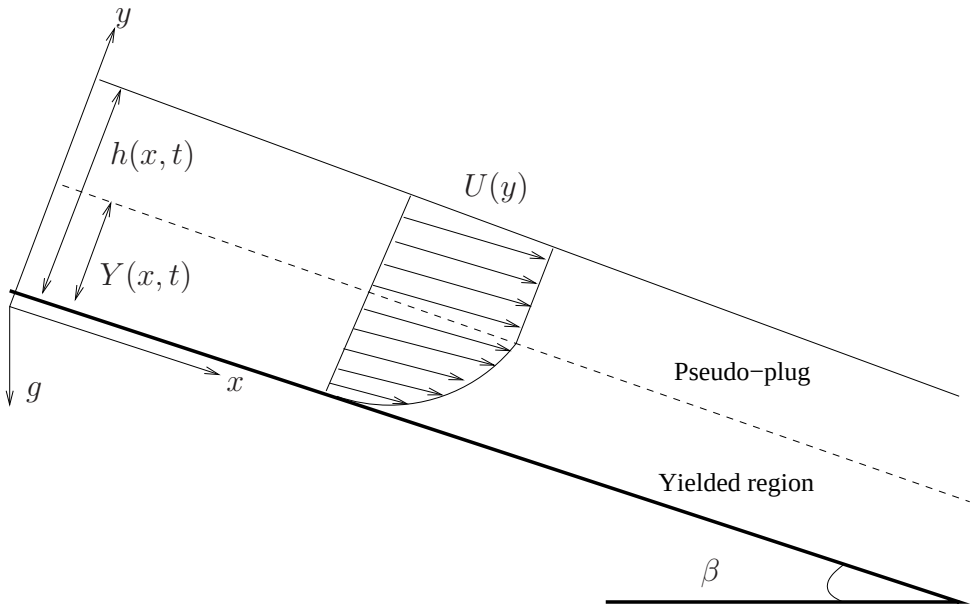

Figure 6.1: A sketch of the geometry for a viscoplastic film flowing down an inclined plane.

where $\Lambda = Re/Fr^2$ and $|\tau_d|^2 = \frac{1}{4}\left(\tau_{xx} - \tau_{yy}\right)^2 + \tau_{xy}^2$ and

$$\kappa_{Bi}(s) = \kappa(s; Bi) \equiv \max\left(0, \frac{s - Bi}{s^n}\right)^{\frac{1}{n}} \tag{6.5g}$$

with boundary conditions at $y = h$

$$\partial_t h + u\partial_x h = v\,, \tag{6.5h}$$

$$\left[1 - (\partial_x h)^2\right]\tau_{xy} + \partial_x h\left(\tau_{yy} - \tau_{xx}\right) = 0\,, \tag{6.5i}$$

$$-p + \frac{\tau_{xx}(\partial_x h)^2 - 2\tau_{xy}\partial_x h + \tau_{yy}}{1 + (\partial_x h)^2} = We\frac{\partial_{xx} h}{\left[1 + (\partial_x h)^2\right]^{3/2}}\,, \tag{6.5j}$$

and the no-slip condition at the wall

$$u = v = 0 \qquad \text{at} \qquad y = 0 \tag{6.5k}$$

The non-dimensionalisation procedure introduces five dimensionless groups in the governing set of equations (6.5), i.e. a Froude number

$$Fr = \bar{V}_{\mathrm{N}}/\sqrt{g\bar{h}_{\mathrm{N}}\sin\beta}\,, \tag{6.6}$$

which compares inertia and gravity, a Reynolds number

$$Re = \frac{\rho\bar{V}_{\mathrm{N}}^{2-n}\bar{h}_{\mathrm{N}}^{n}}{K}\,. \tag{6.7}$$

a Deborah number

$$De = \frac{K}{G}\left(\frac{\bar{V}_{\rm N}}{\bar{h}_{\rm N}}\right)^n \tag{6.8}$$

a Bingham number

$$Bi = \frac{\tau_0}{K\left(\frac{\bar{V}_{\rm N}}{\bar{h}_{\rm N}}\right)^n} \tag{6.9}$$

a Weber number

$$We = \frac{\sigma}{K}\bar{h}_{\rm N}^{n-1}\bar{V}_{\rm N}^{-n}\,. \tag{6.10}$$

It is useful to add to this list the Kapitza number

$$\Gamma = (\sigma/\rho)(K/\rho)^{-4/(n+2)}(g\sin\beta)^{(2-3n)/(n+2)}\,, \tag{6.11}$$

which compares surface tension, gravity and viscosity and depends only on the fluid properties and the inclination of the plane. The Kapitza number can be rewritten $\Gamma = (l_c/l_\nu)^2$ in terms of the ratio of two length scales, the capillary length $l_c = \sqrt{[\sigma/(\rho g\sin\beta)]}$ and the viscous-gravity length $l_\nu = (K/\rho)^{2/(n+2)}\,(g\sin\beta)^{(n-2)/(n+2)}$ defined by the balance of gravity acceleration and viscous drag.

Starting from the length scale l_ν and the time scale $t_\nu = \left(\frac{K}{\rho}\right)^{\frac{1}{n+2}}(g\sin\beta)^{-\frac{2}{n+2}}$, corresponding to the balance of viscosity and gravity acceleration, it will be useful to introduce the definitions of Deborah and Bingham numbers that are independent of the flow rate. Thus I introduce $De_\nu = \frac{K}{G}\left(\frac{1}{t_\nu}\right)^n$ and $Bi_\nu = \frac{\tau_0}{K\left(\frac{1}{t_\nu}\right)^n}$, which are related to De and Bi through the relations $De = De_\nu\left(\frac{\bar{V}_{\rm N}t_\nu}{\bar{h}_{\rm N}}\right)^n$ and $Bi = Bi_\nu\left(\frac{\bar{h}_{\rm N}}{\bar{V}_{\rm N}t_\nu}\right)^n$.

The uniform film solution to (6.5) is given by

$$\tau_{xx} = 2De\Lambda^2(h-y)^2\,, \qquad \tau_{xy} = \Lambda(h-y)\,, \qquad \tau_{yy} = 0\,, \tag{6.12a}$$

$$u = \int_0^y \frac{\left[\Lambda(h-y)\sqrt{1+\Lambda^2De^2(h-y)^2} - Bi\right]^{1/n}}{\sqrt{1+\Lambda^2De^2(h-y)^2}}dy\,, \qquad v = 0\,, \tag{6.12b}$$

$$p = \Lambda(h-y)\cot\beta \tag{6.12c}$$

in the yielded region $y \le Y \equiv h - \sqrt{\sqrt{1+4De^2Bi^2}-1}/(\sqrt{2}\Lambda De)$. In the unyielded plug region $Y \le y \le h$,

$$u = u(y=Y)\,, \qquad v = 0\,, \qquad \tau_{xy} = \Lambda(h-y)\,, \tag{6.12d}$$

τ_{xx} and τ_{yy} are undetermined but verify

$$p - \tau_{yy}|_{y=h} = \Lambda(h-y)\cot\beta\,, \quad \tau_{yy}|_{y=Y} = 0\,, \quad \tau_{xx}|_{y=Y} = \frac{-1+\sqrt{1+4Bi^2De^2}}{De} \tag{6.12e}$$

6.3 Low-dimensional formulation

Let us assume (i) slow space and time evolutions $\partial_{x,t} \sim \epsilon$ where $\epsilon \ll 1$ is a formal film parameter, (ii) surface deformations induce order-ϵ corrections of the velocity profile and stress distribution from the flat film solution, (iii) a weak elastic response of the plug and we consider small Deborah numbers $De = O(\epsilon)$. The dynamics of the film is therefore assumed to be never far from a truly viscoplastic one governed by the Herschel-Bulkley law (6.1). In the lubrication limit $Re \to 0$, whenever the film is deformed, the velocity and stresses are given by Fernández-Nieto *et al.* [44]

$$u = \frac{n}{\Lambda(n+1)}\left[(\Lambda h - Bi)^{\frac{n+1}{n}} - (\Lambda(h-y) - Bi)^{\frac{n+1}{n}}\right] + O(\epsilon)\,, \tag{6.13a}$$

$$\tau = \begin{pmatrix} 0 & \Lambda(h-y) \\ \Lambda(h-y) & 0 \end{pmatrix} + O(\epsilon)\,. \tag{6.13b}$$

In the yielded region $y < h - Bi/\Lambda$, and

$$u = \frac{n}{\Lambda(n+1)}(\Lambda h - Bi)^{\frac{n+1}{n}} + O(\epsilon)\,, \tag{6.13c}$$

$$\tau = \begin{pmatrix} \sqrt{Bi^2 - \Lambda^2(h-y)^2}\mathrm{sign}(\partial_x h) & \Lambda(h-y) \\ \Lambda(h-y) & -\sqrt{Bi^2 - \Lambda^2(h-y)^2}\mathrm{sign}(\partial_x h) \end{pmatrix} + O(\epsilon^n) \tag{6.13d}$$

in the "pseudo-plug" region $y \geq h - Bi/\Lambda$ where the fluid is slightly yielding $\kappa_{Bi}(|\tau_d|) = O(\epsilon)$ and consequently the second invariant of the stress is always slightly larger than the yield stress$\kappa_{Bi}(|\tau_d|) = O(\epsilon^n)$ which allows the pseudo-plug to deform [8]. Now, from the velocity profile (6.13) we can deduce $\Lambda = Re/Fr^2$. Thus $u(y = h; h = 1) = 1$ yields the relation

$$\left(\frac{n+1}{n}\Lambda\right)^{\frac{n}{n+1}} - \Lambda + Bi = 0 \tag{6.14}$$

In the limit $Bi = 0$, we get $\Lambda = [(n+1)/n]^n$ as expected for a power-law fluid.

With the help of the continuity equation, assumption (i) implies that the cross-stream velocity $v = -\int_0^y \partial_x u\, dy = O(\epsilon)$ so that inertia terms can be dropped from the cross-stream momentum equation. At lowest order the pressure distribution is the hydrostatic one corrected by capillary effects

$$p = \tau_{yy} + \Lambda \cot\beta(h-y) - We\partial_{xx}h + O(\epsilon)\,. \tag{6.15}$$

Substitution of the pressure gradient $\partial_x p$ in the streamwise momentum equation then gives

$$Re\,(\partial_t u + u\partial_x u + v\partial_y u) = \Lambda(1 - \cot\beta\partial_x h) + We\partial_{xxx}h + \partial_y\tau_{xy} + \partial_x\left(\tau_{xx} - \tau_{yy}\right)\,, \tag{6.16}$$

which is similar to the Prandtl equation in boundary-layer theory [124] and therefore will be referred to as a boundary-layer momentum equation. I note that the $O(\epsilon)$ contribution of the normal stresses $\partial_x(\tau_{xx}-\tau_{yy})$ was neglected by Balmforth & Liu [8] and their boundary-layer formulation was therefore inconsistent. Equation (6.16) is consistent at order ϵ, i.e. all neglected terms are of higher order.

The coupling of the evolution of the velocity field to the stresses arise from the terms $\partial_y\tau_{xy}$ and $\partial_x(\tau_{xx}-\tau_{yy})$ and therefore it is sufficient to determine τ_{xx} and τ_{yy} at $O(1)$ and τ_{xy} at $O(\epsilon)$. It is therefore tempting to drop $O(\epsilon)$ terms from (6.5d) and (6.5e) and $O(\epsilon^2)$ terms from (6.5f). However, $\kappa_{Bi}(|\tau_d|)$ is $O(\epsilon)$ in the pseudo-plug region and as a consequence, τ_{xy} can be computed up to order ϵ only if second-order terms are retained in (6.5f). I will also retain the elastic terms (proportional to the Deborah number) in (6.5d) and (6.5e) because of their role in the damping of short waves. Finally, our system of boundary-layer equations consists of the continuity equation (6.5a), the momentum equation (6.16), the constitutive equations (6.5d), (6.5e), (6.5f) from which the $O(\epsilon^3)$ term $De\,\tau_{xx}\partial_x v$ is dropped out. This system is completed by (6.5h), (6.5k) and the tangential stress boundary condition truncated at order ϵ,

$$\tau_{xy} = \partial_x h(\tau_{xx}-\tau_{yy}) \qquad \text{at} \qquad y=h\,. \tag{6.17}$$

I shall consider that locally the film is still governed by (6.13) and decompose the stress and velocity distributions in the form

$$\tau = \tau^{(0)} + \tau^{(1)} \qquad \text{and} \qquad u = u^{(0)} + u^{(1)} \tag{6.18a}$$

where $\tau^{(0)}$ is defined by

$$\tau^{(0)} = \begin{pmatrix} T_{xx}(x,t)\sqrt{B(x,t)^2-\eta(x,y,t)^2} & T_{xy}(x,t)\eta(x,y,t) \\ T_{xy}(x,t)\eta(x,y,t) & T_{yy}(x,t)\sqrt{B^2-\eta(x,y,t)^2} \end{pmatrix} \tag{6.18b}$$

if $0\leq\eta\leq B$ and

$$\tau^{(0)} = \begin{pmatrix} 0 & T_{xy}(x,t)\eta(x,y,t) \\ T_{xy}(x,t)\eta(x,y,t) & 0 \end{pmatrix} \tag{6.18c}$$

when $B<\eta\leq 1$. I have introduced a reduced normal coordinate $\eta = 1-y/h(x,t)$ and a local Bingham number $B(x,t) = Bi/|T_{xy}(x,t)|$. Notice that the free surface location is given by $\eta=0$ whereas the wall is located at $\eta=1$ and the fake interface separating the yielded and pseudo-plug region is given by $\eta=B(x,t)$.

The leading order streamwise velocity component is assumed of the form:

$$u^{(0)} = \frac{q(x,t)}{h(x,t)\phi(B(x,t))}g(\eta(x,y,t);B(x,t)) \tag{6.18d}$$

with a velocity profile $g(\eta;B)$ given by

$$g(\eta;B) = \frac{n}{n+1}\left[(1-B)^{\frac{n+1}{n}} - (\eta-B)^{\frac{n+1}{n}}\right] \qquad \text{if} \qquad B \le \eta \le 1\,,$$
$$\text{and} \qquad g(\eta;B) = \frac{n}{n+1}(1-B)^{\frac{n+1}{n}} \qquad \text{otherwise} \tag{6.18e}$$

$\phi(B)$ is defined by

$$\phi(B) = \int_0^1 g(\eta)d\eta = \frac{n(1+n+Bn)}{(2n+1)(n+1)}(1-B)^{\frac{n+1}{n}}\,. \tag{6.18f}$$

The corrections $\tau^{(1)}$ and $u^{(1)}$ are assumed small. $u^{(1)}$ is an $O(\epsilon)$ term induced by the slow deformations of the free surface. In the yielded region of the flow, $\tau^{(1)}$ corresponds to the $O(\epsilon)$ viscous response of the stress to the strain rate. In the pseudo-plug region, $\tau^{(1)}$ contribute to maintain the second invariant of the deviatoric stress $|\tau_d| = Bi + O(\epsilon)$ above threshold and therefore is an $O(\epsilon^n)$ correction.

Besides the film thickness h, the decomposition (6.18) introduces four amplitudes, or degrees of freedom, q, T_{xy}, T_{xx} and T_{yy} depending on x and t. In the limit $\partial_x h \to 0$ and $De \to 0$, i.e. for a slightly deformed viscoplastic film, the solution (6.13) corresponds to

$$q = \Lambda^{1/n}\phi(Bi/(\Lambda h))h^{\frac{2n+1}{n}}\,, \qquad T_{xy} = \Lambda h \qquad \text{and} \qquad T_{xx} = -T_{yy} = \Lambda h\,\mathrm{sign}(\partial_x h)\,. \tag{6.19}$$

Whenever the film interface is deformed, q, T_{xy}, T_{xx} and T_{yy} shall slightly depart from (6.19) and therefore may include $O(\epsilon)$ or $O(\epsilon^n)$ corrections. As a consequence, the decomposition (6.18) of the stress and velocity fields must be made unique by adding gauge conditions. The first of these conditions is $\int_0^h u^{(1)}dy = 0$ which implies that $q(x,t)$ is the volumetric flow rate $q = \int_0^h u dy$. This choice is dictated by the fact that integrating the continuity equation (6.5a) across the film using the kinematic boundary conditions (6.5h) and the no-slip ones (6.5k) gives a mass balance

$$\partial_t h + \partial_x q = 0 \tag{6.20}$$

which is an *exact* evolution equation for the film elevation.

I apply the weighted residual technique and integrate the boundary-layer momentum equation (6.16) and the stress-to-strain relations (6.5d)-(6.5f) across the film with weights $w_M(\eta)$, $w_{xx}(\eta)$, $w_{xy}(\eta)$ and $w_{yy}(\eta)$. Writing formally $BL(u,\tau) = 0$ the boundary-layer set of four equations (6.16), (6.5d)-(6.5f), we set to zero the four residuals $\langle BL(u,\tau)|w\rangle$ where $\langle\cdot|\cdot\rangle = \int_0^1 \cdot d\eta$. The weights and the gauging conditions that single out the decomposition $\tau = \tau^{(0)} + \tau^{(1)}$ are chosen to cancel out the corrective terms induced by the deviations $u^{(1)}$ and $\tau^{(1)}$ from the ansatz (6.18). A suitable choice for the gauging conditions which single out the decomposition of the normal stresses τ_{xx} and τ_{yy} is

$$\int_0^1 w_\alpha(\eta)\kappa_{Bi}(|\tau_d|)\tau_\alpha d\eta = \int_0^1 w_\alpha(\eta)\kappa_{Bi}(|\tau_d^{(0)}|)\tau_\alpha^{(0)} d\eta \tag{6.21}$$

where α stands for the subscripts xx or yy. The averaged viscoplastic response of the normal stresses to the shear is therefore assumed to be all contained in $\tau^{(0)}$. Considering the tangential stress τ_{xy}, we adopt a gauging condition that is compatible with the modeling approach of a power-law falling film developed by Ruyer-Quil *et al.* [116]:

$$\int_B^1 w_{xy}(\eta)\kappa_{Bi}(|\tau_d|)\tau_{xy}d\eta = \int_B^1 w_{xy}(\eta)\kappa_{Bi}(|\tau_d^{(0)}|)\tau_{xy}^{(0)}d\eta \tag{6.22}$$

The viscous response of shear $\dot{\gamma}_{xy}$ to the stress in the yielded region is assumed to be all contained in the definition of $\tau_{xy}^{(0)}$. After linearization,(6.22) can be recast as

$$\int_B^1 w_{xy}(\eta)\left\{\kappa_B(\eta) + \eta\frac{d\kappa_B}{ds}(s=\eta)\right\}\tau_{xy}^{(1)}d\eta = 0 \tag{6.23}$$

It is easy to show that the $O(\epsilon)$ correction to the strain rate $\int_0^h w_{xy}\partial_y u^{[1)}dy$ in (6.5f) is canceled by choosing $w_{xy} = \eta$. To achieve consistency at order ϵ of the averaged balance of the tangential stress (6.5f), the contribution of the deviations $\tau^{(1)}$ to the viscoplastic terms must also be dropped off, which reads

$$\int_0^B w_{xy}(\eta)\kappa_{Bi}(|\tau_d|)\tau_{xy}d\eta = \int_0^B w_{xy}(\eta)\kappa_{Bi}(|\tau_d^{(0)}|)\tau_{xy}^{(0)}d\eta \tag{6.24}$$

Since $w_{xy} = \eta$ and $\tau_{xy}^{(0)} = T_{xy}\eta$ and $\kappa_{Bi}(|\tau_d|) = O(\epsilon)$ in the pseudo-plug region, the following condition

$$\int_0^B \eta^2\left\{\kappa_{Bi}(|\tau_d|) - \kappa_{Bi}(|\tau_d^{(0)}|)\right\}d\eta = 0 \tag{6.25}$$

can be substituted to (6.24) to achieve consistency at $O(\epsilon)$. Considering that $\tau_{xx}^{(0)}$ and $\tau_{yy}^{(0)} \propto \sqrt{B^2-\eta^2}$, (6.25) and (6.21) are identical up to $O(\epsilon^2)$ if

$$w_{xx} = w_{yy} = \eta^2/\sqrt{B^2-\eta^2} \qquad \text{when} \qquad \eta \le B \qquad \text{and} \qquad w_{xx} = w_{yy} = 0 \qquad \text{otherwise} \tag{6.26}$$

However this choice of weight does not lead to convergent integrals when the convected time derivative of τ_{xx} is averaged. Therefore, I choose the simplest uniform weight to evaluate these terms and define the averaged strain balance as

$$\begin{aligned}\int_0^B De\left(\partial_t\tau_{xx}^{(0)} + u^{(0)}\partial_x\tau_{xx}^{(0)} + v^{(0)}\partial_y\tau_{xx}^{(0)} - 2\tau_{xx}^{(0)}\partial_x u^{(0)}\right)d\eta \\ +\frac{4}{\pi B}\int_0^B \frac{\eta^2}{\sqrt{B^2-\eta^2}}\left(\kappa_{Bi}(|\tau_d^{(0)}|)\tau_{xx}^{(0)} - 2\partial_x u^{(0)}\right)d\eta \;=\; O(\epsilon^2) \qquad ,\end{aligned} \tag{6.27}$$

where $\partial_y u^{(0)} = 0$ at $0 \le \eta \le B$ has been taken in account. In equation (6.27), the plastic response of the pseudo-plug to an elongational strain is thus correctly captured

(corrections to the second row of (6.27) are effectively of higher order than ϵ), yet the elastic response of the pseudo-plug is not consistently evaluated.

Turning to the averaged momentum balance, consistency at $O(\epsilon)$ can be achieved when the weight w_M is chosen to cancel out the $O(\epsilon)$ correction from $\int_0^1 w_M(\eta)\partial_\eta \tau_{xy} d\eta$. An integration by parts gives

$$\int_0^1 w_M \partial_\eta \tau_{xy} d\eta = [w_M \tau_{xy}]_0^1 - \int_0^1 w'_M \tau_{xy} d\eta \tag{6.28}$$

$w_M(1)$ can be taken equal to zero and $\tau_{xy}(\eta = 0)$ is given by the boundary condition (6.17). In order to make use of the gauge conditions (6.23), w_M must be chosen proportional to

$$\begin{aligned} w'_M &= \eta\kappa_B(\eta) + \eta^2 \frac{d\kappa_B}{ds}(s=\eta)\,, \quad \text{for}\, \eta > B \qquad \text{and} \quad w'_M = 0 \quad \text{otherwise} \\ w_M(1) &= 0 \end{aligned} \tag{6.29}$$

After integration, we obtain

$$\begin{aligned} w_M(\eta; B) &= \frac{1}{n+1}\left[(nB+1)(1-B)^{\frac{1}{n}} - (nB+\eta)(\eta - B)^{\frac{1}{n}}\right] \qquad \text{if} \qquad \eta > B\,, \\ \text{and} \qquad w_M(\eta; B) &= \frac{1}{n+1}(nB+1)(1-B)^{\frac{1}{n}} \qquad \text{otherwise} \end{aligned} \tag{6.30}$$

Integrating the boundary layer equations (6.16), (6.5d)-(6.5f) with the weight w_M given by (6.30), $w_{xy} = \eta$ and $w_{xx} = w_{yy}$ leads to a set of four residuals which are consistent at order ϵ. However, since $\tau_{xy}^{(0)}\partial_y u^{(0)} = 0$ in the pseudo-plug and $\tau_{yy}^{(0)}\partial_y u^{(0)} = 0$, the nonlinear elastic coupling of the normal and tangential stresses are not taken into account in our derivation. It follows that our system of equations is degenerate. The residual obtained by averaging (6.5e) is identical to the one corresponding to (6.5d) when $-T_{xx}$ is substituted for T_{yy}. Thus $T_{yy} = -T_{xx}$ and a linear combination of the residuals lead to system of evolution equations for q, T_{xx} and T_{xy} completed by the mass balance (6.20). I have further simplified the averaged momentum balance and averaged elongational strain

balance with the substitution $T_{xy} = \Lambda h + O(\epsilon)$.

$$
\begin{aligned}
De\partial_t T_{xy} &= De\left(-F_{xy}(B)\frac{q}{h}\partial_x T_{xy} + G_{xy}(B)\frac{T_{xy}}{h}\partial_x q\right) && \text{(6.31a)}\\
&\quad + \frac{3q}{h^2} - 3\left[\phi(B) + B^{2+1/n}\Gamma(r)\right]|T_{xy}|^{1/n-1}T_{xy} \\
De\partial_t T_{xx} &= De\left(-F_{xx}(B)\frac{q}{h}\partial_x T_{xx} + G_{xx}(B)\frac{T_{xx}}{h}\partial_x q + H_{xx}(B)\frac{qT_{xx}}{h^2}\partial_x h\right) \\
&\quad - \frac{16}{\pi^2}Bi^{1/n-1}\Gamma(r)T_{xx} + L_{xx}(B)\frac{\partial_x q}{h} - M_{xx}(B)\frac{q}{h^2}\partial_x h && \text{(6.31b)}\\
Re\partial_t q &= Re\left[-F_M(B)\frac{q}{h}\partial_x q + G_M(B)\frac{q^2}{h^2}\partial_x h\right] \\
&\quad + I_M(B)\left[\Lambda h(1-\cot\beta\partial_x h) + We h\partial_{xxx}h - T_{xy}\right] \\
&\quad + L_M(B)\left[h\partial_x T_{xx} - T_{xx}\partial_x h\right] && \text{(6.31c)}
\end{aligned}
$$

where

$$
\Gamma(r) = \int_0^1 \frac{\left(\sqrt{\eta^2 + r(1-\eta^2)} - 1\right)^{1/n}}{\sqrt{\eta^2 + r(1-\eta^2)}}\eta^2 d\eta \qquad \text{(6.31d)}
$$

and $r = (T_{xx}/T_{xy})^2$ The coefficients entering into (6.31) are functions of $B(x,t) = Bi/T_{xy}$

that are listed below:

$$F_{xy} = \frac{(1+n)(1+2n)[1+n(4+3B+3(1+B)^2n)]}{(1+3n)(1+4n)(1+n+Bn)^2} \tag{6.32a}$$

$$G_{xy} = \frac{n(1-B)(1+n+Bn)}{(1+n)(1+2n)}F_{xy} \tag{6.32b}$$

$$F_{xx} = \frac{1+2n}{1+n+Bn} \tag{6.32c}$$

$$G_{xx} = \frac{n(1-B)}{1+n+Bn} \tag{6.32d}$$

$$H_{xx} = \frac{Bn(1+2n)}{(1+n+Bn)^2} \tag{6.32e}$$

$$L_{xx} = \frac{8(1+2n)}{\pi B(1+n+Bn)} \tag{6.32f}$$

$$M_{xx} = \frac{(8(1+n)(1+2n)}{B(1+n+Bn)^2\pi} \tag{6.32g}$$

$$F_M = F_{Ma}/F_{Mb} \tag{6.32h}$$

$$\begin{aligned} F_{Ma} = {} & 144+(768+414B)n+(1572+1971B+360B^2)n^2 \\ & +(1548+3346B+1691B^2)n^3+(732+2368B+2816B^2)n^4 \\ & +(132+568B+1928B^2)n^5+432B^2n^6 \end{aligned} \tag{6.32i}$$

$$\begin{aligned} F_{Mb} = {} & 3(2+n)(3+4n)(1+n+Bn) \\ & \times(4+8n+10Bn+4n^2+13Bn^2+9B^2n^2+12B^2n^3) \end{aligned} \tag{6.32j}$$

$$G_M = G_{Ma}/G_{Mb} \tag{6.32k}$$

$$\begin{aligned} G_{Ma} = {} & (1+n)(1+2n)(72+(252+234B)n \\ & +(324+721B+198B^2)n^2+(180+694B+ \\ & 606B^2)n^3+(36+196B+564B^2)n^4+144B^2n^5) \end{aligned} \tag{6.32l}$$

$$G_{Mb} = (1+n+Bn)F_{Mb} \tag{6.32m}$$

$$I_M = \frac{2(2+3n)(1+n+Bn)(1+n(1+2B(1+Bn)))}{(1+2n)(4+n(4(2+n)+B(10+n(13+3B(3+4n)))))} \tag{6.32n}$$

$$L_M = \frac{B^2(2+3n)(1+Bn)(1+n+Bn)\pi}{4+n(4(2+n)+B(10+n(13+3B(3+4n))))} \tag{6.32o}$$

Consistency of the model is achieved up to $O(\epsilon)$, all terms of higher order being omitted. However, the model does not take into account the elongational viscosity of the yielded region, i.e., the viscous contribution to (6.31b) from the evaluation of $\kappa_{Bi}(|\tau_d|)\tau_{xx}$ in the yielded region. A direct consequence is that L_M goes to zero when $B \to 0$. The contribution from the normal stress τ_{xx} disappears in the momentum balance when the pseudo-plug disappears.

Base flow solutions to (6.31) are given by

$$T_{xy} = \Lambda h\,, \qquad |T_{xx}| \leq \Lambda h\,, \qquad q = \Lambda^{1/n}\phi(Bi/(\Lambda h))h^{\frac{2n+1}{n}}\,. \tag{6.33}$$

where Λ is solution to (6.14).

6.4 Linear stability analysis based on the low-dimensional model

Turning to the stability analysis of the low-dimensional model (6.20, 6.31) leads to the dispersion relation:

$$\begin{aligned} \mathrm{i}I_M\Lambda - c^2 kRe + cF_M kRe\tilde{\phi} - G_M kRe\tilde{\phi}^2 + \frac{\mathrm{i}I_M\Lambda n\{c(3+\mathrm{i}DeG_{xy}k\Lambda) - 6\tilde{\phi}\}}{-3\tilde{\phi} + n\{3B\phi' - \mathrm{i}Dek\Lambda(c - F_{xy}\tilde{\phi})\}} \\ +k\left(\cot\beta I_M\Lambda + \frac{cL_ML_{xx} - L_MM_{xx}\tilde{\phi}}{De(c - F_{xx}\tilde{\phi})} + I_Mk^2We\right) = 0 \end{aligned} \tag{6.34}$$

where $\tilde{\phi} = \phi\Lambda^{1/n}$ and ϕ is defined in (6.18f) and all the coefficients F_{xy}, F_{xx}, G_{xy},...,L_M are computed at $B = Bi/\Lambda$. The critical Reynolds number of the long-wave instability mode ($k = 0$) can be obtained through a long-wave expansion of the phase velocity $c = c_0 + \mathrm{i}kc_1$ where k is real, by requiring that $c_1 = 0$. Thus I get

$$Re_c = \Lambda^{-2/n}n^2Re_{ac}/\left(3Re_{bc}\right) \tag{6.35a}$$

$$\begin{aligned} Re_{ac} &= \Lambda I_M[3\cot\beta + De\Lambda(1+G_{xy})] + 3L_ML_{xx}De^{-1} \\ &\quad +\{De[F_{xy} - 2(1+G_{xy})]I_M\Lambda^2n\phi\}[nBi\phi' - \phi]^{-1} \\ &\quad +\{3L_M(M_{xx} - F_{xx}L_{xx})n\phi\}\{De[-1+n(F_{xx}-2)]\phi + nBDe\phi'\}^{-1}\,, \qquad (6.35b) \\ Re_{bc} &= \{1 + n[4 - F_M + (4 - 2F_M + G_M)n]\}\phi^2 \\ &\quad +B\Lambda n[n(F_M - 4) - 2]\phi\phi' + n^2B^2(\phi')^2\,. \qquad (6.35c) \end{aligned}$$

where ϕ' refers to $d\phi/dB$, and all the coefficients are again computed at $B = Bi/\Lambda$. In the limit $De \ll 1$, Re_c simplifies into

$$Re_c = De^{-1}Re_{bc}^{-1}\Lambda^{2-2/n}n^2L_M\left(L_{xx} + \frac{\phi n(M_{xx} - F_{xx}L_{xx})}{[-1+n(F_{xx}-2)]\phi + nBDe\phi'}\right) + O(1) \tag{6.36}$$

In the limit of a negligible elasticity ($De = 0$) and negligible extensional viscous effects ($L_M = 0$), the instability threshold can be written in terms of the Froude number $\tilde{Fr}^2 = Fr^2/\cot\beta$ as

$$\begin{aligned} \tilde{Fr}_c^{\,2} &= (n^2\Lambda^{-2/n}I_M)\left\{[(1+n(4-F_M+n(4-2F_M+G_M))]\phi^2\right. \\ &\quad \left.+nB[n(F_M-4)-2]\phi\phi' + n^2B^2(\phi')^2\right\}^{-1} \end{aligned} \tag{6.37}$$

which further reduces to

$$\tilde{Fr}_c^{\,2} = \frac{n^2(3n+2)}{2(n+1)^2} \tag{6.38}$$

in the limit $B \to 0$ which correspond to the instability threshold for a power-law falling film. The discrepancy between the formula (6.38) and the corresponding one (5.20) in the chapter 5 originates from slightly different scaling choices (I recall here that the free surface velocity is the velocity scale).

6.5 Linear stability analysis of the primitive equations

In this section, I consider the linear stability of the Nusselt uniform film solution. I first linearize the governing equations (6.5). Thus I perturb the basic state (6.12). This base state corresponds to a "true" solid plug which is not yet yielded. As a consequence, we expect that in the lim $De \to 0$, i.e., when the plug has no elastic response, the instability will be entirely damped out since the plug cannot deformed. Introducing a streamfunction and decomposition on normal modes:

$$\begin{aligned}
u &= U + \Re\left(\psi'(y)e^{\mathrm{i}k(x-ct)}\right), \qquad v = \Re\left(-\mathrm{i}k\psi(y)e^{\mathrm{i}k(x-ct)}\right), \\
\tau_{xx} &= T_{xx} + \Re\left(A_{xx}e^{\mathrm{i}k(x-ct)}\right), \qquad \tau_{xy} = T_{xy} + \Re\left(A_{xy}e^{\mathrm{i}k(x-ct)}\right), \\
\tau_{yy} &= T_{yy} + \Re\left(A_{yy}e^{\mathrm{i}k(x-ct)}\right), \qquad \tau_d = T_d + \Re\left(T_d'e^{\mathrm{i}k(x-ct)}\right),
\end{aligned}$$

where k and c are the wavenumber and phase speed, respectively, and $\Re$ stands for the real part. Thus I obtain a Orr-Sommerfeld problem,

$$\mathrm{i}kRe\left[(U-c)\left(D^2-k^2\right)\psi - \psi U''\right] = \left(D^2+k^2\right)A_{xy} + \mathrm{i}k(A_{xx}' - A_{yy}') \tag{6.39a}$$

$$\begin{aligned}
&De\left[\mathrm{i}k[(U-c)A_{xy} - T_{xy}'\psi] - A_{yy}U' - k^2T_{xx}\psi - T_{yy}\psi''\right] = \psi'' \\
&+k^2\psi - A_{xy}\kappa_{Bi} - (T_{xy}\kappa_{Bi}'/4T_d)\left[(A_{xx}-A_{yy})T_{xx} + 4A_{xy}T_{xy}\right],
\end{aligned} \tag{6.39b}$$

$$\begin{aligned}
&De\left[\mathrm{i}k[(U-c)A_{xx} - 2T_{xx}\psi' - T_{xx}'\psi] - 2A_{xy}U' - 2T_{xy}\psi''\right] = 2\mathrm{i}k\psi' \\
&-A_{xx}\kappa_{Bi} - (T_{xx}\kappa_{Bi}'/4T_d)\left[(A_{xx}-A_{yy})T_{xx} + 4A_{xy}T_{xy}\right],
\end{aligned} \tag{6.39c}$$

$$\begin{aligned}
&De\left[\mathrm{i}k[(U-c)A_{yy} + 2T_{yy}\psi' - T_{yy}'\psi] - 2k^2T_{xy}\psi\right] = -2\mathrm{i}k\psi' \\
&-A_{yy}\kappa_{Bi} - (T_{yy}\kappa_{Bi}'/4T_d)\left[(A_{xx}-A_{yy})T_{xx} + 4A_{xy}T_{xy}\right],
\end{aligned} \tag{6.39d}$$

where $D \equiv d/dy$. The system of equations (6.39) is completed by the boundary conditions at the wall and at the interface,

$$\psi(0) = \psi'(0) = 0\,, \qquad (6.39e)$$

$$A_{xy} + T'_{xy}(1)\frac{\psi(1)}{c - U(1)} = 0\,, \qquad (6.39f)$$

$$\frac{\psi(1)}{c - U(1)}\left(We k^3 + k\cot\beta\right) + kReU(1)\psi'(1) - kReU'(1)\psi(1) - ckRe\psi'(1) + \mathrm{i}A'_{xy}(1) - k(A_{xx}(1) - A_{yy}(1)) = 0\,, \qquad (6.39g)$$

The system (6.39) can be reset into a dynamical system in a four-dimensional complex phase space spanned by ψ, ψ', A_{xy}, A'_{xy}. I solve the system of equations (6.39) by

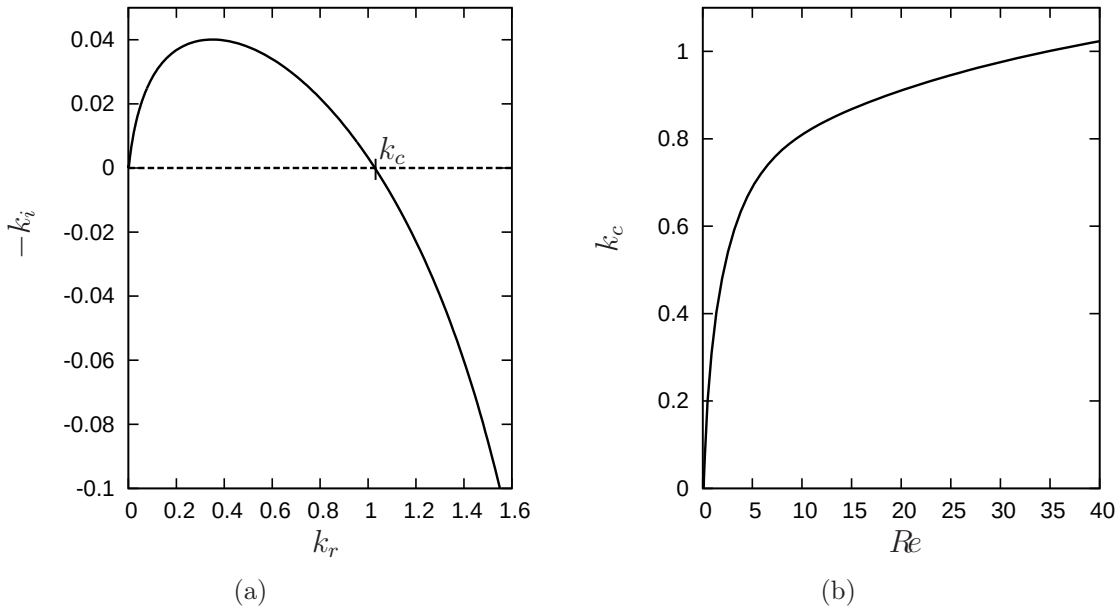

Figure 6.2: (a) Spatial growth rate $-k_i$ versus wavenumber k_r. (b) Marginal stability curve in the plane (Re, k). Inclination angle is $\beta = 45°$. The solid line refer to the solutions to the Orr-Sommerfeld problem (6.39).

continuation using AUTO07P software [40]. I obtain the spatial long-wave mode (k complex and ω real) starting from the solution $k = 0$. This result is obtained for a shear-thinning carbopol fluid whose properties are $\sigma = 0.07 Nm^{-1}$, $n = 0.5$, $G = 28(Pa)$, $K = 3.2(Pas^n)$, $\tau_0 = 3.9(Pa)$ and $\rho = 1010(kgm^{-3})$ [74]. Fig. 6.2(a) shows the behavior of the spatial growth rate $-k_i = -\Im(k)$ as a function of the wavenumber $k_r = \Re(k)$. Reynolds number, $Re = 41$ and the inclination angle $\beta = 45°$ is chosen. Similarly to

the Newtonian case [15], the range of unstable wavenumber extend from zero to the cut-off wavenumber $k_c = 1.038$. Fig. 6.2(b) displays the marginal stability curve in the cut-off wavenumber k_c versus Reynolds number Re plane obtained from solutions to the Orr-Sommerfeld problem (6.39). The range of unstable wave numbers decreases as the Reynolds number is decreased. The instability threshold of the long-wave instability is thus found when the neutral stability curve intenseits the horizontal axis ($k = 0$).

6.6 Determination of the instability threshold

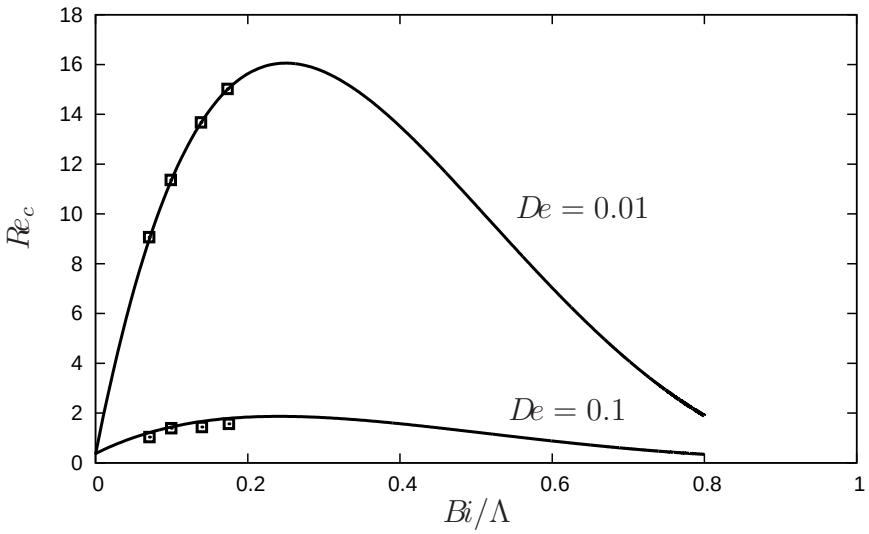

Figure 6.3: Critical Reynolds number Re_c as a function of the relative thickness Bi/Λ of the pseudo-plug region. The solid line correspond to the four equation model (6.31) and squares refer to the numerical solutions to the Orr-Sommerfeld problem (6.39) of the power-law index $n = 0.5$ and inclination angle $\beta = 45°$ (see chapter 6)

In Fig. 6.3, shows the critical Reynolds number against the relative thickness of the pseudo-plug region Bi/Λ. The result of Orr-Sommerfeld problem shows a good agreement with the result of the four-equation model for critical Reynolds number. As expected, lowering the Deborah number has a stabilizing effect. Indeed, if $De = 0$ the plug is solid and cannot deform, as a consequence the instability threshold $Re_c \to \infty$. Yet, the stabilizing effect of the inelastic plug disappears when $Bi \to 0$. This can be explored by the disappearance of the plug region. Surprisingly enough, the same removal of this stabilizing effect also occurs when the plug starts to invade the whole domain.

6.7 Summary and Conclusion

A viscoplastic falling film over an inclined plane is studied. The effect of the elasticity of the pseudo-plug region has been introduced at the free surface by using Saramito's model for elasto-viscoplastic fluid that combines both the Oldroyd viscoelastic model and the Hershel-Bulkley viscoplastic model. A four equation model is produced by using the weighted residual approach for the film thickness h, local flow rate q and amplitudes of the normal and tangential stresses. Orr-Sommerfeld problem is derived to study the linear stability analysis. A linear stability analysis gives values of the critical Reynolds number in remarkable agreement with the Orr-Sommerfeld analysis. A follow-up of this work would be to compute the non-linear roll-wave solutions and to introduce the viscous response of the yielded region. Performing DNSs computations of the non-linear waves will also enable a validation of the modeling approach.

Chapter 7

Conclusion

In this PhD thesis, I have studied the wave dynamics and the stability of a non-Newtonian film falling on an inclined plane under the action of gravitational forces. To this aim, three problems have been explored at low to moderate Reynolds numbers.

Newtonian fluid film flows have been studied from a long time, starting with classical results such as the Benney the equation to two-equation model of Shkadov and so on. Its main features are sketched in the chapter 2. Since the Benney equation is valid only close to the instability threshold and fails to get the true solitary waves for large δ. Kapitz-Shkadov derived a first order model by a uniform averaging, involved a set of two coupled evolution equations for the film thickness h and the local flow rate q which fails to capture the effect of inertia terms when $\delta \gg 1$. It is modified later on by Ruyer-Quil & Manneville [111, 112, 113, 114] who have derived models by applying the weighted residual technique using polynomials as a test functions, and including the effect of the second order viscous dispersion terms. The models, such as full second-order, simplified and regularized models, exhibit one-humped solitary wave branch of solution whose characteristics (speed, amplitude etc.) are close in the drag-gravity regime ($\delta < 1$) but depart significantly one from another in the drag-inertia regime ($\delta \gg 1$). A fundamental question arises: how to obtain the inertia terms in a form that accounts accurately for the drag-inertia regime for the widest possible range of values of the reduced Reynolds number δ? To answer this question, direct numerical simulations (DNSs) are performed. The solitary wave can be characterized by its maximum amplitude, and phase speed in terms of the reduced Reynolds number δ. Solitary-like waves are derived by considering a large enough computational domain in order that the properties of the wave converge asymptotically to the true solitary limit. To compute accurately the properties of stationary traveling wave, Navier-Stokes equations are solved by using the Galerkin finite element method, implemented with periodic boundary conditions and strong mesh refinement in the vicinity of the solitary wave. The results of the solitary wave properties are briefly discussed in chapter 3. A backflow phenomenon is also observed in the origin of capillary ripples at high inertia value. This reversal phenomenon is related to the amplitude of the capillary

waves which will not be observed when viscous dispersion effects become strong at the trough of the wave, i.e., when the capillary ripples are damped. The phase speed of the solitary waves is not affected by the viscosity of the fluid when approaching the asymptotic limit at $\delta \gg 1$ whereas the amplitude of the wave is dependent on viscosity and is stabilized by the viscous diffusion effects at low Γ. In the transition region, both the height and the phase speed of the wave show maximum inflections at intermediate values of δ. These are unique characteristics of the four-equation model by Ruyer-Quil & Manneville [112]. It is also observed that for the same δ, the phase speed and wave height get smaller when approaching the instability threshold or the critical Froude number. It is confirmed by DNSs result that there is no more waves above the $Fr_c^{-2} = 2/5$ and on the other side, the phase speed and the maximum amplitude of solitary wave reaches the largest values at $Fr^{-2} = 0$ for the flow along the vertical wall. The accuracy of the four-equation model has been tested with DNSs using periodic boundary conditions for the solitary wave solutions. The four-equation model captures well the speed, amplitude and shape of the solitary wave and shows a good agreement with the DNSs result.

In chapter 4, most commonly used rheological constitutive laws are described for non-Newtonian fluids. These laws have been used in the falling film problem in chapter 5 and 6.

In chapter 5, a power-law falling film flow over an inclined plate is studied. The viscosity of a power-law fluid diverges when the strain rate goes to zero which has been taken care by introducing a Newtonian plateau at small strain rate. A weighted residual approach is applied to get a two-equation model within the framework of lubrication theory. The derived model is the combination of the exact mass balance and the averaged momentum equation, which is a set of two coupled evolution equations for the film thickness h and the local flow rate q. Consistency of the model is achieved up to first order in the film parameter for inertia terms and up to second order for viscous terms, which is sufficient to capture the onset of instability and the damping of the short waves. In the non-linear regime, the amplitude and wave number of both slow γ_1 and fast γ_2 waves decreases as the power-law index is decreased. The capillary waves of the traveling wave are reduced by the damping of viscosity. In the presence of these terms, γ_2 waves are generated from a Hopf bifurcation point and γ_1 waves from the γ_2 waves through a period doubling bifurcation.

A remarkable agreement with the Orr-Sommerfeld stability analysis has been obtained and particularly, the instability threshold is accurately recovered. Comparisons to the DNSs of two-phase flows demonstrate that the models correctly predicts the phase speed, maximum amplitude and shape of large-amplitude nearly solitary like waves and particularly, the details of the capillary ripples, the capillary shock region, preceding the main humps are captured correctly. Comparisons to Orr-Sommerfeld stability analysis and to DNS shows convincing agreement in both linear and nonlinear regimes. The mechanisms of the primary instability have been deciphered within the framework of Whitham wave hierarchy. The influence of shear-thinning or shear-thickening on the primary instability

is shown to be non trivial. A destabilization of the base flow close to threshold is promoted by the shear-thinning effect, whereas, far from threshold, it tends to stabilize the base flow when the viscous damping of short waves becomes dominant. A reverse situation is observed in the case of shear-thickening fluids. Shear-thinning accelerates solitary waves and promotes a subcritical onset of traveling waves at larger wavenumber than the linear cut-off wavenumber. A conditional stability of the base flow is thus observed. This phenomenon results from a reduction of the effective viscosity at the free surface. When compared to DNS, simulations of the temporal response of the film based on weighted residual model satisfactorily capture the conditional stability of the film.

In chapter 6, the stability of a viscoplastic fluid film falling down an inclined plane is explored, with the aim of determining the critical Reynolds number for the onset of the instability threshold. A low-dimensional model is derived for this flow based on the long-wave expansion method. A four equation model is produced by using the weighted residual approach for the film thickness h, local flow rate q and amplitudes of the normal and tangential stresses. Orr-Sommerfeld problem is derived to study the linear stability analysis. A linear stability analysis gives values of the critical Reynolds number in remarkable agreement with the Orr-Sommerfeld analysis.

As possible perspectives to this work, I want to mention the importance of the complex fluid flow phenomena for understanding some geophysical problems such as slurry flows, debris flow, rill formation and so on. One can include the slip at the wall to simulate real slurry flow and snow avalanches. One can derive a model for falling film problem by taking corrugated, rough or non-flat wall to consider secondary instabilities from two-dimensional to three-dimensional flows.

Appendix A

Appendix

A.1 Self-similarity and definition of the weight function

We shall now show that the solution to $\mathcal{L}w = cst$ is proportional to the constant-thickness velocity profile f_0 as a result of the self-similarity of the constant-thickness solution u_0. Consider a film of thickness $1+\varphi$ with $\varphi \ll 1$, the constant-thickness solution u_0 then writes

$$u_0 = (1+\varphi)^{(n+1)/n} f_0[y/(1+\varphi)] = [1+\varphi(n+1)/n] f_0(Y) + O(\varphi^2)$$

with $Y = y/(1+\varphi)$. The change of scales $Y = y/(1+\varphi)$ gives

$$d_Y[(d_Y u_0)^n] = -(1+\varphi)^{n+1} = -1-(n+1)\varphi + O(\varphi^2)\,.$$

Using $u_0 = f_0 + \varphi(n+1)/n f_0 + O(\varphi^2)$ we get

$$d_Y[(d_Y f_0)^n] + [\varphi(n+1)/n]\,\mathcal{L}f_0 + O(\varphi^2) = -1-(n+1)\varphi + O(\varphi^2)$$

and finally

$$\mathcal{L}f_0 = -n\,. \tag{A.1}$$

A.2 Estimation of the interfacial shear stress

In the present work, we have assumed that the air plays only a passive role in the development of the liquid film dynamics. We thus have written a one-sided description of the problem at hand by assuming the gas phase to stay at rest. This one-sided model relies on the assumption of a negligible friction at the interface between the two phases, which gives the zero tangential stress condition (5.3a).

A direct consequence of assuming a zero tangential stress at the interface is that the strain rate also goes to zero at the interface in the case of the basic uniform film solution

Fluid	τ_i (mPa)	τ_c (mPa)
Set 1	10	14
Set 2	22	140
Set 3	30	360

Table A.1: Interfacial and critical shear stresses τ_i and τ_c for $Re = 100$, $\beta = 15°$ and the fluid properties given in table 5.1. The gas phase properties correspond to air $\nu_{\rm air} = 15 \times 10^{-6}$ m^2/s and $\rho_{\rm air} = 1.3$ kg/m^3.

whose stability has been studied in § 6.5. Because of the divergence of the viscosity in the zero strain rate limit, we have been led to consider a Newtonian layer at the free surface whose presence strongly affects the stability of the basic solution and modifies the nature of the bifurcation of traveling-wave solutions from the marginal stability conditions when shear-thinning fluids are considered.

The presence of this Newtonian layer in the basic state of a shear-thinning liquid film should be proved when the friction of the gas phase is considered. We must thus estimate the shear stress and the strain rates at the interface of the film in the inception region of the flow prior to the instability onset. The time t_0 that is necessary for the uniform film solution to develop from the injection of the fluid can be estimated by considering a plug flow at the injection of the liquid, a quasi-constant thickness $\bar{h}_{\rm N}$ of the film and a gas phase initially at rest, whose density, dynamic and kinematic viscosities are denoted by $\rho_{\rm air}$, $\mu_{\rm air}$ and $\nu_{\rm air}$. An estimation from below can be reached by assuming a constant kinematic viscosity in the liquid equals to its maximum $\nu_0 = \mu_0/\rho$. We thus get $t_0 \approx \bar{h}_{\rm N}^2/[25\nu_0]$ from boundary-layer theory [124]. At this time, the layer of gas that is dragged by the liquid has a thickness roughly equal to $5\sqrt{\nu_{\rm air} t_0} = \bar{h}_{\rm N}\sqrt{\nu_{\rm air}/\nu_0}$. From there, we can estimate the strain rate $\dot{\gamma}_{\rm air}$ in the gas phase from the velocity of the liquid at the interface which reaches $nV/(n+1)$ for the fully developed basic state solution. We get $\dot{\gamma}_{\rm air} \sim nV\sqrt{\nu_0/\nu_{\rm air}}/[(n+1)\bar{h}_{\rm N}]$. The interfacial shear stress is given by $\tau_i = \mu_{\rm air}\dot{\gamma}_{\rm air}$ and shall be compared to the critical shear stress $\tau_c = \mu_0\dot{\gamma}_c$ above which the fluid rheology is non-Newtonian. τ_i and τ_c are compared in table A.1 in the worst case, i.e. for $Re = 100$. In all cases, τ_i is found to be less than τ_c (recall that τ_i is actually estimated from above). We can therefore conclude that the basic uniform solution should present a Newtonian layer before it undergoes an instability, the interfacial shear stress being too weak to get rid of it. We can therefore conclude that taking into account the interfacial shear stress should not modify the conclusion of this study.

A.3 Coefficients of the Newtonian-power-law model

The coefficients of the averaged momentum balance (5.48) are given below in a fraction form $\tilde{X} = \tilde{X}_a/\tilde{X}_b$.

$$\begin{aligned}
\tilde{F}_a &= 630n((n+1)^2(7n+3)) + (n-1)\bar{\eta_c}^{2+1/n}\{105n(4n+3)[n(34n+35)+8] \\
&\quad +14(4n+3)\bar{\eta_c}^{1+1/n}[3(2n+1)(n(9n(n-4)-4)+6)+10(n-1)(n+1)^2(3n+2)\bar{\eta_c}] \\
&\quad +(2n+1)\bar{\eta_c}^{2+2/n}[-15(n-6)(2n+1)(3n+2)(4n-3) \\
&\quad +28(n-1)(n+1)^2(3n-7)(4n+3)\bar{\eta_c}\}] \,, \qquad \text{(A.2a)} \\
\tilde{F}_b &= 42(n+1)(2n+1)(4n+3)\left[15(n+1)\right. \\
&\quad \left.+(n-1)\bar{\eta_c}^{1+1/n}\left(30n+20+(2n+1)(3n-7)\bar{\eta_c}^{1+1/n}\right)\right] \,, \qquad \text{(A.2b)} \\
\tilde{G}_a &= 630n^3(n+1)+(n-1)\bar{\eta_c}^{2+1/n}\left\{105n^2(4n+3)(10n+7)+14(4n+3)\bar{\eta_c}^{1+1/n}\right. \\
&\quad 3(2n+1)\{n[n(3n-25)+3)+6\}+10(n-1)(n+1)^2(3n+2)\bar{\eta_c}\big] \\
&\quad +(2n-1)\bar{\eta_c}^{2+2/n}\left[28\bar{\eta_c}(4n+3)(3n-7)(n+1)^2(n-1)\right. \\
&\quad \left.\left.-15(4n-3)(3n+2)(2n+1)(n-6)\right]\right\} \,, \qquad \text{(A.2c)} \\
\tilde{G}_b &= \frac{n}{n+1}\tilde{F}_b \,, \qquad \text{(A.2d)} \\
\tilde{I}_a &= 5(n+1)(3n+2)\left[3+2(n-1)\bar{\eta_c}^{2+1/n}\right] \,, \qquad \text{(A.2e)} \\
\tilde{I}_b &= \frac{1}{21(2n+1)(4n+3)}\tilde{G}_b \,, \qquad \text{(A.2f)}
\end{aligned}$$

A.4 Orr-Sommerfeld analysis of Carreau-law films

In this section, we consider the primary stability of a uniform film flow when the rheological behavior of the liquid is governed by the three-parameter Carreau law (5.30). The base flow is given by

$$1-y = (s^2+U'^2)^{(n-1)/2}U' \qquad \text{(A.3)}$$

with the no slip condition $U(0)=0$.

Proceeding to The decomposition in normal modes of infinitesimal perturbations around the base state leads to the Orr-Sommerfeld equation

$$\begin{aligned}
\mathrm{i}kRe\left[(U-c)(D^2-k^2)\psi-\psi U''\right] &= \left(D^2+k^2\right)\left[(s^2+U'^2)^{(n-3)/2}(s^2+nU'^2)\left(D^2+k^2\right)\psi\right] \\
&\quad -4k^2D\left[(s^2+U'^2)^{(n-1)/2}D\psi\right] \,, \qquad \text{(A.4)}
\end{aligned}$$

where k and c refer again to the wavenumber and phase speed respectively. The boundary conditions associated with (A.4) are (5.63c), (5.63d) and (5.63e). [109] and [142] have

considered the stability of a shear-thinning falling film using a four-parameter Carreau law accounting for Newtonian plateaus at high and low shear rates. The system (A.4), (5.63c), (5.63d) and (5.63e) corresponds to the Orr-Sommerfeld system of equations derived by [142] when the influence of the Newtonian plateau at high shear rate is neglected, that is when the parameter I is set to zero in their formulation.

A.5 Simulation file of Gerris

Gerris is a console-based program. It takes parameter or simulation files called 'filmst.gfs' as input and produces various types of files as output.

```
# case plan with shear-thinning fluid
# pb detected: it lacks a root of 2 in the definition of D2
# values of the parameters
 Define REYNOLDS 50.
 Define BOND 61.097250694361961
 Define RATIO 21.583246059529323
 Define N 0.607

# computational domain: length and depth level of mesh
 Define LEVEL 11
 Define LENGTH 60.

# plan: height and angle of inclination (in degrees)
 Define RADIUS 0.5
 Define ANGLE 15

# density in the liquid (1) and gas (1 / 100)
 Define RHO(T) (T + 1./100.*(1. - T))

# body of the function: Navier-Stokes(a box with a periodicity of flow)
1 1 GfsSimulation GfsBox GfsGEdge {} {

# parameters of the computational domain length, specific volume
# (gravity = 1 by default)
    PhysicalParams { L = LENGTH }
    PhysicalParams { alpha = 1./RHO(T) }

# refinement default domain
    Refine 6
```

```
# refinement for a maximum surface area < 2 times the height of
# the liquid + Plan
    Refine (y < 2.*(RADIUS + 1.) ? LEVEL : 6)
    Refine (y < RADIUS + 1.1 && y > RADIUS+ 0.9 ? LEVEL+2 : 6)

# definition of map in domain
    Solid (y - RADIUS)

# interface definition, the variable 'radius' Position and function
    VariableTracerVOF T
    VariableCurvature K T Kmax
    VariablePosition Y T y

# definition of surface tension
    SourceTension T BOND K

# initialization of the interface
    InitFraction T (1. + RADIUS + 0.1*sin(2.*M_PI/LENGTH*x) - y)

# initialization of the semi-parabolic velocity in the liquid
    Init {} {
U = {
          y = y - RADIUS;
          if (y < 1.)
            return (N/(N+1.))*(1.- exp((N+1.)*log(1- y)/N))*sqrt(REYNOLDS);
          else
            return sqrt(REYNOLDS)*N/(N+1.);
        }
    }

# definition of volume forces
    Source U T
    Source V -T/tan(ANGLE*M_PI/180.)

# definition of viscosity
  SourceViscosity {} {
    double mu, mumax;
    double m;
    mu = exp (-0.5*N*log (REYNOLDS)) ;
    mumax = RATIO/sqrt(REYNOLDS) ;
    if (D2 > 0.)
```

```
        m = mu*exp ((N - 1.)*log (sqrt(2.)*D2));
    else
        m = mumax;
    return RHO(T)*MIN(m, mumax);
    } {
    # Crank-Nicholson does not converge for these cases, we need backward Euler
    # (beta = 0.5 -> Crank-Nicholson, beta = 1 -> backward Euler)
    beta = 1
  }

# adaptation of the mesh according to the vorticity
    AdaptVorticity { istep = 1 } { maxlevel = LEVEL cmax = 1 }

# adaptation of the mesh in the liquid
    AdaptFunction { istep = 1 } { cmax = 0 maxlevel = (LEVEL - 3) } (T > 0.)

# adaptation of the mesh on the free surface
    AdaptFunction { istep = 1 } {
cmax = 0.
maxlevel = LEVEL
cfactor = 2
    } (T > 0. && T < 1. ? Kmax*dL : 0)

# results: standards enable the position and velocity in the fluid
    OutputScalarNorm { istep = 1 } y { v = Y }
    OutputScalarNorm { istep = 1 } u { v = U*T }
    OutputScalarNorm { istep = 1 } v { v = V*T }

# results: average height of the liquid
    OutputScalarNorm { istep = 1 } h { v = T }

# graphical results for Gfsview
    OutputSimulation { step = 5 } sim-%lf.gfs
    EventScript { step = 5 } { gzip -f -q sim-*.gfs }

# graphical results to form a video
    OutputSimulation { step = 0.1 } stdout
    EventScript { step = 0.1 } { echo "Save stdout { width = 1024 height = 1024 }" }
}
# boundary condition of the domain (Dirichlet condition on the map)
GfsBox {
```

```
    top = Boundary { BcDirichlet U 0 }
}
# periodicity of the flow (from right to left)
1 1 right
```

Bibliography

[1] Adomeit, P. and Renz, U. 2000. Hydrodynamics of three-dimensional waves in laminar falling films. *Int. J. Multiph. Flow* **26**, 1183-1208.

[2] Alekseenko, S.V., Nakoryakov, V.E. and Pokusaev, B.G. 1979. Wave formation in liquid film flow on a vertical wall. *J. App. Mech. Tech. Phys.* **20**(6), 719-727.

[3] Alekseenko, S.V., Nakoryakov, V.Y. and Pokusaev, B.G. 1985. Wave formation on a vertical falling liquid film. *AIChE J.*, **31**, 1446.

[4] Alekseenko, S.V., Nakoryakov, V.Y. and Pokusaev, B.G. 1990. Wave flow of liquid films. 3rd edn. Begell House (New York).

[5] Amaouche, M., Djema, A. and Bourdache, L. 2009. A modified Shkadov's model for thin film flow of a power law fluid over an inclined surface. *Comptes Rendus Mécanique* **337**(1), 48-52.

[6] Bach, P. and Villadsen, J. 1984. Simulation of the vertical flow of a thin wavy film using a finite element method. *Int. J. Heat Mass Transfer* **27**, 815.

[7] Balmforth, N.J. and Provenzale, A. 2001. Geomorphological Fluid Mechanics. Lecture Notes in Physics, **582** Chapter 2, Springer.

[8] Balmforth, N.J. and Liu, J.J. 2004. Roll waves in mud. J. Fluid Mech. **519**, 33-54.

[9] Benney, D.J. 1966. Long waves on liquid films. *J. Math. Phys.* **45**, 150.

[10] Benjamin, T.B. 1957. Wave formation in laminar flow down an inclined plane. J. Fluid Mech. **2**, 554; corrigendum **3**, 657.

[11] Benito, S., Bruneau, C.-H., Colin, T., Gay, C. and Molino, F. 2008. An elasto-visco-plastic model for immortal foams or emulsions. *Eur. Phys. J. E.* **25**, 225-251.

[12] Bewersdorff, H.-W. and Singh, R.P. 1988. Rheological and drag reduction characteristics of xanthan gum solutions. *Rheol. Acta.* **27**, 617-627.

[13] Boudlal, A. and Liapidevskii, V.Yu. 2002. Stability of Roll Waves in Open Channels. Comptes Rendus Mécanique, **330**(4), 209-295.

[14] Boudlal, A. and Liapidevskii, V.Yu. 2010. Stability of Roll Waves on a Vertical Wall. International Conference - Fluxes and Structures in Fluids: Physics of Geospheres. Moscow. 48-53.

[15] Brevdo, L., Laure, P., Dias, F. and Bridges, T.J. 1999. Linear pulse structure and signaling in a film flow on an inclined plane. J. Fluid Mech. **396**, 37-71.

[16] Brauner, N. and Maron, D.M., Dias, F. and Bridges, T.J. 1982. Characteristics of inclined thin films, waviness and the associated mass transfer. *Int. J. Heat Mass Transfer* **25**, 99.

[17] Buchin, V.A. and Shaposhnikova, G.A. 2009. Flow of Shallow Water with a Periodic System of Jumps over a Vertical Surface. Doklady Physics, **54**(5), 248-251.

[18] Carnahan, B., Luther, H.A. and Wilkes, J.O. 1969. Applied Numerical Methods. John Wiley and Sons, Inc.

[19] Chang, H.-C., Demekhin, E.A. and Kopelevitch, D.I. 1993. Construction of stationary waves on a falling film. *Comput. Mech.* **11**, 313-322.

[20] Chang, H.-C., Demekhin, E.A. and Kopelevitch, D.I. 1993. Nonlinear evolution of waves on a vertically falling film. J. Fluid Mech. **250**, 433-480.

[21] Chang, H.-C. 1994. Wave evolution on a falling film. *Ann. Rev. Fluid Mech.*. **26**, 103.

[22] Chang, H.-C., Demekhin, E.A., Kalaidin, E. and Ye, Y. 1996. Coarsening dynamics of falling-film solitary waves. *Phys. Rev. E.* **54**, 1467-1477.

[23] Chang, H.-C., Demekhin, E.A. and Kalaidin. 1998. Generation and suppression of radiation by solitary pulses. *SIAM (Soc. Ind. Appl. Math.) J. Appl. Math.*. **58**, 1246.

[24] Chang, H.-C. and Demekhin, E.A. 2000. Coherent structures, self similarity, and universal roll-wave coarsening dynamics. *Phys. Fluids.* **12**(9), 2268-2278.

[25] Chang, H.-C. and Demekhin, E.A. 2002. Complex Wave Dynamics on Thin Films. D. Möbius and R. Miller, Elsevier.

[26] Chen, L.H. and Chang, H.-C. 1986. Nonlinear waves on liquid film surfaces-ii. bifurcation analysis of the long wave equation. *Chem. Eng. Sci.* **41**, 2477.

[27] Cheddadi, I., Saramito, P., Dollet, B., Raufaste, C. and Graner, F. 2011. Understanding and predicting viscous, elastic, plastic flows. *Eur. Phys. J. E.* **34**, 11001.

[28] Choppe, E., Puaud, F., Nicolai, T. and Benyahia, L. 2010. Rheology of Xanthan solutions as a function of temperature, concentration and ionic strength. *Carbohydrate Polymers* **82**, 1228-1235.

[29] Coussot, P. 1997. Mudflow rheology and dynamics. *IAHR Monograph Series*, Balkema, Brookfield, Vt.

[30] Craster, R.V. and Matar, O.K. 2009. Dynamics and stability of thin liquid films. *Rev. Mod. Phys.* **81**, 1131-1198.

[31] Crochet, M.J. and Waters, K. 1983. Numerical methods in non-Newtonian fluid mechanics. Ann. Rev. Fluid Mech. **15**, 241.

[32] Dandapat, B.S. and Mukhopadhyay, A. 2001. Waves on a film of power-law fluid flowing down an inclined plane at moderate Reynolds number. *Fluid Dyn. Res.* **29**, 199-220.

[33] Dandapat, B.S. and Mukhopadhyay, A. 2003. Waves on the surface of a falling power-law fuid. *Int. J. Non-Linear Mech.* **38**, 21-38.

[34] Demekhin, E.A. and Shkadov, V.Ya. 1984. Three-dimensional waves in a liquid flowing down a wall. Izv. Akad. Nauk SSSR, Meh. zidk. Gaza **5**, 21-27.

[35] Demekhin, E.A., Kaplan, M.A. and Shkadov, V.Ya. 1987. Mathematical models of the theory of viscous liquid films. Izv. Akad. Nauk SSSR, Meh. židk. Gaza **6**, 73-81.

[36] Demekhin, E.A. and Kaplan, M.A. 1989. Construction of exact numerical solutions of the stationary traveling type for viscous thin films. Izv. Akad. Nauk SSSR, Meh. židk. Gaza **6**, 73-81.

[37] Demekhin, E.A., Tokarev, G.Yu. and Shkadov, V.Ya. 1991. Hierarchy of bifurcations of space-periodic structures in a nonlinear model of active dissipative media. *Physica D.* **52**, 338.

[38] Dietze, G.F., Leefken, A. and Kneer, R. 2008. Investigation of the backflow phenomenon in falling liquid films. J. Fluid Mech. **595**, 435-459.

[39] Dietze, G.F., AL-Sibai, F. and Kneer, R. 2009. Experimental study of flow separation in laminar falling liquid films. J. Fluid Mech. **637**, 73-104.

[40] Doedel, E.J. 2008. AUTO07P Continuation and bifurcation software for ordinary differential equations. *Montreal Concordia University.*

[41] Dressler, R.F. 1949. Mathematical solution of the problem of roll-waves in inclined open channels. *Comm. Pure Appl. Math.* **2**, 149-194.

[42] Émery, H. and Brosse, O. 1995. Écoulement d'un film le long d'un plan incliné: développement spatio-temporel des instabilités. PhD thesis, École Polytechnique, Rapport d'option X92.

[43] Engelund, F. and Wan, Z. 1984. Instablity of hyperconcentrated flow. *J. Hydraulic Res.* **110**, 219-233.

[44] Fernández-Nieto, E.D. Noble, P. and Vila, J.-P. 2010. Shallow Water equations for Non-Newtonian fluids. *J. Non-Newtonian Fluid Mech.* **165**(13-14), 712 - 732.

[45] Fonder, N. and Xanthoulis, S. 2007. Roman aqueduct and hydraulic engineering: case of N'imes aqueduct and its Pont du Gard bridge. *Water Sci.Techn.: Water Supply* **7**, 121-129.

[46] Frenkel, A.L. 1992. Nonlinear theory of strongly undulating thin films flowing down vertical cylinders. *Europhys. Lett.* **18**, 583.

[47] Frenkel, A.L. 1993. On evolution equations for thin films flowing down solid surfaces. *Phys. Fluids A.* **5**, 2342.

[48] Griskey, R.G., Nechrebecki, D.G., Notheis, P.J. and Balmer, R.T. 1985. Rheological and pipeline flow beahvior of corn starch dispersion. *J. Rheology* **29**, 349-360.

[49] Hirt, C.W. and Nichols, B.D. 1981. Volume of fluid (VOF) method for the dynamics of free boundaries. *J. Computational Phys.* **39**(1), 201–225.

[50] Ho, L.W. and Patera, A.T. 1990. A legendre spectral element method for simulation of unsteady incompressible viscous free-surface flows. *Comput. Methods Appl. Mech. Eng.* **80**, 335.

[51] Hoffman, K.A. and Chiang, S.T. 2000. Computational Fluid Dynamics. Volume 1, fourth edition. Engineering Education System, Kansas.

[52] Hwang, C.-C., Chen, J.-L., Wang, J.-S. and Lin, J.-S. 1994. Linear stability of power law liquid film flows down an inclined plane. *J. Phys. D: Appl. Phys.* **27**, 2297-2301.

[53] Isaacson, E. and Keller, H.B. 1966. Analysis of Numerical Methods. John Wiley and Sons, New York.

[54] Javdani, K. and Goren, S.L. 1972. Progress in Heat and Mass Transfer **6**, 253-262.

[55] Jeffreys, T. 1925. The Flow of Water in Inclined Channel of Rectangular Section. Philosophical Magazine, **49**(6), 793-807.

[56] Jones, L.O. and Whitaker, S. 1966. An experimental study of falling liquid films. *AIChE J.* **12**, 525.

[57] Joo, S.W., David, S.H. and Bankoff, S.G. 1991. Long-wave instabilities of heated falling films: two-dimensional theory of uniform layers. J. Fluid Mech., **230**, 117.

[58] Julien, P.Y. and Hartley, D.M. 1986. Formation of roll waves in laminar sheet flow. *J. Hydr. Res.* **24**, 5-17.

[59] Kalliadasis, S., Ruyer-Quil, C., Scheid, B. and Velarde, M.G. 2011. Falling liquid films. *Applied Mathematical Sciences* Vol.176, 1st edn. Springer.

[60] Kapitza, P.L. and Kapitza, S.P. 1949. Wave flow of thin layers of a viscous fluid: III. Experimental study of undulatory flow conditions. In *Collected papers of P. L. Kapitza (1965)*(ed. D. T. Haar), pp. 690-709. Pergamon (Oxford), (Original paper in Russian: Zh. Ekper. Teor. Fiz. **19**, 105–120).

[61] Kapitza, P.L. and Kapitza, S.P. 1965. Wave flow of thin fluid layers of liquid. Zh. Ekper. Teor. Fiz. **19**, (1949), also in Collected Works of LP Kapitza, 1965.

[62] Kawahara, T. 1983. Formation of saturated solitons in a nonlinear diepersive system with instability and dissipation. *Phys. Rev. Lett.* **51**, 381-383.

[63] Kawahara, T. and Toh, S. 1988. Pulse interactions in an unstable dissipative-dispersive nonlinear system. *Phys. Fluids.* **31**, 2103-2111.

[64] Kheshgi, H.S. and Scriven, L.E. 1987. Viscous beads on vertical fiber.Disturbed film flow on a vertical plate. *Phys. Fluids* **30**, 990.

[65] Kistler, S.F. 1984. The fluid mechanics of curtain coating and related viscous free surface flows with contact lines. Ph.D Thesis, University of Minnesota.

[66] Kliakhandler, I.L., David, S.H. and Bankoff, S.G. 2001. Viscous beads on vertical fiber. J. Fluid Mech. **429**, 381.

[67] Lee, J.J. and Mei, C.C. 1996. Solitary waves on an inclined sheet of viscous fluid at high reynolds and moderate weber numbers. J. Fluid Mech. **307**, 191.

[68] Leontidis, V., Vatteville, J., Vlachogiannis, M., Andritsos, N., and Bontozoglou, V. 2010. Nominally two-dimensional waves in inclined film flow in channels of finite width. *Phys. Fluids.* **22**, 112106.

[69] Lindner, A., Bonn, D. and Meunier, J. 2000. Viscous fingering in a shear-thinning fluid. *Phys. Fluids.* **12**, 256-261.

[70] Liu, J. and Gollub, J. P. 1994. Solitary wave dynamics of film flows. *Phys. Fluids.* **6**, 1702-1712.

[71] Liu, J., Schneider, J.B. and Gollub, J.P. 1995. Three-dimensional instabilities of film flows. *Phys. Fluids* **7**, 55-67.

[72] Liu, Q.Q., Chen, L., Li, J.C. and Singh, V.P. 2005. Roll waves in overland flow. *J. Hydrologic Engng.* **10**(2), 110-117.

[73] Liu, K. and Mei, C.C. 1994. Roll waves on a layer of a muddy fluid flowing down a gentle slope -a Bingham model. *Phys. Fluids.* **6**(8), 2577-2589.

[74] Luu, L.-H. and Forterre, Y. 2009. Drop impact of yield-stress fluids. J. Fluid Mech. **632**, 301-327.

[75] Malamataris, N.A. 1991. Computer added analysis of flows on moving and unbounded domains: Phase change fronts and liquid leveling. Ph.D. thesis, University of Michigan, Ann Arbor, MI.

[76] Malamataris, N.A. and Papanastasiou, T.C. 1991. Unsteady free surface flows on truncated domains. *Ind. Eng. Chem. Res.* **30**, 2210.

[77] Malamataris, N.A. and Bontozoglou, V. 1999. Computer aided analysis of viscous film flow along an inclined wavy wall. *J. Comp. Phys.* **154**, 372.

[78] Malamataris, N.A., Vlachogiannis, M. and Bontozoglou, V. 2002. Solitary waves on inclined films: Flow structure and binary interactions. *Phys. Fluids.* **14**, 1082-1094.

[79] Manneville, P. 1990. Dissipative Structures and Weak Turbulence. Academic Press, New York

[80] Mei, C.C. 1966. Nonlinear gravity waves in a thin sheet of viscous fluid. J. Math. Phys. **45**, 266.

[81] Meza, C.E. and Balakotaiah, V. 2008. Modeling and experimental studies of large amplitude waves on vertically falling films. *Chem. Eng. Sci.* **63**, 4704.

[82] Miladinova, S., Lebonb, G. and Toshev, E. 2004. Thin-film flow of a power-law liquid falling down an inclined plate. *J. Non-Newtonian Fluid Mech.* **122**, 69-78.

[83] Millet, S., Botton, B., Rousset, F. and Hadid, H.B. 2008. Wave celerity on a shear-thinning fluid film flowing down an incline. *Phys. Fluids.* **20**, 031701.

[84] Nakaya, C. 1989. Waves on a viscous fluid film down a vertical wall. *Phys. Fluids A,* **1**, 1143.

[85] Ng, C.-O. and Mei, C.C. 1994. Roll waves on a shallow layer of mud modelled as a power-law fluid. J. Fluid Mech. **263**, 151-184.

[86] Nguyen, L.T. and Balakotaiah, V. 2000. Modeling and experimental studies of wave evolution on free falling viscous films. *Phys. Fluids.* **12**, 2236.

[87] Noh, W.F. and Woodward, P. 1976. SLIC (Simple Line Interface Calculation). In proceedings of 5th International Conference of Fluid Dynamics, edited by A. I. van de Vooren and P.J. Zandbergen. *Lecture Notes in Physics* **59**, 330–340.

[88] Northey, P.J. Armstrong, R.C. and Brown, R.A. 1990. Finite element calculation of time-dependent two-dimensional viscoelastic flow with explicitly elliptic momentum equation formulation. *J. Non-Newtonian Fluid Mech.* **36**, 109.

[89] Nosoko, T. and Miyara, A. 2004. The evolution and subsequent dynamics of waves on a vertically falling liquid film. *Phys. Fluids.* **16**(4), 1118-1126.

[90] Nosoko, T., Yoshimura, P.N., Nagata, T. and Okawa, K. 1996. Characteristics of two-dimensional waves on a falling liquid film. *Chem. Eng. Sci.* **51**, 725-732.

[91] Nusselt, W. 1916. Die oberflachenkondensation des wasserdampfes. *Z. VDI* **50**, 541-546.

[92] Olson, M.D. 1977. Comparison of various Finite Element Solution Methods for the Navier-Stokes Equation. Finite Elements in Water Resources, Pentech Press London.

[93] Ooshida, T. 1999. Surface equation of falling film flows with moderate Reynolds number and large but finite Weber number. *Phys. Fluids.* **11**, 3247-3269.

[94] Oron, A., Davis, S.H. and Bankoff, S.G. 1997. Long-scale evolution of a thin liquid films. *Rev. Mod. Phys.* **69**, 931-980.

[95] Orr, F.M. 1976. Numerical simulation of viscous flow with a free surface. Ph.D Thesis, University of Minnesota.

[96] Panga, M.K.R. and Balakotaiah, V. 2003. Low-dimensional models for vertically falling viscous films. *Phys. Rev. Lett.* **90** (15), 1.

[97] Park, C.D. and Nosoko, T. 2003. Three-dimensional wave dynamics on a falling film and associated mass transfer. *AIChE J.* **49**, 2715-2727.

[98] Pascal, J.P. and D'Alesio, S.J.D. 2007. Instability of power-law fluid flows down an incline subjected to wind stress. *Appl. Math. Model.* **31**, 1229-1248.

[99] Popinet, S. 2003. Gerris: a tree-based adaptive solver for the incompressible Euler equations in complex geometries. *J. Comp. Phys.* **190**, 572-600.

[100] Popinet, S. 2009. An accurate adaptive solver for surface-tension-driven interfacial flows. *J. Comp. Phys.* **228**, 5838–5866.

[101] Pradas, M., Tseluiko, D. and Kalliadasis, S. 2011. Rigorous coherent-structure theory for falling liquid films: Viscous dispersion effects on bound-state formation and self-organization. *Phys. Fluids* **23**, 044104.

[102] Prokopiou, T., Cheng, M. and Chang, H.C. 1991. Long waves on inclined films at high reynolds number. J. Fluid Mech. **222**, 665.

[103] Pumir, A., Manneville, P. and Pomeau, Y. 1983. On solitary waves running down an inclined plane. *J. Fluid Mech.* **135**, 27-50.

[104] Ramaswamy, B., Chippada, S. and Joo, S.W. 1996. A full-scale numerical study of onterfacial instabilities in thin-film flows.. *J. Fluid Mech.* **325**, 163-194.

[105] Reynolds, O. 1986. Philos. Trans. R. Soc. London **177**, 157.

[106] Richardson, S.M. 1989. Fluid Mechanics, Hemisphere. New York.

[107] Roberts, A.J. 1996. Low-dimensional models of thin film fluid dynamics. *Phys. Lett. A* **212**, 63-71.

[108] Roberts, A.J. and Li, Z.-Q. 2006. An accurate and comprehensive model of thin fluid flows with inertia on curved substrates. J. Fluid Mech. **553**, 33-73.

[109] Rousset, F., Millet, S., Botton, V. and Hadid, H.B. 2007. Temporal stability of Carreau fluid flow down an incline. *J. Fluid Eng.* **129** (7), 913-920.

[110] Rochefort, W.E. and Middleman, S. 1987. Rheology of xanthan gum: salt, temperature and strain effects in oscillatory and steady shear experiments. *J. Rheology.* **31**, 337-369.

[111] Ruyer-Quil, C. and Manneville, P. 1998. Modeling film flows down inclined planes. *Eur. Phys. J. B* **6**, 277.

[112] Ruyer-Quil, C. and Manneville, P. 2000. Improved Modeling of flows down inclined plane. *Eur. Phys. J. B* **15**, 357-369.

[113] Ruyer-Quil, C. and Manneville, P. 2002. Further accuracy and convergence results on the modelling of flows down inclined planes by weighted-residual approximations. *Phys. Fluids.* **14**, 170.

[114] Ruyer-Quil, C. and Manneville, P. 2005. On the speed of solitary waves running down a vertical wall. J. Fluid Mech. **531**, 181–190.

[115] Ruyer-Quil, C., Treveleyan, P., Giorgiutti-Dauphiné, F., Duprat, C. and Kalliadasis, S. 2008. Ann. Rev. Fluid Mech. **20**: 487-526. J. Fluid Mech. **603**, 431-462.

[116] Ruyer-Quil, C., Chakraborty, S. and Dandapat, B.S. 2011. Wavy regime of a power-law film flow. J. Fluid Mech. **508**, 1-37.

[117] Ruyer-Quil, C. and Kalliadasis, S. 2012. Wavy regimes of film flow down a fiber. *Phys. Rev. E* **85**, 046302.

[118] Saito, H. and Seriven, L.E. 1981. Study of coating flow by the Finite Element Method. J. Comp. Phys. **42**, 53.

[119] Salamon, T.R., Armstrong, R.C. and Brown, R.A. 1994. Traveling waves on inclined films: Numerical analysis by the finite-element method. *Phys. Fluids* **6**, 2202.

[120] Saramito, P. 2007. A new constitutive equation for elastoviscoplastic fluid flows. *J. Non-Newtonian Fluid Mech.* **145** 1-14.

[121] Saramito, P. 2009. A new elastoviscoplastic model based on the Herschel-Bulkley viscoplastic model. *J. Non-Newtonian Fluid Mech.* **158** 154-161.

[122] Scheid, B., Ruyer-Quil, C., Thiele, U., Kabov, O.A., Legros, J.C., and Colinet, P. 2005. Validity domain of the Benney equation including the Marangoni effect for closed and open flows. J. Fluid Mech. **527**, 303-335.

[123] Scheid, B., Ruyer-Quil, C. and Manneville, P. 2006. Wave patterns in film flows: modelling and threedimensional waves. J. Fluid Mech. **562**, 183-222.

[124] Schlichting, H. and Gersten, K. 2001. Boundary-Layer Theory, eighth edn. Springer-Verlag (New York).

[125] Seevaratnam, G.K., Suo, Y., Ramé, E., Walker, L.M. and Garoff, S. 2007. Dynamic wetting of shear thinning fluids. *Phys. Fluids.* **19**, 012103.

[126] Shkadov, V.Ya. 1967. Wave modes in the flow of thin layer of a viscous liquid under the action of gravity. *Izv. Akad. Nauk SSSR, Mekh. Zhidk. Gaza,* **1**, 43.

[127] Shkadov, V.Ya. 1968. Theory of wave flows of a thin layer of a viscous liquid. *Izv. Akad. Nauk SSSR, Mekh. Zhidk. Gaza,* **2**, 20.

[128] Silliman, W.J. 1979. Viscous film flows with contact lines. Ph.D Thesis, University of Minnesota.

[129] Sisoev, G.M., Dandapat, B.S., Matveyev, K.S. and Mukhopadhyay, A. 2007. Bifurcation analysis of the travelling waves on a falling power-law fluid film. *J. Non-Newtonian Fluid Mech.* **141**, 128-137.

[130] Sivashinsky, G.I. and Michelson, D.M. 1980. On the irregular wavy flow of a liquid film downa vertical plane. *Prog. Theor. Phys.* **63**, 2112.

[131] Smith, M.K. 1990. The mechanism for the long-wave instability in thin liquid filmss. J. Fluid Mech. **217**, 469-485.

[132] Song, K.-W., Kim, Y.-S. and Chang, G.-S. 2006. Rheology of concentrated xanthan gum solutions: steady-shear flow behavior. *Fibers Polym.* **7**, 129-138.

[133] Strang, G. and Fix, G.J. 1973. An analysis of the finite element method. Second Ed., Prentice Hall Inc.

[134] Takahama, H. and Kato, S. 1980. Longitudinal flow characteristics of vertically falling liquid films without concurrent gas flow. *Int. J. Multiphase Flow* **6**, 203.

[135] Tanner, R.I. 1985. *Engineering Rheology* (Clarendon Press, Oxford).

[136] Tailby, S.R. and Portalski, S. 1962. The determination of the wavelength on a vertical film of liquid flowing down a hydrodynamically smooth plat. *Trans. Inst. Chem. Eng.* **40**, 114.

[137] Thomas, H.A. 1939. The propagation of waves in steep prismatic conduits. *In: Proc. Hydraulics Conf.*, 214-229. Univ. of Iowa City.

[138] Tihon, J., Serifi, K., Argyriadi, K. and Bontozoglou, V. 2006. Solitary waves on inclined films: their characteristics and the effects on wall shear. *Experiments in Fluids* **41**, 79-89.

[139] Trifonov, Y.Ya. and Tsvelodub, O.Yu. 1991. Nonlinear waves on the surface of a falling liquid film. part 1. waves of the first family and their stability. J. Fluid Mech. **229**, 531.

[140] Tsvelodub, O.Yu. and Trifonov, Y.Ya. 1989. On steady-state travelling solutions of an evolution describing the behaviour of disturbances in an active dissipative media. *Physica D.* **39**, 336.

[141] Tsvelodub, O.Yu. and Trifonov, Y.Ya. 1992. Nonlinear waves on the surface of a falling liquid film. part 2. bifurcations of the first-family waves and other types of nonlinear waves. J. Fluid Mech. **244**, 149.

[142] Usha, R., Millet, S., Benhadid, H. and Rousset, F. 2011. Shear-thinning film on a porous subtrate: Stability analysis of a one-sided model. *Chemical Engineering Science* **66** (22), 5614–5627.

[143] Vlachogiannis, M. and Bontozoglou, V. 2001. Observations of solitary wave dynamics of film flows. J. Fluid Mech. **191**, 435.

[144] Vlachogiannis, M., Samandas, A., Leontidis, V. and Bontozoglou, V. 2010. Effect of channel width on the primary instability of inclined film flow. *Phys. Fluids.* **22**, 12106.

[145] Whitcomb, P.J. and Macosko, C.W. 1978. Rheology of xanthan gum. *J. Rheology* **22**, 493-505.

[146] Whitham, G.B. 1974. *Linear and Nonlinear Waves.* Wiley-Interscience.

[147] Yih, C.-S. 1955. Stability of two-dimensional parallel flows for three dimensional disturbances. *Quart. Appl. Math.* **12**, 434-435.

[148] Yu, L.Q., Wasden, F.K., Dukler, A.E. and Balakotaiah, V. 1991. Nonlinear waves on the surface of a falling liquid film. part 1. waves of the first family and their stability. J. Fluid Mech. **229**, 531.

[149] Yu, L.-Q., Wasden, F.K., Dukler, A.E. and Balakotaiah, V. 1995. Nonlinear evolution of waves on falling films at high Reynolds numbers. *Phys. Fluids* **7**, 1886-902.

Résumé

Dans cette thèse, la dynamique et la stabilité d'un film mince tombant sur un plan incliné sous l'action de la pesanteur sont étudiées. Un schéma de la géométrie étudiée est présenté dans la figure A.1. Un film mince s'écoulant sur un plan incliné ou une paroi verticale en présence de surface libre présente une variété de comportements fascinants. La dynamique des ondes à la surface de films minces est important pour nombre d'industries en raison de ses effets dramatiques sur les transferts de masse, de chaleur et de quantité de mouvement qui déterminent la conception de colonnes de distillation et d'adsorption, des évaporateurs et les condenseurs, ainsi que la qualité des revêtements d'émulsions photographiques, de peintures de protection etc. En outre, la stabilité d'un écoulement de film tombant le long d'un plan incliné sous l'action de la pesanteur est un sujet de recherche fondamental. Le travail présenté dans ce manuscrit porte principalement sur les effets de la rhéologie du fluide sur la dynamique complexe des ondes qui se développent à la surface libre. Pour cet objectif, trois problèmes ont été explorés pour des valeurs faible à modérée du nombre de Reynolds.

(I) Ondes solitaires sur un film tombant newtonien où je considère un film newtonien s'écoulant sur un plan incliné avec pour objectif de décrire les propriétés (vitesse de phase, amplitude maximale et la forme) des ondes solitaires, voir le chapitre 3. Les films tombants ont la particularité d'être des écoulements à faible nombre de Reynolds dont le régime ondulatoire est supercritique et déclenché par une instabilité grande de longueur d'onde. Par conséquent, les ondes observées à la surface du film sont beaucoup plus longues que l'épaisseur typique du film et une séparation des échelles peut être utilisé avec l'introduction d'un paramètre du film $\epsilon \sim \partial_{x,t}$ rendant compte des déformations lentes en temps et en espace des ondes par rapport à la diffusion rapide au travers de la couche de film rendue possible par la viscosité. Les films tombants sont donc susceptibles d'une description détaillée en termes de modèles de faible dimension. Pour être plus précis, une description de l'écoulement en termes d'un nombre limité de variables fonctions du temps t et de la position x sur le plan peut être substituée aux équations de Navier-Stokes, après élimination de la coordonnée normale au plan y.

Le problème de la stabilité d'un écoulement laminaire d'un film fluide visqueux sur un plan incliné sous l'effet de la gravité a d'abord été formulé et résolu numériquement par Yih [147]. Les écoulements de films liquides newtoniens ont été étudiées depuis un certain temps déjà, en commençant avec des résultats classiques tels que l'équation Benney ou le modèle à deux équations de Shkadov. La phénoménologie d'un tel écoulement est esquissée au chapitre 2. Le travail présenté au chapitre 3 peut servir de validation à la technique des résidus pondérés initiée par Ruyer-Quil et Manneville [111, 112, 113, 114]. Un test crucial pour la validation des modèles consiste en la reproduction des propriétés (forme, vitesse de phase, amplitude) des ondes solitaires en fonction de la distance au seuil de l'instabilité. La plupart des modèles prédisent un comportement similaire près du seuil (apparition du régime visco-gravitaire - ce qui correspond à un équilibre entre la traînée visqueuse sur

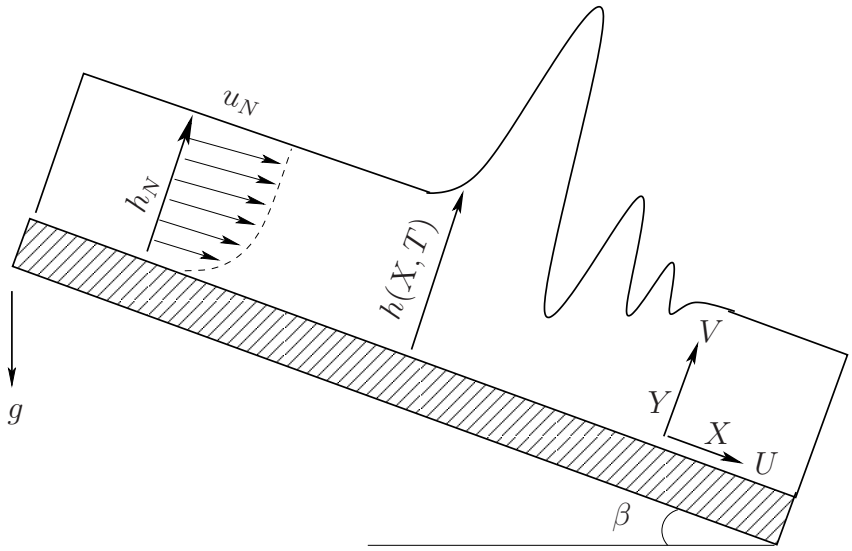

Figure A.1: Un croquis de la géométrie d'un film mince tombant sur un plan incliné.

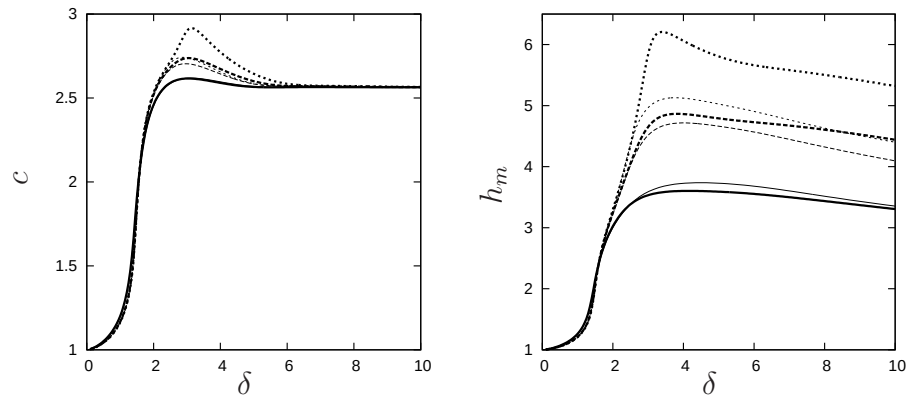

(a) (b)

Figure A.2: **DNS - modèle au second ordre** La vitesse de phase c et l'amplitude h_m des ondes solitaires en fonction du nombre de Reynolds réduit δ. Les traits épais et les traits minces correspondent à la DNS et au modèle au second ordre respectivement. Traits pleins $\Gamma = 193$ (solution eau-glycérine); pointillés longs $\Gamma = 3400$ (eau), pointillés courts $\Gamma = 10000$. Vitesse de phase asymptotique, $c \approx 2.57$.

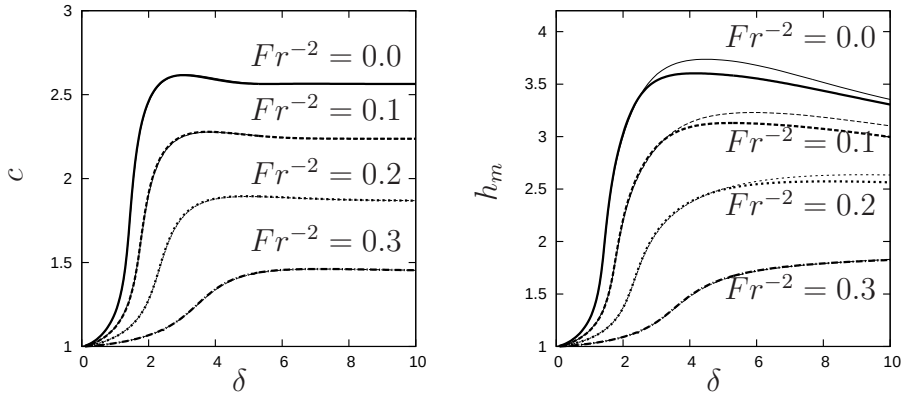

Figure A.3: Vitesse de phase a) et b) amplitude des ondes en fonctions de δ pour une paroi verticale ($1/Fr^2 = 0.0$) et des parois inclinées ($1/Fr^2 = 0.1, 0.2, 0.3$). Les traits épais et les traits minces correspondent à la DNS et au modèle au second ordre respectivement. Le fluide correspond à un nombre de Kapitza $\Gamma^* = 193$.

le mur et l'accélération de la pesanteur, où l'inertie joue un rôle seulement perturbatif) - mais les résultats présentent de grandes différences dans le régime intermédiaire et aux grandes valeurs de δ, c'est à dire lorsque l'inertie devient significative (transition et régime inertiel). Ainsi, une simulation rigoureuse des équations de Navier-Stokes est nécessaire pour résoudre ce problème.

Dans la figure. A.2 les résultats du modèle du second ordre (vitesse de phase et amplitude maximale de l'onde) sont comparés aux simulations numériques directes DNSs (où les équations de Navier-Stokes sont résolues en utilisant la méthode des éléments finis et une projection de Galerkin). Les ondes presque solitaires sont calculées en considérant un domaine de calcul assez grand afin que les propriétés des ondes convergent asymptotiquement vers la limite de ondes solitaires (domaine infini). Un phénomène de formation d'un contre-écoulement est observé au creux des ondes capillaires lorsque l'inertie est grande. Puisque l'amplitude des ondes dépend de l'inertie, la formation d'un contre-écoulement est liée à l'amplitude des ondes capillaires qui ne seront pas observées lorsque les effets de dispersion visqueuse deviennent forts, c'est à dire, lorsque les ondulations capillaires sont amorties. La vitesse de phase des ondes solitaires n'est pas affectée par la viscosité du fluide et elle se rapproche de la limite asymptotique à ($\delta \gg 1$) alors que l'amplitude de l'onde dépend de la viscosité et est atténuée à faibles nombres de Kapitza (Γ). On observe également que, pour une même valeur du nombre de Reynolds réduit δ, la vitesse de phase et l'amplitude des ondes deviennent plus faibles à l'approche du seuil d'instabilité

correspondant à une valeur constante du nombre Froude. Le seuil de l'instabilité d'onde longue, $Re_c = 5\cot\beta/6$ peut en effet se récrire en terme du nombre de Froude $Fr_c^{-2} = 2/5$. Les DNSs confirment qu'il n'y a plus d'ondes au-dessus de cette valeur critique et que, par ailleurs, la vitesse de phase et l'amplitude maximale de l'onde solitaire atteignent les valeurs les plus élevées à $Fr^{-2} = 0$ pour un écoulement le long d'une paroi verticale. Dans la figure A.3, les résultats du modèle au second ordre et des DNSs sont comparés en ce qui concerne la vitesse de phase et la hauteur d'onde pour un plan vertical ou incliné. Le modèle au second ordre prédit correctement la vitesse, l'amplitude et la forme de l'onde solitaire et présente un bon accord avec les résultats des simulations numériques directes.

Au chapitre 4, je décris différents types de fluides non-newtoniens et de lois de comportement que je prends en considération aux chapitre 5 et chapitre 6 dans le contexte des films tombants.

(II) Fluides newtoniens généralisés où je considère un fluide en loi de puissance qui coule sur un plan incliné sous l'action de l'accélération gravitationnelle. Un écoulement de fluide en loi de puissance est modélisé dans le cadre de l'approximation de lubrification au moyen de la technique des résidus pondérés en termes de l'épaisseur locale du film h et du débit local q (où $q = \int_0^h u dy$). L'étude porte sur les effets d'un fluide rhéofluidifiant ou rhéoépaississant sur la stabilité de la couche mince de fluide cisaillé. Dandapat et Mukhopadhay [32] ont étudié les solutions quasi-staionnaires d'une équation d'évolution modélisant la dynamique d'un film de fluide en loi de puissance. Ils ont constaté que l'interaction non linéaire entre les ondes cinématiques, inertielles et de gravité était responsable de la formation des ondes sur un film mince d'un fluide en loi de puissance et que l'indice n de la loi de puissance joue un rôle essentiel dans le mécanisme de formation des ondes. Il est donc souhaitable d'étudier les régimes d'ondes qui se forment à la surface du film en faisant varier les différents paramètres pour une meilleure compréhension des phénomènes physiques. Un modèle en loi de puissance représente une classe de fluides newtoniens généralisés qui ne présentent pas de propriétés de relaxation des contraintes, d'élasticité ou de plasticité. Toutefois, ces fluides exhibent un comportement rhéofluidifiant (pseudo-plastique) ou rhéoépaississant (dilatant) (pour plus de détails voir les chapitres 4 et 5). Une loi de comportement en loi de puissance permet de décrire le comportement des suspensions colloïdes et d'une gamme de liquides polymères et de liquides biologiques à faible poids moléculaire, est utile pour la glaciologie, restitue la rhéologie du sang. Cette loi de comportement diffère de celle d'un fluide newtonien en ce que la viscosité dépend de la partie symétrique du gradient de vitesse de sorte que, sous un cisaillement simple, la viscosité dépend de la vitesse de cisaillement. Pour être plus précis de tels effets sont sans conséquence, la principale différence avec le fluide newtonien étant le comportent rhéofluidifiant ou rhéoépaississant.

Les ondes à rouleaux (ou "roll waves"), c'est-à-dire des ressauts hydrauliques reliés par des sections d'écoulements laminaires, sont généralement observées en milieu naturel dans les régimes torrentielles des rivières et aussi dans les conduits faits de main d'homme tels que les déversoirs [41, 24, 58]. L'apparition possible d'ondes à rouleaux était déjà prise

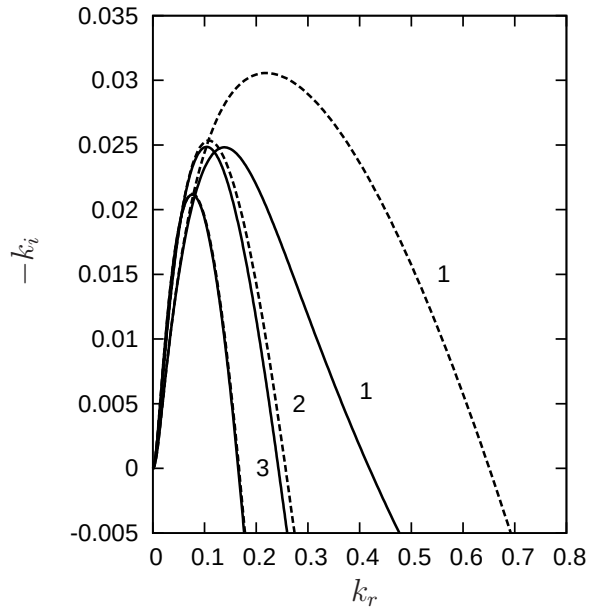

(a)

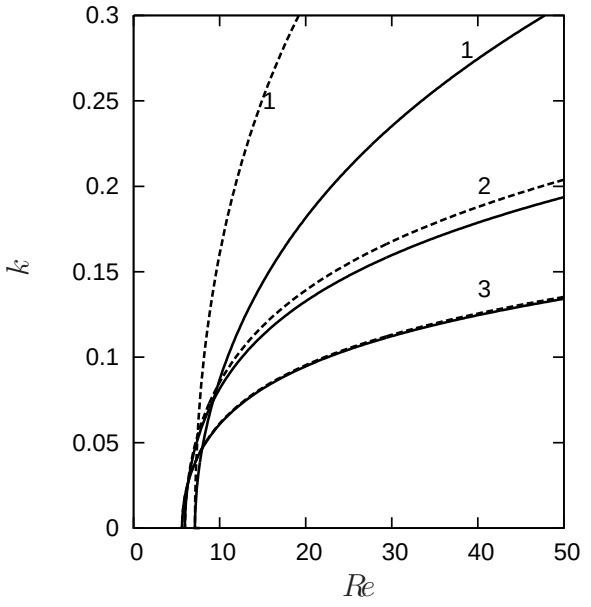

(b)

Figure A.4: Taux de croissance spatial $-k_i$ en fonction du nombre d'onde k_r à $Re = 100$. (b) courbes de stabilité marginale dans le plan (Re, k). L'angle d'inclinaison est $\beta = 15°$. Les numéros font référence aux propriétés de différentes solutions de gomme xanthane (voir le chapitre 5). Les lignes continues correspondent à des solutions du problème d'Orr-Sommerfeld. Les lignes pointillées correspondent aux résultats lorsque la tension de surface n'est pas prise en compte ($We = 0$).

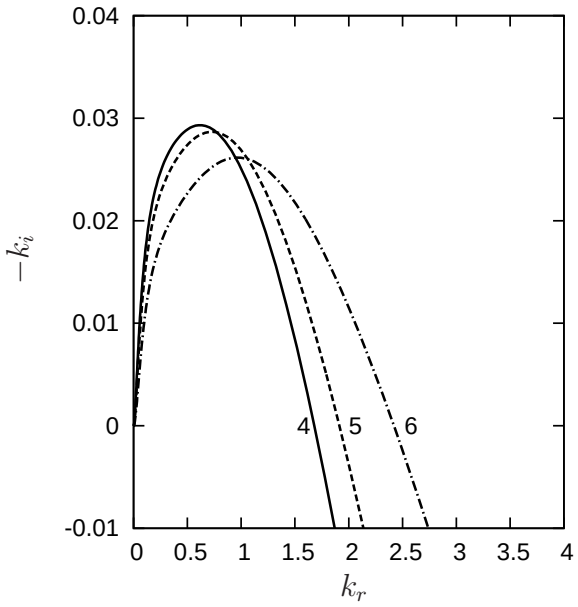

(a)

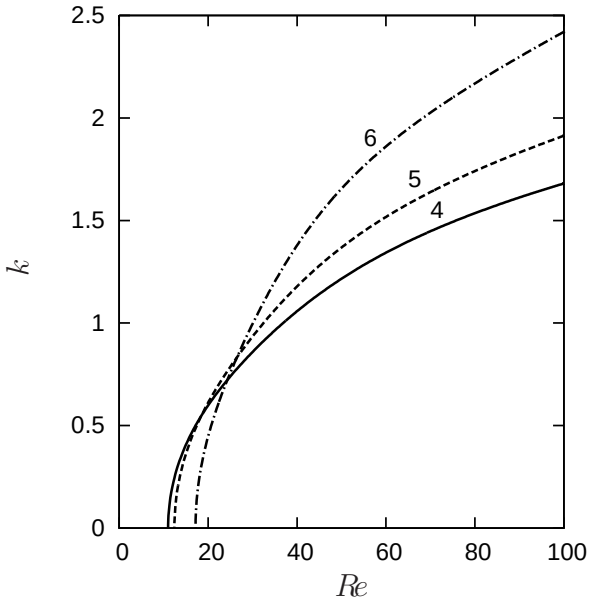

(b)

Figure A.5: Analyse spatiale de stabilité linéaire fondée sur le problème d'Orr-Sommerfeld. (a) Taux de croissance spatiale $-k_i$ par rapport au nombre d'onde k_r à $Re = 100$. (b) courbes de stabilité marginale dans le plan (Re, k). L'angle d'inclinaison est $\beta = 15°$. Les numéros font références aux propriétés de différentes solutions de fécule de maïs (voir le chapitre 5).

en compte dans la conception d'aqueducs par les ingénieurs romains [45]. L'apparition d'ondes à rouleaux est le résultat d'un mécanisme d'instabilité qui est similaire à la formation d'ondes solitaires à la surface d'un film liquide laminaire tombant sur un plan incliné. Dans ce dernier cas, la tension de surface empêche le déferlement de l'onde et arrête la la formation des ressauts hydrauliques. Ces ondes sont parfois nommées 'ondes capillaires à rouleaux' [8]. En tant que tels, les écoulements de film peuvent être vus comme un système miniature dont la dynamique ondulatoire est étroitement liée au régime torrentiel des cours d'eau à des débits bien plus importants.

Dans la figure. A.9 formation d'ondes de rouleaux observée dans un mélange d'eau et de kaolinite. Les ondes à rouleaux peuvent également être observées dans les processus de ruissellement par la pluie avec une augmentation potentielle de l'érosion des sols [72]. Dans les estuaires, les rivières peuvent porter de grande quantité d'argile et les coulées de boue qui en résultent sont souvent pulsés et ressemblent à des ondes à rouleaux dans des écoulements turbulents en eau claire [73]. Pour ces deux derniers exemples, les interactions entre les particules d'argile peuvent créer des structures microscopiques étendues qui sont déformées et peu à peu décomposées quand une contrainte est appliquée. En conséquence, la réponse du fluide à une contrainte est non linéaire et cette boue présente un comportement rhéofluidifiant. Ng et Mei [85] ont étudié les ondes à rouleaux à la surface d'une couche mince de boue modélisée par un fluide en loi de puissance. Les résultats ont montré que les ondes très longues présentant une dissipation au niveau des fronts discontinus, ne pouvaient pas être observés si l'écoulement uniforme est linéairement stable et lorsque le fluide est légèrement non-newtonien. Toutefois, lorsque le fluide présente un comportement non-newtonien marqué, les ondes à rouleaux de très grandes longueurs peuvent encore exister, même si l'écoulement uniforme correspondant est stable vis à vis de perturbations infinitésimales. Hwang *et al.* [52] ont étudié la stabilité linéaire d'un film de fluide en loi de puissance tombant sur un plan incliné en utilisant une méthode intégrale. Les résultats révèlent que le système est plus instable lorsque l'indice n diminue.
Le problème d'Orr-Sommerfel est résolu afin d'étudier l'analyse de stabilité linéaire d'un film d'épaisseur uniforme. La cohérence du modèle est assurée jusqu'au premier ordre vis à vis du paramètre du film pour ce qui concerne l'inertie et au second ordre pour les termes visqueux, ce qui est suffisant pour capturer le seuil de l'instabilité et l'amortissement des ondes courtes. La figure. A.4(a) illustre le comportement du taux de croissance spatial $-k_i = -\Im(k)$ en fonction du nombre d'onde $k_r = \Re(k)$. La figure. A.4(b) présente la courbe de stabilité marginale, c.-à-dire le nombre d'onde de coupure k_c en fonction du nombre de Reynolds Re. Comme la concentration en gomme xanthane des solutions augmente, le seuil d'instabilité est déplacé avec des valeurs du nombre de Reynolds critique plus basse, tandis que la gamme de nombres d'onde instables est réduite. Les effets rhéofluidifiants favorisent donc l'instabilité primaire près du seuil [83], mais ont aussi tendance à stabiliser l'écoulement de base loin du seuil. Les analyses d'Orr-Sommerfeld ont été comparées avec ($We \neq 0$) ou sans la tension de surface ($We = 0$). En ce qui concerne les solutions rhéoépaississantes de fécule de maïs, les courbes de stabilité marginale dans

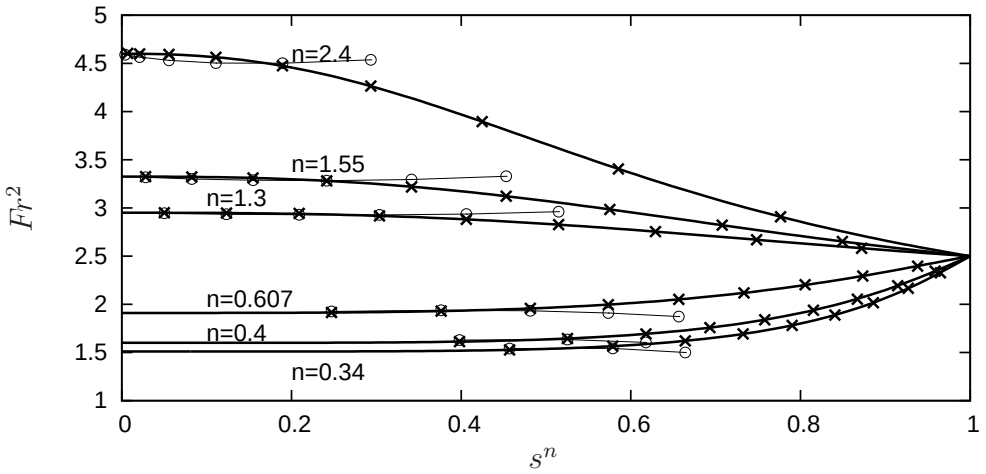

Figure A.6: Nombre de Froude critique $Fr^2 = Re/Ct$ en fonction de l'épaisseur de la région newtonienne s^n pour des valeurs différentes de l'indice n de loi de puissance. Les traits pleins correspondent au modèle et les croix aux solutions numériques du problème d'Orr-Sommerfeld (voir le chapitre 5).

le plan (Re, k) sont présentées dans la figure. A.5. Les numéros 4, 5 et 6 se réfèrent aux propriétés des solutions de fécule de maïs étudiées au chapitre 5. Avec une augmentation de la concentration en fécule de maïs, le seuil d'instabilité est déplacé vers de plus grandes valeurs du nombre de Reynolds critique, alors que la gamme des nombre d'onde instables est élargie. Contrairement à ce qui est observé pour les fluides rhéofluidifiants, les effets rhéoépaississants défavorisent donc l'instabilité primaire près du seuil [83], mais ont aussi tendance à déstabiliser l'écoulement de base loin du seuil. Dans la figure. A.6 j'ai représenté les variations du nombre de Froude critique en fonction de l'épaisseur relative s^n de la région newtonienne près de la surface libre pour l'écoulement de base pour des fluides rhéoépaississants et rhéofluidifiants. Le seuil prédit par le modèle à deux équations est comparé à celui obtenu en résolvant numériquement le problème d'Orr-Sommerfeld. Un accord remarquable a été obtenu, et en particulier, le seuil d'instabilité est précisément prédit.

Les comparaisons avec les simulations numériques directes diphasiques montrent que le modèle prédit correctement la vitesse de phase, l'amplitude maximale et la forme des ondes périodiques, et en particulier, les détails des ondulations capillaires, la région de choc capillaire, précédant les fronts principaux sont prédits correctement. Les comparaisons avec l'analyse de la stabilité d'Orr-Sommerfeld et la DNS présentent un accord convaincant dans les régimes à la fois linéaires et non linéaires. Les mécanismes de l'instabilité primaire ont été étudiés dans le cadre de la hiérarchie d'ondes de Whitham. L'influence des effets rhéofluidifiants ou rhéoépaississants sur l'instabilité primaire est non triviale. Dans

γ_1

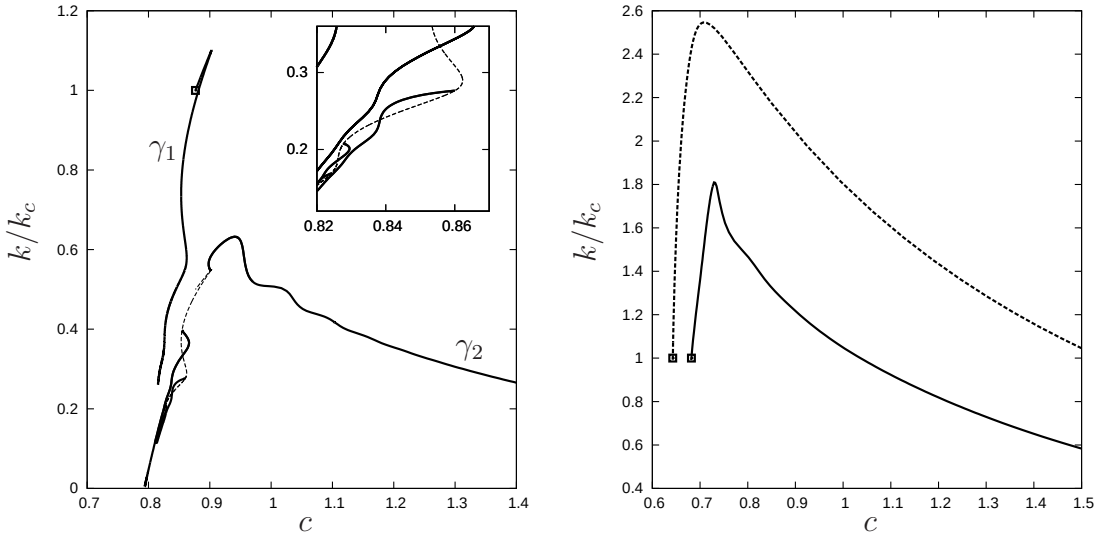

(a) (b)

Figure A.7: Vitesse de phase c des ondes propagatives en fonction du nombre d'onde k/k_c normalisé par le nombre d'onde de coupure k_c. La bifurcation de Hopf pour k égal au nombre d'onde de coupure k_c est indiqué par des carrés. (a) solution rhéofluidifiante de xanthane dans de l'eau à 500 ppm, les lignes pointillées (traits mixtes) représentent les lieux des solutions formées de deux ou quatre ondes γ_1. $Re = 20$, $\beta = 15°$. (b) Les traits pointillés et continus correspondent à des solutions de xanthane à 1500 ppm et 2500 ppm (voir chapitre 5).

le régime non-linéaire, le nombre d'onde et l'amplitude des ondes lentes γ_1 et rapides γ_2 diminue à mesure que l'indice n de la loi de puissance est réduit. Les ondes capillaires à l'avant du front sont atténuées par la viscosité. En présence de ces termes visqueux, les ondes γ_2 apparaissent à partir d'une bifurcation de Hopf (voir fig. A.7) et les ondes γ_1 à partir des ondes γ_2 par une bifurcation en doublement de période. Les effets rhéofluidifiants accélèrent les ondes solitaires et favorisent une apparition sous-critique des ondes non linéaires à un nombre d'onde plus grand que le nombre d'onde de coupure linéaire. Une stabilité conditionnelle de l'écoulement est ainsi observée. Ce phénomène résulte d'une réduction de la viscosité effective à la surface libre. En comparaison avec la DNS, les simulations de la réponse temporelle du film fondé sur le modèle aux résidus pondérés permet de reproduire de manière satisfaisante la stabilité conditionnelle du film.

(III) Film tombant viscoplastique où je considère un film viscoplastique tombant sur un plan incliné qui est décrit par une loi de comportement de Herschel-Bukley au chapitre 6. L'élasticité de la région pseudo-bouchon près de l'interface est prie en compte par une relation constitutive élasto-viscoplastique formulée par Saramito [121]. Un modèle est obtenu sous forme de quatre équations d'évolution pour l'épaisseur du film, le débit local et les amplitudes des contraintes normales et tangentielles. La stabilité d'un film tombant de liquide viscoplastique est explorée dans ce chapitre, dans le but de déterminer le nombre de Reynolds critique pour l'apparition du seuil de l'instabilité. En fait, certains arguments de stabilité indiquent qu'une instabilité interfaciale est absente pour les films viscoplastiques [8]. L'essence de cet argument est associé à la façon dont on perturbe les régions de l'écoulement qui ne sont pas encore déformées. Au sein d'un film viscoplastique d'épaisseur uniforme, une telle région se trouve toujours près de la surface libre, formant un bouchon rigide. Balmforth et Liu [8] ont d'abord cherché à décrire l'apparition d'ondes de rouleaux observables dans les coulées de boue. En conséquence, ils ne considèrent pas la tension de surface, ni les effets visqueux élongationnels. Dans ce cadre, des perturbations de faible amplitude à la surface libre sont suffisants pour déclencher l'instabilité et les écoulements de films viscoplastiques devraient être conditionnellement stable. Afin de décrire la dynamique d'un film viscoplastique, la tension de surface et la diffusion visqueuse d'origine élongationelle doivent être prises en compte. Par conséquent, la théorie du pseudo-bouchon proposée par Balmforth et Liu [8] est adaptée à l'aide de la loi constitutive proposée par Saramito [121] au chapitre 6.

Outre ses propriétés rhéofluidifiantes, une autre propriété importante de la boue est que les interactions entre les particules d'argile permettent de créer des structures microscopiques qui résistent à un certaine contrainte avant de se déformer et de permettre au fluide de s'écouler. Ainsi, la boue est un fluide à seuil. Ces effets viscoplastiques jouent un rôle clé dans la dynamique des écoulements de boue et place ce fluide dans le domaine de la mécanique des fluides non-newtoniens. Des coulées intermittentes ont été observées dans les écoulements de boue dans des rivières inondées ainsi que dans des canaux (Engelund & Wan [43], Coussot [29]). Une analyse de stabilité linéaire donne des valeurs du nombre de Reynolds critique en accord remarquable avec l'analyse d'Orr-Sommerfeld. La

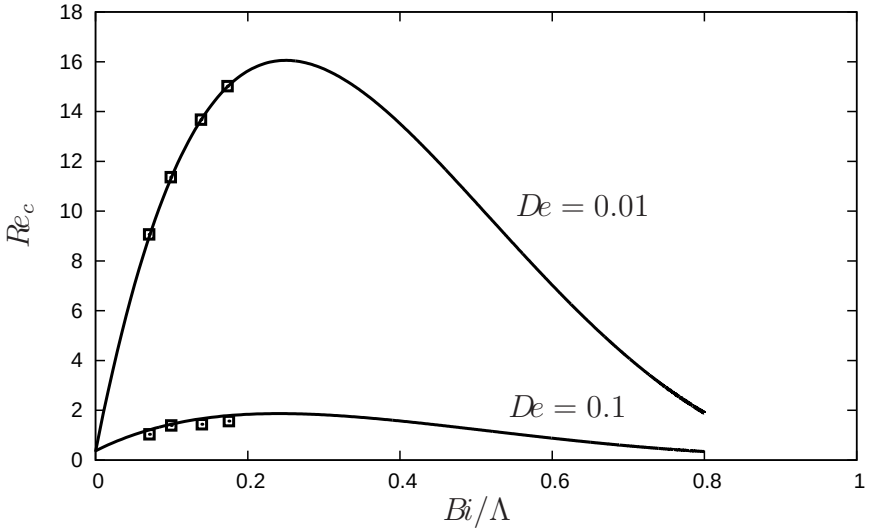

Figure A.8: Nombre de Reynolds critique Re_c en fonction de l'épaisseur relative Bi/Λ de la région de pseudo-bouchon. Les lignes continues correspondent au modèle à quatre équations et les carrés font référence aux solutions numériques du problème d'Orr-Sommerfeld. L'indice de la loi de puissance est $n = 0.5$ et l'angle d'inclinaison est $\beta = 45°$ (cf. chapitre 6).

figure A.8 représente le nombre de Reynolds critique en fonction de l'épaisseur relative de la région pseudo-bouchon Bi/Λ. Le résultat du problème d'Orr-Sommerfeld présente un bon accord avec le résultat du modèle à quatre équations en ce qui concerne le nombre de Reynolds critique. Comme prévu, l'abaissement du nombre de Deborah a un effet stabilisant. En effet, à la limite $De = 0$ le bouchon est solide et ne peut plus se déformer, et par conséquent,le seuil d'instabilité est repoussé à l'infini $Re_c \to \infty$. Pourtant, l'effet stabilisateur de l'inélasticité du bouchon disparaît lorsque $Bi \to 0$. Cela peut être expliqué par la disparition de la région bouchon. Curieusement, une suppression de cet effet stabilisant est aussi observé lorsque le bouchon commence à envahir l'ensemble du domaine fluide.

Comme perspectives possibles à ce travail, je tiens à mentionner l'importance des phénomènes d'écoulement de fluides complexes pour comprendre certains problèmes géophysiques tels que les laves torrentielles, les écoulements de débris ou le ruissellement en lien avec les phénomènes d'érosion. Une suite possible de mon travail serait de tenir compte d'un glissement à la paroi pour simuler des écoulement des boues réels et des avalanches de neige par exemple. Il est possible d'obtenir un modèle pour un écoulement de film tombant en tenant compte d'une paroi ondulée, rugueuse ou non-plane, et de considérer des instabilités secondaires tridimensionnelles.

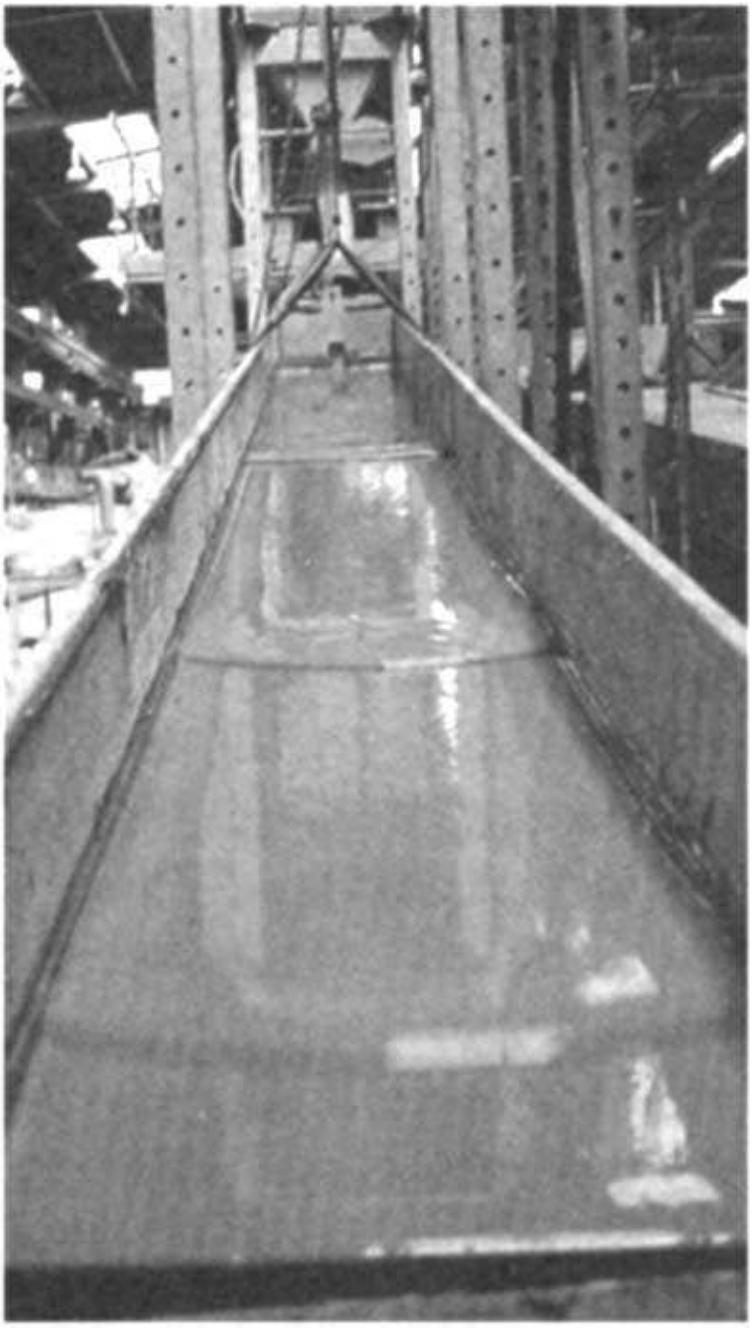

Figure A.9: Observation d'ondes à rouleaux dans un ecoulement d'un mélange d'eau et de kaolinite, tiré de Coussot [29].